Colloidal flocks in challenging environments

Alexandre Morin

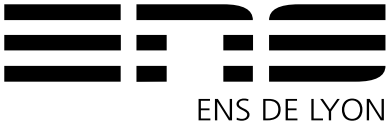

Numéro National de Thèse : 2018LYSEN047

THÈSE de DOCTORAT DE L'UNIVERSITÉ DE LYON
opérée par
l'École Normale Supérieure de Lyon

École Doctorale N°52
École Doctorale de Physique et Astrophysique de Lyon (PHAST)

Spécialité de doctorat : Physique

Soutenue publiquement le 18/09/2018, par :

Alexandre Morin

Colloidal flocks in challenging environments

Troupeaux colloidaux en milieux défavorables

Devant le jury composé de :

Bartolo, Denis	Professeur	ENS de Lyon	Directeur de thèse
Baskaran, Aparna	Associate Professor	Brandeis University	Rapporteure
Bocquet, Lydéric	Directeur de recherche	ENS Paris	Examinateur
Cipelletti, Luca	Professeur	L2C	Examinateur
Cottin-Bizonne, Cécile	Directrice de recherche	ILM	Examinatrice
Dauchot, Olivier	Directeur de recherche	Gulliver	Rapporteur
Kellay, Hamid	Professeur	LOMA	Examinateur

Je remercie Denis qui a tant fait pour moi ces dernières années ! Pour sa confiance des premiers jours qu'il a sans cesse renouvelée, pour ses projets toujours ambitieux et passionnants, pour son implication quotidienne dans leurs réalisations, et pour plein d'autres choses encore, comme avoir donné à ces belles années une saveur des 80's...

Je suis reconnaissant aux membres du Laboratoire de Physique au sein duquel il a toujours fait bon travailler. Je remercie Fatiha et Laurence pour leur accueil et pour avoir si souvent simplifié commandes et autres procédures administratives. Je remercie Thierry pour son attention et sa bienveillance au quotidien.

J'ai eu la chance de rejoindre le groupe de Denis il y a très, très longtemps. Je remercie Jean-Baptiste et Nicolas pour m'avoir beaucoup appris et pour leurs travaux qui ont constitué une base solide de ma recherche.

Denis a su sans cesse maintenir un groupe nombreux et dynamique. Je remercie Céleste pour avoir partagé joies et peines en salle de manips, sur les terrains de volley et le sable de Majorque. Je remercie Nicolas (3ème du nom) pour les échanges qu'on a eu tout au long de ces trois ans et ses jeux de mots audacieux. Je remercie Delphine qui, bien qu'ayant subi quelques défaites au fleuret, a veillé à mes côtés sur nos troupeaux colloïdaux. Je remercie Amélie pour avoir pris la relève à mon départ. Je suis certain que les découvertes ne vont pas tarder et les loukoums approcher l'excellence. Je remercie Joost, Michael et David, tous trois postdocs aux projets variés, qui m'ont toujours apporté aide et savoir avec beaucoup de disponibilité.

Je remercie Marine pour avoir amené avec elle tant de vitalité au sein du groupe. J'espère que les discussions très ouvertes et stimulantes qu'on a pu avoir ne s'arrêteront pas avec la fin de ma thèse ; qu'on trouvera l'occasion d'atteindre ensemble le haut du Galibier.

Je remercie Timothée, Baptiste et Benjamin, qui ont toujours cru que les bancs de poissons me mèneraient à bon port.

Je remercie mes parents qui m'ont encouragé et soutenu dans cette voie. Je dois beaucoup à leur attention et à leur soutien.

Merci Casey ! Les aventures à Lyon se terminent, d'autres commencent. Que je suis chanceux de t'avoir à mes côtés ! Tu me donnes beaucoup de courage, l'oatmeal ne me fait plus peur.

Table of contents

Chapter 1

Flocking physics

The collective motion of living organisms is a spectacular feature of nature. Herds of mammals, schools of fishes, flocks of birds, swarms of insects and colonies of bacteria are many examples of large groups of individuals that collectively migrate without leaders, see Fig. 1.1. The emergence of such collective dynamics, together with the broad range of scales at which they take place, have attracted the interest of physicists. Questions include: How do individuals spontaneously move together over scales much larger than the size of the individuals? Do different flocks share common features regardless of the species of their members? These interrogations are all part of a broader one: Does a physics of flocking exist?

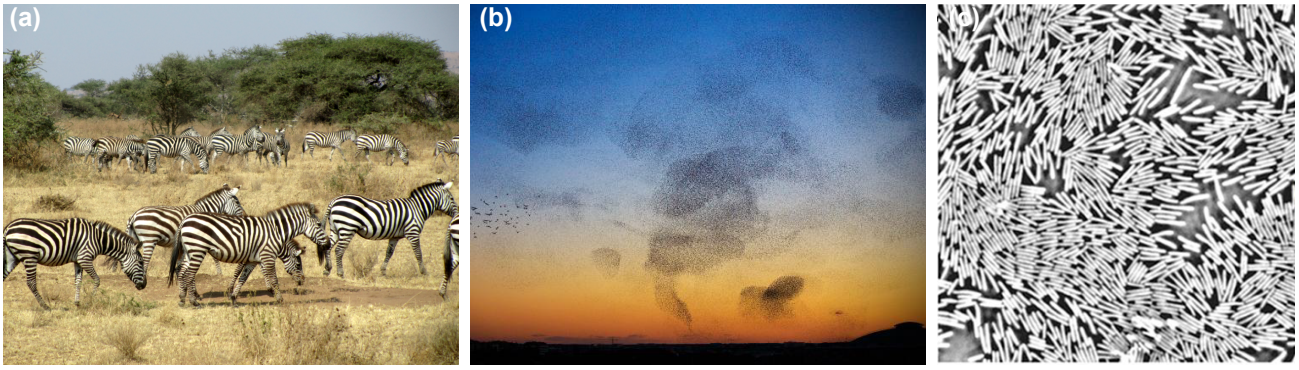

Figure 1.1 | **Collective motion in nature. (a)** A herd of zebras. Picture by P. Morin. **(b)** Starling flocks. Figure from the Collective Behaviour in Biological Systems laboratory, Roma. **(c)** Bacteria colony. Figure from [144].

1.1 Synthetic active materials

Investigating the dynamics of flocks occuring in the wild is a challenging task, particularly performing quantitative measurements [1]. Additionally, the many parameters that influence flocking correlate with a poor control over these parameters. As an alternative to the study of natural flocks, physicists have therefore turned to the design of simpler flocks that can be handled in the laboratory, and for which some key parameters can be controlled at will. Thus, they have created synthetic flocks.

The first step has consisted in making motile units in the laboratory: polar active particles that individually turn energy into directed motion. For twenty years, experimentalists have been very successful in motorizing a wealth of different elements. In particular, all the constituents of conventional soft materials have been endowed with the ability to self-propel. Several forms of *active* colloids [13, 59, 89, 47, 88], emulsions [118], gels [102, 100] and grains [8, 35, 137] are now available to physicists for laboratory experimentation.

As these various synthetic active particles became easily accessible, it became possible to study groups of such particles, and hence the testing for the emergence of flocks in these active materials. Surprisingly, populations of synthetic active particles showed a rich variety of collective behaviors. Emergent structures with directed collective motion, known as *flocks*, were revealed to be only one of the many emergent collective behaviors observed. Some of the prominent collective dynamical patterns recorded are depicted in Fig. 1.2. Active microtubules are seen to form an active nematics that constantly evolves and whose topological defects endlessly merge and nucleate, see Fig. 1.2a. Active Janus colloids show some dynamical phase separation with clustering, given by a balance between particle aggregation and dissociation, see Fig. 1.2b. Ephemeral clusters of active droplets collectively move and re-arrange as they collide with each others, see Fig. 1.2c. These few examples show that several classes of active materials have to be distinguished from one another. Being interested in flocking, I hereafter restrict my discussion to polar active materials. Polar active materials are made of motile individuals that move in the same direction on average, thereby forming flocks.

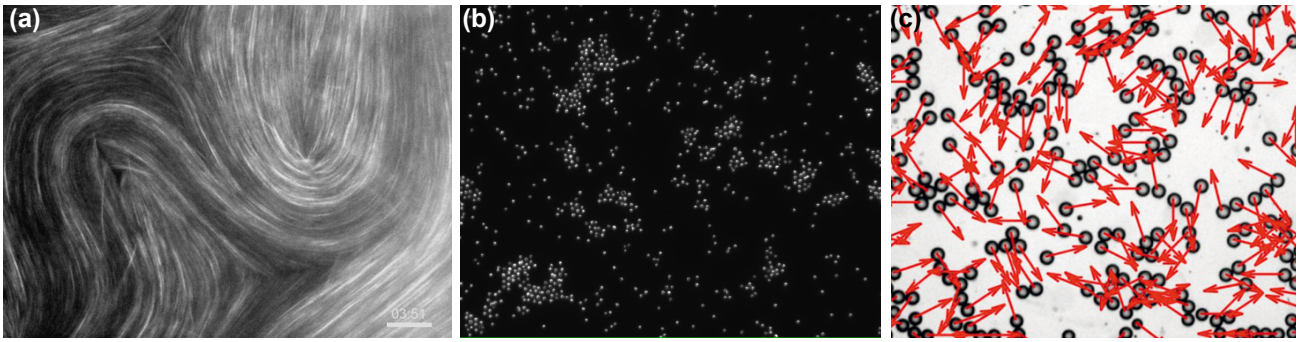

Figure 1.2 | **Collective behaviors in synthetic active matter. (a)** Active nematics with topological defects. Figure from [100]. **(b)** Clusters of active Janus colloids. Figure from [51]. **(c)** Motile clusters of active droplets. Figure from [118].

1.2 Synthetic flocks

Synthetic flocks out of polymers, grains and colloids have been made in laboratory experiments. The diversity of the size, nature and propulsion mechanism of these motile units echoes the diversity found in natural flocks. An overview of these systems is the opportunity to stress this variety while bringing out the unity in the ordering mechanism. I first list these different experiments by insisting on their differences. Then, I come back on the features they share.

Actin filaments on a motility assay

The motility assay experiments performed by Schaller and co-workers [102] are among the first realizations of flocks in the laboratory. Actin filaments, proteins of length $\sim 10\,\mu$m, are made active by linking them to an array of molecular motors, see Fig. 1.3a. As it happens in cells, adding adenosine tri-phosphate to the system triggers the molecular motors. Consequently, the filaments start moving at a typical speed $v_0 \sim 5\,\mu$m/s.

Figures 1.3b-c show that different dynamical states occur upon increasing the filament density ρ. At low density, the filaments perform persistent random walks and form a homogeneous and isotropic gas, see Fig. 1.3b. At intermediate density, polar clusters emerge and move through a dilute gaseous background, see Fig. 1.3c. At high density, a pattern of polar waves that propagate along a common direction form. Remarkably, the polar clusters and polar waves that emerge in the system can be up to $500\,\mu$m in size, orders of magnitudes larger than the filaments. Recently, the authors have provided a detailed account of multiple-body collision events that highlights the role of alignment interactions in for emergence of these polar structures [115, 114].

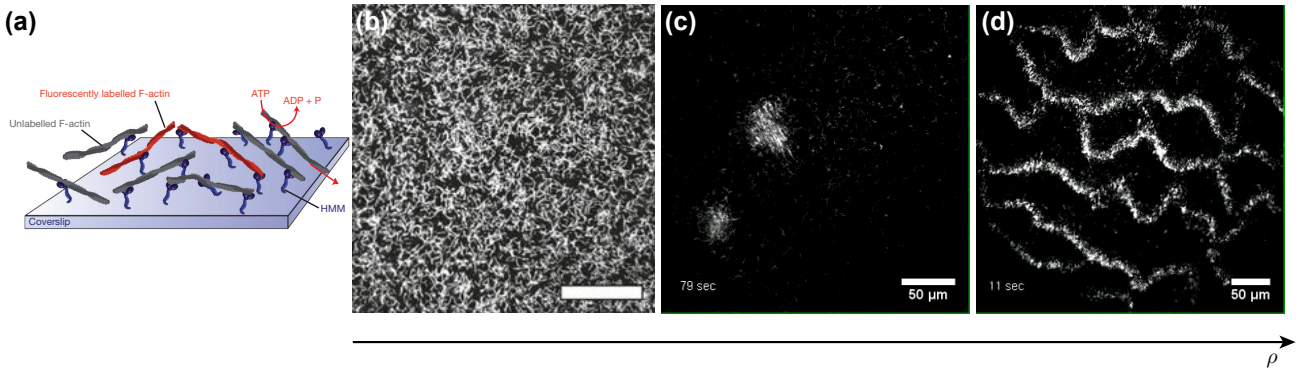

Figure 1.3 | **Actin filaments on a motility assay.** **(a)** Sketch of the motility assay experiments. Actin filaments (F-actin) are linked to molecular motors (HMM). The addition of adenosin tri-phosphate (ATP) motorizes the filaments. Figure from [102]. **(b)** Snapshot of a homogeneous and isotropic gas of filaments at low density. Scale bar: $50\,\mu$m. Figure from [101]. **(c)** Snapshot of polar clusters of filaments propagating through a dilute gas at intermediate density. Scale bar: $50\,\mu$m. Figure from [102]. **(d)** Snapshot of polar waves of filaments propagating through a dilute gas at high density. Scale bar: $50\,\mu$m. Figure from [102].

Vibrated polar disks

Inspired by granular media experiments, Deseigne and co-workers [35, 36] designed an experiment based on self-propelled hard disks. They engineered 4 mm-diameter circular grains having two legs of different materials and geometries, see Fig. 1.4a. Under vertical vibration with acceleration relative to gravity $\Gamma \sim 3$, these polar disks individually behave as persistent random walkers with a typical speed $v_0 \sim 10\,\mathrm{mm/s}$ and orientation diffusivity $D \sim 1\,\mathrm{s}^{-1}$. Typical trajectories are shown in Fig. 1.4b.

Collective motion occurs in this system of vibrated polar grains as shown in Fig 1.4c. The emergence of polar order origins in the hard-core collisions between disks. As shown in Fig. 1.4d, the repeated collisions lead to alignment of the grains. As the grains are spherical, this experiment evidences that a polar shape is not necessary to the existence of polar interactions. An other experiment based on vibrated grains have demonstrated that polar interactions taking place at a distance also give rise to collective motion [65].

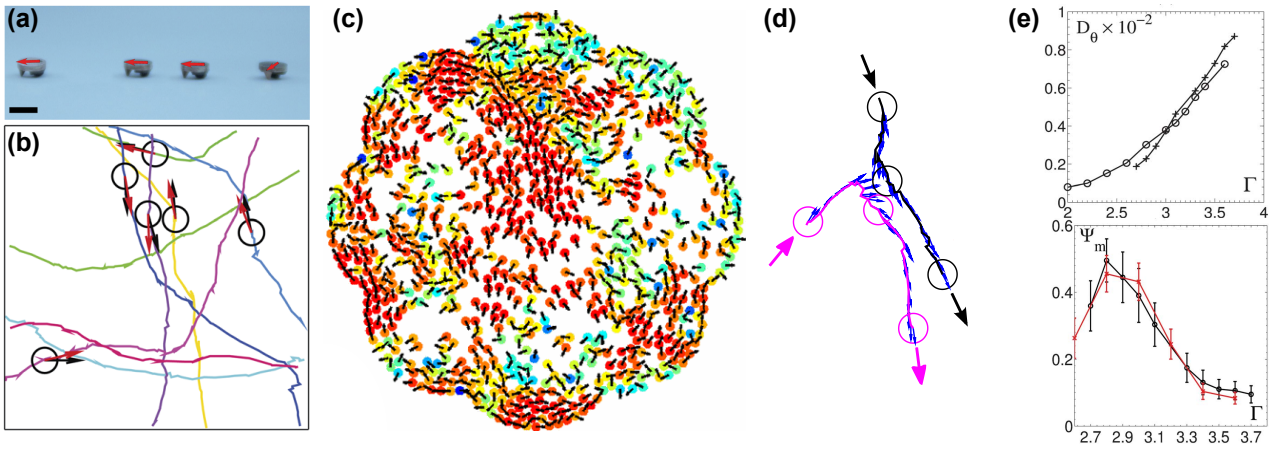

Figure 1.4 | **Vibrated polar disks.** **(a)** Photograph of the polar disks. Scale bar: 4 mm. Figure from [36]. **(b)** Persistent random walks performed by vibrated polar disks at low density. Each color codes for a different disk. Figure from [36]. **(c)** Snapshot of a polar flock. The color codes for the local alignment between self-propelled grains: from perfect alignment in red to perfect anti-alignment in blue. Figure from [35]. **(d)** The trajectories of vibrated disks during a collision reveal the alignment of their direction of motion. Figure from [35]. **(e)** The vibration acceleration Γ is a convenient control parameter. Top: the orientation diffusivity of individual grains increases with Γ. Bottom: the decrease of polarization with Γ reveals that collective motion is altered. Figures from [36].

The density is, as for the actin-filament experiment, a key parameter of the system. While grains barely interact and form a gas at low density, they display collective motion at high density. Recently, the authors have investigated the regime near close-packing of the disks [10]. The emergence of crystalline order does not suppress collective motion and the system form a flowing crystal. Another convenient control parameter is the vibration acceleration Γ. Interestingly, changing Γ has a strong impact on the grains dynamics, see Fig. 1.4e. At the individual level, increasing Γ yields an increase in the orientation diffusivity D. Importantly, this higher randomization translates, at the collective level,

into a lowering of alignment between particles: collective motion is reduced.

Electrically-powered colloids

As of today, two different experimental systems based on electrically-powered colloidal particles display flocking. One of this system was developed in the group of Denis Bartolo [13]. It consists in assemblies of spherical colloids powered by a DC electric field. Figure 1.5 shows a typical colloidal flock. It forms a polar liquid whose colloids move in a common direction while no position order is present. I thoroughly describe this model experiment in Chapter 2, as it is at the foundations of my work.

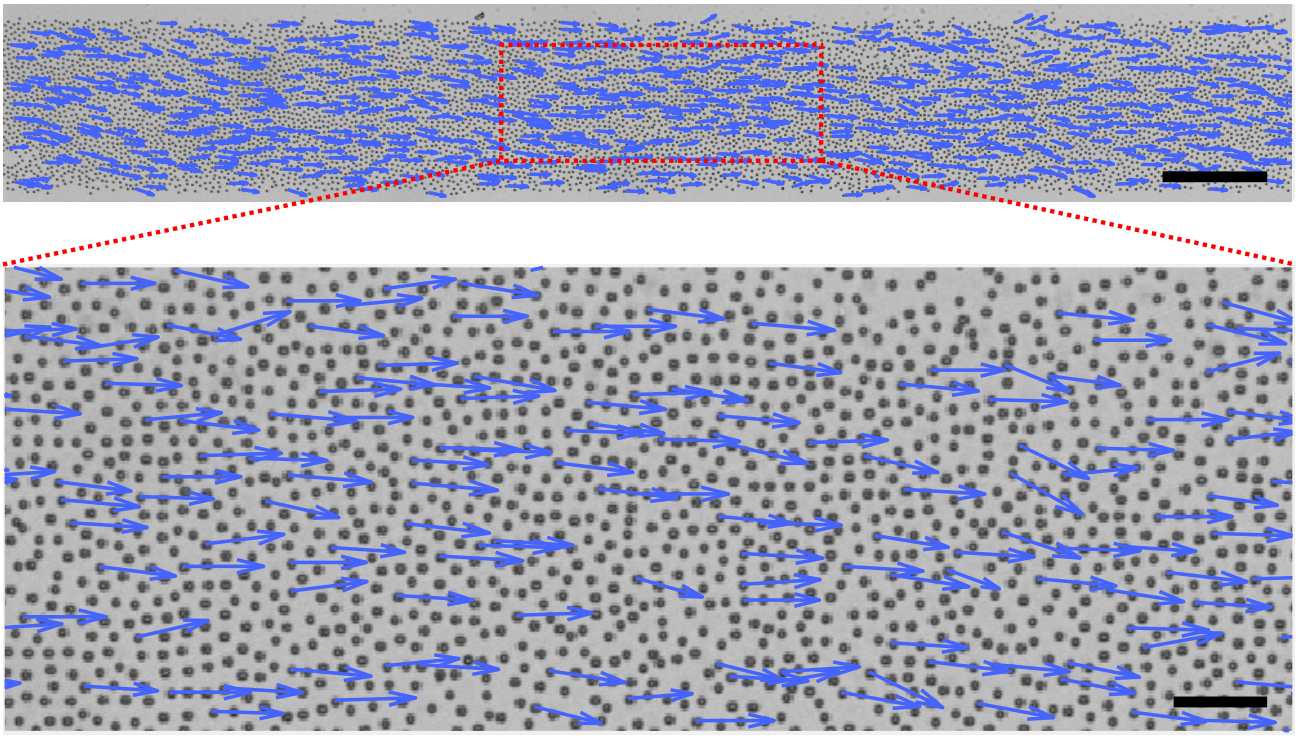

Figure 1.5 | **Spherical colloids powered by a DC electric-field.** Top: snapshot of a flock assembled from self-propelled colloids. Their instantaneous direction of motion is indicated by blue arrows (1/10 are shown for clarity). Scale bar: 250 μm. Bottom: close-up. Scale bar: 50 μm.

A more recent proposition is due to Yan and co-workers [138]. They use Janus colloids of radius $\sim 3\,\mu$m made of a silica and a titanium hemispheres. These colloids are powered by an AC electric field whose direction does not impose the particle direction of motion, see Fig. 1.6a. The control of the oscillation frequency does not only tune the propulsion velocity ($v_0 \sim 30\,\mu$m/s, see Fig. 1.6a) but also changes the pair interactions between colloids. By favoring alignment interactions (Fig. 1.6b), Yan and co-workers successfully recovered macroscopic polar phases, see Fig. 1.6c.

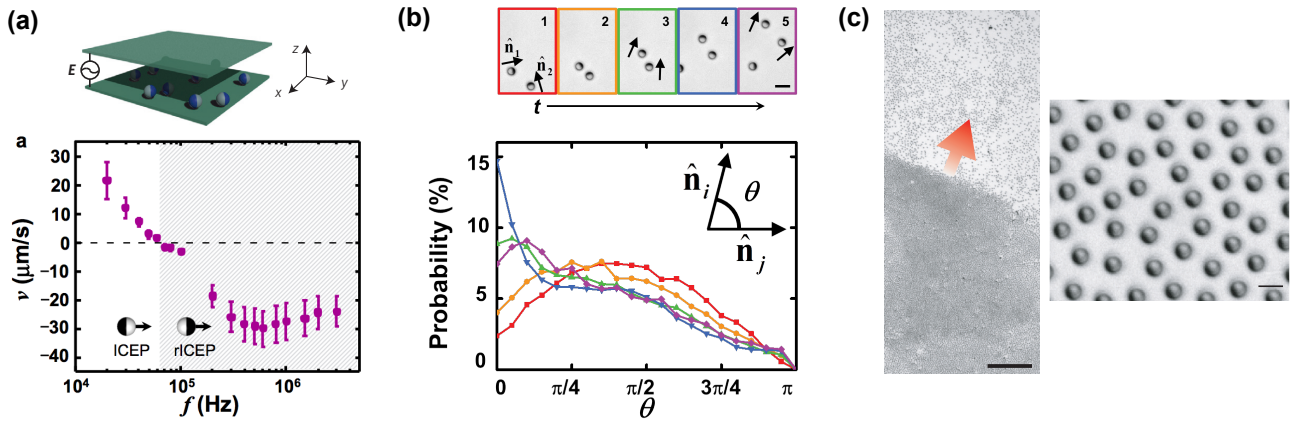

Figure 1.6 | **Electrically-powered colloids. (a)** Active Janus colloids. Top: sketch of the experimental setup. An AC electric-field E is applied to Janus colloids confined between two electrodes. Bottom: the speed of the colloids is tuned by varying the electric-field frequency f. Figures from [138]. **(b)** Binary alignment interactions. Top: subsequent snapshots showing a collision between two colloids. $f \sim 30\,\mathrm{kHz}$. Scale bar: $5\,\mu\mathrm{m}$. Bottom: statistics from $\sim 10^4$ collisions reveal a transient alignment effect as the green, blue and purple curves have a peak at $\theta = 0$. Figures from [138]. **(c)** Snapshots of the polar phase. Left: a polar flock propagates through a gas of colloids. Scale bar: $200\,\mu\mathrm{m}$. Right: a close-up on the polar flock shows that particles, that move towards their dark hemisphere, are aligned. Scale bar: $5\,\mu\mathrm{m}$. Figures from [138].

Generic features in the emergence of flocks

A few principles underlying flocking can be identified from these synthetic-flock experiments. First, alignment interactions are a key ingredient for the emergence of flocks. Polar interactions between individuals are necessary for the emergence of large-scale polar structures. Such interactions can take place between geometrically non-polar units, as self-propulsion itself already singles out a direction. Second, density is a control parameter of major importance. As the number of individual increases, interactions become more frequent, therefore promoting the emergence of flocks. Finally, orientation diffusivity of individuals competes with alignment interactions. The formation of flocks is hindered by the randomization of the directions of motion at the individual level.

1.3 Flocks as active ferromagnets

The major importance of alignment interactions between particles to allow for flocking was actually pointed out at the very beginning of active matter physics. In 1995, Vicsek and co-workers proposed to describe flocks as active ferromagnets: ferromagnets where each spin moves along the direction it points to. More precisely, they constructed a Heisenberg-like model by considering collections of spins interacting with each other *via* ferromagnetic couplings [129]. The seminal work by Vicsek has not only participate in the soar of active matter research but it has also served as a paradigm in the study of

polar active matter. For these reasons, it is worth recalling the main features of the Vicsek model: its equations of motions and phase diagram will prove to be of great relevance in the study of colloidal flocks.

Equations of motion in the Vicsek model

The Vicsek model consists in an assembly of pointwise particles at density ρ that move off-lattice at a constant speed v_0. The position $\hat{\mathbf{r}}_\mathbf{i}$ of the particle i evolves according to a discrete-time scheme of step Δt:

$$\mathbf{r_i}(t+\Delta t) = \mathbf{r_i}(t) + v_0 \Delta t \hat{\mathbf{v}}_\mathbf{i}(t), \tag{1.1}$$

where v_0 is the particle speed and $\hat{\mathbf{v}}_\mathbf{i} = (\cos\theta_i, \sin\theta_i)$ is the direction of motion of particle i. Interactions between particles do not alter the speed of the particles, but they act as torques that change the particle orientation θ_i. The angular dynamics is overdamped and given by:

$$\theta_i(t+\Delta t) = \arg\left(\langle \hat{\mathbf{v}}_\mathbf{j}(t)\rangle_{j\in\mathcal{D}(\mathbf{r_i},R)}\right) + \eta\xi_i(t), \tag{1.2}$$

which means that particle i changes its orientation to align with neighbor particles that belong to a disk of radius R centered at $\mathbf{r_i}(t)$. However, this goal is not perfectly met: the change in orientation is also subject to some random noise of strength η. More precisely, $\xi_i(t)$ is a random variable uniformly distributed in the interval $[-\pi\ \pi]$ with correlations $\langle \xi_i(t)\xi_j(t')\rangle = \delta_{ij}\delta(t-t')$. Figure 1.7 illustrates the dynamics of Eqs. (1.1) and (1.2). For clarity, it only shows how a single particle evolves from one time to the next, while, in the Vicsek model, all particles synchronously update their positions and orientations.

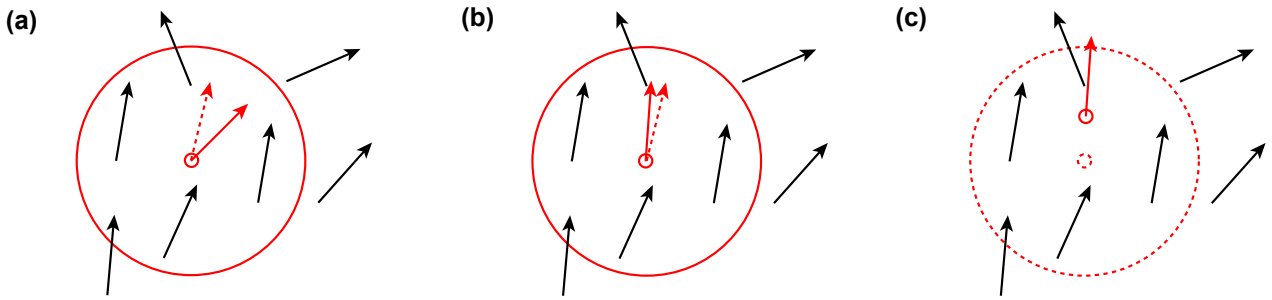

Figure 1.7 | **Alignment in the Vicsek model. (a)** The red particle that initially moves at $\mathbf{v}$ (red arrow) interacts with its neighbors. It aims at aligning with their mean direction of motion (dashed red arrow). **(b)** The red particle imperfectly aligns with its neighbors. **(c)** The red particle moves along its new direction of motion.

Flocking transition in the Vicsek model

The Vicsek model has three independent control parameters. The time step Δt and the interaction range R are conveniently chosen as units of time and length. The particle speed v_0, the noise strength η

and the density ρ remain as control parameters. Studies of the Vicsek model have focused on the role of η and ρ. In particular, the noise strength η plays a role similar to the temperature in equilibrium systems. As for many equilibrium phase transitions, ordering occurs upon decreasing the noise strength in the Vicsek model. This is also reminiscent of the vibrated grain experiments, see Fig. 1.4. Figures 1.8a-c show snapshots from my simulations of the three different phases found. These simulations of the Vicsek model are conducted at density $\rho = 0.5$ and velocity $v_0 = 0.5$. At high noise strength, particles move in all directions with equal probabilities, see Fig. 1.8c. The system is homogeneous and isotropic: it forms a gas. Below a threshold noise strength η^*, the rotational symmetry is spontaneously broken. A dense flock emerges, see Fig. 1.8b. This flock is made of particles that move in average in the same direction. This flock coexists with an gas phase. While particles are continuously exchanged between the two phases, the flock is a stationary structure that behaves as a traveling wave. Finally, at low noise strength, a flock that spans the whole system forms, see Fig. 1.8a. This flock is homogeneous both in density and orientational order: all spins move in average in the same direction. As this active ferromagnet lacks any positionning order, it is commonly referred to as a *polar liquid*.

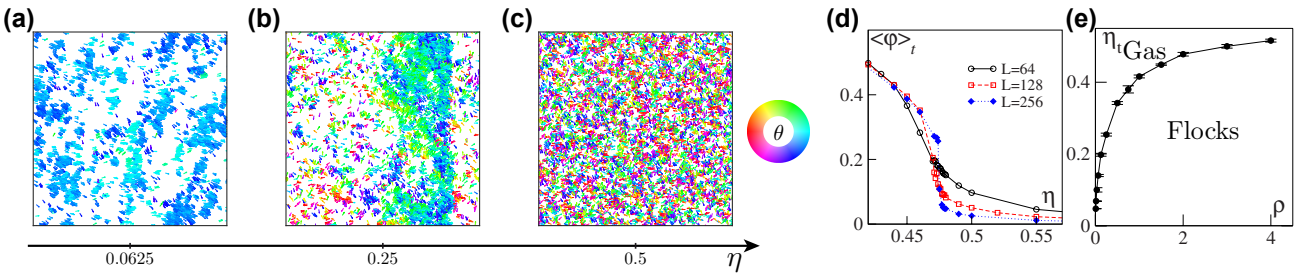

Figure 1.8 | **The Vicsek model: phases, first-order transition, phase diagram. (a)** Homogeneous polar-ordered flock at low noise strength η. $\rho = 0.5$, $v_0 = 0.5$ and $L = 128\,R$. **(b)** Heterogeneous phase at the onset of collective motion. A band-shaped polar-ordered flock propagates through a gas. $\rho = 0.5$, $v_0 = 0.5$ and $L = 128\,R$. **(c)** Homogeneous and isotropic gas of particles at high noise strength. $\rho = 0.5$, $v_0 = 0.5$ and $L = 128\,R$. **(d)** The polarization sharply decreases upon increasing the noise strength η. The discontinuity of the Vicsek transition is unveiled in large systems $L \geq 256\,R$. $\rho = 2$ and $v_0 = 0.5$. Figure from [23]. **(e)** Phase diagram of the Vicsek model in the density-noise plane. Flocks emerge at high density ρ and small noise strength η. Figure from [23].

To monitor the transition between the disordered and ordered phases, the relevant order parameter to consider is the polarization:

$$\mathbf{\Pi} = \langle \hat{\mathbf{v}}_\mathbf{i} \rangle_i \,. \tag{1.3}$$

The polarization is nothing but the magnetization of Vicsek's moving spins. Its modulus $|\mathbf{\Pi}|$ equals 1 when the system is perfectly ordered and all particles move exactly in the same direction. At the contrary, $|\mathbf{\Pi}|$ vanishes when the particles form an isotropic gas. Figure 1.8d shows the evolution of $|\mathbf{\Pi}|$ with η. Importantly, the polarization increases sharply at η^*: the flocking transition is discontinuous. The first order nature of this transition, which has been debated for many years, origins in the phase

coexistence at the onset of collective motion, see Fig. 1.8b. The band-shaped flock can therefore be seen as a droplet of polar liquid coexisting with a gas phase.

As mentioned above, the particle density is an other control parameter in the Vicsek model. As it was observed in experiments on synthetic flocks, increasing the density favors the emergence of flocks. The full two-dimensional phase diagram of the Vicsek model is shown in Fig. 1.8e. Basically, the transition to collective motion is set by the competition between alignment interactions and the randomization of particle orientations due to the noise. By pointing out the key ingredients necessary to allow for flocking, the Vicsek model has won its paradigmatic status.

1.4 Flocks as spontaneously flowing liquids

If the Vicsek model correctly accounts for flocking, its phenomenology presents some intriguing aspects. Two features are particularly surprising when having in mind analogous equilibrium models. First is the coexistence phase where a flock propagates through a disordered background. No such heterogeneous state exists in ferromagnets. Second is the very existence of the polar liquid phase. Indeed, at equilibrium, long-range order that relies on the breaking of a continuous symmetry is impossible in dimension 2. This is in essence the Mermin-Wagner theorem [79]. The polar liquid in the Vicsek model displays, however, true long-range order [30]. Ordered active states appear to be fundamentally different from their passive counterparts, thereby making the limit $v_0 \to 0$ singular.

Such features have not only been observed in the Vicsek model, but also in a wide variety of models and systems that display flocking. These observations suggest that the formation of a heterogeneous phase at the onset of flocking as well as the true long-range order in flocks are robust to the details of their microscopic mechanisms. Hydrodynamics provides the general framework best suited to find their origins and test their universal nature. Toner and Tu have introduced the analogous of Navier-Stokes equations for flocks [122]. By doing so, they have proposed a complementary perspective on the study of flocking. While Vicsek had compared flocks to active ferromagnets, Toner and Tu have considered flocks as spontaneously flowing liquids.

Hydrodynamics of flocks

Based on symmetry arguments, Toner and Tu have established the hydrodynamic equations for flocking [122, 66]. As in any hydrodynamic theory, the focus is on large time and length scales. In writing the equations that rule the dynamics of the density field ρ and the velocity field $\mathbf{v}$, Toner and Tu have limited to gradients of order 2. The Toner and Tu equations for flocking read:

$$\partial_t \rho + \nabla(\rho \mathbf{v}) = 0, \tag{1.4}$$

$$\partial_t \mathbf{v} + \Lambda[\nabla \mathbf{v}\mathbf{v}] = U(\rho, |\mathbf{v}|)\mathbf{v} + \mathbf{D}[\nabla\nabla\mathbf{v}] + \mathbf{F_P} + \mathbf{f}. \tag{1.5}$$

Equation (1.4) translates mass conservation. Equation (1.5) includes additional terms with respect to the Navier-Stokes equation. On the left-hand side of Eq. (1.5), all convective-like contributions are cast into $\Lambda[\nabla\mathbf{v}\mathbf{v}] = \lambda_1(\mathbf{v}\cdot\nabla)\mathbf{v} + \lambda_2(\nabla\cdot\mathbf{v})\mathbf{v} + \lambda_3\nabla(|\mathbf{v}|^2)$. On the right-hand side, the viscous contributions read $\mathbf{D}[\nabla\nabla] = D_1\nabla(\nabla\cdot\mathbf{v}) + D_2(\mathbf{v}\cdot\nabla)^2\mathbf{v} + D_3\nabla^2\mathbf{v}$. The pressure term $\mathbf{F_P}$ tends to suppress density fluctuations. The random force $\mathbf{f}$ accounts for fluctuations. It is a Gaussian white

noise with zero mean and correlations:

$$\langle f_i(\mathbf{r},t) f_j(\mathbf{r}',t')\rangle = \eta\delta_{ij}\delta(\mathbf{r}-\mathbf{r}')\delta(t-t'), \tag{1.6}$$

where i and j denote Cartesian components and η is a constant.

The crucial term in Eq. (1.5) is $U(\rho,|\mathbf{v}|)\mathbf{v}$ which governs the existence of collective motion. For a collective moving state with velocity v_0 to be favored, $U(\rho,|\mathbf{v}|)$ has to change sign from positive to negative values at $|\mathbf{v}| = v_0$. A Landau-like force meets this requirement:

$$U(\rho,|\mathbf{v}|)\mathbf{v} = (a_2 - a_4|\mathbf{v}|^2)\mathbf{v}, \tag{1.7}$$

where a_2 and a_4 may depend on ρ. When $a_2 > 0$ and $a_4 > 0$, a non-zero local velocity is promoted. This contribution thus accounts at the hydrodynamic level for microscopic alignment interactions. The transition to collective motion upon increasing density is captured by keeping $a_4(\rho) > 0$ while taking $a_2(\rho) \propto \rho - \rho^\star$. As ρ approaches $\rho^\star$ from above, $a_2(\rho) \propto \rho - \rho^\star$ vanishes and $v_0 = \sqrt{a_2/a_4}$ continuously goes to 0: a homogeneous polar liquid with arbitrarily small velocity can form. Below the critical density $\rho^\star$, the sole homogeneous stationary state is a gas with $\mathbf{v} = 0$.

Heterogeneous polar phases: theoretical predictions

The continuous nature of the flocking transition suggested by the previous analysis is somewhat misleading. Indeed, Eqs. (1.4) and (1.5) may also admit stationary but heterogeneous solutions. The coexistence between a flock and a gas in the Vicsek model suggests that such solutions do exist. Occuring at the onset of collective motion, this coexistence greatly impacts the nature of the transition. Motivated by such considerations, Caussin, Solon and co-workers have looked for propagative solutions of Toner and Tu equations [19, 109]. More precisely, they have looked for constant-speed (c_F) waves with a homogeneous structure transverse to their propagation direction. By reducing the problem to the study of a dynamical system, they have evidenced that only three heterogeneous states exist. The profiles in the propagating direction of the current $\mathbf{W} = \rho\mathbf{v}$ of these three states are shown in Fig. 1.9.

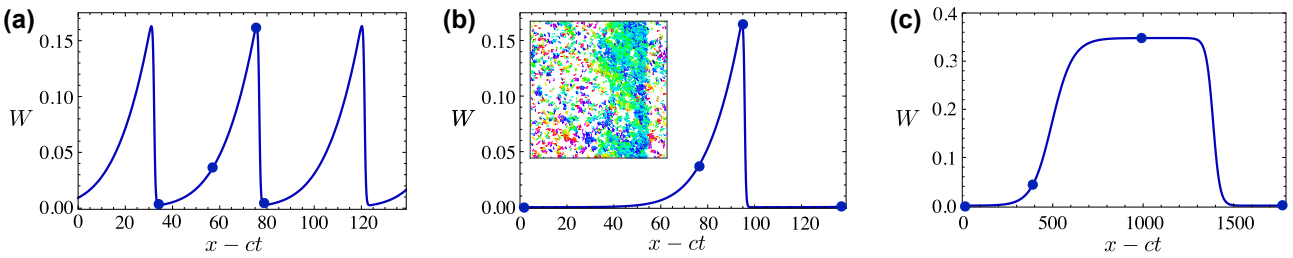

Figure 1.9 | **Heterogeneous polar flocks predicted from hydrodynamics. (a)** Peridodic travelling waves. Figure from [19]. **(b)** Solitonic band propagating through a gas. Figure from [19]. **(c)** A polar liquid droplet. Figure from [19].

Some key points of Caussin's work deserve to be mentioned here.

(i) The three heterogeneous states depicted in Fig. 1.9 can coexist. Indeed, for some parameter sets $(\rho, c_{\rm F})$, several patterns are solutions of Eqs. (1.4) and (1.5). The pattern selection problem remains to be elucidated. This is a difficult task as microscopic details play a role in this process [17].

(ii) Importantly, the three heterogeneous states are all stable below $\rho^\star$. Coexistence with a homogeneous gas can occur, which explains the first order nature of the flocking transition as observed in the Vicsek model.

(iii) Of particular interest, is the solitonic structure of Fig. 1.9b, which is reminiscent of the heterogeneous state at the onset of flocking in the Vicsek model. Not only the theory by Caussin qualitatively accounts for such heterogeneous phases, but it also brings quantitative predictions that benefit from the generic nature of the hydrodynamic approach, as first suggested by Bertin and co-workers [5]. As an example, the finite flock of Fig. 1.9b has an exponential tail with a characteristic length:

$$L_{\rm F} = \frac{v_0}{a_2}\left[\frac{\frac{c_{\rm F}}{v_0} - \frac{v_0}{2c_{\rm F}}\left(1+\frac{\beta\rho_{\rm g}}{v_0^2}\right)}{\rho^\star - \rho_{\rm g}}\right], \tag{1.8}$$

where $\rho_{\rm g}$ is the density of the gas phase that coexists with the finite flock and the coefficient β comes from taking $\mathbf{F_P} = -\beta\nabla\rho$ for the pressure contribution. All the other coefficients were introduced above. Interestingly, the length of the flock can be arbitrarily large as $\rho_{\rm g}$ gets closer to $\rho^\star$. Equation (1.8) does not only capture the shape of Vicsek finite flocks. It also correctly accounts for colloidal synthetic flocks, as we shall see in Chapter 4.

Homogeneous polar liquid: theoretical predictions

The precise phenomenology at the onset of collective motion is expected to bear no influence on the properties of the polar liquid, in particular deep in the ordered phase , when $\rho \gg \rho^\star$. Starting from Eqs. (1.4) and (1.5), Toner and Tu have extensively studied the polar liquid phase [122, 123, 127, 119]. They have singled out three major characteristics of the polar liquid.

(i) They have evidenced that the polar liquid exhibits true long-range order in dimension 2, unlike equilibrium systems. This result involves highly technical derivations. It was obtained going beyond the linear approximation of Eqs. (1.4) and (1.5) around the polar liquid state by taking fluctuation and non-linear contributions into account.

(ii) The polar liquid displays giant density fluctuations. The variance of the number of particles N increases with $\langle N\rangle$ according to $\Delta N^2 \propto \langle N\rangle^\gamma$ with $\gamma = 1.6$ within the polar liquid. This increase is faster than if the central theorem applied as $\gamma = 1$ in this case.

(iii) Underlying these giant density fluctuations, are sound modes very specific to the polar liquid state. Indeed, these sound modes originate from the interplay between mass conservation and the Goldstone mode related to the spontaneous breaking of the rotational symmetry.

Experimental characterization: the current status

The hydrodynamic approach of flocking has kept its promise. It has unveiled some general features of flocks that equilibrium considerations would not allow. Both this generality and originality demonstrate

that a physics of flocking does exist. This would be all the more exciting if the theoretical predictions were corroborated by experimental observations on real flocks. In introducing synthetic flocks, the emphasis was on the microscopic mechanisms that give rise to the emergence of collective motion. At the light of the hydrodynamics predictions, it is worth going back to these very same experimental systems and look for the expected universal characteristics.

Onset of collective motion. At the onset of collective motion, the emergence of heterogeneous states is a usual phenomenon. Clusters and waves of collectively moving filaments are found in the motility assay experiments by Schaller and co-workers [102], see Figs. 1.3c and 1.3d. These polar structures co-exist with homogeneous gas of filaments moving in random directions. Yan and co-workers have also reported polar waves of active colloids that propagate through a gas, see 1.6c. Finally, flocks assembled from colloidal rollers [13] display the exact band-shape structures predicted by hydrodynamics theories (see Fig. 1.9) and found in the Vicsek model (see Fig. 1.8). This is discussed in more details in Chapter 2.

These observations therefore support the existence, in real flocks, of stable propagative heterogenous density excitations as the ones considered by Caussin and co-workers. A thorough quantitative study of the structures found in these experiments remains undone. Such a study would be of great interest. It could help understand the pattern selection process, hence the emergence of heterogeneous flocks. It could also lead to the finding of new polar states: genuine two-dimensionnal dynamical phases or simple transient excitations, for instance.

Polar liquid state. Regarding the characterization of the polar liquid phase, many efforts have been devoted to the measurements of the density fluctuations. Virtually all synthetic flocks have been reported to display giant density fluctuations. Unfortunately, the accuracy and confidence in these measurements are somehow limited. For example, the density fluctuations measured in the vibrated disk experiments are in good agreement with the theoretical prediction, see Fig. 1.10a. However, the system is not deep in the ordered phase (see Fig. 1.4e) and the proximity of the transition to collective motion may also affect density fluctuations through the nucleation of droplets [35]. In the motility assay experiments, a homogeneous polar liquid actually never forms. Measurements of density fluctuations were performed within a subsystem that consisted in a polar cluster of size $\sim 1\,\mathrm{mm}$ instead. Though in quantitative agreement with Toner and Tu predictions (see Fig. 1.10b), the measured giant fluctuations could also have a different origin. The stability of these clusters may rely on cohesive interactions and these polar structure may not belong to the class of Toner and Tu fluids for which the expectation $\gamma = 1.6$ hold. The measure of density fluctuations within flocks assembled from colloidal rollers has met a similar fate [48]. As shown in Fig. 1.10c, giant density fluctuations have been evidenced. However, despite very good statistics, the determination of γ lacks the precision necessary to compare with the Toner and Tu prediction.

In the similar context of active nematics, the measure of density fluctuations has revealed to be as much difficult. Even the very convincing data by Nishiguchi and co-workers [87] are somewhat irregular as density fluctuations escape from a mere algebraic increase. Since density fluctuations resist accurate experimental measurements, it may be worth investigating some of the other features of Toner and Tu polar liquids. Following this idea, a thorough characterization of the polar liquid has recently been performed on colloidal flocks assembled from colloidal rollers [48]. I discuss in more details some of the results from [48] in Chapter 2. One of the main findings is that density and velocity fluctuations

propagate according to the Toner and Tu theory. More generally, all the measurements in [48] show an excellent agreement with the *linear* theory by Toner and Tu. This agreement actually questions the possibility to experimentally demonstrate the true long-range order within flocks, or, from a dual point of view, the relevance of Toner and Tu fluctuating hydrodynamics to describe real flocks.

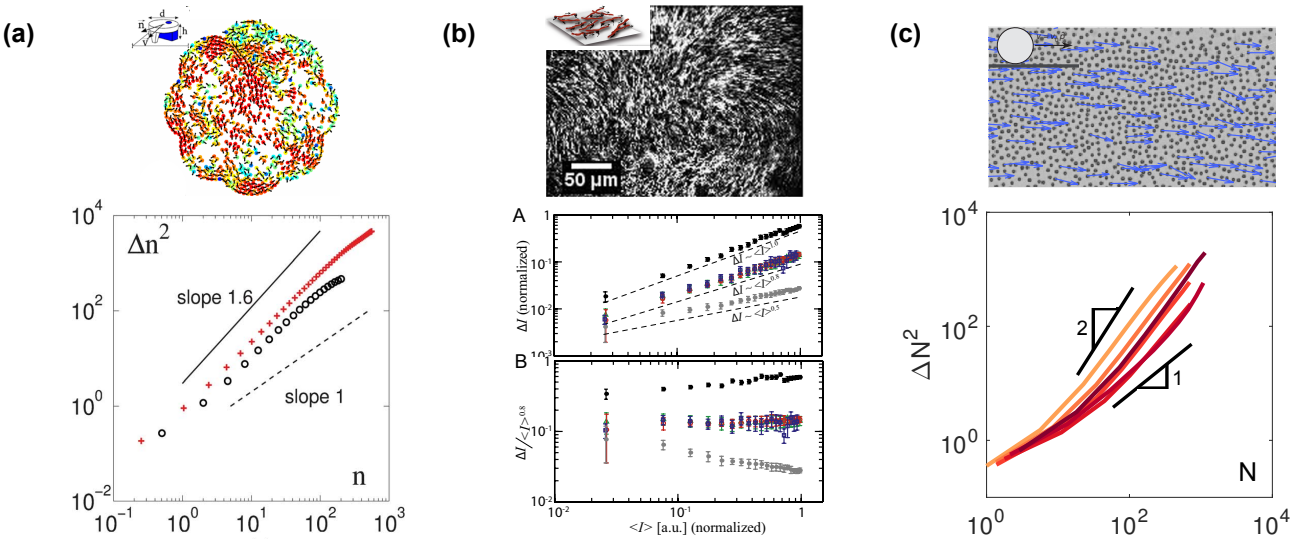

Figure 1.10 | **Giant density fluctuations in synthetic flocks. (a)** Giant density fluctuations are measured in flocks assembled from self-propelled polar disks. Red crosses and black circles are data from diferent experiments. Figures from [35] and [36]. **(b)** Giant density are measured in polar clusters of actin filaments (green, red and blue data points). Conversely, normal fluctuation are measured in the gas phase (grey data points). Figures from [101]. **(c)** Giant density are measured in polar liquids of self-propelled colloids. Figure from [48].

1.5 Flocks in challenging environments

All the works mentioned so far have intended to describe flocks in their essence: the focus was on their intrinsic structure and dynamics. In order to complement our understanding of flocking, need is to go beyond such a primary characterization and address how flocks interacts with their surroundings. To this regards, two settings immediately come in mind:

(i) the response of flocks to external fields.

(ii) the propagation of flocks through quenched disorder.

Indeed, describing the response of a material to external perturbations and the changes of its properties in the presence of disorder are crucial interrogations of condensed matter. As well, the physics of flocking through such challenging environments is worth being investigating. It would allow to further testing how theoretical developments accurately describe real flocks. From a more practical perspective, the robustness of flocks to external perturbations and disorder is of major importance

to the exploitation of these active materials. Any future application that would rely on polar liquids requires to control their behaviors in involved situations.

In this thesis, I investigate how synthetic flocks behave in the presence of an external field and how they propagate through quenched disorder. No experimental work has addressed these situations before. This is all the more surprising than the few numerical and theoretical related studies have drawn interesting conclusions and have suggested surprising behaviors.

Response of flocks to external fields

Building on the analogy with ferromagnetism, Czirók, Stanley and Vicsek have adapted the original Vicsek model to investigate flocking in the presence of an external field [30]. He has considered a homogeneous and stationary field $\mathbf{h}$ that tends to align particles in a given direction $\hat{\mathbf{h}}$. This field thus plays the role of a magnetic field acting on Vicsek's moving spins. More precisely, the update of orientation of particle i now follows:

$$\theta_i(t+\Delta t) = \arg\left(v_0 \sum_{j\in\mathcal{D}(\mathbf{r_i},R)} \hat{\mathbf{v}}_\mathbf{j}(t) + h\hat{\mathbf{h}} \right) + \eta\xi_i(t), \tag{1.9}$$

where the notations are the same than in Eq. (1.2).

Figure 1.11 shows that the polarization $\Pi|(\eta, h)$ increases with the amplitude of the external field h for all values of the noise strength η. The increase of Π at small h defines the susceptibility:

$$\chi(\eta) = \lim_{h\to 0} \frac{\Pi(\eta,h) - \Pi(\eta,0)}{h}. \tag{1.10}$$

Unfortunately, Czirók and co-workers have focused on the susceptibility of the gas phase [30] and they have sparsely scanned the low-h regime, see Fig. 1.11.

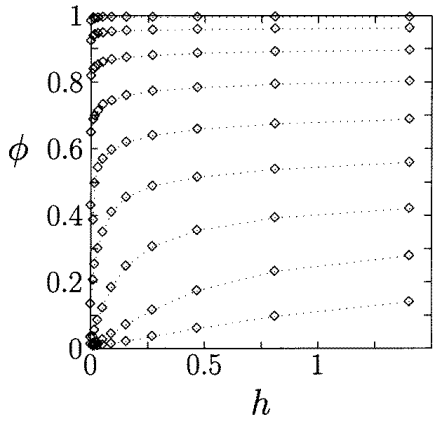

Figure 1.11 | **Response to an external field in the Vicsek model.** Polarization ϕ with respect to the external field h for various nois strength η. From top to bottom, η decreases. Figure from [30].

More recently, Kyriakopoulos, Ginelli and Toner have thoroughly studied the longitudinal response of the polar liquid by combining hydrodynamics theory and numerical simulations of the Vicsek model [66]. They have shown that the static response of 2-dimensional flocks to small homogeneous external field is given by:

$$\chi \propto \begin{cases} h^{-2/3}, \ h \gg h_c(L) \\ L^{4/5}, \ h \ll h_c(L), \end{cases} \tag{1.11}$$

where L is the system size, and the critical field amplitude $h_c(L) \propto L^{-6/5}$. Equation (1.11) implies that, in the limit of infinite systems, the susceptibility diverges at vanishing h. In finite system, however, the susceptibility saturates and the polarization linearly increases at small h.

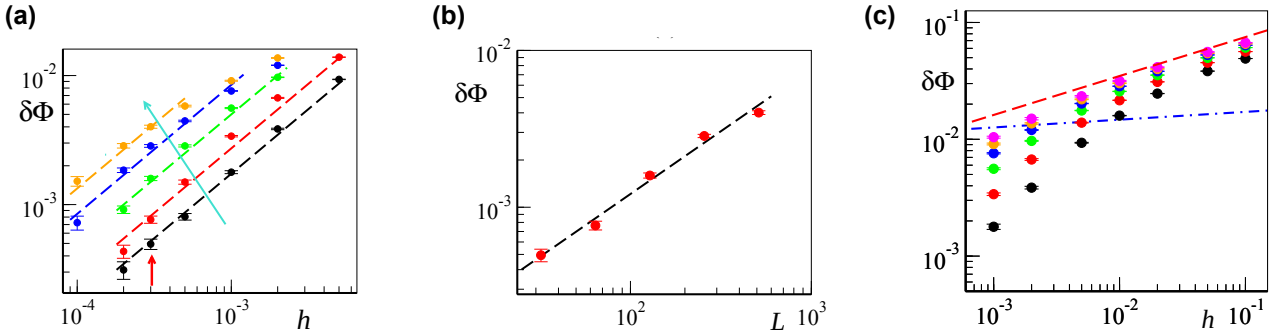

Figure 1.12 | **Response to an external field in the Vicsek model. (a)** Linear increase of polarization for low external field h. The color codes for the system size. Figure from [66]. **(b)** The increase of polarization goes as $L^{4/5}$ for a fixed low value of h. Here $h = 3 \times 10^{-4}$. Figure from [66]. **(c)** The non-trivial scaling at high h of Eq. (1.11) is found for large system size ($L = 1024$ pink data points). Figure from [66].

These theoretical predictions have been confirmed by performing a finite-size analysis of simulations of the Vicsek model. Figure 1.12a shows that the polarization increases linearly with h in the low-h regime. In this regime, the slopes display the exact scaling that is expected with L, see Fig. 1.12b. The non-trivial scaling $\chi \propto h^{-2/3}$ at large h is also supported by the numerical simulations, see Fig. 1.12c. To obtain this result, very large system sizes, up to $L = 1024R$ (R being the interaction range), had to be investigated.

Obviously, any real flock has a finite size. To this respect, the finite size effects uncovered by Kyriakopoulos and co-workers are very important. Understanding, and ultimately predicting, the response of real flocks requires to deal with these effects. As it will be shown in Chapter 3, confinement plays a crucial role in the response of synthetic flocks assembled from colloidal rollers. The presence of impenetrable boundaries yield an even richer phenomenology than the one found out in numerical simulations where periodic boundary conditions have always been considered [30, 66].

Flocking through quenched disorder

A few numerical works have addressed flocking in disordered media [25, 96, 142, 32]. Strikingly, all the studies concerned with quenched disorder have reported some very non-trivial phenomenologies [25, 96, 32]. Figure 1.13 gives a highlight of their results. Chepizhko and co-workers have considered a Vicsek-like model where the particles not only align with their neighbors but also interact with point-wise obstacles so as to move away from them [25]. Figure 1.13a shows the polarization for various pairs of the control parameters: the obstacle density ρ_o and the noise strength η. In the presence of disorder, an optimal noise strength exists that maximizes the polarization.

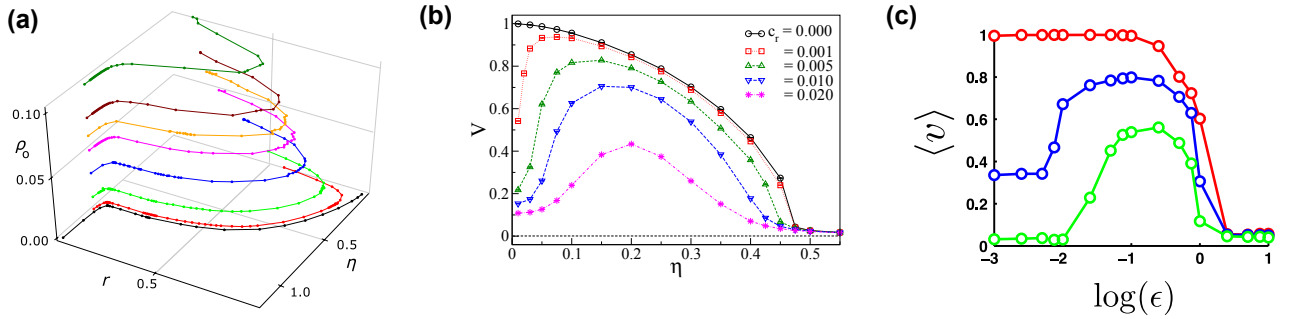

Figure 1.13 | **Optimized flocking through quenched disorder.** **(a)** Polarization $r \equiv \Pi$ with respect to the obstacle density ρ_o and noise strength η. An optimal noise regarding flocking exists for any disorder $\rho_o \neq 0$. Figure from [25]. **(b)** Polarization $V \equiv \Pi$ with respect to noise strenght η for various density of quenched rotators c_r. In the presence of quenched rotators, an optimal noise exists that maximizes the polarization. Figure from [32]. **(c)** Polarization $\langle v \rangle \equiv \Pi$ with respect to the repulsion between colloids ϵ for three different value of disorder density. Red: no disorder. Blue: 1 broken bond out of 10. Green: 1 broken bond out of 5. When disorder is present, the repulsion between particles can be optimally tuned to favor flocking. Figure from [96].

A recent work by Das, Kumar and Mishra has also disclosed such a non-monotonic behavior [32]. Das and co-workers have considered an adaptation of the Vicsek model in which particles interact with quenched polar obstacles. These obstacles act as *rotators* that bear a constant random orientation along which neighboring particles would tend to align. Figure 1.13b shows that an optimal noise strength η exists with regards to polar order for any obstacle density $c_r \neq 0$.

Quint and Gopinathan have introduced an on-lattice Vicsek-like model where stationary disorder is introduced in the form of broken bonds [96]. Not only the motion is forbidden along these broken bonds, but the transfer of information is also disrupted. One of the main conclusions of this work is that flocking can benefit from well-tune repulsive interactions between particles. Figure 1.13c shows that an optimal repulsion strength ϵ exists that maximizes the polarization when a finite number of bonds are missing.

Interestingly, quenched disorder and orientational noise do not play symmetric roles, even though particles are motile and therefore sample in time different local realizations of disorder. In all these

works, increasing disorder at fixed noise strength *always* reduces order in the system, see Fig. 1.13. As a matter of fact, quenched disorder and annealed noise alter flocking in fundamentally different ways. Das and co-workers have evidenced that long-range order was suppressed by the quenched rotators. Instead, quasi-long-ranged order is found in the system for small disorder densities. Figure 1.14 shows the algebraic decay of the polarization with increasing system sizes that attests to this fact.

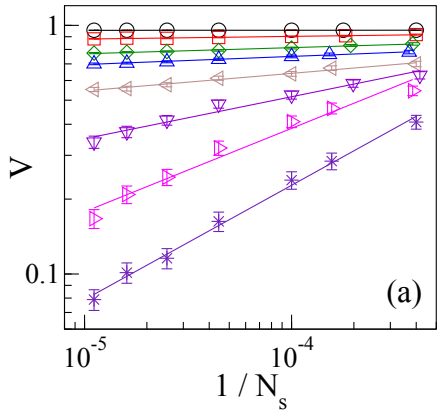

Figure 1.14 | **Quasi-long-ranged order in flocks with quenched disorder.** The polarization V decreases algebraically with increasing the system size $1/N_S$ in the presence of quenched rotators. The obstacle density increases from top to bottom. Black circles: no disorder. Figure from [32].

The occurrence of quasi-long-ranged order of flocks with quenched disorder has been very recently demonstrated analytically [121, 120]. Toner and co-workers have considered the hydrodynamic equations of flocking (1.4) and (1.5) in the presence of quenched disorder in place of the annealed disorder given by Eq. (1.6). In the case of a quenched disorder, the random force $\mathbf{f}$ of Eq. (1.5) is therefore static and only depends on space. More precisely, $\mathbf{f}$ is Gaussian with zero mean and spatial correlations in the direction transverse to the flock propagation given by:

$$\left\langle f_\perp(\mathbf{r}) f_\perp(\mathbf{r}') \right\rangle = \Delta \delta(\mathbf{r} - \mathbf{r}'), \tag{1.12}$$

where Δ denotes the quenched disorder strength. Toner and co-workers have proved that any small amount of quenched disorder $\Delta > 0$ destroys long-ranged order of flocks in dimension 2. Quasi-long-ranged order occurs instead, making the flocks still more robust to quenched disorder than equilibrium systems.

In contrast with Toner's prediction, Chepizhko and co-workers have reported a transition from true long-ranged order to quasi long-ranged order occcuring at a *finite* disorder density [25]. This difference in phenomenology stresses that the precise nature of the disorder matters. Repulsive obstacles and polar obstacles do not alter flocking the same way. Flocking through quenched disorder could cover a rich variety of behaviors.

1.6 Organization of this thesis

As exemplified by the disorder-induced suppression of long-ranged order, dramatic changes can arise in flocks' behavior when they evolve in complex environments. In this thesis, I build on the realization of synthetic flocks from self-propelled colloids [13, 12] to explore the thrilling physics of flocking. I experimentally investigate how flocking occurs in challenging environments. This thesis is organized as follows.

Chapter 2: A model experiment for flocking

In Chapter 2, I introduce synthetic flocks assembled from motile colloids. I first show how to make colloidal rollers out of bare plastic microbeads. Then, I discuss the pair interactions between these colloidal rollers. Alignment interactions are evidenced and increasing the roller density yields the same phenomenology as in the Vicsek model, see Figs. 1.8 and 1.15. Finally, the homogeneous flocks that form at high densities is shown to be an actual representative of Toner and Tu polar liquids.

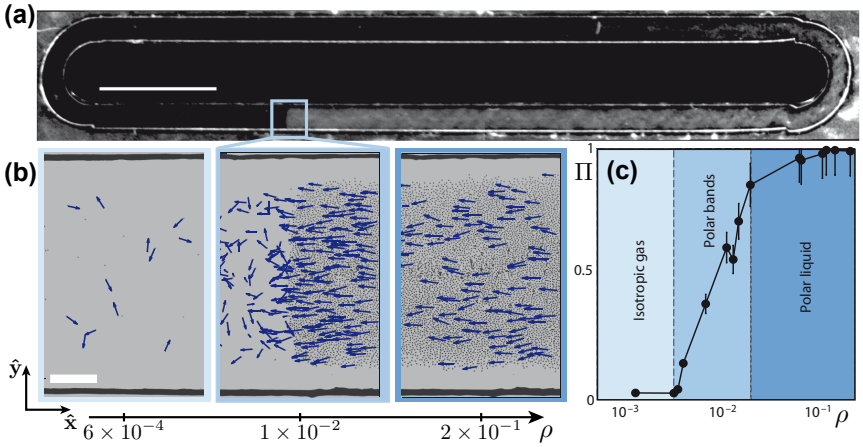

Figure 1.15 | **A model experiment for flocking.**

Chapter 3: Collective stubbornness resisting opposing flows

In Chapter 3, I investigate the response of colloidal flocks to longitudinal perturbations. I show how to take advantage of the microfluidic device where the synthetic flocks are manipulated to apply external drives. Second, I probe the response of colloidal polar liquids to longitudinal fields. Remarkably, colloidal flocks can sustain opposing fields. This robustness is made possible by the presence of boundaries that confine the flock laterally. A detail examination of the flock dynamics reveals a buckled pattern that leans on these walls, see Fig. 1.16. A minimal hydrodynamic theory correctly accounts for these observations. Over a finite range of field amplitude, buckled flocks that resist opposing fields are shown to be stable. Finally, the non-linear response of flocks to external fields is exploited to realize autonomous oscillators. Most of this work has been published in the article "Flowing active liquids

in a pipe: Hysteretic response of polar flocks to external fields", which is reproduced at the end of Chapter 3.

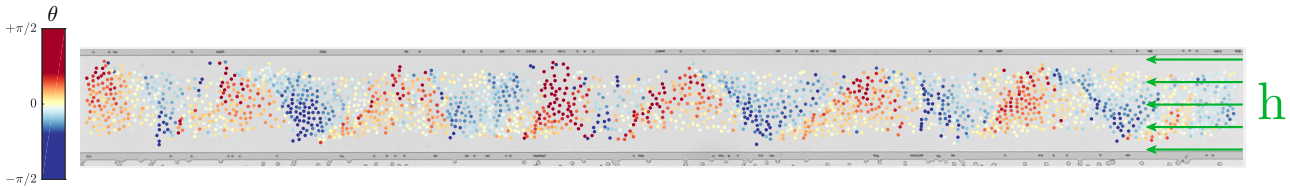

Figure 1.16 | **Collective stubbornness resisting opposing flows.**

Chapter 4: Colloidal rollers in microfluidic forests

In Chapter 4, I study the dynamics of flocks in the presence of quenched disorder. First, small cylindrical posts are shown to act on particles through repulsive torques. The dynamics of individual self-propelled colloids in heterogeneous environments is then investigated. A localization scenario *à la* Lorentz is recovered upon increasing the obstacle density. Finally, I address the robustness of colloidal flocks to quenched disorder. Melting of flocks occur upon increasing disorder. The dynamics of flocks is dramatically altered near the transition. The random distribution of obstacles yields the emergence of a network of rivers along which the flocks preferentially propagate, see Fig. 1.17. The emergence of these favored routes is rationalized within the hydrodynamic framework. This network results from the competition between disorder and the flock orientation elasticity (D_3 in Eq. (1.5)). While disorder tends to randomly stir the flocks, their elasticity prevent changes of direction to occur on small lengthscales.

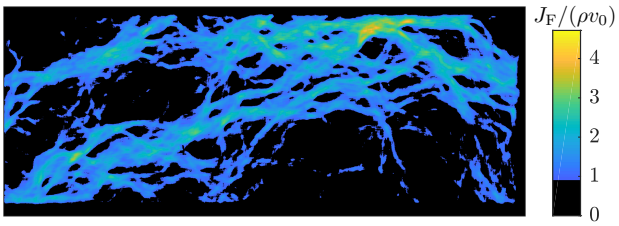

Figure 1.17 | **Colloidal rollers in heterogeneous environments.**

Chapter 2

A model experiment for flocking

From grains to emulsions and gels, all soft materials have successfully been motorized this past decade [35, 102, 118, 117, 100]. In particular, several strategies have been developed to turn passive colloids into self-propelled bodies. Here, I focus on colloidal rollers: colloids that are made active by use of the Quincke rotation mechanism. In this chapter, I first present the Quincke rotation and its application to colloids. Then, from this motorization principle, I show how interactions between colloidal rollers can be rationalized hence collective motion. Finally, I give some insights into the resulting colloidal flocks to show that they constitute genuine Toner-and-Tu fluids. The experimental system that I am about to describe was first introduced in [13]. The experimental set-up was primarily developped by Antoine Bricard [11] and Nicolas Desreumaux [37], while Jean-Baptiste Caussin worked out the theoretical description of the system [17]. In the following sections, I also provide additional results from my own work which are denoted by a star symbol $\star$.

2.1 Colloids made active

2.1.1 Quincke rotors $\star$

To make colloids active, we take advantage of an electro-hydrodynamic instability first introduced by Georg Quincke in 1896 [95]. The Quincke mechanism sets into rotation an insulating body immersed in a conductive liquid. Figure 2.1a shows the original sketch of Quincke's set-up. A DC electric field is applied to a cylinder immersed in a conductive liquid. Spontaneous rotation of the cylinder occurs under specific conditions [78].

Though it was first envisioned by Quincke at the macro-scale, the Quincke rotation is a scale-free mechanism that also applies to the micro-scale. To present the Quincke rotation, I will rely on an experimental realization of $10\,\mu$m-diameter rotors. These rotors are shown in Fig. 2.1b. They were made in a process of 2-photon lithography from SU8 photoresist by Gazton Vizsnyiczai and Roberto Di Leonardo. When a DC electric field $\mathbf{E_0}$ is applied to a rotor, it is polarized due to charge transport within the fluid, see Fig. 2.1c. As the resulting dipole $\mathbf{P}$ is opposite to the electric field, fluctuations

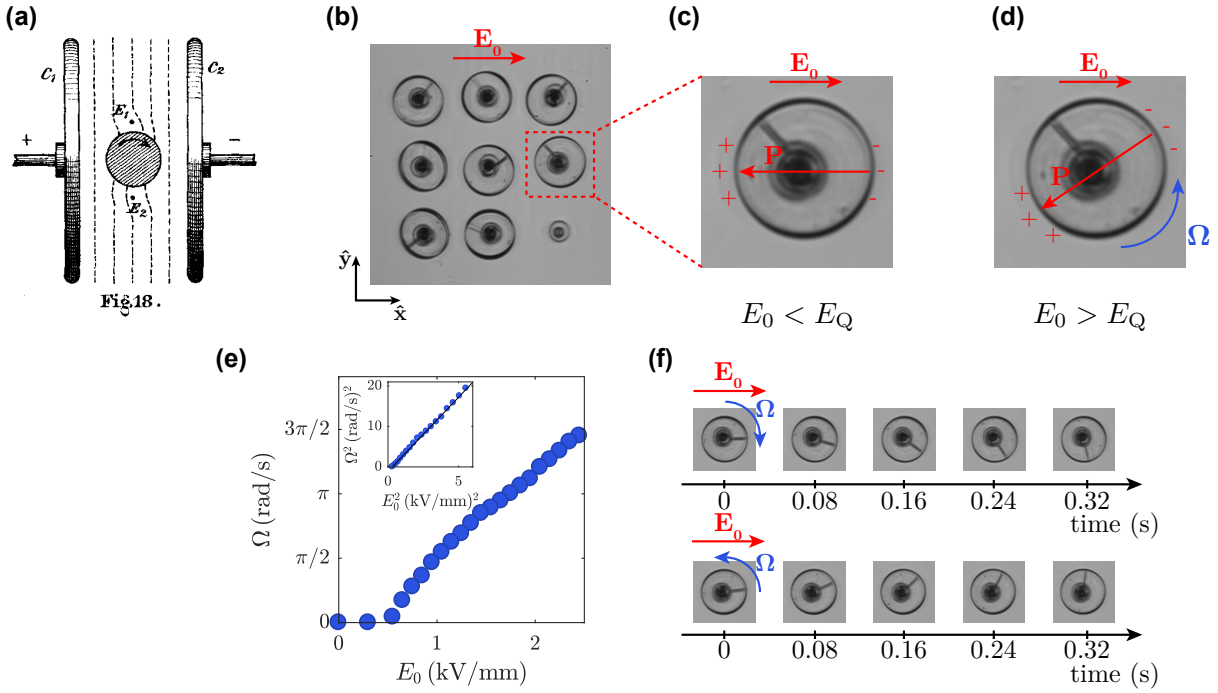

Figure 2.1 | **Quincke rotors.** **(a)** Schematic of the original macro-scale rotor from Quincke [95]. The electrodes C_1 and C_2, of diameter 3.5 cm were spaced by 1.5 cm. **(b)** Micrograph of nine SU8 Quincke rotors, see from above. **(c)** Below the Quincke threshold, for $E_0 < E_Q$, the dipole $\mathbf{P}$ stays anti-aligned with the electric field $\mathbf{E_0}$. No rotation occurs. **(d)** Above the Quincke threshold, for $E_0 > E_Q$, $\mathbf{P}$ and $\mathbf{E_0}$ make a finite angle. A steady rotation at speed Ω occurs. **(e)** The rotor speed Ω increases with the applied DC electric field E_0. Inset: Ω^2 varies linearly with E_0^2, in agreement with the theory. **(f)** Two time series showing the rotation of a rotor at constant speed $\Omega = 3.5\,\mathrm{rad/s}$ under an electric field $E_0 = 2\,\mathrm{V}/\mu\mathrm{m}$. The rotation occurs either clockwise (top) or counter-clockwise (bottom) with equal probability.

of its orientation lead to a finite electric torque $\mathbf{P} \times \mathbf{E_0}$ that favors the rotor rotation. Conversely, viscous friction tends to suppress any rotation. The result of the competition between viscous friction and electric torqued depends on the field amplitude. Below a threshold E_Q, the fluctuations are overdamped and the system is stable: no rotation occurs, see Fig. 2.1c. Above E_Q, the system is unstable and the rotor reaches a new steady state with a constant rotation speed Ω, see Fig. 2.1d. Ω is set by the electric field amplitude: $\Omega \propto \sqrt{\left(\frac{E_0}{E_Q}\right)^2 - 1}$. Figure 2.1e shows that the measured increase of the rotation speed with the electric field amplitude perfectly matches this prediction. An important feature of Quincke rotation is that the direction of rotation is random. This randomness stems from the initial fluctuation of the dipole orientation $\mathbf{P}$ that initiates the rotation. As a consequence, the rotor has equal probability to rotate clockwise or counter-clockwise, as illustrated by the two time series of Fig. 2.1f.

2.1.2 Quincke rollers

The Quincke mechanism is directly applicable to induce the rotation of insulating spheres dispersed in a conducting liquid. We use Polystyrene colloids of radius $a = 2.4\,\mu$m dispersed in a mixture of dioctyl sulfosuccinate sodium salt (AOT) and hexadecane. We control the conductivity of the liquid σ_l through the concentration of salt. Typically we use [AOT] $= 0.15$ mol/l. As shown in Fig. 2.2a, the colloidal solution is confined between two electrodes spaced by $H = 110\,\mu$m. Applying a DC electric field above the Quincke threshold leads to the rotation of the colloids. In our experiments, we let the colloids settle on the bottom electrode where they start to roll.

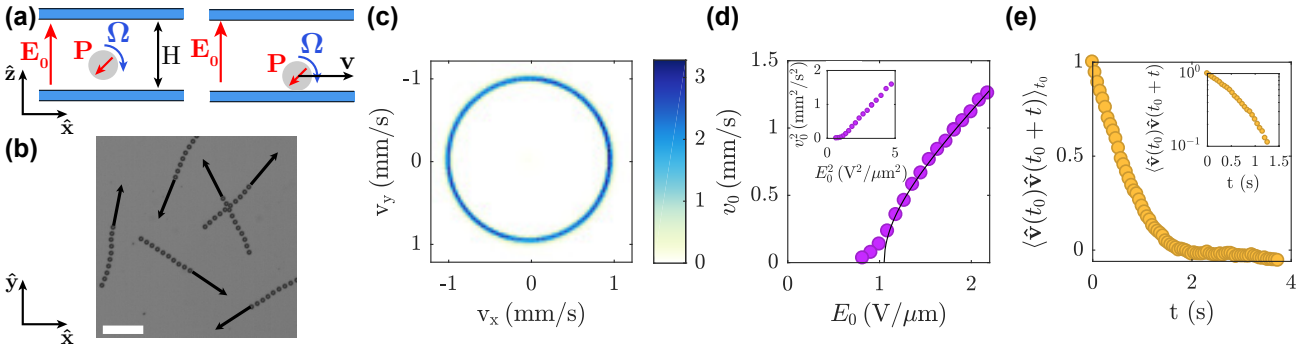

Figure 2.2 | **Quincke rollers.** **(a)** Schematics of colloidal rollers. Top: Quincke mechanism powers the rotation of colloids. Bottom: at the bottom of the microfluidic chamber, rotation of the colloids is converted into translation. **(b)** Superimposed snapshots of colloidal rollers. They move at constant speed in various directions. Scale bar: $50\,\mu$m. **(c)** Histogram of the roller's velocities. **(d)** The roller speed v_0 increases with the electric field E_0. Inset: v_0^2 increases linearly with E_0^2 as predicted by the theory. **(e)** Velocity autocorrelation function $\langle \hat{\mathbf{v}}(t_0)\hat{\mathbf{v}}(t_0+t)\rangle_{t_0}$. The orientation of the rollers is randomized at a typical rate of $D \sim 0.8\,\mathrm{s}^{-1}$.

Typical trajectories of such Quincke rollers are shown in Fig. 2.2b. These superimposed snapshots reveal two main features. First, the colloids move at constant speed v_0, as the distance traveled between two subsequent frames appears constant. Second, they move in various directions. More quantitatively, Fig. 2.2c shows the two-dimensional histogram of the velocities of the Quincke rollers. This histogram is isotropic and peaked along a circle of radius v_0. As for the rotors, the amplitude of the electric field $\mathbf{E_0}$ sets the rotation speed and thus v_0. Figure 2.2d shows that the rollers' speed increases with E_0 as:

$$v_0 = \frac{a}{\tau}\frac{\tilde{\mu}_t}{\mu_r}\sqrt{\left(\frac{E_0}{E_\mathrm{Q}}\right)^2 - 1}, \tag{2.1}$$

where a is the roller radius, τ is the time of charge relaxation within the fluid and $\tilde{\mu}_t$ and μ_r are mobility coefficients. $\mu_r = 1/(8\pi\eta a^3)$ where η is the liquid viscosity. E_Q is the Quincke threshold under which no motion occurs:

$$E_\mathrm{Q} = \left[4\pi\epsilon_l a^3\left(\chi^\infty + \frac{1}{2}\right)\mu_r\tau\right]^{-1/2} = \sqrt{\frac{8}{3}\eta\frac{\sigma_l}{\epsilon_l\epsilon_p}}. \tag{2.2}$$

The Quincke threshold depends on the material properties of both the fluid and the insulating sphere. η is the fluid viscosity, σ_l is the fluid conductivity, ϵ_l and ϵ_p are the dielectric constants of the liquid and the colloid respectively and $\chi^\infty = (\epsilon_p - \epsilon_l)/(\epsilon_p + 2\epsilon_l)$. The second equality follows from taking $\mu_r = 1/(8\pi\eta a^3)$ (thus neglecting the change of μ_r due to the proximity of the bottom electrode). Figures 2.2c and 2.2d demonstrate that the rollers' dynamics results from the Quincke motorization. However, the trajectories displayed in Fig. 2.2b show a feature that is not captured by the Quincke mechanism: rollers do not propel along straight lines but seem to diffuse orientionally. We quantify this orientation diffusivity by measuring the velocity orientation correlations $\langle \hat{\mathbf{v}}(t_0)\hat{\mathbf{v}}(t_0+t)\rangle_{t_0}$, see Fig. 2.2e. The decorellation is exponential with a typical rate $D \sim 0.8\,\mathrm{s}^{-1}$. We note that Brownian diffusion would yield orders of magnitude lower re-orientation rates $D_\mathrm{B} \sim 4\times10^{-3}\,\mathrm{s}^{-1}$. The origin of the roller orientation diffusivity thus remains unclear. It could be due to surface heterogeneities as well as the Brownian diffusion of the surface charges involved in the Quincke mechanism. In the latter case, a rough estimate of the roller orientation diffusivity gives $D \sim 0.1 - 1\,\mathrm{s}^{-1}$ by considering ion clouds of size $100 - 10\,\mathrm{nm}$.

To sum up, we use the Quincke mechanism to make colloids active. Our colloidal rollers behave as persistent random walkers with speed v_0 and orientation diffusivity D. Therefore, the equations of motion of roller i take the simple form:

$$\frac{\partial \mathbf{r_i}}{\partial t} = v_0 \hat{\mathbf{v}}_\mathbf{i}, \tag{2.3}$$

$$\frac{\partial \theta_\mathbf{i}}{\partial t} = \sqrt{2D}\xi_i, \tag{2.4}$$

where $\mathbf{r_i}(t)$ is the position of roller i, $\hat{\mathbf{v}}_\mathbf{i}(t) = (\cos\theta_i(t), \sin\theta_i(t))$ its direction of motion and $\xi_i(t)$ is a white noise with zero mean and unit variance. Colloidal rollers behave individually like active Brownian particles.

2.2 From active colloids to colloidal flocks

Dense assemblies of colloidal rollers form active phases of matter that display collective motion: flocks. In this section, I provide a comprehensive picture of the formation of colloidal flocks. The formation of flocks from colloidal rollers is rationalized by understanding the interactions between pairs of rollers. This is done in two steps: elucidating the perturbations caused by a roller to its surrounding electric field and hydrodynamic flow on one end, and elucidating the individual response of a roller to electric fields and hydrodynamic flows on the other.

2.2.1 Roller's response to perturbations ⋆

To establish the response of rollers to perturbations of both electric and hydrodynamic fields, we benefit from the versatility of our microfluidic device. The response of colloidal rollers to a hydrodynamic forcing is achieved by flowing the hexadecane solution at a constant flow rate within the microfluidic cell. This situation is depicted in Fig. 2.3a and more information is provided about it in section 2.4. Given the geometry of the microfluidic cell, a Poiseuille flow $h(z)\hat{\mathbf{x}}$ results in the $\mathbf{z}$

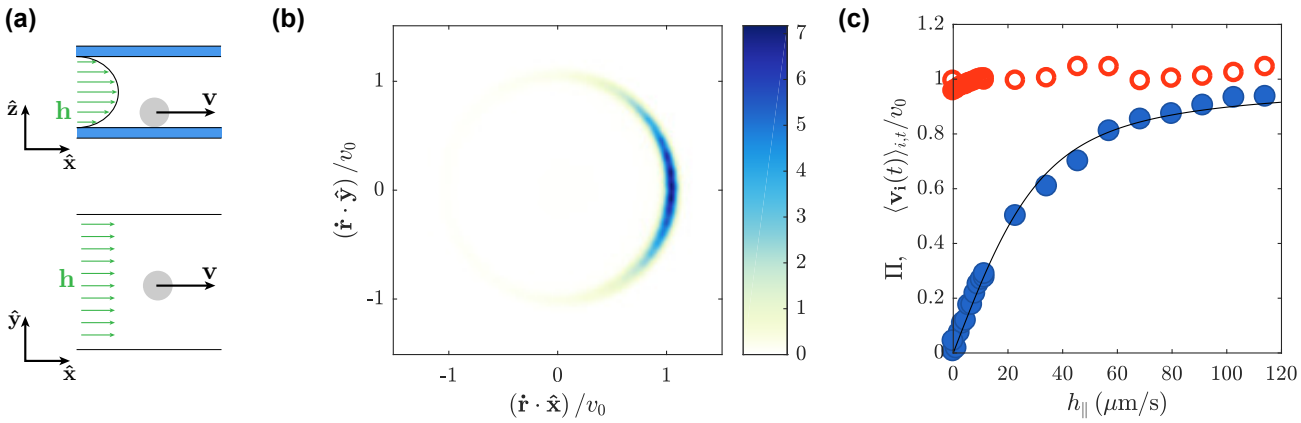

Figure 2.3 | **Individual response of Quincke rollers to tangential hydrodynamic fields. (a)** Schematics of a Quincke roller facing a hydrodynamics flow. Top: side view. Bottom: top view. **(b)** Histogram of the roller's velocities under a hydrodynamics flow of amplitude $h_\parallel = 57\,\mu$m/s. **(c)** Average polarization (blue circles) and normalized speed (red open circles) of the rollers with respect to the flow amplitude. The black line is the theoretical prediction for the polarization $\Pi(h)$.

direction. A high precision syringe pump controls the flow amplitude. I refer to the flow amplitude by evaluating the flow velocity at the height of a colloid radius: $h_\parallel \equiv h(z = a)$. Figure 2.3b shows that the bi-dimensional histogram of the roller velocities is biased in the direction of $\mathbf{h}$: colloidal rollers align with the flow. Remarkably, the interaction with the flow leaves the speed of colloidal rollers unchanged. More quantitatively, Fig. 2.3c shows that the alignment process is all the more efficient as the solvent flow strengthens: the polarization of the system $\Pi = \langle\hat{\mathbf{v}}_\mathbf{i}(t)\rangle_{i,t}$ increases with $h_\parallel$. It is interesting to note that the polarization is as high as $\Pi = 0.9$ for a flow amplitude $h_\parallel = 0.1\,v_0$.

Following the same scheme, we investigate the response of colloidal rollers to tangential electric fields. To do so, the two electrodes are positioned to form a wedge as depicted in Fig. 2.4a. This slight tilt of order $\alpha \sim 1\,$deg gives rise to a finite in-plane electric field $E_\parallel \sim E_0 \sin\alpha$. Figure 2.4b shows that the dynamics of colloidal rollers is altered by this field: they align opposite to $\mathbf{E}_\parallel$. The experimental setup does not permit measurements as accurate as for the hydrodynamic forcing. Figure 2.4c nonetheless unambiguously demonstrates that the polarization of the system increases with the electric field amplitude.

Based on these two experimental observations, we can infer the following equations of motion for colloidal rollers under tangential hydrodynamics flows and electric fields:

$$\frac{\partial \mathbf{r_i}}{\partial t} = v_0 \hat{\mathbf{v}}_\mathbf{i}, \tag{2.5}$$

$$\frac{\partial \theta_\mathbf{i}}{\partial t} = -\frac{\partial}{\partial \theta_i}\left[-\mu_\mathrm{h}\hat{\mathbf{v}}_\mathbf{i}\cdot\mathbf{h} + \mu_\mathrm{E}\hat{\mathbf{v}}_\mathbf{i}\cdot\mathbf{E}_\parallel\right] + \sqrt{2D}\xi_i. \tag{2.6}$$

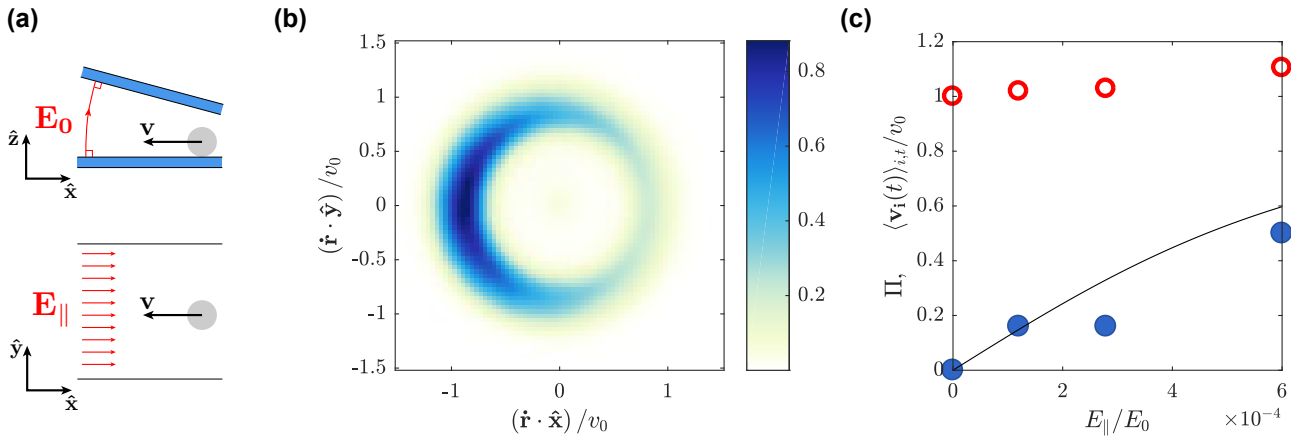

Figure 2.4 | **Individual response of Quincke rollers to tangential electric fields. (a)** Schematics of a Quincke roller facing a tangential electric field. Top: side view. Bottom: top view. **(b)** Histogram of the roller's velocities under a tangential electric field $E_{\parallel} = 0.6 \times 10^{-3} E_0$. **(c)** Average polarization (blue circles) and normalized speed (red open circles) of the rollers with respect to the magnitude of the tangential electric field. The black line is the theoretical prediction for the polarization $\Pi(h)$.

In this expression, μ_{h} and μ_{E} are positive mobility coefficients linked to the alignment with a flow and the anti-alignment with the in-plane electric field, respectively. Given the quality of the data shown in Fig 2.3c, an accurate evaluation of μ_h is possible. In the absence of tangential electric field, Eq. (2.6) is the analogous of the Langevin equation describing the re-orientation dynamics of a magnetic spin in an external magnetic field at finite temperture. It is readily solved to get an estimate of the average polarization: $\Pi(h) = \frac{I_1(\mu_{\mathrm{h}} h/D)}{I_0(\mu_{\mathrm{h}} h/D)}$, where I_0 and I_1 are modified Bessel functions of the first kind. By fitting the data with this prediction, we get:

$$\mu_{\mathrm{h}} = 0.075\,\mu\mathrm{m}^{-1}. \tag{2.7}$$

I have demonstrated experimentally how the colloidal rollers respond to perturbations of the hydrodynamic and electric fields. This question was originally adressed theoretically in [13]. As a matter of fact, Eqs. (2.5) and (2.6) can be derived from the Stokes and Maxwell equations only. Expressions of the mobility coefficients μ_{h} and μ_{E} in terms of microscopic parameters also follow from this theoretical treatment [13, 17]. Estimations of their numerical values gives $\mu_{\mathrm{E}} \sim 2 \times 10^3\,(\mathrm{V}/\mu\mathrm{m})^{-1}/\mathrm{s}$ and $\mu_{\mathrm{h}} = 0.085\,\mu\mathrm{m}^{-1}$ in excellent agreement with the experimental data of Figs. 2.3c and 2.4c.

2.2.2 Roller-roller interactions

We now know that colloidal rollers align with hydrodynamic flows and anti-align with in-plane electric fields. To understand how the rollers interact with each others, one last concern needs to be elucidated: how does a single roller perturbs these fields? The in-plane perturbation of the electric field from a roller can be qualitatively captured by a simple line of argument which is illustrated in Fig. 2.5. Let

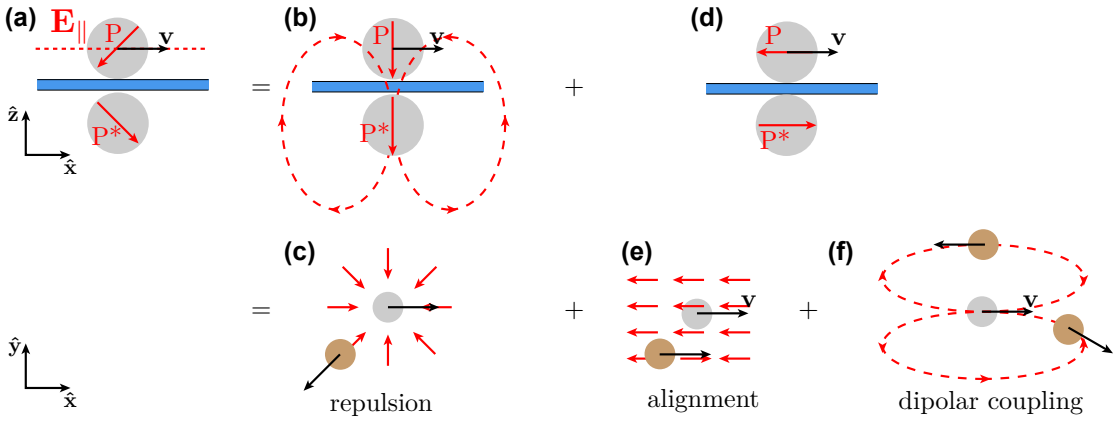

Figure 2.5 | **Electrostatic interactions between Quincke rollers.** **(a)** Schematic of a colloidal roller (grey circle) with an electric dipole $\mathbf{P}$ sitting on an electrode together with its image $\mathbf{P}^*$. How does the roller perturbs the electric field in the $z = a$ plane? **(b)** The orthogonal component of $\mathbf{P}$ yields no tangential field, while the orthogonal component of $\mathbf{P}^*$ gives rise to a monopolar field in the $z = a$ plane. **(c)** The monopolar field due to $\mathbf{P}^*$ points toward the colloid. A neighbour colloid (brown circle) anti-aligns with this field, hence being repulsed. **(d)** The longitudinal components of $\mathbf{P}$ and $\mathbf{P}^*$ both contribute to a non-vanishing $E_\parallel$ in the $z = a$ plane. The resulting field is the superposition of a uniform field (e) and a dipolar field (f). **(e)** The uniform field, originating from the longitudinal components of $\mathbf{P}$ and $\mathbf{P}^*$, points in the direction opposite to the colloid velocity (black arrow). As a neighbor colloid (brown circle) anti-aligns with this field, it aligns to move in the same direction. **(f)** The dipolar field, originating from the longitudinal components of $\mathbf{P}$ and $\mathbf{P}^*$, results in a dipolar coupling between rollers. Two neighbor colloids (brown circles) are shown to align within this field.

us consider a roller laying on the bottom electrodes, see Fig. 2.5a. As the roller bears an electric dipole $\mathbf{P}$, the proximity of the electrode requires considering its image $\mathbf{P}^*$ to satisfy the condition of a vanishing tangential field at the electrode. This situation is depicted in Fig. 2.5a. The goal is now to evaluate the tangential component of the electric field $\mathbf{E}_\parallel$ at a height $z = a$ from the electrode. To do so, it is convenient to separate the contributions of the orthogonal components of $\mathbf{P}$ and $\mathbf{P}^*$ from the contributions of their longitudinal components. As shown by the schematic of Fig. 2.5b, the orthogonal component of $\mathbf{P}$ yields no tangential electric field at $z = a$, while the orthogonal component of $\mathbf{P}^*$ yields a monopolar field, Fig. 2.5c. The longitudinal components of $\mathbf{P}$ and its image both contribute to a non-vanishing tangential field at $z = a$, Fig. 2.5d. They give rise to a field $\mathbf{E}_\parallel$ which is the superposition of a uniform field, Fig. 2.5e, and dipolar field, Fig. 2.5f (this last decomposition being hard to see schematically).

The electrostatic interactions between rollers can be readily inferred from Fig. 2.5. As the monopolar field points towards the colloid, a neighbor roller would tend to align its direction of motion with the center-to-center line so as to move away from the colloid, see Fig. 2.5c. Thus the monopolar field yields to repulsion between colloids. The same reasoning applies to the uniform component of the field which

leads to alignment (Fig. 2.5e), as well as to the dipolar component (Fig. 2.5f).

This analysis was rigorously performed analitically in [13], together with the same treatment regarding hydrodynamic interactions. Deriving the hydrodynamic perturbations involves hydrodynamic images somewhat more complex than their electrostatic counterparts. Ultimately, the equations governing the microscopic dynamics of interacting colloidal rollers were derived. The equations of motion of the roller i take the following form:

$$\frac{\partial \mathbf{r_i}}{\partial t} = v_0 \hat{\mathbf{v}}_\mathbf{i}, \tag{2.8}$$

$$\frac{\partial \theta_i}{\partial t} = -\frac{1}{\tau}\frac{\partial}{\partial \theta_i}\sum_{j\neq i}\mathcal{H}(\mathbf{r_i}-\mathbf{r_j}, \hat{\mathbf{v}}_\mathbf{i}, \hat{\mathbf{v}}_\mathbf{j}) + \sqrt{2D}\xi_i(t), \tag{2.9}$$

where the sum runs over all neighbor rollers j, and $\mathcal{H}$ is an effective potential describing the pair interactions between rollers. $\mathcal{H}$ is established by injecting the expressions for the fields $\mathbf{E}_\parallel$ and $\mathbf{h}$ created by a neighbor roller in Eq. (2.6). This procedure leads to the following expression for $\mathcal{H}$, where contributions of the same symmetries have been grouped together:

$$\mathcal{H}(\mathbf{r}, \hat{\mathbf{v}}_\mathbf{i}, \hat{\mathbf{v}}_\mathbf{j}) = A(r)\hat{\mathbf{v}}_\mathbf{j}\cdot\hat{\mathbf{v}}_\mathbf{i} + B(r)\hat{\mathbf{r}}\cdot\hat{\mathbf{v}}_\mathbf{i} + C(r)\hat{\mathbf{v}}_\mathbf{j}\cdot(2\hat{\mathbf{r}}\hat{\mathbf{r}} - \mathbf{I})\cdot\hat{\mathbf{v}}_\mathbf{i}. \tag{2.10}$$

$A(r)$, $B(r)$ and $C(r)$ are dimensionless prefactors which weight the alignment, repulsion, and dipolar interactions, respectively. $A(r)$, $B(r)$ and $C(r)$ not only contain the contributions of electrostatic interactions described in Figs. 2.5e, 2.5c, 2.5f, but also contributions from the hydrodynamic interactions. Their detailed expressions are given below, discriminating between the electrostatic contributions in red and the hydrodynamic contributions in blue:

$$A(r) = A_1\left(\frac{a}{r}\right)^3\Theta(r) + A_2\left(\frac{a}{r}\right)^5\Theta(r), \tag{2.11}$$

$$B(r) = B_1\left(\frac{a}{r}\right)^4\Theta(r), \tag{2.12}$$

$$C(r) = C_1\left(\frac{a}{r}\right)^3\Theta(r) + C_2\left(\frac{a}{r}\right)^5\Theta(r) + C_3\left(\frac{a}{r}\right)^2. \tag{2.13}$$

A_1, A_2, B_1, C_1, C_2 and C_3 are coefficients that depend on microscopic parameters [13]. $\Theta(r)$ is a screening function that reaches zero at a typical distance $r \sim H$. Indeed all interactions between colloidal rollers are short-ranged and screened over a distance set by the gap between the two confining electrodes. The only long-range interaction is a dipolar interaction that stems from hydrodynamic interactions [38]. The value of C_3 is, however, orders of magnitude smaller than the other coefficients. It turned out that, unlike what was first conjectured in [13], this interaction plays no role [48]. Neglecting this long-range contribution in the theoretical developments discussed in Chapters 3 and 4 leads to very convincing agreements with experimental measurements [84, 82].

2.2.3 Colloidal flocks

Colloidal rollers interact with each other. Equations (2.11), (2.12) and (2.13) show that one of the dominant interactions is a ferromagnetic coupling that promotes alignment among rollers. As for the

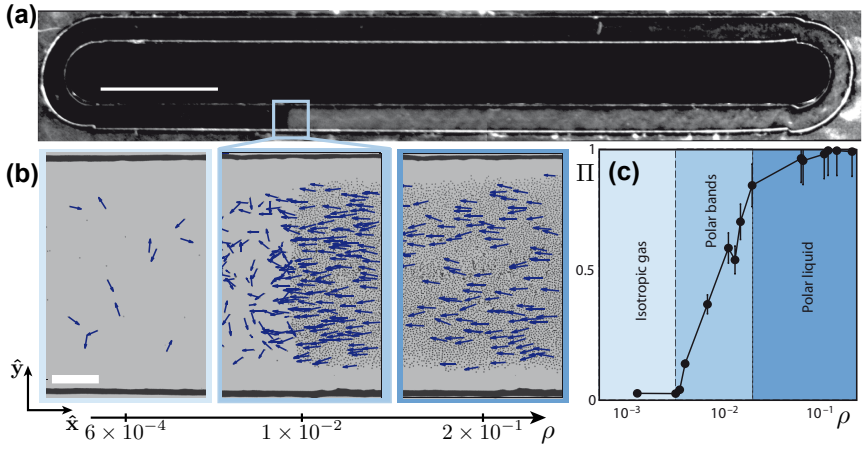

Figure 2.6 | **Colloidal flocks.** **(a)** Colloidal flocks formed into a racetrack. Scale bar: 5 mm. **(b)** Snapshots of the three phases displayed by assemblies of colloidal rollers. As the roller density is increased, colloidal flocks from. Scale bar: 200 μm. **(c)** Polarization of the system with respect to the roller area fraction.

Vicsek model introduced in Chapter 1, the interactions compete with the rotational diffusion. Thus, we can expect that ordered phases emerge when the interactions overcome rotational diffusion. As we have no control over rotational diffusion, it is most easily achieved increasing the roller density. To do so, we confine the colloidal rollers to racetracks by patterning the bottom electrode, see Fig. 2.6a. Typically, we use either Scotch tape (Fig. 2.6) or photo-lithography techniques with 2 μm-thick S1818 photoresist to make this patterning, see section 2.4. As this layer is electrically insulating, only the colloids inside the racetrack are made active.

Increasing the density of rollers within such racetracks, flocks form [13]. Two different polar ordered phases are found. Typical snapshots of this phases are shown in Fig. 2.6b. At intermediate densities the flock has a finite extent and propagates through an homogeneous and isotropic gas of rollers. The flock itself is heterogeneous, as both the density and the polar order decrease from its head to its tail. At high densities, $\rho > 1.8\,\%$, polar order spans the entire racetrack. The colloidal flock is homogeneous and is highly polarized: it forms an active polar liquid. More quantitatively, Fig. 2.6c shows that the polarization of the system increases with the roller density and that the polarization of the polar liquid is always $\Pi > 0.85$.

2.3 Colloidal flocks as prototypical Toner-Tu fluids

Assemblies of colloidal rollers display the same qualitative phenomenology as the Vicsek model presented in Chapter 1. At the macroscopic level, the colloidal-roller polar liquid is akin to the spontaneously flowing liquids described by Toner and Tu hydrodynamics. Some specific features of the roller polar liquid, however, are not accounted for within these theoretical frameworks. First, among the

interactions between rollers is a long-range contribution, the C_3 term in Eq. (2.13). Given the small strength of this dipolar coupling, we expect that this contribution can be neglected in the description of colloidal flocks, but this needs to be checked further. Second, our colloidal flocks are confined into finite cells. Flocks that spontaneously form into racetracks as the one shown in Fig. 2.6a are expected to propagate either clockwise or counter-clockwise. This could be significantly different from the continuous symmetry breaking of Toner and Tu fluids. The confinement-induced constraints on the propagation direction could make the symmetry discrete Z_2. A question then arises: are colloidal flocks prototypical Toner and Tu fluids [122] or prototypical active Ising magnets [111]?

To answer this question, it is necessary to go beyond the macroscopic characterization of colloidal flocks first performed in [13]. More recently, Delphine Geyer has conducted a thorough experimental characterization of the spontaneous density and velocity fluctuations within colloidal polar liquids [48]. As it turns out, colloidal flocks behave as generic Toner and Tu fluids. Here, I will discuss some of Delphine Geyer's results that support this statement. Finally, I will provide the hydrodynamic equations of colloidal roller polar liquids.

2.3.1 Experiments

Goldstone modes in confined colloidal flocks

The continuous symmetry breaking of flocks results in Goldstone modes for the transverse velocities, with respect to the flock propagation direction. Delphine Geyer has measured the transverse velocity auto-correlations and found that these correlations decay algebraically. Figure 2.7a shows the decrease of the transverse velocity auto-correlation both in the transverse and orthogonal directions together with their best power law approximations. Their slow decay are markers of the corresponding Goldstone modes which prove that confinement does not suppress the continuous symmetry degeneracy at scales smaller than W.

Sound propagation in colloidal flocks

Going beyond the static description of the polar liquid, Geyer has also measured their dynamics. She has uncovered the propagation of two sound modes within colloidal roller polar liquid, confirming a two-decade-old theoretical prediction by Toner and Tu [122, 124]. Figure 2.7b shows the speed of sound $c(\theta)$, where θ is the angle of sound propagation with respect to the flock direction of motion. Some of the hydrodynamic coefficients of the flocks can be inferred from these measurements. The sound propagation in the longitudinal direction $\theta = 0$ gives access to the convective coefficient λ_1 in the Toner and Tu hydrodynamics presented in Chap. 1. The propagation of sounds in the transverse direction is only governed by the compressibility β^{-1} of the polar liquid, involved in the pressure term of Toner and Tu hydrodynamics. The propagation of sound in any direction θ is given by the interplay between these two components. Figure 2.7b shows that the interpolation predicted by the theory between $\theta = 0$ and $\theta = \pi/2$ (solid line) perfectly fits the direct measurements (circles). More generally, Geyer's work proposes a generic method to perform the spectroscopy of any liquid with spontaneous symmetry breaking. This technique gives access to numerical estimations of all the hydrodynamic coefficients, without the need for any microscopic considerations. By performing such a spectroscopy on colloidal

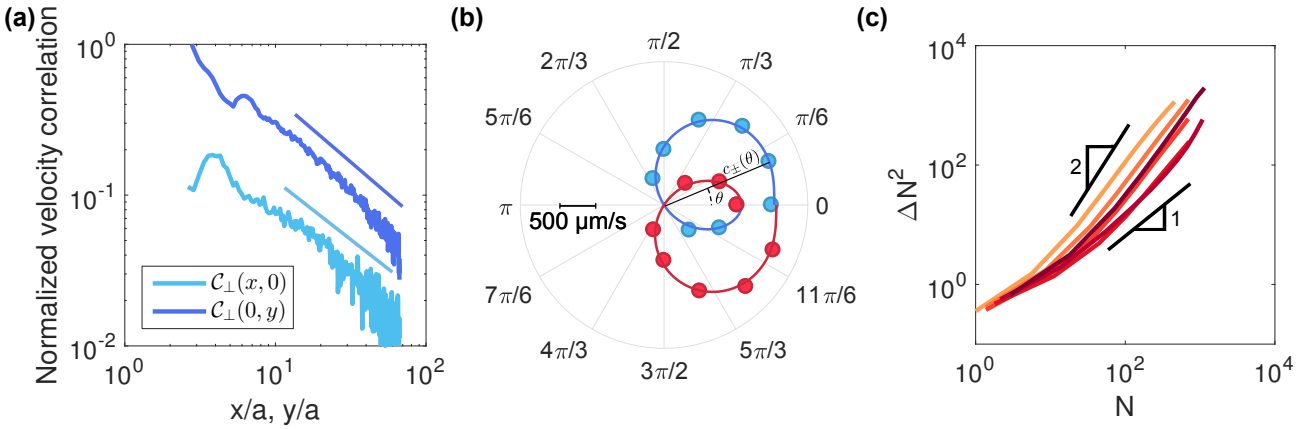

Figure 2.7 | **Colloidal flocks as prototypical Toner and Tu fluids. (a)** Transverse velocity autocorrelations. Black lines: best power-laws. **(b)** Polar plot of the speed of the sound $c(\theta)$ in a colloidal flock at $\rho = 0.11$. Circles: direct measurements. Solid line: analytical prediction from the Toner and Tu linear theory and the measurements at $\theta = 0$ and $\theta = \pi/2$. **(c)** Giant density fluctuations in colloidal flocks.

flocks, Geyer has shown that, at the scales of the experiments discussed in this manuscript, the linear Toner and Tu theory correctly captures the dynamics of colloidal roller polar liquids.

Giant density fluctuations in colloidal flocks ⋆

Among the hallmarks of Toner and Tu fluids are the giant density fluctuations that originate form the interplay between self-propulsion and splay fluctuations. Together with Geyer, we have performed accurate measurements of the density fluctuations within roller flocks. We have eventually rectified the prediction of normal density fluctuations made in [13]. Figure 2.7c shows that density fluctuations are unambiguously anomalous: $\Delta N^2 \propto \langle N \rangle^\alpha$ with $1.5 < \alpha < 2$. These measurements, unfortunately, do not allow us to distinguish between the predictions from the linear Toner and Tu theory ($\alpha = 2$) and their renormalization group prediction ($\alpha = 1.6$ [49]). A discussion of the giant density fluctuations in colloidal flocks can be found in [48], which is reproduced in Appendix.

2.3.2 Hydrodynamics of colloidal flocks

The above experiments provide strong evidence that colloidal-roller liquids form a genuine Toner and Tu fluid. From a complementary perspective, the hydrodynamics of colloidal roller polar liquid was theoretically established in [13] by means of standard kinetic theory procedures, starting from the microscopic equations of motion Eqs. (2.8) and (2.9). Importantly, the resulting equations indeed correspond to Toner-and-Tu-like equations. Of particular interest for the discussion presented in Chapters 3 and 4 is the hydrodynamic description of strongly polarized flocks. Within this limit, the

hydrodynamics of colloidal polar liquids read similar to Eqs. (1.4) and (1.5):

$$\partial_t \rho + \nabla(\rho \mathbf{v}) = 0, \tag{2.14}$$

$$\partial_t \mathbf{v} + \lambda_1(\mathbf{v}\cdot\nabla)\mathbf{v} + \lambda_2(\nabla\cdot\mathbf{v})\mathbf{v} + \lambda_3\nabla(|\mathbf{v}|^2) = U(\rho,|\mathbf{v}|) + D_{\mathrm{B}}\nabla(\nabla\cdot\mathbf{v}) + D_{\mathrm{T}}\nabla^2\mathbf{v} + \mathcal{O}(\nabla\rho). \tag{2.15}$$

The expressions of the hydrodynamics coefficients are shown in the Table below. A few remarks are in order. First, most of these coefficients are tensors. The polar liquid is anisotropic with different properties in the longitudinal and transverse directions, the dynamics along these two directions being coupled. Second, all these hydrodynamics coefficients can be expressed from microscopic parameters [13]. In particular, α_1 and α_2 stem from the ferromagnetic interaction between rollers of Eq. (2.11). These alignment interactions thus favor the polar ordering of the liquid through $U(\rho,|\mathbf{v}|)$ and also contribute to the bending stiffness D_T. The repulsive interaction of Eq. (2.12) contributes to the pressure-like term $\mathcal{O}(\nabla\rho)$. This term (not detailed for the sake of simplicity) promotes the homogenization of the liquid. The short-range dipolar coupling of Eq. (2.13) yields the coefficient γ within this hydrodynamic framework. Finally, in the Table, the operator $\mathbb{P}_{\mathbf{v}} = (1+\mathbf{v}^4/v_0^4)\mathbb{I} - 2v^2\mathbf{v}\mathbf{v}/v_0^4$ reduces to twice the projector on the transverse direction $\mathbb{P} = \mathbb{I} - \hat{\mathbf{v}}\hat{\mathbf{v}}$ in the limit of very polarized flocks for which $|\mathbf{v}| = v_0$. These operators arise because torques dominate the dynamics of interacting rollers at the microscale, see Eqs. (2.8) and (2.9).

	λ_1	λ_2	λ_3	$U(\rho,\lvert\mathbf{v}\rvert)$	D_B	D_T
Polarized flocks	$\frac{\lvert\mathbf{v}\rvert^2}{v_0^2}$	$\left(\frac{\lvert\mathbf{v}\rvert^2}{v_0^2}-1\right)$	$\frac{\mathbf{v}\mathbf{v}-\lvert\mathbf{v}\rvert^2\mathbb{I}}{v_0^2}$	$(\alpha_1\rho - D) - \alpha_1\rho\frac{\lvert\mathbf{v}\rvert^4}{v_0^4}$	$2\gamma\rho\mathbb{P}_{\mathbf{v}}$	$(\alpha_2-\gamma)\rho\mathbb{P}_{\mathbf{v}}$
Extremely polarized flocks	1	0	0	0	$4\gamma\rho\mathbb{P}$	$2(\alpha_2-\gamma)\rho\mathbb{P}$

In the works presented in Chapters 2 and 3, we complement these equations to account for challenging environments by adding an external drive and a random force field respectively. Importantly, in these works as well as in Geyer's work (reproduced in Appendix), the linear Toner and Tu theory correctly accounts for virtually all experimental observations. Whether invoking the more involved renormalization group theory is necessary to correctly describe real realizations of flocks is still unsure. Testing the limit of Toner and Tu linear theory and the breakdown of hydrodynamics remains an experimental challenge to date.

2.4 Performing quantitative measurements on flocks

Synthetic flocks assembled from colloidal rollers are among the most promising model experiments to study flocking for two main reasons. At a fundamental level, we have just seen that colloidal flocks are prototypical realizations of Toner and Tu fluids. From a more practical perspective, colloidal flocks are assembled from up to million of colloids thus offering a unique opportunity to perform quantitative analysis on large scale populations in the laboratory.

2.4.1 Microfluidic devices to handle colloidal flocks

Colloidal flocks are manipulated within microfluidic devices. Figure 2.8 shows a sketch of a typical device. Two glass slides are spaced by a hollow double-sided tape which defines a microfluidic pool.

The inner surface of each glass slide is covered with a thin layer of indium tin oxide which makes them electrically conducting. A power supply is connected to the sides of the electrodes to apply a DC electric field in the $\hat{\mathbf{z}}$ direction. Colloids are flown inside the device through microfluidic connections. They are realized by drilling holes in the upper glass slide and connecting tubes using plastic blocks.

Colloids are confined within racetrack channels by patterning the bottom electrode prior to assembling the device. The patterning consists in covering some parts of the electrode with an insulating material. Even though colloids cover the whole bottom surface upon injection, only the ones laying on the conducting oxide are motorized, see Fig. 2.8b. The patterns were originally made from tape [13, 12]. We now pattern photoresist by mean of UV lithography instead.

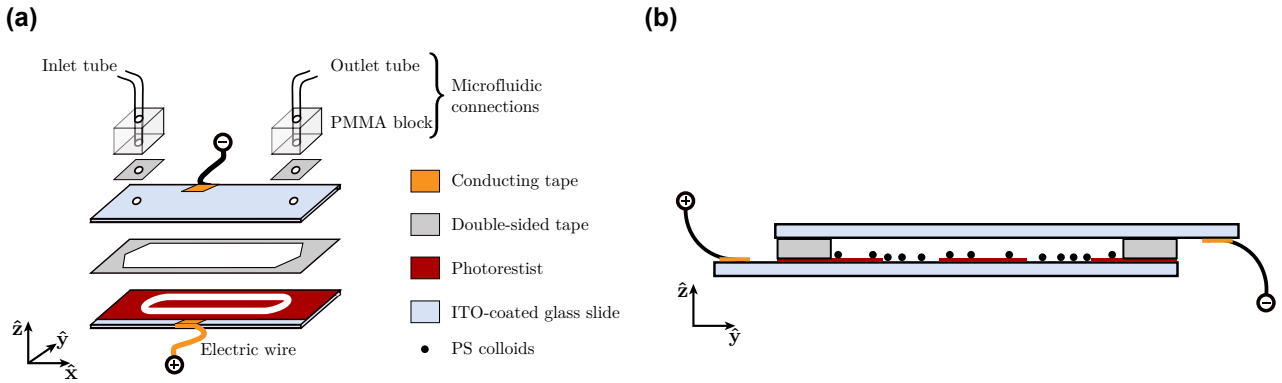

Figure 2.8 | **Microfluidic device. (a)** Exploded view of the device. **(b)** Side view of the device. The sketch is not at scale. The photoresist layer is only 2 μm-thick while the colloid diameter is 4.8 μm. The double-sided tape is 110 μm-thick.

By handling colloidal flocks within such devices, we inherit from the versatility of microfabrication and the adaptability of microfluidics. In my thesis, I have taken advantage of this framework mainly in two ways:

(i) Controlling the microfluidic flow within the device. By connecting a high-precision syringe pump to the inlet of the device, a controlled flow of solvent can be applied. I have used this control to investigate the response of individual rollers to an external perturbation. I have combined this control to the channeling of the solvent flow in order to investigate the response of flocks in to external perturbations. More details about this adaptation can be found in Chapter 3. The basic idea is to pattern the double-sided tape to create channels instead of a bare pool.

(ii) Introducing micron-sized obstacles. UV lithography makes the creation of small features very easy. To study the behavior of flocks in heterogeneous environments, we positioned cylindrical posts of 10 μm diameter in a controlled way. I come back to this adaptation in Chapter 4.

2.4.2 Keeping tracks of large populations of colloids

A million colloids form a flock within a racetrack of width 2 mm and length 10 cm at a packing fraction $\rho = 10\,\%$. Following the microscopic dynamic of every single colloid within such a huge population is obviously impossible. However, by recording 4 Mpx microscope images at high frequency (190 Hz), we are able to measure the instantaneous position and velocity of about 10^4 colloids in a few millimeter-square domain. The basic strategy has been introduced by J. C. Crocker and D. G. Grier [29]. It consists in two steps. First, the colloids are located in every images. Second, the trajectory are build by linking the positions between two subsequent images based on proximity criteria. Figure 2.9 illustrates that this process allows to successfully keep track of thousands of colloidal rollers.

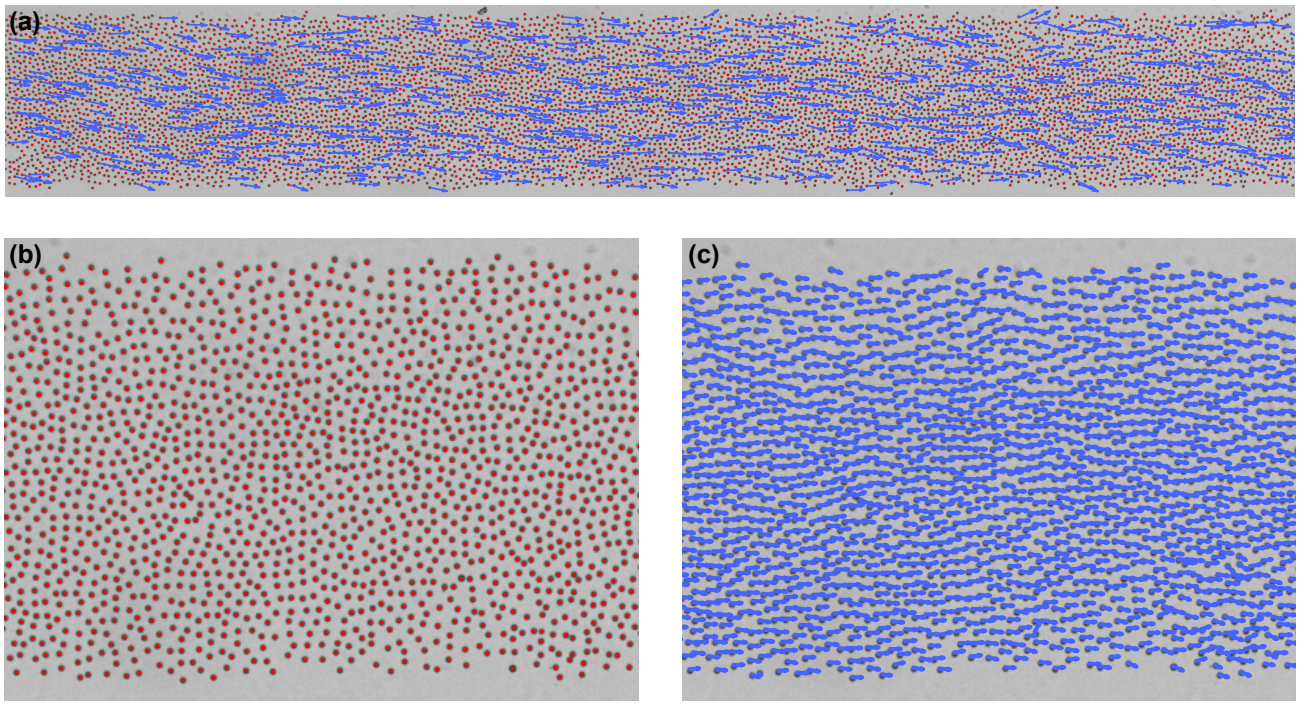

Figure 2.9 | **Detecting and tracking thousands of colloids. (a)** Microscope image of a colloidal flocks. 7877 colloids are detected and tracked. The positions (red circles) and instantaneous velocities (blue arrows) are shown. 1/10 of the velocities are shown for better visibility. The channel is 0.5 mm width. 3 mm of the channel is imaged. **(b)** Close-up on the colloidal flock. The positions (red circles) are shown. All colloids are successfully detected. **(c)** Close-up on the colloidal flock. The velocities (blue arrows) are shown. All colloids are successfully tracked.

The positions of the colloids are determined using the algorithm implemented by P. Lu [72] that searches for local maxima in intensity. I have adapted the C++ code to allow for a background subtraction prior to the execution of the detection routine. This feature is convenient to detect colloids in bright field imaging. It also avoids that obstacles are detected in place of colloids. Using Lu's code is very advantageous as it is very fast compared to other equivalent algorithms.

The tracking of the colloids is performed using the algorithm written in Matlab by D. Blair and E. Dufresne [7]. I have slightly modified the original code to make some subroutines faster. A shown in Fig. 2.9c, this tracking algorithm works perfectly to follow the dynamics of all the colloids.

2.5 Conclusion: colloidal flocks to unveil the physics of flocking

Colloids are motorized by taking advantage of an electro-hydrodynamics instability within microfluidic devices. These active colloids behave as active Brownian particles in dilute systems while polar-ordered flocks emerge in dense systems. Experiments have proved that these flocks are prototypical polar liquids, as introduced two decades ago by Toner and Tu [122]. This system presents several assets. In particular, it gives a unique opportunity to perform quantitative measurements on flocks made of millions of particles. In addition, this active-colloid system is tractable theoretically. Starting from first principles, accurate descriptions of the particle dynamics can be formulated. This theoretical framework spans from the scale of individual particles to the macroscale with the hydrodynamics descriptions of flocks. In Chapters 3 and 4, I take advantage of the versatility of this model experimental system to address some fundamental questions regarding the physics of flocking.

Chapter 3

Collective stubbornness resisting opposing flows

As the design of new active materials with emergent collective behaviors has concentrated most efforts in the field, the response of active materials to external perturbations has been overlooked so far [66, 44]. Manipulating colloidal rollers within microfluidic devices offers a chance to probe the response of spontaneously flowing liquids to external perturbations.

In Chapter 2, I showed that isolated colloidal rollers are docile: they roll preferentially in the direction set by the external flows as exemplified in Fig. 2.3. More quantitatively, the orientation dynamics of an isolated roller subject to a homogeneous shear flow is the exact analogous to that of a classical spin in a magnetic field. To better assess the reach of this result, it is worth having in mind the analogy between polar active matter and ferromagnetism first proposed by Vicsek [129]. Within this context, the velocity of an isolated colloidal roller is the analogous of a spin. From a collective point of view, the transition from an isotropic gas of colloidal rollers to a flock is akin to the transition from a paramagnet to a ferromagnet. In monitoring this transition, the average velocity of rollers plays the role of the system magnetization. The results of Chapter 2 complement this analogy: the analogous of an external magnetic field is the solvent flow for colloidal rollers. From this perspective, studying the response of flocks, active ferromagnets, would first start with the elucidation of their magnetization curve.

In the following sections, I elucidate how confined active fluids with broken rotational symmetry respond to external fields. First, I provide experimental insights into the response of the two ordered phases assembled from colloidal rollers: the finite flocks and the polar liquids. In stark contrast with individual rollers, polar liquids display an hysteretic response and can proceed against external flows. Secondly, the collective stubbornness of flocks is theoretically explained using an active hydrodynamic description that relies on experimental observations. I show that transverse confinement and bending elasticity act together to protect the direction of collective motion against external flows. Finally, I demonstrate how the hysteretic response of colloidal flocks to external flows can be used to realize autonomous active clocks from confined colloidal flocks.

3.1 How to experimentally test the response of flocks?

Two different polar ordered phases are found upon increasing the roller density, as already introduced in Fig. 2.6. At intermediate densities, i.e. at the onset of collective motion, flocks have a finite extent. They correspond to polar-liquid drops that coexist with a gas of rollers. As depicted in Fig. 3.1a, these flocks are heterogeneous as both the density and polar order decrease from their heads to their tails. Such finite flocks not only form within racetrack channels (Fig. 2.6a) but also within rectangular channels. This slab geometry is very convenient to study the response of flocks, as a homogeneous field is easily achieved through the entire channel by flowing solvent as illustrated in Fig. 3.1b. Following the notation introduced in Chapter 2, we note $\mathbf{h}_{\parallel}$ the solvent velocity evaluated at the height of a roller.

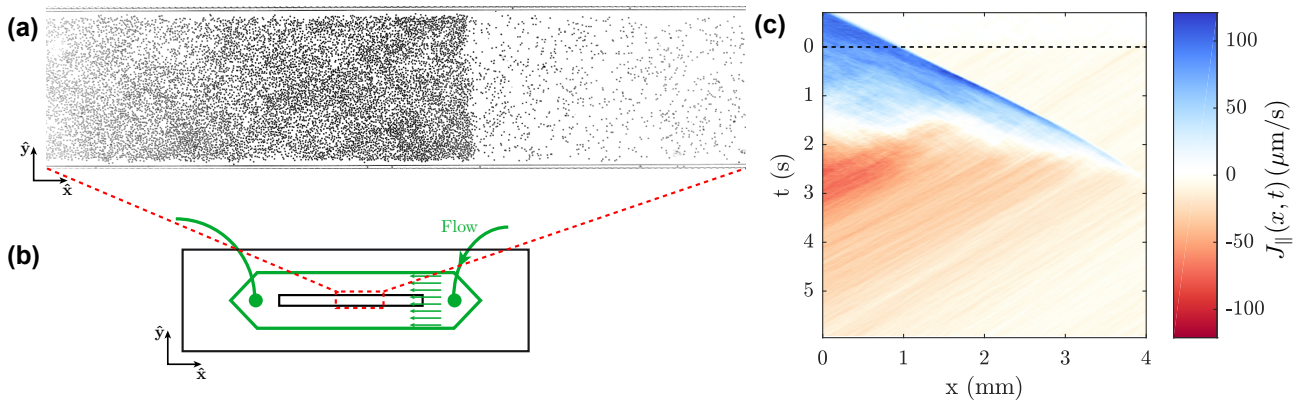

Figure 3.1 | **Response of finite colloidal flocks to longitudinal flows. (a)** Snapshot of a finite flock confined in a rectangular channel. Channel width is 1 mm. **(b)** Sketch of the microfluidic device. Finite flocks are confined in a rectangular channel. A homogeneous and stationary solvent flow is applied through the channel. **(c)** Heatmap of the longitudinal roller current $J_{\parallel}(x,t)$. After an opposing solvent flow is set within the channel ($t = 0\,$s, dashed horizontal line), the flock breaks apart ($t = 1.5\,$s) and eventually reverses to flow along the flow direction ($t = 2.6\,$s).

Figure 3.1c shows the evolution of the longitudinal roller current $J_{\parallel}(x,t) = \langle \rho \mathbf{v} \cdot \hat{\mathbf{x}} \rangle_y$ after an opposing longitudinal field $\mathbf{h}_{\parallel}$ has been established in the channel. The flock resists the field for a few seconds and keeps on propagating along its initial direction. At $t = 1.5\,$s the flock breaks apart: its head still move against the external field while its body reverses its direction to flow along the field direction. Eventually, the head reverses its motion at $t = 2.6\,$s. This complex response originates from the intrinsically heterogeneous structure of these finite flocks which makes the interpretation of the experiments too difficult to draw general conclusions.

By increasing the roller density within racetracks, the finite flock gets larger and larger until its head reaches its tail. A polar liquid then forms with uniform density and polar order, see Fig. 3.2a. Unfortunately, the microfluidics device where colloidal flocks are handled does not allow to realize a uniform longitudinal field along the whole polar liquid. Instead, a uniform longitudinal field $\mathbf{h}_{\parallel}$ was

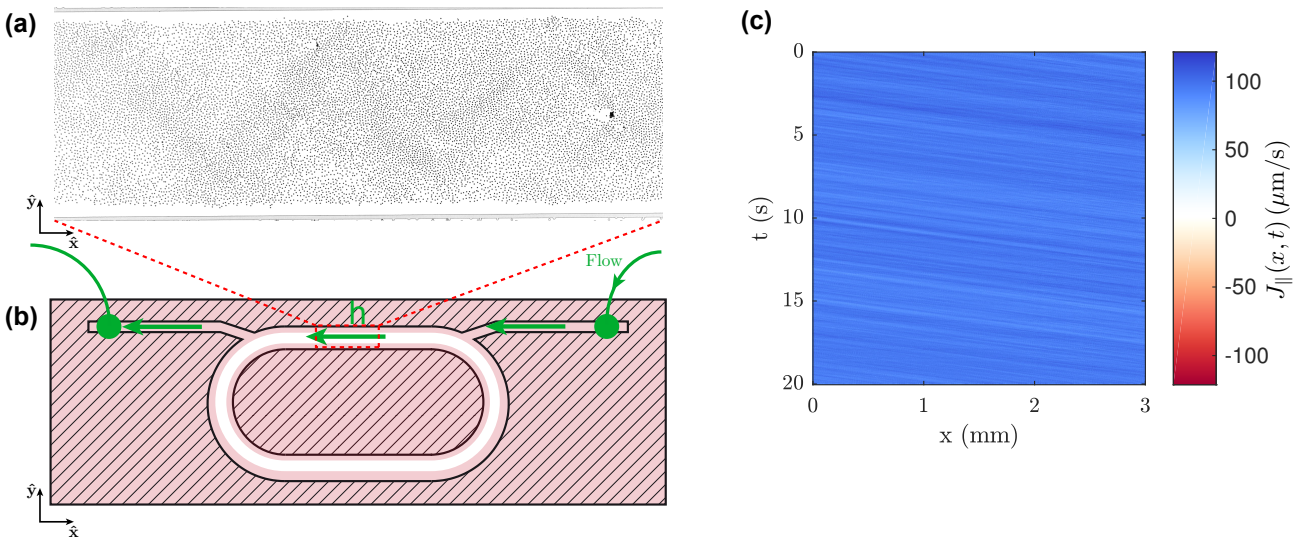

Figure 3.2 | **Response of colloidal polar liquids to longitudinal flows. (a)** Snapshot of a polar liquid confined in a racetrack channel. Channel width is 0.5 mm. **(b)** Sketch of the microfluidic device. Polar liquids are confined in a racetrack channel. A homogeneous and stationnary solvent flow is applied through one of the straight branch of the channel. **(c)** Heatmap of the longitudinal roller current $J_\parallel(x,t)$. The homogeneous polar liquid displays a steady response to an opposing solvent flow.

applied within a single straight part of the racetrack. This configuration is depicted in Fig. 3.2b. Solvent is flown through an assymetric channel that consists in two branches of different lengths. As the hydrodynamic resistance increases with the branch length, the solvent flow is weaker in the longest branch than it is in the smallest one. I have adjusted the geometry so that the residual flow in the long branch is only 1/20 of the flow in the small branch.

Figure 3.2c shows the evolution of the longitudinal roller current $J_\parallel(x,t)$ under a constant and opposing external field. Unlike the response of finite flocks shown in Fig. 3.1c, Fig. 3.2c reveals no evolution in the polar liquid dynamics. The polar liquid displays a steady response to longitudinal fields, therefore making this setup advantageous to quantitatively investigate the response of flocks to external fields.

3.2 Hysteretic behavior of confined flocks

3.2.1 Hysteretic response of colloidal flocks

As for any magnet, characterizing the response of an active ferromagnet starts with the establishment of its magnetization curve. To do so, the solvent flow was systematically varied within the channel and the polarization of the polar liquid $\mathbf{\Pi} = \langle \hat{\mathbf{v}}_\mathbf{i}(t) \rangle_{i,t}$ was measured. Figure 3.3a shows the evolution of the longitudinal polarization $\Pi_\parallel = \mathbf{\Pi} \cdot \hat{\mathbf{x}}$ upon cycling the strength of the external longitudinal field $h_\parallel$.

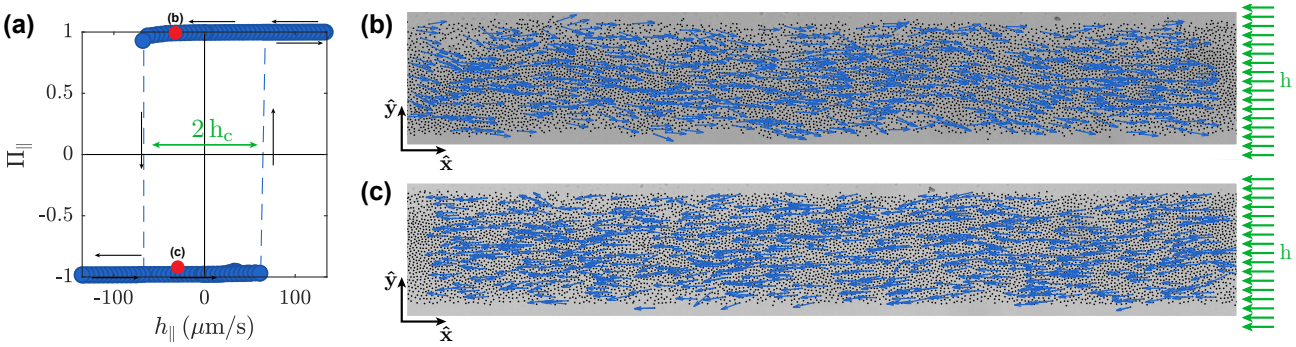

Figure 3.3 | **Bistability of colloidal polar liquids.** **(a)** Magnetization curve of a colloidal flock confined in a 0.5 mm-wide channel. **(b)** Snapshot of a colloidal polar liquid propagating against a longitudinal flow $\mathbf{h}_\parallel = -36\,\mu$m/s. The flock polarization is $\mathbf{\Pi} = 0.98\,\hat{\mathbf{x}}$. Channel width is 0.5 mm. **(c)** Snapshot of a colloidal polar liquid propagating along a longitudinal flow $\mathbf{h}_\parallel = -34\,\mu$m/s. The flock polarization is $\mathbf{\Pi} = -0.98\,\hat{\mathbf{x}}$. Channel width is 0.5 mm.

This figure displays a closed loop: polar liquids have an hysteretic response to external fields. Over a finite range of field amplitudes, flocks are bistable. They can either flow in the direction imposed by the external field, Fig. 3.3b, or opposite to the field, Fig. 3.3c. However, flocks can not overcome opposing fields of any strength. For field amplitudes higher than the coercive field h_c, flocks can only flow in the direction set by the external field. A flock that initially propagates against the field eventually flips its direction of motion under such a strong perturbation. Remarkably, prior to this reversal, the decrease in the flock polarization is minute, see Fig. 3.3.

3.2.2 Confinement-induced stubbornness

In stark contrast to isolated rollers, flocks are stubborn and can resist opposing fields. The collective stubbornness of polar liquids is all the more surprising that a uniform rotation of all the roller velocities would yield no elastic penalty. The colloidal flocks are, however, confined within finite channels. A uniform rotation of the roller velocities would cause them to hit the side walls, which in turn would induce finite wavelength distortion of polar order. Confinement is therefore expected to play a crucial role in the hysteretic response of flocks.

To test for this hypothesis, the response of polar liquids confined in racetracks of width varying from $W = 0.175$ mm to $W = 3$ mm were investigated. Figure 3.4a shows that the coercive field h_c decreases with increasing W. The more confined the flock is, the more robust it is.

Understanding how confinement protects the spontaneous flows of flocks requires looking at their dynamics in more details and inspecting the inner structure of the flocks. Figure 3.4b shows snapshots of polar liquids confined in channel of widths $W = 175\,\mu$m, $W = 250\,\mu$m and $W = 500\,\mu$m while facing an opposing field of amplitude $|h_\parallel| \simeq h_c(W)$. These snapshots reveal oscillating patterns of the polar liquids: flocks resist opposing fields by buckling their spontaneous flow. Again, confinement is of major

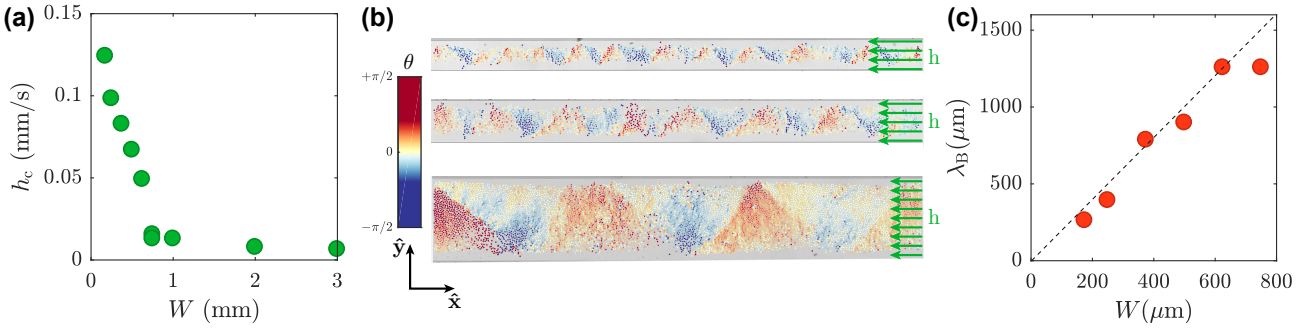

Figure 3.4 | **Confinement-induced hysteresis. (a)** The coercive field h_c decreases with increasing confinement width W. **(b)** Snapshots of polar liquids confined in channels of width $W = 175\,\mu$m, $W = 250\,\mu$m and $W = 500\,\mu$m, and resisting opposing fields of amplitudes slightly below $h_c(W)$. The spontaneous flows of polar liquids display a buckled pattern. **(c)** The wavelength of the buckled pattern λ_b increases with the confinement width W. The dashed line indicates that $\lambda_b \sim 2W$.

importance as the buckling wavelength λ_b seems to increase with W. More quantitatively, Fig. 3.4c shows that the buckling wavelength is set by the confinement width to $\lambda_B \sim 2W$.

To account for the phenomenology revealed by the experiments as well as to prove the relevance of our findings beyond the specifics of colloidal rollers, we derived a minimal theory starting from the Toner and Tu equations of flocking in the presence of an external field:

$$\partial_t \rho + \nabla \cdot (\rho \mathbf{v}) = 0, \tag{3.1}$$

and

$$\begin{aligned} \partial_t \mathbf{v} + \lambda_1 (\mathbf{v}\cdot\nabla)\mathbf{v} + \lambda_2 (\nabla\cdot\mathbf{v})\mathbf{v} + \lambda_3 \nabla(|\mathbf{v}|^2) = {} & \alpha\mathbf{v} - \beta|\mathbf{v}|^2\mathbf{v} - \nabla P \\ & + D_B \nabla(\nabla\cdot\mathbf{v}) + D_T \nabla^2\mathbf{v} + D_2(\mathbf{v}\cdot\nabla)^2\mathbf{v} \\ & + \tilde{\mu}_h \mathbf{h}_\parallel . \end{aligned} \tag{3.2}$$

Equations (3.1) and (3.2) only differ from the Toner an Tu equations introduced in Chapter 1 by the addition of the external field contribution $\tilde{\mu}_h \mathbf{h}_\parallel$. The coefficient $\tilde{\mu}_h$ follows directly from our quantitative knowledge of the individual response of rollers: $\tilde{\mu}_h = \mu_h v_0/2$, where μ_h is the mobility coefficient given by Eq. (2.7). Solving the full Toner and Tu equations with the addition of an external field and the presence of boundaries is well beyond the scope of the project. Instead, we have used the experimental observations to make the problem simpler. Figures 3.4b and 3.4c suggest looking for velocity field solutions $\mathbf{v}(x,t)$ that are superpositions of only two modes:

$$\mathbf{v}(x,t) = v_x(t)\hat{\mathbf{x}} + v_y(t)\cos(qx - \omega t)\hat{\mathbf{y}}, \tag{3.3}$$

the first mode is a uniform flow along the longitudinal direction. The second mode, of amplitude $v_y(t)$, is a buckling mode with a wavevector constrained by our experimental measurements to $q = \pi/W$,

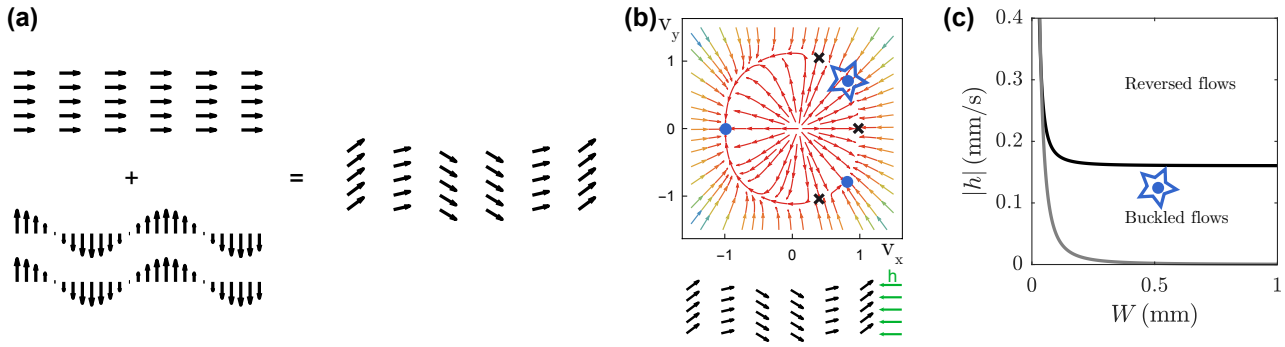

Figure 3.5 | **Hydrodynamic theory captures the bistable response of flocks. (a)** Sketches of the two modes of the velocity field and a superposition. **(b)** Force-field $\mathbf{F}$ plotted in the (v_x, v_y) plane for $\mathbf{h} = -120\hat{\mathbf{x}}\,\mu$m/s. Dark crosses highlight unstable fixed points. Blue circles highlight stable fixed point. The blue star highlights the stable buckled state sketched below. **(c)** Phase diagram predicted by the two-mode theory. The blue star denotes the configuration that corresponds to (b).

see Fig. 3.5a. By injecting the ansatz Eq. (3.3) into the Toner and Tu equations, and neglecting contributions of frequencies higher than q that arise from nonlinear contributions, the theory reduces to the study of a dynamical system:

$$\partial_t \mathbf{V} = \mathbf{F}(\mathbf{V}, h), \tag{3.4}$$

where $\mathbf{V} = [v_x, v_y]$, and $\mathbf{F}$ is a force field that depends on $\mathbf{V}$, h, W and other hydrodynamics coefficients. A typical force field is shown in Fig. 3.5b for $W = 0.5\,$mm and $\mathbf{h} = -120\hat{\mathbf{x}}\,\mu$m/s. Looking for the stable fixed points $\mathbf{F} = [0, 0]$ gives the stable velocity field configurations. In Fig. 3.5b, a stable fixed point is found with $v_x > 0$ and $v_y \neq 0$ which corresponds to a buckled flow of polar liquids moving opposite to the external field. This situation, sketched in Fig. 3.5b, corresponds to the buckled configurations recorded experimentally and shown in Fig. 3.4b.

The salient predictions of the model are summarized in the phase diagram of Fig. 3.5c. In particular, buckled patterns are predicted for external field amplitudes higher than the buckling threshold given by:

$$\tilde{\mu}_h h_\mathrm{b} = D_\mathrm{T} v_0 q^2 + \mathcal{O}(D_\mathrm{T} q^2/\alpha). \tag{3.5}$$

This buckling threshold is set by the competition between the polar liquid elasticity D_T and confinement q. As W increases, q decreases, h_b decreases, and stable buckled pattern occurs at lower h. This configuration is found to be stable over a finite range of field amplitudes. The buckled state becomes eventually unstable when the coercive field h_c is reached. This limit reads:

$$\tilde{\mu}_h h_\mathrm{c} = (2/\sqrt{243})\alpha v_0 \left(1 + 2D_\mathrm{T} q^2/\alpha\right)^{3/2}. \tag{3.6}$$

Alignment interactions (α) act together with elasticity (D_T) and confinement ($q = \pi/W$) to protect the flow of the polar liquid against the opposing field. The model correctly accounts for our experimental result: the more confined the flock is, the more robust it is.

Given the very general Toner and Tu framework used to obtain the phase diagram of Fig. 3.5c, we expect that it correctly describes the static response of any polar liquid.The pattern selection remains, however, to be elucidated.

3.2.3 Emergent oscillators

Going beyond the fundamental understanding of polar liquid bistability, we take advantage of this property to engineer an autonomous clock. More precisely, the hysteretic response of flocks to external field (Fig. 3.3) offers the opportunity to realize oscillators based on the oscillation-relaxation mechanism first proposed by Van der Pool [128]. Figure 3.6a shows the spontaneous oscillations of a polar liquid droplet confined in a circular well under a *uniform* and *stationary* field $\mathbf{h} = h\hat{\mathbf{x}}$. As the droplet moves along the circular boundary, it experiences an increasing longitudinal field $h_{\parallel}$ and reverses when $h_{\parallel} = h_c$. Here, the time-dependence is achieved by exploiting the mobility of the flock together with the geometry of confinement.

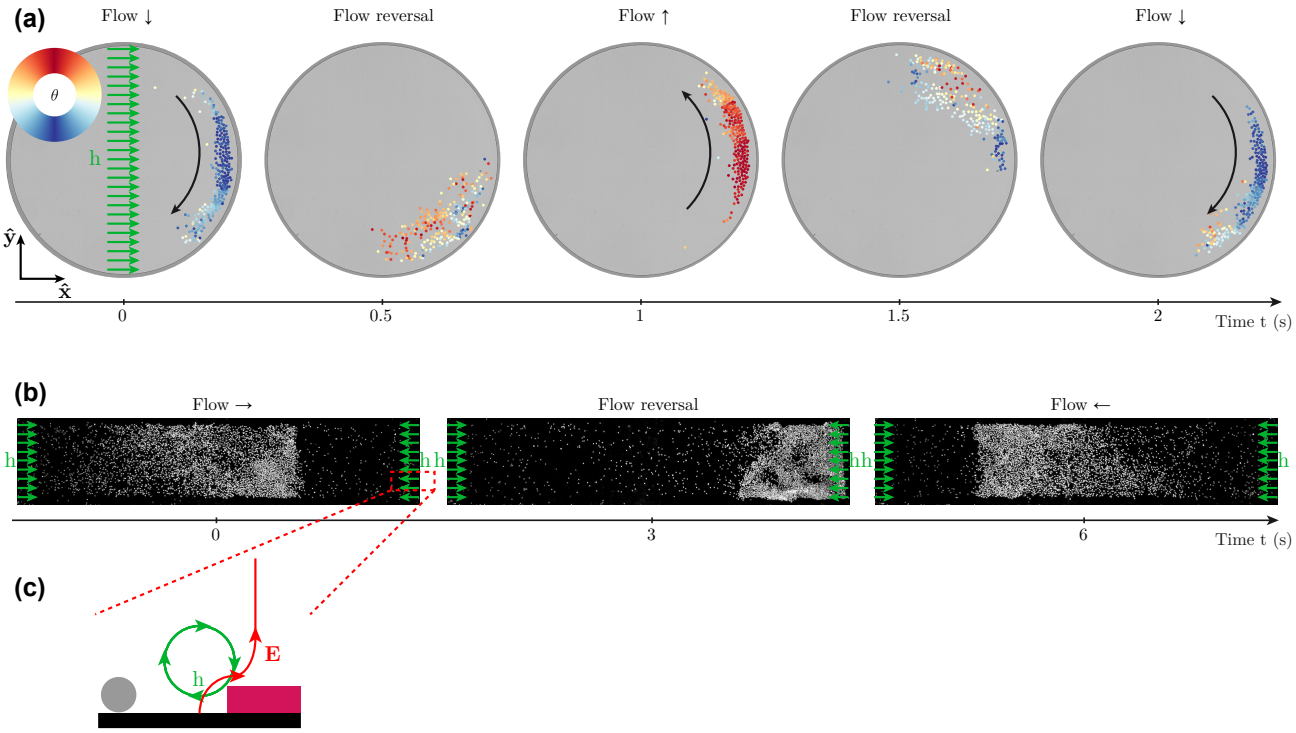

Figure 3.6 | **Spontaneous active fluid oscillators. (a)** Time series showing snapshots of a droplet of polar liquid confined in a circular well of radius $R = 0.5\,\mathrm{mm}$. Under a steady and homogeneous solvent flow, the flock spontaneously oscillates. **(b)** Time series showing snapshots of a finite flock confined in a rectangular channel of width $W = 1\,\mathrm{mm}$. **(c)** Sketch of the local fields that confine the flock and yield its periodic motion.

Spontaneous oscillations of flocks can even be achieved without any hydrodynamic actuation. For

example, a finite flock confined in a rectangular channel undergoes an oscillatory motion, see Fig. 3.6b. This dynamics finds its origin in the response of flocks to longitudinal fields. The insulating layer of photoresist used to confine the rollers generates local fields that are sketched in Fig. 3.6c. The bounces of the flock at the ends of the channel result from these fields. Actually, the bare confinement of the flock is made possible by these local fields of amplitudes higher than h_c.

These very simple realizations of oscillators achieved within microfluidics devices are a first step towards more involved functionalities as the ones recently proposed by the group of Jörn Dunkel [135, 45, 134]. Indeed, our efforts to understand the fundamentals of the response of active materials to perturbations is also of technological relevance. On one hand, the future uses of active materials strongly depend on their robustness against external perturbations. On the other hand, the design of new functionalities based on active materials would benefit from the coupling between their emergent properties, external actuation and internal patterning.

Article

Flowing active liquids in a pipe: Hysteretic response of polar flocks to external fields

We investigate the response of colloidal flocks to external fields. We first show that individual colloidal rollers align with external flows as would a classical spin with magnetic fields. Assembling polar active liquids from colloidal rollers, we experimentally demonstrate their hysteretic response: confined colloidal flocks can proceed against external flows. We theoretically explain this collective robustness, using an active hydrodynamic description, and show how orientational elasticity and confinement protect the direction of collective motion. Finally, we exploit the intrinsic bistability of confined active flows to devise self-sustained microfluidic oscillators.

I Introduction

For centuries, applying an external pressure difference has remained the only solution to flow a liquid in a pipe. Over the last ten years, by engineering soft materials from self-propelled units we have learned how to drive fluids from within [102, 100, 133, 13, 88, 28, 138, 132, 136, 145]. The generic strategy consists in assembling orientationally ordered liquids from self-propelled particles [76, 130, 124]. From a fundamental perspective, significant efforts have been devoted to explaining the emergence of collective motion in ensembles of interacting motile bodies, and the flow patterns of the resulting polar and nematic phases [145, 76, 130, 124]. However, we still lack basic understanding of these non-equilibrium materials. One of the major questions that remains to be elucidated is the response of active phases to external fields [30, 66]. The situation is all the more unsatisfactory because, from an applied perspective, the potential of active fluids as smart materials will be chiefly determined by their ability to sustain their spontaneous flows against external perturbations.

Here, combining experiments and theory, we elucidate how confined active fluids with broken rotational symmetry respond to external fields. Our experiments are based on colloidal rollers self-assembled into polar flocks, i.e. active liquids with orientational order akin to that of a ferromagnet [13, 12, 84]. We first demonstrate that isolated colloidal rollers align their direction of motion with an external flow as would classical spins with a magnetic field. In contrast, we establish that the response of polar liquids is intrinsically non-linear. When confined in channels, transverse confinement and bending elasticity act together to protect the direction of collective motion against external flows. We close this paper showing how the resulting hysteretic relation between the flock velocity and external flows results in the spontaneous oscillations of confined polar-liquid droplets.

II Response of motile colloids to external flows: Alignment with external fields

In our experiments, we exploit the so-called Quincke mechanism to motorize inert colloidal particles and turn them into self-propelled particles [13]. We recall the motorization principle in Appendix VI.i, and provide details about the experimental set-up in Appendix VI.ii. In brief, we observe the 2D motion of colloidal rollers of diameter $2a = 4.8\,\mu$m confined in $50\,\text{mm} \times 16\,\text{mm} \times 0.1\,\text{mm}$ channels filled with hexadecane oil, as illustrated in Fig. 3.7a. They behave as persistant random walkers moving at a constant speed $v_0 = 0.98 \pm 0.1\,$mm/s, and having a rotational diffusivity $D = 1.5\,\text{s}^{-1}$ [83]. As a result, the distribution of the roller velocities is isotropic and narrowly peaked on a circle of radius v_0, see Fig. 3.7b.

We investigate their individual response to external flows by injecting a fresh hexadecane solution at constant flow rate. Given the aspect ratio of the fluidic channel, the flow varies only in the z direction along which it has a Poiseuille profile, Fig. 3.7a. We denote h the magnitude of the hexadecane flow evaluated at $z = a$ along the $\hat{\mathbf{x}}$ direction. Over a wide range of h, the speed of the rollers is virtually unchanged, see Figs. 3.7b and 3.7c. Their orientational distribution is however strongly biased. As seen in Fig. 3.7b, the average roller velocity points in the direction of the flow and the angular fluctuations are reduced upon increasing h. More quantitatively this behavior is very well captured by the following equations of motion:

$$\partial_t \mathbf{r}_i(t) = v_0 \hat{\mathbf{v}}_i, \tag{3.7}$$

$$\partial_t \theta_i(t) = -\mu h \sin\theta_i + \sqrt{2D}\xi_i(t), \tag{3.8}$$

where the $\mathbf{r}_i(t)$ and $\hat{\mathbf{v}}_i \equiv (\cos\theta_i(t), \sin\theta_i(t))$ are respectively the positions and velocity orientations of the colloids. μ is a constant mobility coefficient and $\xi(t)$ is a Gaussian white noise of unit variance. Eq. (3.8) corresponds to the over-damped Langevin dynamics of a classical spin coupled to a constant magnetic field. We henceforth use this magnetic analogy and define the average roller magnetization as $\boldsymbol{\mathcal{V}} = \langle \hat{\mathbf{v}}_i \rangle_i$. Eq. (3.8) is readily solved and used to measure the rotational mobility $\mu = 0.08\,\mu\text{m}^{-1}$ from the magnetization curve in Fig. 3.7d. This value is in excellent agreement with the estimate derived from first principles in [13] and has a sign opposite to that of the colloidal surfers studied in [90]. Isolated rollers align with a flow field as would uncoupled XY spins with a magnetic field.

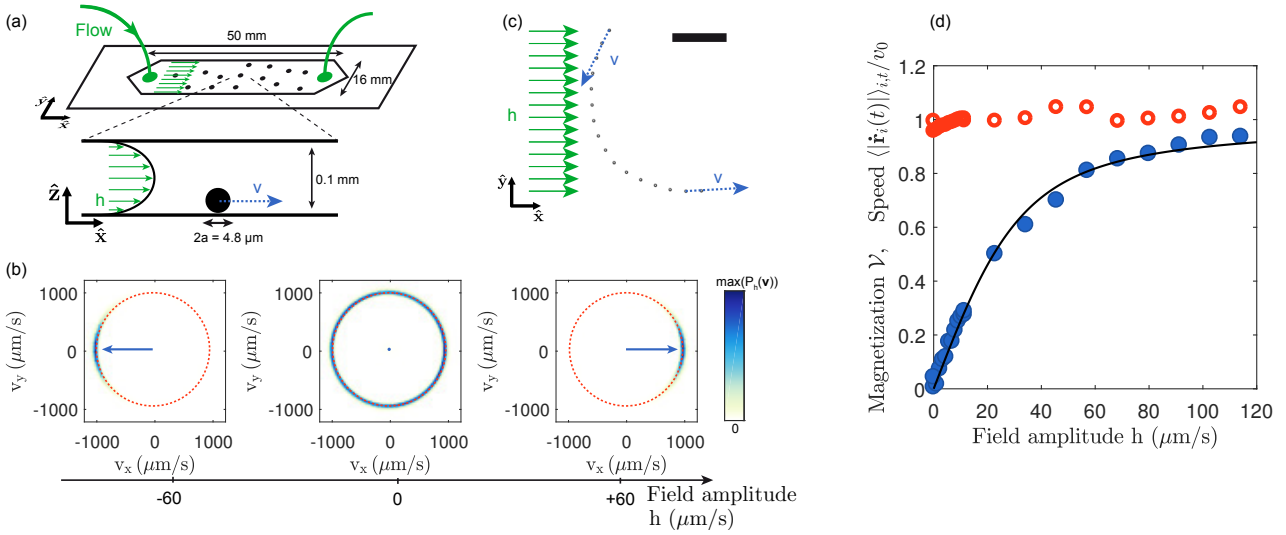

Figure 3.7 | Isolated colloidal rollers align with external flows as XY spins with magnetic fields. (a) Sketch of the microfluidic setup. Top: top view. Bottom: side view. Colloidal rollers (black dots) of diameter $2a = 4.8\,\mu$m and speed $\mathbf{v}$ (blue arrow) are confined in a $50\,\text{mm} \times 16\,\text{mm} \times 0.1\,\text{mm}$ channel. Hexadecane is injected through the channel at a constant flow rate. A Poiseuille flow results in the $\hat{\mathbf{z}}$ direction (green arrows). The strength of the external field h is defined as the magnitude of the hexadecane flow at a distance $z = a$ from the bottom wall. (b) Probability density function of the roller velocities for three different hexadecane flows $\mathrm{P_h}(\mathbf{v})$. The dashed circles are guidelines corresponding to $v = v_0$. When $h = 0$, the distribution is isotropic and strongly peaked around $v = v_0$. When $h \neq 0$, the distributions are biased along the direction of $\mathbf{h}$, resulting in finite average velocities (blue arrows). (c) Superimposed images of a colloidal roller in a hexadecane flow ($h = +60\,\mu$m/s). Time interval between two pictures: 30 ms. The roller reorients at constant speed along the flow direction. Scale bar: $100\,\mu$m. (d) Blue circles: Magnetization curve $\mathcal{V}(h)$ of the noninteracting rollers. Red open circles: time and ensemble average of the normalized roller speed $\langle|\dot{\mathbf{r}}_\mathbf{i}(t)|\rangle_{i,t}/v_0$. The rotational mobility $\mu = 0.08\,\mu\text{m}^{-1}$ is evaluated from the best fit of the magnetization curve with the theoretical formula (dark solid line): $\mathcal{V} = I_1(\mu h/D)/I_0(\mu h/D)$, where I_n is the modified Bessel function of order n.

III Robustness to external fields: Hysteretic response of polar liquids

III.i Experiments

In the absence of external flows, ferromagnetic orientational order emerges over system-spanning length scales when increasing the roller packing fraction ρ above 10^{-2} [13]. A homogeneous polar liquid then forms and spontaneously flows through the microchannels as illustrated in Fig. 3.8a and Supplementary video 1. We now address the response of this active ferromagnet to external fields taking advantage of the coupling between the roller velocity and the surrounding fluid flows. To do so, we assemble a polar liquid confining hundreds of thousands of rollers in a race-track pattern of width $W = 0.5\,\mathrm{mm}$ (the area fraction is set to $\rho = 0.1$). Once a homogeneous and stationary polar order is established, we study its longitudinal response by applying a uniform flow along one of the two straight parts of the channel as sketched in Fig. 3.8a, and detailed in Appendix VI.ii. For the sake of clarity, we henceforth refer to the hexadecane flow field evaluated at $z = a$ as the external field $\mathbf{h} = h\hat{\mathbf{x}}$. Fig. 3.8b shows that applying a field $\mathbf{h}$ along the direction of $\boldsymbol{\mathcal{V}}$ reduces the transverse velocity fluctuations of collective motion. In stark contrast to the individual response, Fig. 3.8b also shows that collective motion can occur in the direction *opposite* to the external field with a high level of ordering. But this robustness has a limit. Increasing $|h|$ above $h_\mathrm{c} = 63\,\mu\mathrm{m/s}$, the rollers abruptly change their direction of motion and align with $\mathbf{h}$. As quantitatively demonstrated in Fig. 3.8c, this behavior translates into a strong hysteresis of the magnetization curve $\boldsymbol{\mathcal{V}}(h)$ upon cycling the magnitude of the external field.

We now elucidate the origin of this collective robustness, or more precisely, what sets the magnitude of the coercive field h_c in this active ferromagnet. We thus focus on the regime where $\boldsymbol{\mathcal{V}}\cdot\mathbf{h} < 0$, and leave the discussion of the case where $\boldsymbol{\mathcal{V}} \cdot \mathbf{h} > 0$ to Appendix VI.iii. In an infinite system h_c should vanish as the polar-liquid flow stems from the spontaneous breaking of a continuous rotational symmetry. In this active system, however, orientation is intimately coupled to mass transport. Therefore, the homogeneous rotation of the roller velocity is forbidden by the confining boundaries: reversing the direction of the flock requires finite wave-length distortions. As shown in Fig. 3.8d, this picture is supported by the very sharp increase of h_c measured when decreasing the channel width.

To gain a more quantitative insight, we inspect the inner structure of the roller flow field. Supplementary video 2 and Fig. 3.9a both show that applying a field in the upstream direction causes finite wave-length distortions dominated by bending deformations. We introduce the Fourier transform of the roller flow field as $\mathbf{v}(\mathbf{q}, t) = \langle \mathbf{v}_i(t) \exp[i\mathbf{q} \cdot \mathbf{r}_i(t)]\rangle_i$, and plot in Fig. 3.9b the time-averaged spectrum of the bending modes along the $\mathbf{q} = (q_x, 0)$ direction: $B(q_x) = \langle |v_y(q_x, t)|^2\rangle_t$. The bending deformations are dominated by spatial oscillations at a well-defined wave-length λ_B. Fig. 3.9c indicates that confinement sets $\lambda_\mathrm{B} = 2W$, see also Supplementary video 3. Increasing the magnitude of the field strongly increases the amplitude of the bending oscillations until $|h| = h_\mathrm{c}$, Fig. 3.9d. As exemplified in Supplementary video 4, the bending waves are then destabilized into vortices leading to flow reversal. Subsequently, the external field stabilizes a strongly polarized homogeneous polar liquid flowing in the direction of $\mathbf{h}$. We stress that the reversal of the flow is completed *without* resorting to local melting. Orientational order is locally preserved regardless of the direction and magnitude of the external field. The weak decrease of the magnetization curve seen in Fig. 3.8c in the negative $\boldsymbol{\mathcal{V}}\cdot\mathbf{h}$ region chiefly stems

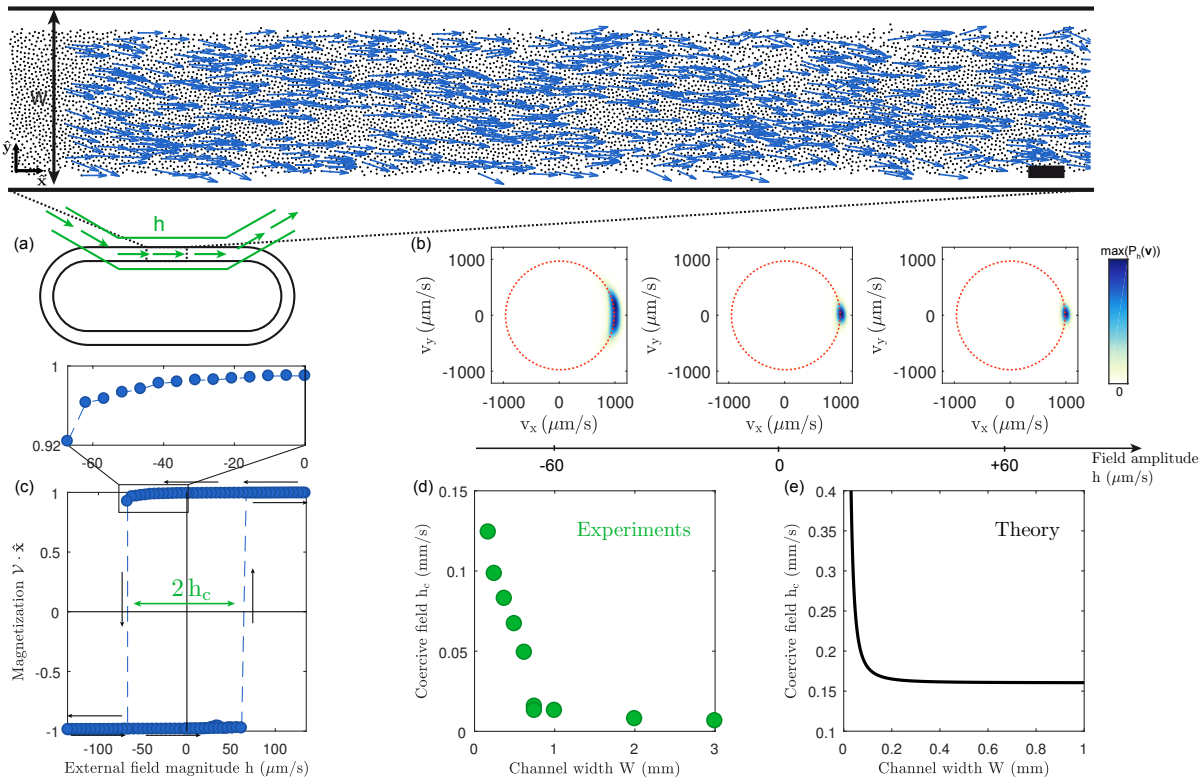

Figure 3.8 | Non-linear response of polar liquids to longitudinal external fields. (a) Sketch of the microfluidic geometry. The rollers are confined in a photolithographied race-track (black). A constant hexadecane flow is applied to the rollers by means of an additional microfluidic channel (green). Top picture: close-up on the homogeneous polar liquid flowing in a race-track of width $W = 0.5\,\mathrm{mm}$ when $h = 0$. In this experiment, the polar liquid spontaneously flows along the clockwise direction as indicated by the instantaneous particle velocities (the velocity of one roller out of ten is plotted, blue arrows). Scale bar: $100\,\mu\mathrm{m}$. (b) Probability density function of the roller velocities in the polar-liquid state. At $h = 0$, the distribution is biased revealing the spontaneous symmetry breaking of the roller orientation. At $h = +60\,\mu\mathrm{m/s}$ transverse velocity fluctuations are reduced. At $h = -60\,\mu\mathrm{m/s}$, the polar liquid cruises against the external field and velocity fluctuations are enhanced. The speed of the rollers v_0 (red dotted circles) is left unchanged by the external field. (c) Magnetization curve $\boldsymbol{\mathcal{V}}\cdot\hat{\mathbf{x}}(\mathbf{h})$ of the polar liquid. Upon cycling the external field $\mathbf{h}$ (dark arrows) the active ferromagnet displays an hysteretic behavior. The coercive field h_c is defined as the width of the hysteresis loop. Top panel: close-up showing the minute decrease of the magnetization prior to reversal. (d) The coercive field h_c decreases with the channel width W (green dots). (e) Theoretical prediction $h_c(W) = (2/\sqrt{243})\alpha v_0 \left(1 + 2D_T q^2/\alpha\right)^{3/2}$. As a technical remark, we note that the limit $W \to \infty$ is not relevant. Our two-mode model is intrinsically based on the scale separation between the variations of the longitudinal and transverse components of $\mathbf{v}$: v_x varies over the scale of the channel length while v_y varies over the channel width. Unconfined polar liquids cannot resist to external fields.

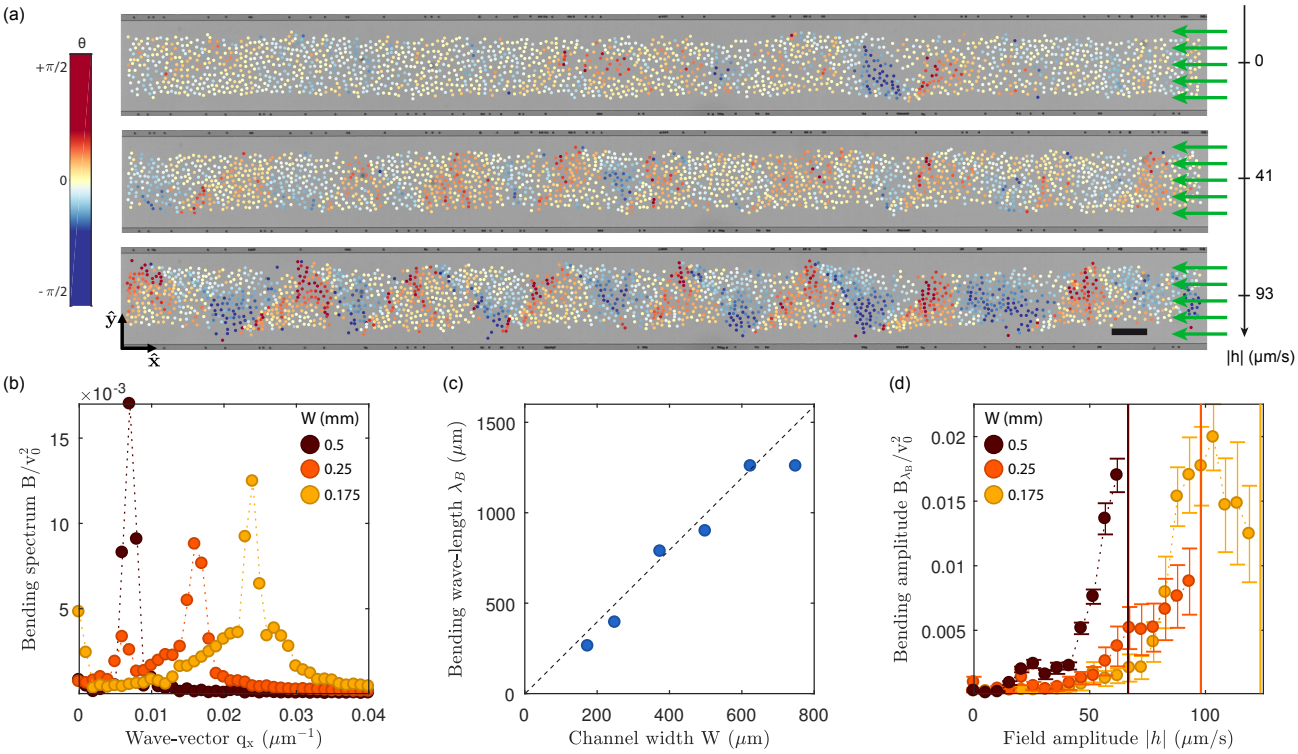

Figure 3.9 | Bending deformations of a polar liquid flowing against an external field. (a) Snapshots of polar liquids flowing against external fields of increasing magnitude. The color indicates the angle of the instantaneous velocity of the rollers θ. As $|h|$ increases, a bending-oscillation pattern grows. $W = 0.25\,\mathrm{mm}$. Scale bar: $100\,\mu\mathrm{m}$. (b) The time-average spectra of the bending modes along $\mathbf{q} = (q_x, 0)$ ($B(q_x) = \langle |v_y(q_x,t)|^2 \rangle_t$) are plotted for three different confinement widths $W = 0.5,\ 0.25,\ 0.175\,\mathrm{mm}$. The values of h are taken just before flow reversal: $h = 62,\ 93,\ 119\,\mu\mathrm{m/s}$, respectively. λ_B is defined by the wavelength where B is maximal. (c) Variations of λ_B with W. Dashed line: $\lambda_\mathrm{B} = 2W$. (d) Variations of the amplitude of the bending mode at $q = 2\pi/\lambda_\mathrm{B}$ with $|h|$. The bending deformations at λ_B increase when increasing $|h|$. The vertical lines indicate the values of $h_\mathrm{c}(W)$ for the three experiments. Error bars: 1 sd (time statistics).

from the constrained oscillations of the spontaneous flow.

III.ii Theory

We use a hydrodynamic description of the polar liquid to theoretically account for the bistability of the spontaneous flows and for the variations of the coercive field $h_c(W)$ with confinement. The Toner-Tu equations are the equivalents of the Navier-Stokes equations for polar active liquids. They describe the dynamics of the velocity $\mathbf{v}(\mathbf{r},t)$ and density fields $\rho(\mathbf{r},t)$. In the presence of an external driving field $\mathbf{h}(\mathbf{r},t)$, they take the generic form:

$$\partial_t \rho + \nabla \cdot (\rho \mathbf{v}) = 0, \tag{3.9}$$

and

$$\begin{aligned} &\partial_t \mathbf{v} + \lambda_1 (\mathbf{v}\cdot\nabla)\mathbf{v} + \lambda_2 (\nabla\cdot\mathbf{v})\mathbf{v} + \lambda_3 \nabla(|\mathbf{v}|^2) \\ &= \alpha \mathbf{v} - \beta |\mathbf{v}|^2 \mathbf{v} - \nabla P \\ &+ D_{\mathrm{B}} \nabla(\nabla\cdot\mathbf{v}) + D_{\mathrm{T}} \nabla^2 \mathbf{v} + D_2 (\mathbf{v}\cdot\nabla)^2 \mathbf{v} + \mu_h \mathbf{h} \end{aligned} \tag{3.10}$$

These phenomenological equations involve a number of hydrodynamic coefficients which we do not describe here (see e.g. [124] for a comprehensive discussion). The only two parameters relevant to the following discussion are: (i) the convective coefficient λ_1 which translates the lack of translational invariance of the system: the rollers drag on a fixed substrate defining a specific frame. (ii) D_{T} and D_2 which are two elastic constants of the broken symmetry fluid. D_{T} and D_2 both hinder the orientational distortions of the velocity field.

Describing the flow-reversal dynamics and the underlying spatiotemporal patterns would require solving the strongly non-linear system given by Eqs. (3.9) and (3.10). This task goes far beyond the scope of this article. Here, we instead exploit our experimental observations to construct a minimal model. As Fig. 3.9 indicates that a single bending mode of wavevector $\mathbf{q} = \pi/W\hat{\mathbf{x}}$ dominates the deformations of the velocity and density fields, we make a simplifying ansatz writing: $\mathbf{v}(x,t) = v_x(t)\hat{\mathbf{x}} + v_y(t)\cos(qx-\omega t)\hat{\mathbf{y}}$, and neglect all contributions from spatial frequencies higher than π/W. We also ignore density fluctuations and restrain our analysis to longitudinal external fields $\mathbf{h} = -h\hat{\mathbf{x}}$. Within this two-mode approximation, Eq. (3.9) is always satisfied and Eq. (3.10) reduces to the dynamical system:

$$\partial_t \mathbf{V} = \mathbf{F}(\mathbf{V}, h) \tag{3.11}$$

for the amplitudes of the two coupled velocity modes: $\mathbf{V}(t) = (v_x(t), v_y(t))$. The generalized force $\mathbf{F}(\mathbf{V},h) = (F_x, F_y)$ is given by

$$F_x = \left[\alpha - \beta\left(v_x^2 + \frac{1}{2}v_y^2\right)\right] v_x - h \tag{3.12}$$

$$F_y = \left[\left(\alpha - D_{\mathrm{T}} q^2\right) - D_2 q^2 v_x^2 - \beta\left(v_x^2 + \frac{3}{4}v_y^2\right)\right] v_y \tag{3.13}$$

These equations are completed by the relation $(\omega - \lambda_1 q v_x) v_y = 0$ defining the oscillation frequency ω.

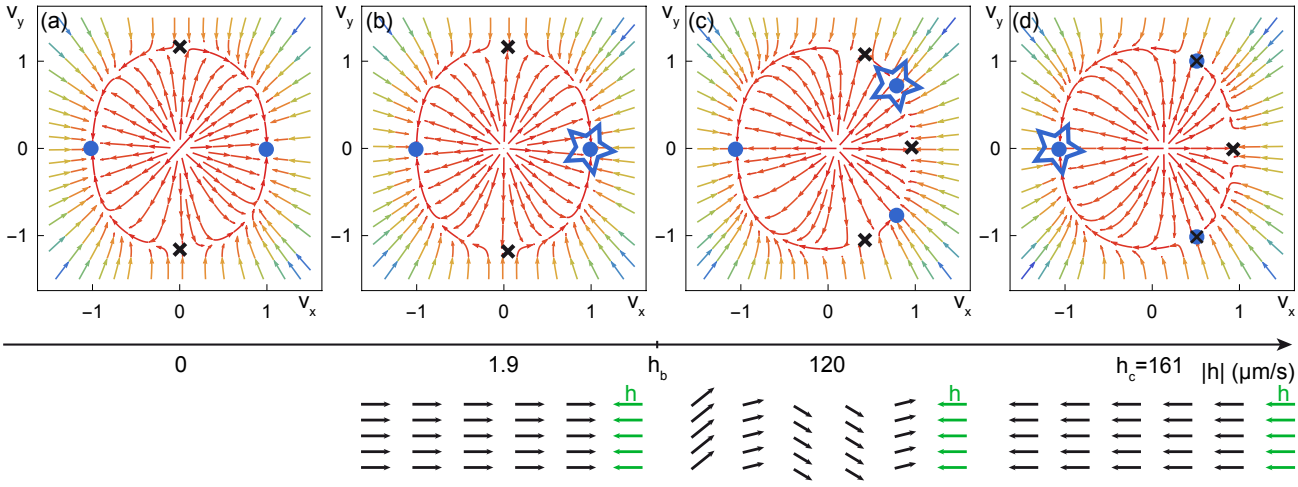

Figure 3.10 | Two-mode theory of the hysteretic response. We look for stationary solutions of the hydrodynamics of polar liquids taking the form $\mathbf{v} = v_x(t)\hat{\mathbf{x}} + v_y(t)\cos(qx - \omega t)\hat{\mathbf{y}}$. The problem then reduces to studying a dynamical system: $\partial_t \mathbf{V} = \mathbf{F}(\mathbf{V}, h)$ where $\mathbf{V} = (v_x, v_y)$. (a) Force-field $\mathbf{F}(\mathbf{V}, h = 0)$ in the absence of external field, plotted for $W = 0.5\,\mathrm{mm}$. The blue circles correspond to stable fixed points where $F = 0$. The crosses indicate the position of saddle points. A trivial unstable point is located at $(0, 0)$, not shown. (b) Force-field $\mathbf{F}(\mathbf{V}, h)$ at finite h. The star symbol indicates the stationary position of the dynamical system. When $|h| < h_\mathrm{B}$, the system stays in the stable fixed point corresponding to a uniform longitudinal flow in the direction opposite to $\mathbf{h}$ as sketched in the bottom panel. (c) Increasing $|h|$ the homogeneous solution of (b) becomes unstable. Another stable point emerges between two saddle points and corresponds to the buckled flow sketched in the bottom panel. Such stable buckled flows are consistent with the experimental observations of Fig. 3.9. (d) At $|h| = h_\mathrm{c}$ the topmost saddle point collides with the stable fixed point (superimposed cross and dot symbols). As a result, the only stable conformation corresponds to a flow aligned with $\mathbf{h}$.

To gain more intuition on the physical meaning of the dynamical system, we plot the force field $\mathbf{F}(v_x, v_y)$ in Fig. 3.10 for four values of h. Anticipating on the comparison with our measurements, we use the parameter values estimated in [13] and recalled in Appendix VI.iv. Looking for fixed points in the absence of external field, $\mathbf{F}(\mathbf{V}, h = 0) = 0$, we find five solutions for $\mathbf{V}$ when $\alpha > D_{\mathrm{T}}q^2$, see Fig. 3.10a [1]. The trivial solution $(0, 0)$ is obviously unstable and corresponds to a fluid at rest. The four other solutions are given by $(0, v_{y,\pm}) = \pm\left(0, 2\sqrt{(\alpha - D_{\mathrm{T}}q^2)/(3\beta)}\right)$ and $(v_{x,\pm}, 0) = \pm\left(\sqrt{\alpha/\beta}, 0\right)$ as illustrated in Fig. 3.10a. The former are saddle points while the latter are linearly stable fixed points corresponding to the two possible homogeneous flows at speed $v_0 = \sqrt{\alpha/\beta}$ along the $\pm\hat{\mathbf{x}}$ directions. It is worth noting that the force field focuses the position of the dynamical system along a closed line connecting the four fixed points thereby making the dynamics of $\mathbf{V}$ almost one dimensional, see Fig. 3.10a.

The bistability of the flow at finite h, viz the existence of a finite coercive field, is understood from the dynamics of the fixed points in phase space. Upon increasing h the dynamical system, and therefore the active flow, explore three different states labeled with a star symbol in Figs. 3.10b, 3.10c and 3.10d:

(i) We start from a polar liquid flowing in the $+\hat{\mathbf{x}}$ direction, and an opposing external field $\mathbf{h} = -h\hat{\mathbf{x}}$, with $h > 0$. As sketched in Fig. 3.10b, this state where $\mathbf{V} = (v_0 - h/(2\alpha), 0)$ corresponds to a polar fluid uniformly flowing against the external field. This situation remains stable until h reaches $h_{\mathrm{b}} = D_{\mathrm{T}}v_0q^2 + \mathcal{O}(D_{\mathrm{T}}q^2/\alpha)$, Fig. 3.10b. Above this value, the homogeneous flow is unstable to buckling, and the stable point $\mathbf{V} = (v_0 - h/(2\alpha), 0)$ becomes a saddle point.

(ii) Yet, the flow is not reversed. The system indeed reaches one of the two new stable fixed points with $v_y \neq 0$. They both correspond to homogeneously buckled conformations, see Fig. 3.10c. This prediction is consistent with the buckled patterns observed prior to flow reversal shown in Fig. 3.9 and Supplementary videos 2 and 3.

(iii) Further increasing h, the buckled state approaches the topmost saddle point. The two points eventually merge at a critical value h_{c} corresponding to Fig. 3.10d. The only stable conformation then corresponds to a situation where $\mathbf{V} = (-v_x, 0)$. The flow is reversed and aligns along the direction prescribed by $\mathbf{h}$. h_{c} defines the value of the coercive field.

The value of h_{c} is determined analytically by the merging condition between the saddle and the fixed point, see Fig. 3.10d. We find that h_{c} stems from the competition between the external field and all the velocity-alignment terms (α and D_{T}): $h_{\mathrm{c}} = (2/\sqrt{243})\alpha v_0 \left(1 + 2D_{\mathrm{T}}q^2/\alpha\right)^{3/2}$. Our model correctly predicts that the stability of the flows opposing an external field is enhanced when further confining the polar liquid, i.e increasing $q = \pi/W$. Remarkably, this simplified picture also provides a reasonable estimate of the magnitude of the coercive field, see Figs. 3.8d, and 3.8e.

In summary, we have established the bistability of polar active fluids. Their hysteretic response originates from buckled flow patterns stabilized by orientational elasticity. We expect this phenomenology to apply to all confined active fluids with uniaxial orientational order. Our theory builds on the observation of a single set of buckling modes. Explaining the pattern-selection process remains, however, a significant technical challenge.

[1] We focus on the situation where $\alpha > D_{\mathrm{T}}q^2$. In the case of extreme confinement where this condition is not met, flow reversal can occur only via local melting.

IV Application: Spontaneous oscillations of polar-liquid droplets

We close this article exploiting the intrinsic multistability of polar-liquid flows and demonstrating emergent functionalities in active microfluidics [135, 45, 134]. The existence of a hysteresis loop in the response function provides a very natural design strategy for spontaneous oscillators via the relaxation-oscillation mechanism [86]. Simply put, and having mechanical devices in mind, relaxation oscillations stem from the coupling between a system with a hysteretic "force-velocity" relation and a harmonic spring. This minimal design rule is transposed to active fluids by confining them in curved containers, and applying a constant and homogeneous external field $\mathbf{h} = h\hat{\mathbf{x}}$. As illustrated in Supplementary video 5, and in the image sequence of Fig. 3.11a, the colloids form a polar-liquid droplet that spontaneously glides along the confining boundary in an oscillatory fashion. We denote α the polar angle defining the position along the confining disc, and $\mathbf{v}(\alpha, t)$ the azimuthal component of the velocity field averaged over the radial direction. Fig. 3.11b shows the variations of the velocity field $\mathbf{v}(\alpha, t)$. The oscillatory dynamics of the polar-liquid droplets is clearly periodic with well-defined period and amplitude both decreasing with the magnitude of the stationary external field, Figs. 3.11c, and 3.11d.

We now explain these collective oscillations as the periodic exploration of the four states (i), (ii), (iii) and (iv) along the hysteresis loop established in Fig. 3.8c and sketched in 3.11e . The key observation is that the droplet follows the boundary of the circular chamber. The droplet hence experiences a longitudinal field of magnitude $h_\parallel(\alpha) = h \sin\alpha$ which either favors or hinders its motion. The periodic exploration of the hysteresis loop is supported by Fig. 3.11e. Fig. 3.11e shows the distribution $P(v_{\mathrm{CoM}}, h_\parallel)$, where v_{CoM} is the polar-liquid velocity evaluated at the center of mass of the droplet α_{CoM}. The support of this distribution corresponds to the rectangular shape of the velocity-field relation measured in Fig. 3.8 for a straight channel. The droplet spends most of its time exploring the stable horizontal branches and quickly jumps from one stable conformation to the other along the vertical ones. We can gain more intuition on this oscillatory dynamics describing the four states one at a time:

In state (i), the head of the flock is located at $\alpha < 0$ and $\mathbf{v}(\alpha) \cdot \mathbf{h} < 0$. The flock proceeds in the direction opposite to the azimutal component of the external field. The system moves toward the left of the bottom branch of the hysteresis loop, Fig. 3.11e. As the flock moves toward the negative α direction, the field strength $|h_\parallel|$ increases and reaches the maximal value h_{c} at an angle $-\alpha_{\mathrm{c}}$. The system then reaches the left vertical branch of the response curve and hence becomes unstable, state (ii). The flock bends and reverses its direction to reach the upper branch of the response curve, state (iii). When the flock proceeds in the positive α region, it experiences an increasingly high field in the direction opposite to its motion. As $h_\parallel = h_{\mathrm{c}}$ the flock reaches the right vertical branch of the response curve at the maximal angle $+\alpha_{\mathrm{c}}$ (state iv), thereby leading the system back to state (i). The hysteresis loop is periodically explored.

This oscillatory motion relates to the conventional relaxation-oscillation picture as follows: the response curve $(h, \mathcal{V})$ plays the role of the force-velocity relation in a mechanical system, and the angle-dependent longitudinal flow plays the role of the harmonic spring.

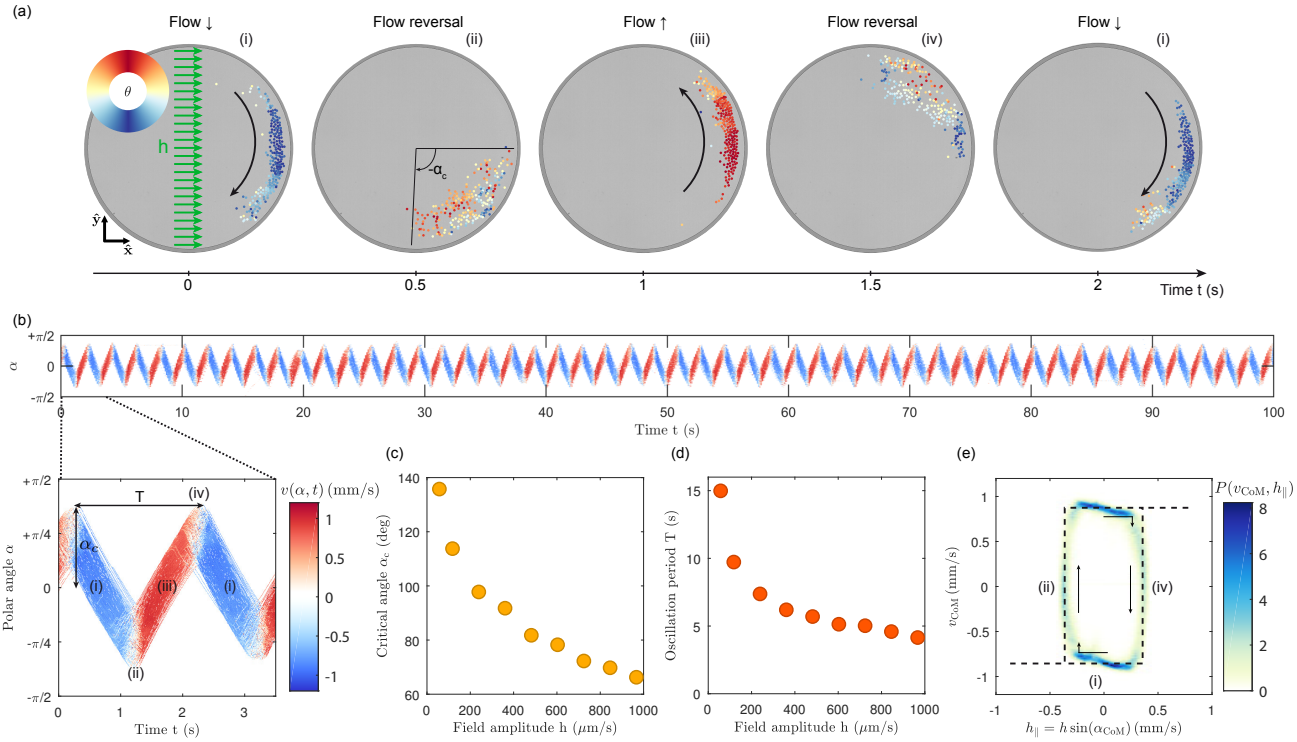

Figure 3.11 | Spontaneous oscillations of a polar-liquid droplet. (a) Subsequent pictures of a polar liquid droplet oscillating spontaneously in a circular chamber of radius $R = 0.5\,\mathrm{mm}$. The green arrows indicate the direction of $\mathbf{h}$. The color of the particles indicates the instantaneous direction of their velocity θ. The polar-liquid droplet reverses its motion when it reaches a critical angle $\pm\alpha_c$ along the curved boundary. $h = 485\,\mu\mathrm{m/s}$. (b) Time variations of the radial average of the active-liquid flow $v(\alpha, t)$ showing a well defined period T and amplitude α_c of oscillations. The four states defined in (a) are indicated in the close-up view. (c) The critical angle α_c is reduced when increasing the magnitude of the external field h. $R = 2.3\,\mathrm{mm}$. (d) The period of the oscillations T is reduced when increasing the magnitude of the external field h. $R = 2.3\,\mathrm{mm}$. (e) Density of probability $P(v_{\mathrm{CoM}}, h_{\parallel})$. The support of this probability is defined by the hysteresis cycle. Dashed line: sketch of the dynamical response of the polar liquid. Arrows: direction of the cycle exploration. The four states defined in (a) correspond to the four branches of the hysteresis loop.

V Conclusion

In conclusion, we have established that colloidal rollers respond to external flows as classical spins to magnetic fields. Assembling active fluids with broken orientational symmetry from these elementary units, we have experimentally demonstrated, and theoretically explained, the hysteretic response of polar-active-fluid flows. We have shown how confinement and bending elasticity act together to protect emergent flows against external fields. Finally, we have effectively exploited the bistability of active flows to engineer active-fluid oscillators with frequency and amplitude set by the geometry of the container. Together with the virtually unlimited geometries accessible to microfabrication, the intrinsic nonlinearity of active flows offer an effective framework for the design of emergent microfluidic functions [135, 45, 134].

VI Appendix

VI.i Motorizing colloidal rollers.

Our experiments are based on colloidal rollers, see [13]. We turn inert polystyrene colloids of diameter $a = 4.8\,\mu$m into self-propelled bodies by taking advantage of the so-called Quincke electro-rotation mechanism [95, 78]. Applying an electric field to an insulating body immersed in a conducting fluid results in a dipolar distribution of its surface charges. Increasing the magnitude of the electric field, E_0, above the Quincke threshold E_Q destabilizes the dipole orientation, which in turn makes a finite angle with the electric field. A net electric torque builds up and competes with viscous friction to power the spontaneous rotation of the colloids at constant angular velocity. As sketched in Fig. 3.7a, the colloids are let to sediment on a flat electrode, rotation is then readily converted into translational motion at constant speed v_0 in the direction opposite to the charge dipole. The direction of motion is randomly chosen and freely diffuses as a result of the spontaneous symmetry breaking of the surface-charge distribution.

VI.ii Methods

We disperse commercial polystyrene colloids (Thermo Scientific G0500) in a mixture of hexadecane and AOT with concentration $[AOT] = 0.13\,$mol/L. We inject this solution into microfluidic chambers made of two electrodes spaced by a $110\,\mu$m-thick scotch tape. The electrodes are glass slides, coated with indium tin oxide (Solems, ITOSOL30, thickness: 80 nm). A voltage amplifier (TREK 609E-6) applies a DC electric field between the two electrodes. We image the system with a Nikon AZ100 microscope with a 3.6X magnification and record videos with a CMOS camera (Basler Ace) at framerate up to 380 Hz. We use conventional techniques to detect and track all particles [29, 72, 7]. To confined the colloidal rollers inside racetracks, we pattern the bottom electrode by mean of photolithography using a $2\,\mu$m-thick layer of UV photoresist (Microposit S1818) as in [84]. The geometry of the microfluidic device is detailed in Fig. 3.12. We study the response of rollers to external field, by injecting a fresh hexadecane solution at a controlled flow-rate using a high-precision syringe pump (Cetoni neMESYS). Each measurement was done at least 60 seconds after the relaxation of the flow pattern in the main

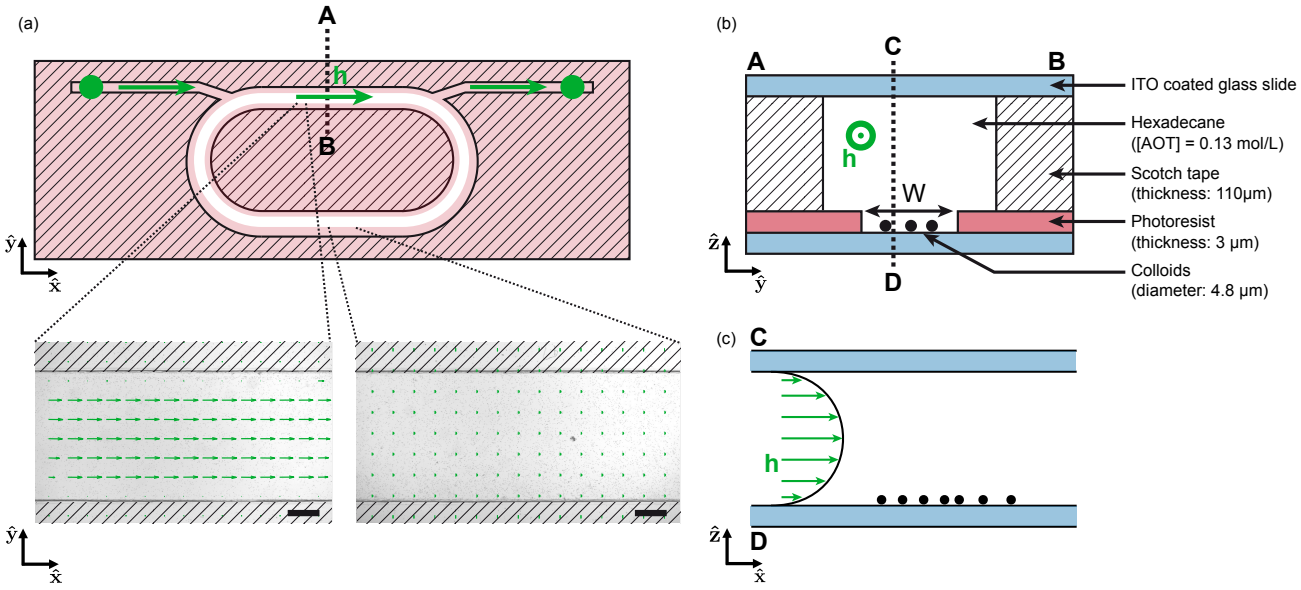

Figure 3.12 | Schematics of the microfluidic device. (a) Top view. The photoresist pattern is shown in red color. The racetrack along which the active-liquid flows corresponds to the white path. The geometry of the fluidic channel corresponds to the black solid lines. The flow direction is indicated with a green arrow. The two bottom pictures show the solvent flow field measured by particle image velocimetry seeding the hexadecane oil with colloids. Due to the imbalance between the two hydrodynamic resistances, the residual flow in the bottom branch is negligible (right picture) compared to the flow in the observation window (left picture). Scale bar: 500 μm (b) Side view in the A-B section defined in (a). Two ITO coated glass slides are assembled with a double-sided tape. The colloids roll on the bottom ITO surface and are confined by the photoresist pattern (red color). (c) Side view in the C-D section as defined in (b). The hexadecane flow has a Poiseuille profile along the z-direction.

branch of the racetrack. The construction of the hysteresis loop in Fig. 3.8b corresponds to a seven-hour long experiment.

VI.iii Non-linear response of the ordered phase: $\mathcal{V} \cdot h > 0$

We discuss here the strengthening of orientational order when $\boldsymbol{\mathcal{V}} \cdot \mathbf{h} > 0$. We plot in Fig. 3.13a the variations of $\delta\mathcal{V} \equiv |\mathcal{V}(h) - \mathcal{V}(h=0)|$ in this regime. At small h, $\mathcal{V}$ responds linearly to the external field. However, the increase of $\delta\mathcal{V}(h)$ becomes sub-linear for field amplitudes as small as $h = 3\times10^{-2}v_0$. The simplest possible explanation of this anomalous attenuation is that $\mathcal{V}$ is a bounded quantity which is maximal and equals 1 when all the rollers move along the very same direction. A second and more involved explanation was put forward in [66]. For finite systems, a crossover from linear response at small h to the anomalous scaling law $\delta\mathcal{V}(h) \sim h^{1/3}$ was predicted from renormalization group analysis [66]. As shown in Fig. 3.13a, this scaling law is consistent with our experiments for system sizes ranging from

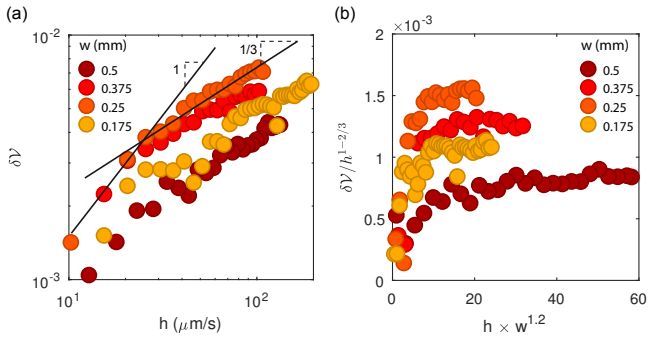

Figure 3.13 | Non-linear response of a polar liquid flowing in the same direction as the external field. (a) The increase of $\delta\mathcal{V} \equiv |\mathcal{V}(h) - \mathcal{V}(h=0)|$ is linear at small h and consistent with a $h^{1/3}$ scaling at high h. This behavior is compatible with the theoretical predictions of [66] based on renormalization group calculations. (b) Finite-size scaling of $\delta\mathcal{V}(h, W)$. Unlike what would be expected from the RG theory of [66], all plots do not collapse on the same master curve.

$W = 0.175\,\mathrm{mm}$ to $W = 0.5\,\mathrm{mm}$. However, the finite size scaling shown in Fig. 3.13b fails to ascertain this explanation. Disentangling the two effects would require operating closer to the transition toward collective motion where the fluctuations of $\mathcal{V}$ are more prominent. Such a regime cannot be achieved in our experiment due to the strongly first-order nature of the transition toward collective motion.

VI.iv Hydrodynamic parameters of the roller fluid

We recall the estimates of the hydrodynamic parameters relevant to the computation of the coercive field h_c. Starting from the Stokes and Maxwell equations describing the microscopic dynamics of the colloids, we established in [13] the hydrodynamics of colloidal-roller liquids. The results of this kinetic theory are summarized in Table 3.1. We determined the value of μ_h following the same procedure, and found $\mu_h = \frac{1}{2}\mu v_0$, where μ is the rotational mobility measured in Fig. 3.7.

α	β	D_T	D_2	μ_h
$50\,\mathrm{s}^{-1}$	$50\,\mathrm{mm}^{-2}\mathrm{s}^{1}$	$2\times10^{-3}\,\mathrm{mm}^{2}\mathrm{s}^{-1}$	0	$40\,\mathrm{s}^{-1}$

Table 3.1 | Values of the hydrodynamic coefficients of the colloidal-roller liquid.

Chapter 4

Colloidal rollers in microfluidic forests

The effects of defects on material properties are crucial in condensed matter physics. For example, the robustness of ferromagnetic order remains a topic of high interest in industrial applications, like data storage, which drive intense research efforts. In the same way, virtually all applications of active materials would also require that their intrinsic properties survive the complexity of their operating environments. By combining experiments on colloidal rollers, numerical simulations of active particles, and hydrodynamic theory, I address the dynamics of self-propelled particles in crowded environments. I first present how to realize microfluidic forests by positioning obstacles that create a repulsive torque on rollers. I demonstrate that individual colloidal rollers exploring random forests form a Lorentz gas: they undergo a transition from diffusive to localized dynamics upon increasing the obstacle density. This transition originates from the underlying percolation transition of the forest. In contrast, disorder yields spectacular changes in the collective dynamic of flocks far below the percolation threshold. I demonstrate that, upon increasing disorder, flocking is suppressed in the form of a first-order phase transition generic to all polar active materials. Near the transition, a sparse network of flowing rivers emerges. I elucidate how disorder competes with the bending elasticity of the polar flock to channel the spontaneous flow along this network.

4.1 Wandering of individual rollers in microfluidic forests

Understanding how random walkers explore random media has enabled physicists to understand a host of transport phenomena: from conduction in metals to protein transport in the crowded intracellular medium. Forty years ago, De Gennes used the ant-in-a-maze analogy to illustrate this physical paradigm [33]. From a somehow dual perspective, colloidal rollers may be thought as robotic "ants" whose dynamics in disordered media require to be elucidated. The questions I address are: how long would a creature wander in a forest before finding its way out? Are some forests impossible to escape? These seemingly naive questions expand the concept of diffusion and localization in crowded media to self-propelled particles. This situation is obviously relevant both to living creatures exploring their natural habitats (from ants to bacteria), and to man-made autonomous machines operating in heterogeneous environments.

4.1.1 What would a microfluidic forest be?

Obstacles are introduced within the microfluidic channel by taking advantage of the versatility of UV lithography. Figure 4.1a shows an obstacle of radius $b = 5\,\mu$m made of $2\,\mu$m-thick photoresist. It lies on the bottom electrode where the colloids roll. Interestingly, colloidal rollers interact with obstacles at a distance, see Fig. 4.1a. As a roller approaches the obstacle, it reorients to move away from it. This repulsive interaction is quantitatively characterized in Fig. 4.1b. The scattering angle α decreases with increasing impact parameters d/b. The interaction between the roller and the obstacle is rather weak: a head-to-head collision ($d/b = 0$) leads to a deflection as small as $\alpha = 60$ deg. This interaction has also a finite range of about six obstacle radii. Furthermore, the reorientation of the roller takes place at constant speed as shown by the inset of Fig. 4.1b.

The origin of this repulsive interaction can be captured from simple arguments. An obstacle is nothing but a small electrically insulating post. Consequently, it distorts the surrounding electric field, as shown in Fig. 4.1c. By symmetry, the resulting in-plane component $\mathbf{E}_\parallel$ is radial. Any electrophoretic flow that could arise due to the obstacle [85, 141] would also be axisymmetric. In Chapter 2, the response of individual rollers to in-plane perturbations has been elucidated. Accordingly, the obstacle-induced tangential flows and electric fields lead a roller to reorient and align in the radial direction. This situation is the analogous of the electrostatic repulsion between two rollers, depicted in Fig. 2.5.

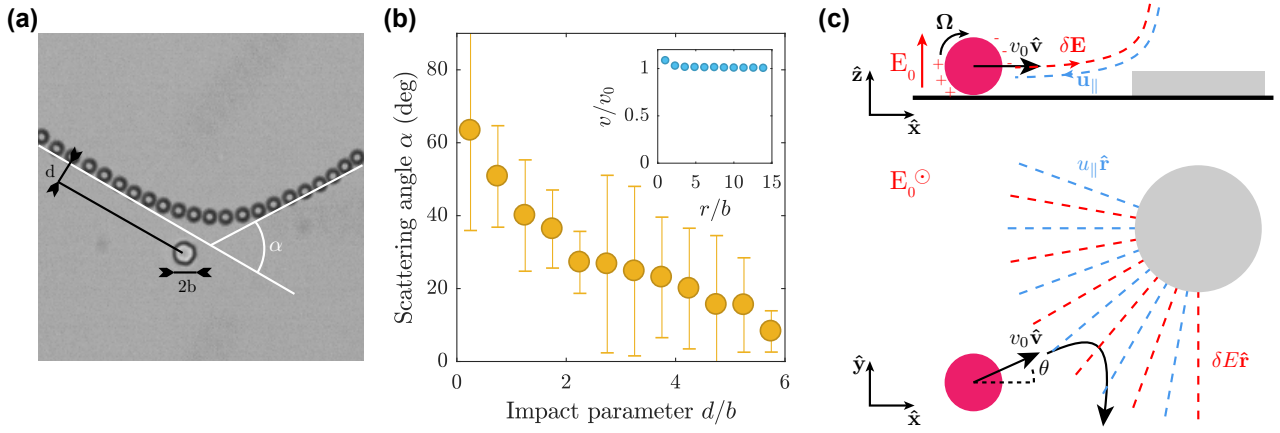

Figure 4.1 | **Roller-obstacle interaction.** **(a)** Superimposed snapshots showing a collision between a roller and an obstacle of radius $b = 5\,\mu$m. **(b)** The scattering angle α decreases with the impact parameter d/b. Inset: normalized roller velocity with respect to the distance to the obstacle. **(c)** Sketches of the obstacle-induced flow and electric field, and the resulting repulsive interaction with a roller. Top: side view. Bottom: top view.

4.1.2 Active Lorentz gas

Microfluidic forests are formed by randomly positioning obstacles within the channel, see Fig. 4.2. To investigate how an individual roller explores such forests, I have performed a series of experiments

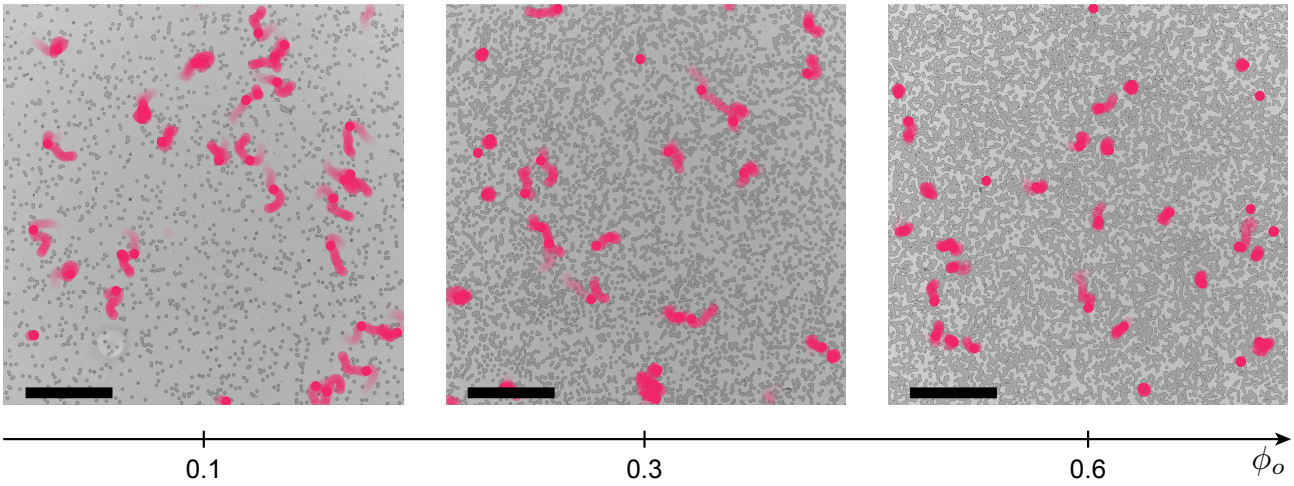

Figure 4.2 | **Colloidal rollers explore random forests.** Increasing the obstacle packing fraction ϕ_o slows down the exploration of space of individual rollers. 2 s-long trajectories are shown in pink. The obstacles are 5 μm radius. Scale bars: 500 μm.

varying the obstacle packing fraction ϕ_o while keeping the density of rollers far below the onset of collective motion. Figure 4.2 shows 2 s-long trajectories of rollers within microfluidic forests of increasing densities $\phi_o = 0.1$, $\phi_o = 0.3$ and $\phi_o = 0.6$. As ϕ_o increases, the roller trajectories are tighter. Not so surprisingly, the denser the forest, the slower the exploration of space by the rollers.

This simple result hides, however, much more complexity regarding the roller dynamics. In particular, two scenarios could explain the slowing down of the exploration of space by the rollers. These two scenarios exclude each other and yield very distinct particle dynamics at long times. They are sketched in Fig. 4.3. The first scenario consists in a dynamics *à la* Lorentz. In a model proposed by Lorentz in 1905 [71], particles move ballistically between hard-core obstacles. At contact, the particles are reflected specularly which randomizes their direction of motion. This behavior is sketched in Fig. 4.3a. The resulting long-time dynamics depends on the obstacle density. Above the percolation threshold, when the void between obstacles does not span the entire system, particles are trapped in compact regions of space. Their long-time dynamics is localized. Below the percolation threshold, for *any* obstacle packing fraction, the long-time dynamics of the particles is diffusive. Increasing the forest density merely reduces the particle diffusivity.

A recent work by Peruani and coworkers [26] has reported a very different phenomenology. In this numerical work, the authors have studied the dynamics of active particles being deflected by soft-core obstacles. No localization transition was recorded and the asymptotic dynamics of particles revealed to be subdiffusive rather than diffusive. This long-time dynamics was explained by the fact that the particles get trapped for long times by some obstacle arrangements: they follow closed trajectories while escaping from time to time from a trap to an other, see Fig. 4.3b. The subdiffusive dynamics of particles was supported by the measurements of the trapping time distribution that was argued to

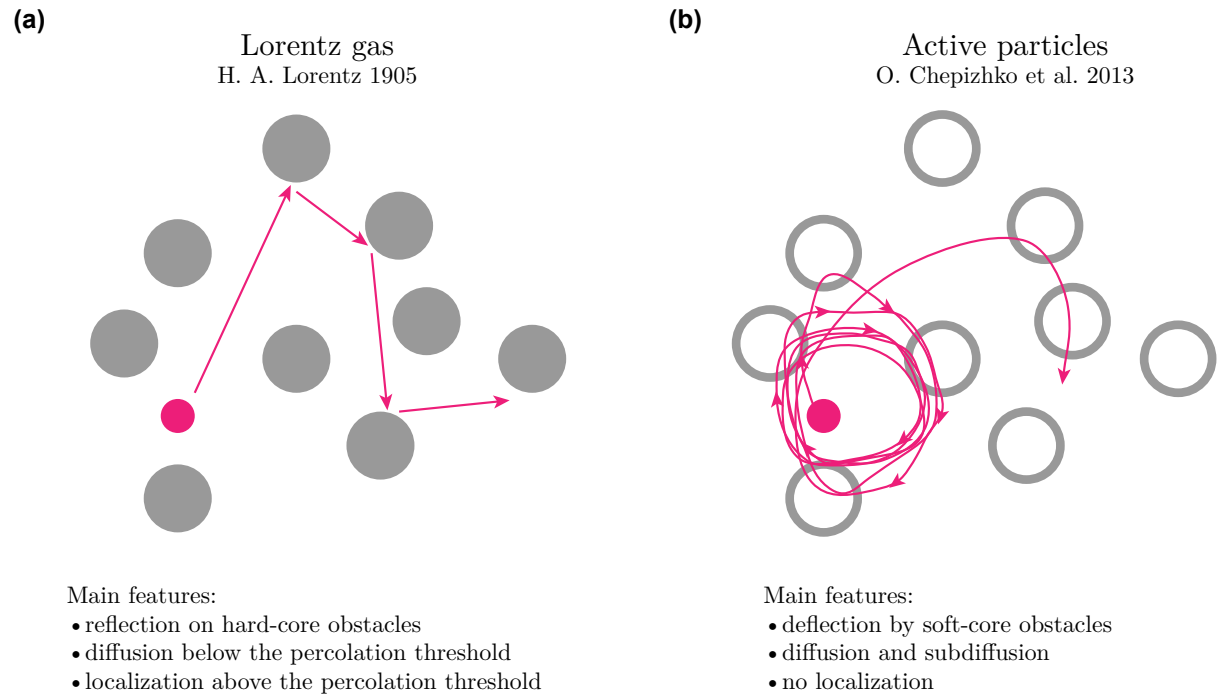

Figure 4.3 | **Two possible dynamics for particles exploring random forests. (a)** Lorentz gas [71]. Particles moving ballistically are reflected specularly on hard-core obstacles. **(b)** Long-time trapping of active particles [26]. Active particles moving at constant speed are deflected by soft-core obstacles.

asymptotically follow a power-law such that the mean trapping time was diverging faster than $\ln(t)$ [26].

Having in mind these two scenarios, to unveil the exploration dynamics of random forests by colloidal rollers necessitates going beyond the qualitative analysis of Fig. 4.2. The roller dynamics is quantitatively captured by the mean squared displacement $\Delta r^2(t) = \langle |\mathbf{r_i}(t_0+t) - \mathbf{r_i}(t_0)|^2 \rangle_{t_0,i}$, where $\mathbf{r_i}(t)$ is the position of roller i at time t. Figure 4.4a shows the mean squared displacements of rollers for obstacle packing fractions ranging from $\phi_o = 0$ to $\phi_o = 0.7$. These measurements reveal that the long-time roller dynamics depend on ϕ_o. At low obstacle densities, rollers diffuse, as already demonstrated in Chapter 2 for $\phi_o = 0$. At high obstacles densities, the mean squared displacements saturate: rollers are localized into compact regions of space. This localization seems to occur at $\phi_o \sim 0.5$, therefore reflecting the percolation transition of the obstacle forest that takes place at $\phi_o^* = 0.518$ (for obstacles of effective radius $b+a$ to account for the finite size of the rollers). At intermediate obstacle densities, the roller dynamics appear subdiffusive which is confirmed by the measure of the growth exponent α, defined as $\Delta r^2(t) \sim t^\alpha$. Figure 4.4b shows that α takes values in-between 0 and 1 for intermediate obstacle packing fractions.

Figures 4.4a and 4.4b suggest that the particle dynamics continuously goes from normal diffusion

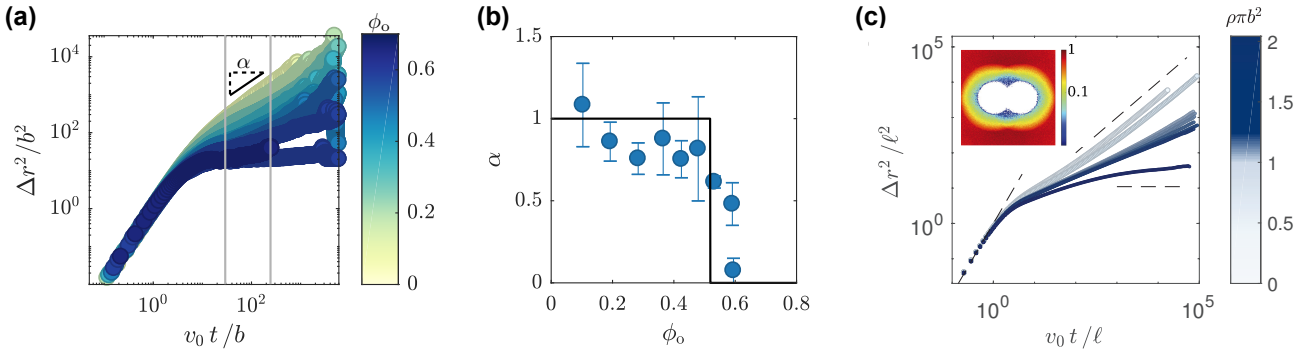

Figure 4.4 | **Active Lorentz gas. (a)** Mean squared displacements of colloidal rollers exploring random forest of various densities ϕ_o. **(b)** Growth exponent α, defined as $\Delta r^2(t) \sim t^\alpha$. The blue circles are values of α measured from the region delimited by the two vertical lines in (a). The solid line corresponds to the Lorentz gas scenario predicted by numerical simulations. **(c)** Mean squared displacements of active particles from simulations. Dashed lines are guides to the eyes and show evolutions with growth exponents $\alpha = 2$, $\alpha = 1$ and $\alpha = 0$. Inset: average particle density around a pair of obstacles (white). Both repulsion at a distance and hard-core exclusion were implemented here. The density of obstacles is $\rho = 0.65/\ell^2$, where ℓ is the interaction range. The color codes for variations of the hard-core radius b. It goes from $b = 0.5\ell$ (light grey) to $b = 0.9\ell$ (dark blue).

to subdiffusion to localized dynamics upon increasing disorder. However, the experiments do not give access to very large time and length scales. The roller behaviors we observe could be their genuine asymptotic dynamics or a crossover. To complement our experimental measurements, David Lopes Cardozo has performed numerical simulations that closely relate to the experiments. He has probed the asymptotic dynamics of active particles propelling at constant speed and interacting with obstacles *via* repulsive torques. One of the conclusion of this numerical investigation, is that this system displays a localization transition *à la* Lorentz provided that the hard-core exclusion by the obstacles is also accounted for. The asymptotic dynamics is either diffusive (below ϕ_o^*) or localized (above ϕ_o^*), see Figs. 4.4b and 4.4c. Genuine subdiffusion only occurs exactly at ϕ_o^*.

By combining experiments on colloidal rollers and extensive numerical simulations, we have explained how random repelling obstacles hinders and ultimately localizes the motion of robotic "ants". While at small obstacle densities the rollers explore space as would random walkers, the obstacles significantly slow down their dynamics and ultimately limit their exploration to finite regions of space. This behaviour is analogous to that found in a model introduced by Lorentz to account for the transport of electrons in metals. While both repulsion at a distance and hard-core exclusion reduce the particle diffusivity, the localization of the particle trajectories only occurs due to hard-core interactions. In other words, "ants" would spend more time to escape a dense forest, and they would always succeed in finding a way out as long as an exit path exists. This work has been published in the article untitled "Diffusion, subdiffusion and localisation of active colloids in random post lattices" [83] which is

reproduced on page 75.

4.2 Flocking through microfluidic forests

Having explained the dynamics of individual rollers within heterogeneous environments, I now turn my attention to the emergence and propagation of colloidal flocks through disorder. How does disorder hinder collective motion?

4.2.1 Destruction of colloidal flocks in disordered environments

The robustness of colloidal flocks to heterogeneous environments is addressed by confining rollers within rectangular channels patterned with random arrays of obstacles, see Fig. 4.5. The roller packing fraction is set to $\rho = 1\,\%$, above the onset of collective motion in an obstacle-free channel. A flock thus propagates bouncing back and forth at the two ends of its confining channel. The roller density is kept constant and the obstacle packing fraction ϕ_o is increased.

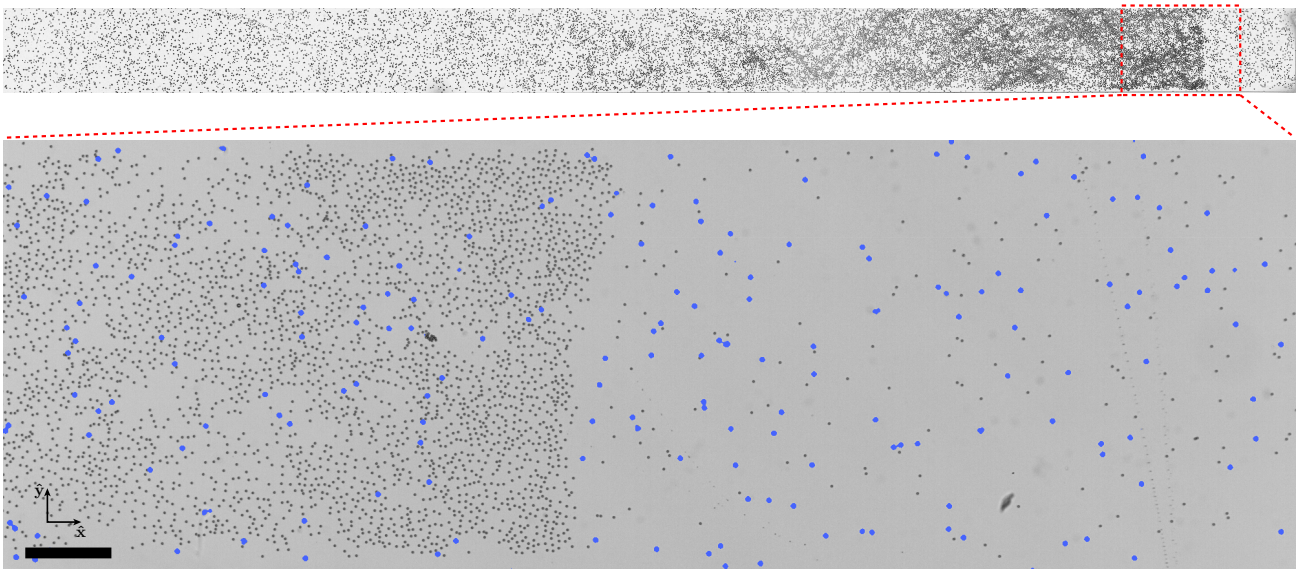

Figure 4.5 | **Colloidal flock in disordered environment.** Top: snapshot of a full rectangular channel where a colloidal flock propagates through a disordered environment. Channel width is 1 mm. Bottom: close-up on the head of a colloidal flock that propagates through a random array of obstacles (blue circles). Scale bar: 200 μm.

Figure 4.6a shows that the longitudinal current of rollers $J_{\parallel}$ decreases upon increasing the obstacle packing fraction. Above $\phi_o^* = 4\,\%$, the current vanishes: no flock form within the channel. The suppression of collective motion is rationalized by looking at the orientation diffusivity D of the rollers.

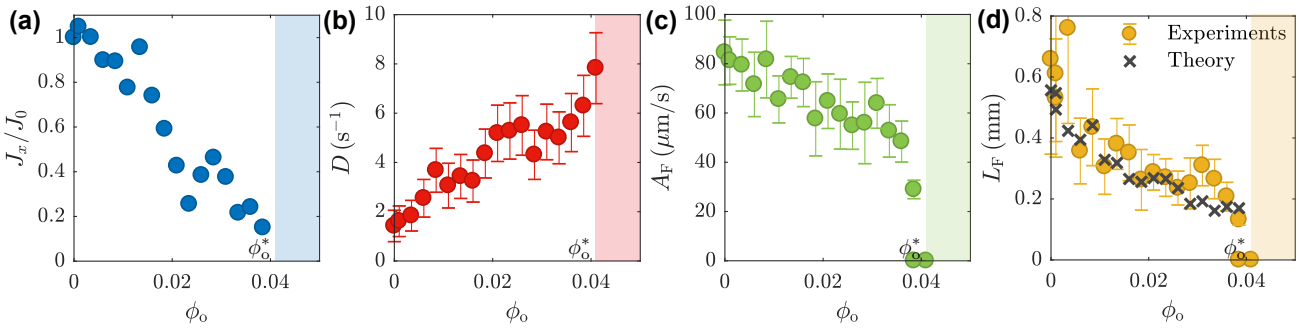

Figure 4.6 | **Destruction of colloidal flocks. (a)** The roller current decreases with increasing disorder. **(b)** The orientation diffusivity of the rollers increases linearly with the obstacle packing fraction ϕ_o. **(c)** The flock amplitude A_F defined as the roller current at the head of the flock, reveals a discontinuity at ϕ_o^* at which collective motion is suppressed. **(d)** The length of the flock L_F measured from the experiment (yellow circles) decreases with increasing disorder. The measures are in agreement with the prediction from hydrodynamic arguments (dark crosses).

From the previous section, we know that the roller dynamics is always diffusive within this range of obstacle densities. Moreover, increasing the obstacle density increases the orientation diffusivity D. This expectation is confirmed in Fig. 4.6b where D is shown to linearly increase with ϕ_o.

From this perspective, the suppression of collective motion upon increasing disorder is similar to a Vicsek transition. The combination of the roller motility and quenched disorder effectively acts like a time-dependent angular noise that eventually overcomes interactions between rollers at ϕ_o^*. Vicsek transition being first order, at first glance the rather smooth decrease shown by the roller current below ϕ_o^* might look surprising (Fig. 4.6a). A carefull analysis, however, reveals the discontinuous nature of the disorder induced suppression of flocks. Figure 4.6c show that polar order at the head of the flock abruptly vanishes at ϕ_o^*. A quantitative comparison with a Vicsek transition was made possible thanks to the theoretical prediction for the flock lengths L_F by Caussin and coworkers [19] from hydrodynamic arguments, see Eq. (1.8). Figure 4.6d shows that this prediction quantitatively agrees with the direct measurement of the extent of the flocks. Undoubtebly, disorder causes the flock to melt in a Vicsek-like fashion.

4.2.2 Distortion of colloidal flocks in disordered environments

Disorder-induced melting is robust to the obstacle arrangement. Figure 4.7b shows a flock propagating through a crystalline forest of obstacles. Unlike the random arrays considered thus far (Fig. 4.7a), the obstacles now lie on a square lattice, whose main axis is tilted by an angle of 45 deg with respect to the flock propagation direction (Fig. 4.7b). This configuration results in little difference regarding the suppression of flocking. Figure 4.7c shows the variations of the roller density at the head of the flock ρ_F with respect to the mean roller density ρ within the channel. The data obtained with disordered and crystalline forests of the same obstacle packing fraction $\phi_\mathrm{o} = 3\,\%$ are very close to each others. This result further support the Vicsek-like suppression of collective motion: whatever the obstacle ar-

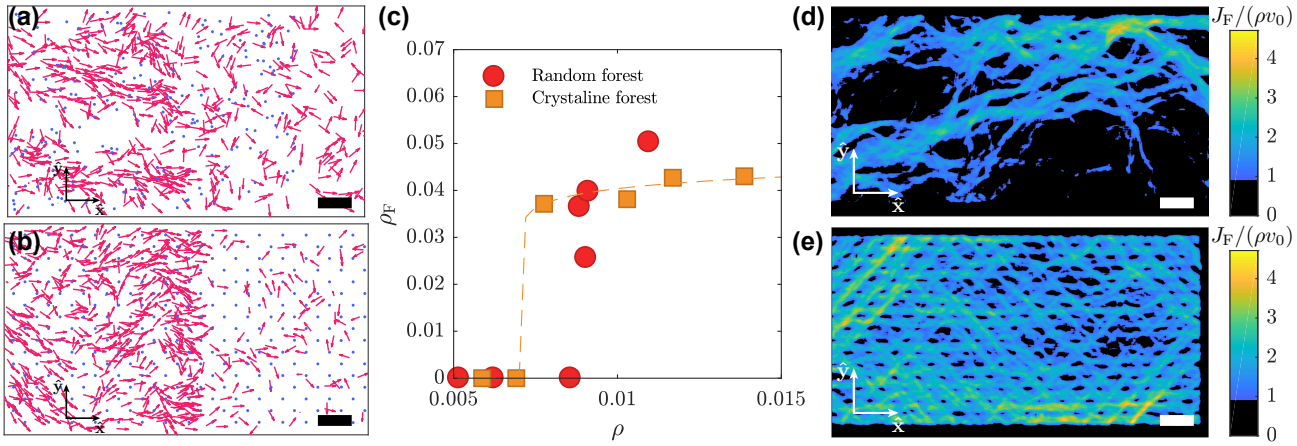

Figure 4.7 | **Distortion of colloidal flocks. (a)** Snapshot of the head of a colloidal flock propagating through a random forest of obstacles. Scale bar: $100\,\mu$m. **(b)** Snapshot of the head of a colloidal flock propagating through a crystalline forest of obstacles. Scale bar: $100\,\mu$m. **(c)** Variations of the roller density at the head of the flock ρ_F with the mean roller density ρ for random (red circles) and crystalline (orange squares) arrays of obstacles with a packing fraction $\phi_o = 3\,\%$. **(d)** Heatmap of the roller current within a flock that propagates through a random array of obstacles with a packing fraction slightly below ϕ_o^*. A sparse and tortuous network of flowing rivers emerges. Scale bar: $100\,\mu$m. **(e)** Heatmap of the roller current within a flock that propagates through a crystalline array of obstacles with a packing fraction slightly below ϕ_o^*. The spontaneous flow remains homogeneous. The obstacles only induce small depleted wakes. Scale bar: $100\,\mu$m.

rangement, quenched heterogeneities yield the increase of rotational diffusivity, hence the destruction of flocks.

A careful examination of the inner structures of the flocks reveals, however, a striking difference. Figures 4.7d and 4.7e show fields of the roller current averaged over the time spent by the flocks in the observation window. The flock that propagates through the disordered forest is very heterogeneous (Fig. 4.7d) while the flock that propagates through the crystalline forest is quite homogeneous (Fig. 4.7e). Importantly, both the flocks considered in Figs. 4.7d and 4.7e are the smallest flocks that form before a small increase in ϕ_o leads to their destruction. We explained this difference by providing a hydrodynamic description of flocking through quenched disorder [84]. In particular, this theory is qualitatively consistent with the emergence of a sparse and tortuous network of flowing rivers in the disordered configuration. Here, I give a simple overview of this theory. The hydrodynamic equations for extremely polarized flocks (see Eqs. (2.14) and (2.15) and the Table in Section 2.3.2) read in the presence of disorder:

$$\partial_t \rho + \nabla \cdot (\rho \mathbf{v}) = 0, \tag{4.1}$$

$$\partial_t \mathbf{v} + (\mathbf{v} \cdot \nabla)\mathbf{v} = \mathbb{P} \cdot [4\gamma \nabla(\nabla \cdot \rho\mathbf{v}) + 2(\alpha_2 - \gamma)\nabla^2(\rho\mathbf{v}) - \beta\nabla\rho + \mathbf{F}_o]. \tag{4.2}$$

In these equations, α_2 and γ are elastic constants and β^{-1} is the compressibility. Disorder alters the flock dynamics through the random force field $\mathbf{F}_o(\mathbf{r})$. Since obstacles exert a finite-range repulsive torque on rollers, the disorder contribution takes the form:

$$\mathbf{F}_o(\mathbf{r}) = -\beta_o \nabla \phi_o(\mathbf{r}), \tag{4.3}$$

where β_o is a positive constant that gives the strength of this random force and $\phi_o(\mathbf{r})$ is the local obstacle density. This expression implies that the flock would preferentially flow towards the valleys of the disorder landscape. This obstacle induced focusing is, however, limited by the repulsion between rollers at the origin of the pressure term $-\beta\nabla\rho$ in Eq. (4.2). Indeed, the fluctuations of density in the direction transverse to the propagation direction are given by:

$$\overline{|\delta\rho|^2}(\mathbf{q}) = \left(\frac{\beta_o}{\beta}\right)^2 \phi_o, \tag{4.4}$$

and do not depend on the modulus of the transverse wave vector $\mathbf{q} = [0, q_y]$.

Interestingly, the emergence of a sparse and tortuous river network is rationalized by looking at the bending fluctuations of the flock. For a flock that propagates along the direction $\hat{\mathbf{x}}$, $\mathbf{v} = v_x\hat{\mathbf{x}} + \delta v_y \hat{\mathbf{y}}$ and the bending fluctuations read in Fourier space:

$$\overline{|\delta v_y|^2}(\mathbf{q}) = \frac{\beta_o^2 \phi_o}{v_o^2 + 4q_x^2(\alpha_2 - \gamma)^2\rho^2} \left(\frac{q_y}{q_x}\right)^2. \tag{4.5}$$

where $\bar{\cdot}$ stands for average over disorder, and $\mathbf{q} = [q_x, q_y]$ is a quasi longitudinal wavevector. Disorder enhances bending fluctuations. Conversely, elasticity reduces bending fluctuations and in particular suppresses the small wavelength contributions.

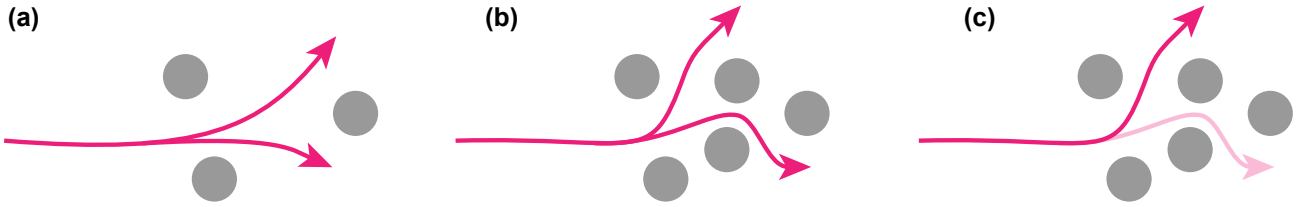

Figure 4.8 | **Channeling of the flock.** **(a)** At low disorder, a flock (pink) propagates through a disorder landscape with three hills (grey disks). **(b)** Increasing disorder yields the distortion of the flock. **(c)** Bending elasticity suppresses short wavelength distortions. As a result, the flock flows through a subset of the valleys of the disorder landscape. A sparse network of flowing rivers forms.

Figure 4.8 illustrates the consequence of this competition. The increase of disorder from Fig. 4.8a to 4.8b makes the flock to distort. The elasticity prevents such a bending and the flock can not explore all the valleys in the disorder landscape, see Fig. 4.8c. Therefore, the flock only propagates through a subset of all the valleys, hence the emergence of the sparse network of flowing rivers of Fig. 4.7c. In

contrast, crystalline obstacle arrangements make $\mathbf{F}_o$ identically zero, therefore predicting no fluctuation for the velocity field $\mathbf{v}$ in agreement with the homogeneous current map of Fig. 4.7c.

As a concluding remark, flowing rivers are also observed above ϕ_o^*, in particular at high roller density. None of them, however, spans the entire channel. Amélie Chardac, who has just joined the group, is currently investigating this regime where, despite the absence of macroscopic transport, collective motion locally prevails.

4.2.3 Conclusion

We have investigated how colloidal flocks can form and propagate in heterogeneous environments. Obstacles prevent flocking by randomizing the direction of motion of the rollers. Consequently, apparently small obstacle densities, way below the percolation threshold, are enough to inhibit collective motion. Orientation diffusivity is found to be the good parameter to monitor the robustness of flocks. If the obstacle density controls the emergence of collective motion, the fluctuations in their relative positions change the propagation pattern of the spontaneous flow. Disordered arrangements of obstacles yield very heterogeneous flows of the flocks caused by their elastic resistance to bending. From the perspective of designing robotic swarms and flows, these findings may guide the implementation of interaction laws between robots that enhance their autonomous behavior efficiency. This work has been published in the article "Distortion and destruction of colloidal flocks in disordered environments" [84] which is reproduced on page 91.

Article

Diffusion, subdiffusion, and localization of active colloids in random post lattices

Combining experiments and theory, we address the dynamics of self-propelled particles in crowded environments. We first demonstrate that motile colloids cruising at constant speed through random lattices undergo a smooth transition from diffusive, to subdiffusive, to localized dynamics upon increasing the obstacle density. We then elucidate the nature of these transitions by performing extensive simulations constructed from a detailed analysis of the colloid-obstacle interactions. We evidence that repulsion at a distance and hard-core interactions both contribute to slowing down the long-time diffusion of the colloids. In contrast, the localization transition stems solely from excluded-volume interactions and occurs at the void-percolation threshold. Within this critical scenario, equivalent to that of the random Lorentz gas, genuine asymptotic subdiffusion is found only at the critical density where the motile particles explore a fractal maze.

I Introduction

From intracellular transport to the motion of living creatures in natural habitats, virtually all instances of active transport at small scales occur in crowded environments, see e.g. [92, 57]. These observations together with potential applications of synthetic active matter, have resulted in a surge of interest in self-propulsion through heterogeneous media [146, 3]. However, apart from rare exceptions [14, 26, 143], most studies have focused on the two-body interactions between self-propelled particles and isolated obstacles or walls [67, 146, 3, 107, 116, 39, 6].

In contrast, a different line of research has been devoted to the dynamics of ballistic tracers and random walkers in extended crowded media, see e.g. [9, 60, 80, 55]. From a theoretical perspective, the gold standard is the Random Lorentz Gas model, where passive tracers move ballistically, or diffuse, through a random lattice of hard-core obstacles [71]. The salient features of this minimal model have been quantitatively explained, from transient subdiffusion, to the localization transition

occurring at the void percolation threshold, see [58, 2, 46, 62, 113] and references therein. From an experimental perspective, the Lorentz localization scenario has been qualitatively confirmed only very recently using Brownian colloids [108]. However, unlike passive colloids, self-propelled particles couple to their environment not only via their position, but also via their intrinsic orientation, which chiefly dictates their active dynamics. As a consequence the interactions between motile bodies and fixed obstacles can result in counterintuitive behaviors such as collision and avoidance at constant speed [99, 27, 84]. Considering the dynamics of self-propelled particles steadily moving in random lattices of repelling obstacle, Chepizhko et al found a phenomenology which qualitatively differs from that of the Lorentz gas [26]. Numerical simulations indeed suggest that active particles undergo genuine subdiffusion as a result of transient trapping over a range of obstacle densities while localization was not reported. In any realistic setting both reorientation at a distance and excluded volume would affect the particle trajectories. However, until now no experiment has addressed the localization of self-propelled bodies in crowded environments. We rectify this situation

In this article, we combine quantitative experiments and extensive numerical simulations to elucidate the dynamics of self-propelled particles in disordered lattices. We first investigate the trajectories of non-interacting active colloids moving at constant speed through repelling obstacles. We quantitatively demonstrate how disorder hinders their diffusion and ultimately confines their trajectories to compact regions. The very nature of this localization transition is then identified by disentangling the contributions of finite-range deflection and hard-core repulsion. We evidence that both excluded volume and deflection at a distance result in finite-time subdiffusion. However at long times, deflection at a distance merely renormalizes the particle diffusivity while hard-core repulsion results in a localization transition à la Lorentz, from diffusive to fully localized behavior.

II Experiments

II.i Exploration of random lattices by colloidal rollers.

The experimental setup is thoroughly described in Appendix V.i. Briefly, by taking advantage of the so-called Quincke electro-rotation, we turn polystyrene beads of radius $a = 2.4\,\mu$m immersed in hexadecane (viscosity $\eta \sim 2\,$mPa/s) into self-propelled colloidal rollers [95, 78, 70, 13]. The basic mechanism of Quincke electro-rotation is recalled in Appendix V.ii. When let to sediment on a flat surface, the colloids roll at constant speed $v_0 = 225\,\mu$m/s along a direction $\hat{\mathbf{v}}$ which diffuses on the unit circle with an angular diffusivity $D = 1.5\,s^{-1}$. Note that thermal diffusion would yield a much lower value of the order of $\sim 5 \times 10^{-3}\,\mathrm{s}^{-1}$. We believe the particle roughness to be chiefly responsible for the spontaneous orientational diffusivity of the rollers. Disorder is introduced by adding UV-lithographied cylindrical posts of radius $b = 10\,\mu$m on the surface, see Fig. 4.9 and [84]. The obstacles are placed at random and can overlap. The obstacle density, defined as the number of obstacle centers per unit area, is varied from $\rho = 0$ to $\rho = 1.1/(\pi b^2)$. We focus on a situation opposite to [84], where we considered high roller densities leading to collective flocking motion in dilute obstacle lattices. Here, in all experiments, we minimize the interactions between the rollers by keeping their packing fraction far below the onset of collective motion [13, 12]. In this regime the rollers behave as independent persistent random walkers [13, 12]. We simultaneously track the trajectories of $\sim$ 100 colloids in

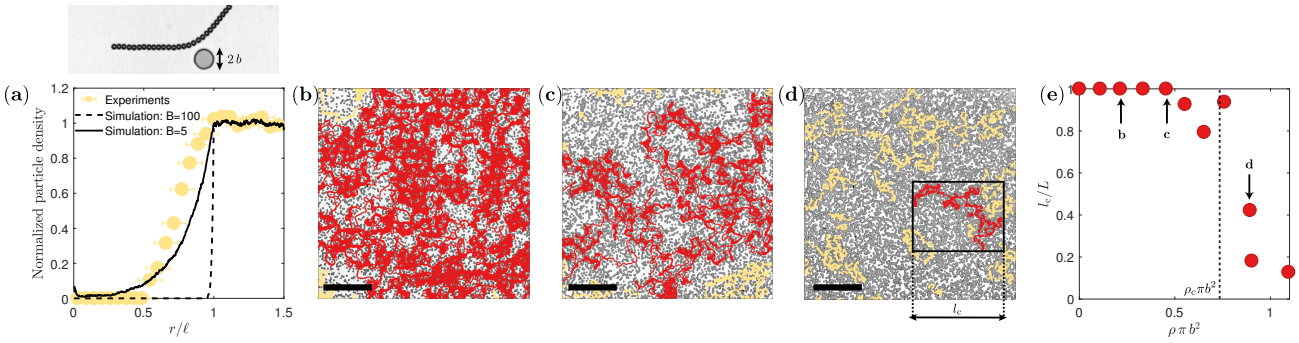

Figure 4.9 | Colloidal rollers in random obstacle lattices. (a) Top panel: Superimposed pictures taken at *equal time intervals* of a colloidal roller deflected by a lithographied post of radius $b = 10\,\mu$m. Note that the direction of motion is changed at constant speed. Bottom panel: Radial density of colloidal rollers propelling around an isolated obstacle. Circles: Experiments. Dark lines: Simulated radial densities. Solid line: $B\ell/v_0 = 5$, dashed line: $B\ell/v_0 = 100$ as defined in (4.7). ℓ is defined as the value where the density plateaus. In all our experiments we find $\ell \sim 2b$. Error bars: binning size. (b), (c) and (d) Trajectories of colloidal rollers (red and yellow) superimposed to the pictures of the obstacle lattices. Scale bar: $500\,\mu$m. Total time: $300\,s$. (b) $\rho = 0.21/(\pi b^2)$, the trajectories form a single percolating cluster. (c) $\rho = 0.45/(\pi b^2)$, the trajectories form disconnected clusters. The largest cluster (in red) percolates through the observation region. (d) $\rho = 0.89/(\pi b^2)$, none of the disconnected clusters percolate, and no macroscopic transport is observed. The largest cluster of maximal dimension l_c is colored in red. (e) Variations of the normalized maximal cluster size with the obstacle density. L is the width of the observation window. The dashed line indicates the critical density ρ_c. Experimental errors on the determination of the cluster sizes are smaller than the figure markers. Defining a statistical error on this extremal quantity would require a number of independent realisations beyond our experimental reach.

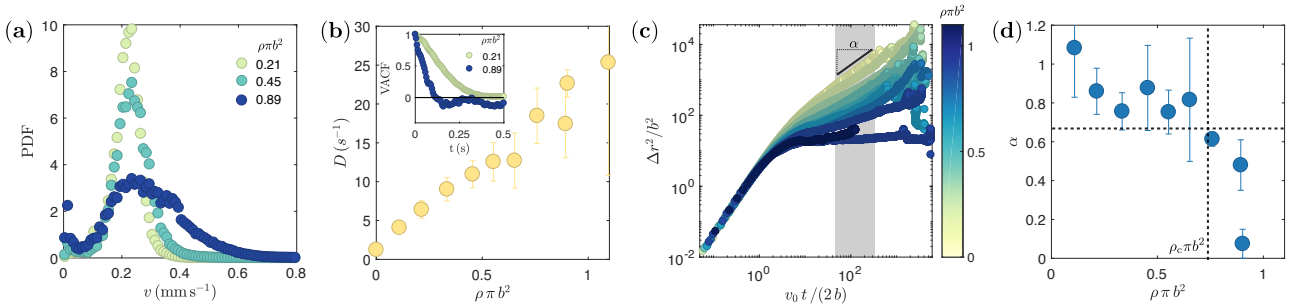

Figure 4.10 | From active diffusion to localization. (a) Probability distribution function of the roller speed for three obstacle densities. $\rho = 0.21/(\pi b^2)$, $\rho = 0.45/(\pi b^2)$ and $\rho = 0.89/(\pi b^2)$. The three distributions are peaked at the same typical speed value: $v_0 = 250\,\mu$m/s. (b) The angular diffusivity D increases with the obstacle fraction. D is measured as the inverse of the time of half decorrelation of the velocity autocorrelation shown in the inset. Error bars: 1 sd. Inset: Autocorrelation function of the instantaneous orientation of the rollers velocity VACF $= \langle \hat{\mathbf{v}}(t_0) \cdot \hat{\mathbf{v}}(t_0 + t) \rangle_{t_0}$. (c) Mean squared displacements of the rollers as a function of time. The colors indicate the obstacle density. The rollers are localized in finite regions at high obstacle densities. (d) Variations of the dynamical exponent α defined as $\Delta r^2 \sim t^\alpha$. α is estimated using power-law fits of the mean squared displacements. For each obstacle density, independent fits have been performed in 7 intervals of width $v_0 t/(2b) = 50$ in the shaded region in (c). α represents the mean of the fitted exponents and error bars represents one σ. The vertical dashed line indicates the value of the critical density ρ_c defined in the last section. The horizontal dashed lines indicates the value $\alpha = 0.66$ corresponding to an ideal overlapping Lorentz gas.

a square observation window of size $L = 2.4\,$mm, and all quantities reported below correspond to ensemble and time averages. The trajectories are recorded at 188 fps over 5 minutes. During this time interval, particles rolling along straight lines would move over distances of about half a meter.

As illustrated in Fig. 4.9a the obstacles repel the rollers at a finite distance while leaving their speed unchanged. We stress that this behavior is typical of active particles and cannot be observed with passive colloids at thermal equilibrium. The range of the interaction, $\ell \sim 2b$, is measured from the roller density around isolated obstacles, Fig. 4.9a. Appendix V.ii provides a detailed analysis of the roller-obstacle interaction (see also the Supplementary Informations of [84] for a thorough experimental characterization). Typical trajectories in random lattices are shown in Figs. 4.9b, c, d, and in a Supplementary Video. At low obstacle densities, the rollers freely propagate through the entire system. The ensemble of their trajectories forms a single connected cluster covering most of the free space left around the obstacles. Increasing ρ, the trajectories form disconnected and increasingly sparse clusters: a finite fraction of the colloids remains trapped in compact regions. The extent of the largest cluster is plotted for all obstacles densities in Fig. 4.9e. In agreement with our qualitative observations, above $\rho = 0.45/(\pi b^2)$ none of the colloids is observed to cruise through the entire field of view, and the extent of the largest cluster decreases very sharply at $\rho_c \sim 0.75/(\pi b^2)$.

II.ii Localization of colloidal-roller trajectories.

The obstacles clearly hinder the exploration of space by the active colloids. However, unlike the situation theoretically considered in [143], the rollers do *not* behave as Active Brownian Particles. They rarely contact the obstacles, and are not slowed down by the collisions. The distribution of their instantaneous speed is peaked at the same value, $v_0 = 250\,\mu$m/s, for all obstacle densities, Fig. 4.10a. Even more surprisingly, the distribution broadens towards high speeds as ρ increases. This observation alone would imply a faster exploration of space at high obstacle densities in obvious contrast with our experimental observation, Figs. 4.9b, c, and d. We therefore conclude that disorder predominantly impedes the motion of the rollers by altering their orientational dynamics.

In Figs. 4.10b, we plot the roller orientational diffusivity D, defined as the inverse of the velocity decorrelation time, Fig. 4.10b inset. D increases linearly with ρ. This scaling is expected for uncorrelated collisions with scatterers all contributing identically to the deflection of the roller trajectories. Within this simple picture the reduction of the cluster size would merely translate the algebraic decay of the translational diffusivity: $D_{\mathrm{T}} \sim v_0^2/D$, see e.g. [77, 3, 75]. However, the inspection of the mean squared displacements, Δr^2, in Fig. 4.10c invalidates this hypothesis.

At small times, the colloids undergo ballistic motion, however we do not find a universal scaling of the MSDs at long times. The growth exponent α defined as $\Delta r^2 \sim t^\alpha$ is a decreasing function of the obstacle density, Fig. 4.10d. Increasing ρ from 0 to ρ_{c}, the long-time dynamics smoothly evolves from normal diffusion ($\alpha = 1$) to subdiffusion ($\alpha < 1$). Above ρ_{c} the dynamics slows down abruptly and the rollers undergo a localization transition ($\alpha = 0$). The rollers propelling at constant speed, this rich behavior is necessarily encoded in the long-time decay of the orientational correlations, and therefore cannot be captured by a mere description in terms of an effective orientational diffusivity [56, 74].

The central question we aim at answering now is whether the continuous evolution from normal diffusion, to subdiffusion, to localization, is an asymptotic behavior or a finite-time trend. Recent simulations of active particles ignoring excluded volume contributions indicate that finite-range repulsion bend the trajectories to form long-live closed orbits. This dynamical trapping results in genuine asymptotic subdiffusion [26]. In contrast, within the geometrical picture of the Lorentz gas, subdiffusion should be only observed over finite time scales diverging only at a critical obstacle fraction ϕ_{L} [1]. At ϕ_{L}, the asymptotic value of α would discontinuously jump from 1 to 0 thereby reflecting a transition toward a fully localized dynamics [58, 2, 143].

Clear anticorrelations typical of trapped trajectories are seen in Fig. 4.10b inset, yet they are not sufficient to distinguish between the two possible scenarios [56]. Elucidating the exact nature of the localization transition requires accessing much longer time-scales out of range of our experiments. We resolve this situation by confronting our findings to extensive numerical simulations.

[1] Here ϕ_{L} is defined as $\phi_{\mathrm{L}} = \rho_{\mathrm{L}}\pi b^2$, where b in the hard-core radius and ρ_{L}, the critical number density for obstacles of radius b. Note that ϕ_{L} is not the area covering fraction which is given by $1 - \exp(-\phi_{\mathrm{L}})$

III Numerical simulations

III.i Roller-obstacle interactions

Let us first build a simplified phenomenological description of the roller dynamics. Details on the numerical resolution of this model are given in Appendix V.i. We need to capture three central features: (i) the obstacles repel the active colloids isotropically, (ii) the interaction range is finite, (iii) collisions consist in reorientations at constant speed. We also discard spontaneous angular diffusion as it yields minute corrections to the obstacle scattering contributions as $\rho\pi b^2 > 0.1$, see Fig. 4.10b. Assuming pairwise additive interactions, these observations are sufficient to introduce a general form for the equations of motion of both the roller position $\mathbf{r}$ and orientation $\hat{\mathbf{v}} = (\cos\theta, \sin\theta)$:

$$\partial_t \mathbf{r} = v_0 \hat{\mathbf{v}}(\theta) \tag{4.6}$$

$$\partial_t \theta = -\partial_\theta \sum_j B(\delta r_j) \hat{\delta \mathbf{r}_\mathbf{j}} \cdot \hat{\mathbf{v}} \tag{4.7}$$

where $\mathbf{r}_j$ is the position of the j^{th} obstacle, and $\delta\mathbf{r_j} = \mathbf{r_j} - \mathbf{r}$. For sake of simplicity $B(\delta r_j)$ is chosen to be a positive constant, B, for $\delta r_j < \ell$ and 0 otherwise. We present in Appendix V.ii a series of experiments complemented by a microscopic theoretical model which ascertains this phenomenological description.

Before presenting the results of our simulations, let us gain some insight into the roller-obstacles scattering. (4.6) reflects motion at constant speed along $\hat{\mathbf{v}}$. (4.7) has a simple meaning: the rollers turn their back to the obstacles in a typical time B^{-1}. In agreement with the trajectory shown in Fig. 4.9a, a roller interacting with an obstacle experiences a torque which orients its velocity in the direction opposite to the vector connecting the roller to the obstacle center. One important comment is in order. The repelling torques cannot fully exclude the active particles from the interaction regions. Take for instance two obstacles with overlapping interaction disks. In the overlap region, the two repulsive torques compete to bend the particle trajectory in opposite directions. As a result, there always exist a finite channel between the obstacles through which the particle can almost freely proceed as illustrated in Fig. 4.11. Such interaction-free channels would not exist if the particles were repelled by an isotropic force (as opposed to an isotropic torque).

III.ii Strong Repulsion Torque and Overlapping Lorentz Gas

The particle dynamics is parametrized by a single dimensionless number that compares the time spent in the vicinity of an obstacle (ℓ/v_0), and the reorientation time B^{-1}. In order to see whether repulsion torques can yield subdiffusion and localization as observed in our experiments, it is worth analysing first the asymptotic case where $B\ell/v_0 \gg 1$. The MSD corresponding to $B\ell/v_0 = 100$ are plotted in Fig. 4.12a. At short times (short distances), the dynamics is ballistic. At intermediate time scales, as in the experiments, we observe a continuous slowing down of the dynamics in the form of subdiffusion as ρ increases. However a careful inspection of the long-time dynamics reveals that this apparent subdiffusion is merely a transient behavior. Fig. 4.12b shows how the instantaneous value of the exponent $\alpha(\rho, t)$ evolves with time and obstacle density, where $\alpha(\rho, t) = \frac{\mathrm{d}}{\mathrm{d}\log \mathrm{t}} \log \Delta r^2$. The $\alpha(\rho)$ curves converge toward a step function as $t \to \infty$. For $\rho < \rho_\mathrm{c} = 0.3725$, $\alpha(\rho)$ converges to 1. The

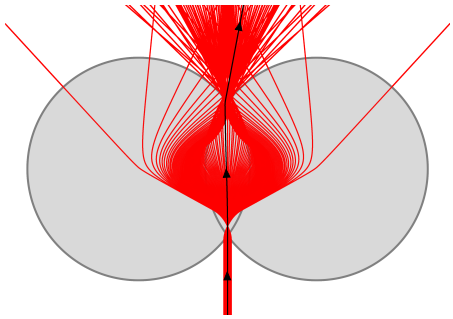

Figure 4.11 | Channeling through the obstacles. Ensemble of numerical particle trajectories crossing two obstacles through a narrow channel. $B\ell/v_0 = 5$. The initial velocity is transverse to the line joining the centers of the two discs. The black trajectory indicates the direction of propagation. Note that particle trajectories nearly equidistant to the obstacles are hardly deflected. All trajectories are spanned at constant speed.

particles undergo normal diffusion at long times. Conversely, for $\rho > \rho_c$, $\alpha \to 0$ and particle motion is localized. As it turns out, the active-particle dynamics is genuinely subdiffusive only at $\rho = \rho_c$ which corresponds to a fixed point of the $\alpha(\rho, t)$ curves. At ρ_c, $\Delta r^2 \sim t^{\alpha_c}$ with $\alpha_c = 0.6 \pm 0.02$, see Fig. 4.12b. Surprisingly, both the value of this anomalous exponent and of $\rho_c \pi \ell^2 = 1.17$ suggest that this localization transition belongs to the universality class of the overlapping Lorentz gas model [71, 2]. The predictions of the overlapping Lorentz gas would be $\alpha_c = 0.66$, and $\rho_c \pi \ell^2 = 1.13$. This hypothesis is further confirmed by Fig. 4.12c, which shows the collapse of the MSD curves when time and distances are suitably rescaled by the distance to the critical density $\epsilon = (\rho - \rho_c)/\rho_c$ using the Lorentz hyperscaling relations [2, 58].

The universality of the Lorentz localization transition stems from an underlying percolation transition [113]. Localization occurs as the voids separating *impenetrable* obstacles stop percolating through the system. In contrast, we have neglected the hard-core repulsion from the obstacles in (4.6) and (4.7), and the repelling torques cannot fully exclude active particles from the interaction regions. However, in practice, when $B\ell/v_0 = 100$ the channels allowing the penetration of the interaction discs become so narrow that we do not observe a single obstacle-crossing event in our simulations, see Fig. 4.12a inset. The particles merely penetrate the interaction discs over minute distances of the order of $v_0/B = \ell/100$ before being strongly repelled. This small yet finite penetration explains the slight discrepancies with the values of the critical density and exponent compared to the ideal Lorentz gaz scenario [108, 103]. Both α_c and ρ_c exceed the Lorentz-gas value by 10%. The latter difference consistently corresponds to smaller hard-core particles of radius $\ell - 2(v_0/B)$. Is this localization scenario relevant to our experiments? In order to answer this question, we now need testing the robustness of this phenomenology to finite repulsion strength.

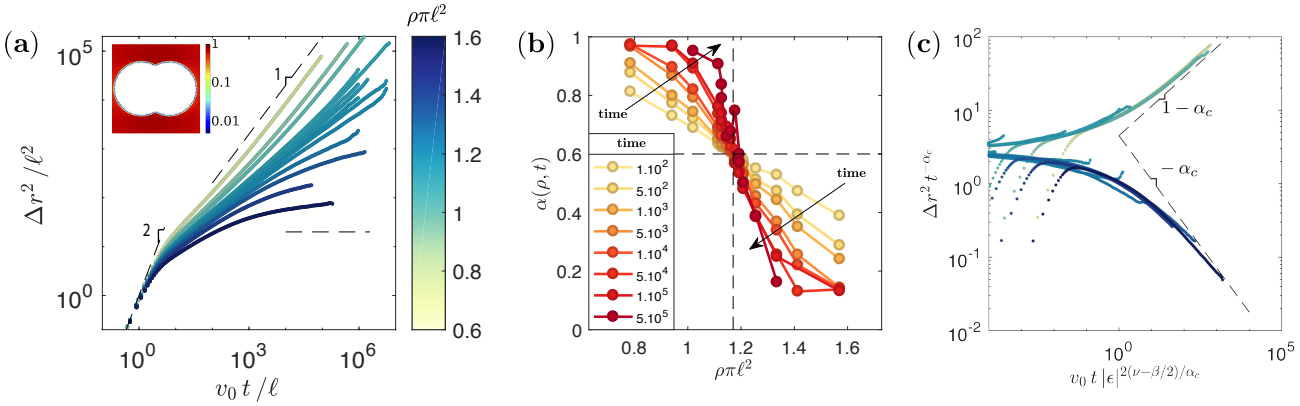

Figure 4.12 | Localization transition in the large repulsion limit: $B\ell/v_0 = 100$. (a) Numerical mean squared displacements of the active particles. The color codes for the obstacle density. Dashed lines correspond to power laws with exponents 2, 1 and 0. Inset: normalized density map of the active particles around two overlapping interaction discs (log-scale histogram). (b) Instantaneous dynamical exponent plotted versus the obstacle density. The different colors correspond to measurements of α at increasing times (expressed in unit of ℓ/v_0). The dashed lines locate the localization transition. (c) Scaled MSDs. ρ_c and α_c are measured from (b) and $\epsilon = (\rho - \rho_c)/\rho_c$. β and ν correspond to the classical percolation exponents. The theoretical values for the overlapping Lorentz gas yield $2(\nu-\beta/2)/\alpha_c = 4.2$. The best collapse is obtained for $2(\nu-\beta/2)/\alpha_c = 4.5$. This discrepancy is very likely to stem from the finite penetration in the obstacles.

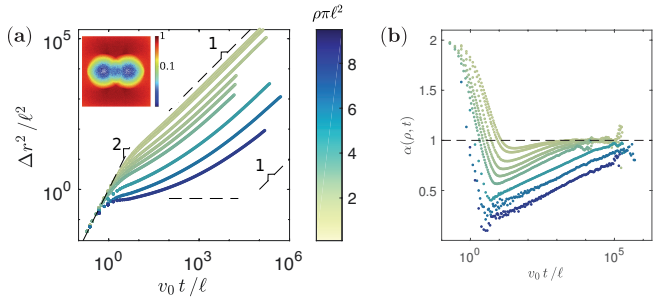

Figure 4.13 | No localization at finite repulsion: $B\ell/v_0 = 5$. (a) Numerical mean squared displacements of the active particles. The color indicates the obstacle density. The dashed lines correspond to power laws with exponents 2, 1 and 0. Inset: normalized density map of the active particles around two overlapping interaction discs (log-scale histogram). (b) Time variations of the instantaneous dynamical exponent at different obstacle densities. All exponents converge toward $\alpha = 1$ at long time. The asymptotic dynamics corresponds to normal diffusion.

III.iii Finite Repulsion: Diffusion Through Disorder

The comparison between the numerical and experimental densities around isolated obstacles indicates that $B\ell/v_0 = 5$ correctly approximates the repulsion strength of the lithographied obstacles, see Fig. 4.9a. The MSDs corresponding to $B\ell/v_0 = 5$ are plotted in Fig. 4.13a. Surprinsingly, although $B\ell/v_0 > 1$, they show a stark difference with the strong repulsion limit discussed in the previous section. From $\rho\pi\ell^2 = 0.95$ to $\rho\pi\ell^2 = 7.8$, where the interaction disks cover about 99.96% of the simulation box, we do not observe any sign of localization. Whereas repulsion still results in subdiffusion at intermediate time scales, the instantaneous dynamical exponent α converges to 1 at long times even for the highest obstacle densities, Fig. 4.13b. Disorder does not yield asymptotic subdiffusion, and only slows down the rollers motion by reducing their translational diffusivity.

Repulsion at finite B fails in building effective barriers as illustrated in Fig. 4.13a inset. For $B\ell/v_0 = 5$, we see that the width of the channel going through a pair of obstacles compares to the inter-obstacle distance thereby preventing any form of long-time trapping. As a result, at long times, neither localization nor subdiffusion can be achieved as both processes rely on the formation of traps with diverging escape times [9].

III.iv Origin of the Localization Transition in Colloidal-Roller Experiments

We infer from the above analysis that the localization transition must arise from the excluded-volume interactions as it cannot stem from hydrodynamic and electrostatic repulsions alone. In order to test this final hypothesis, we add steric repulsion to the finite-range repulsion torque (keeping $B\ell/v_0 = 5$). Given the observations reported before, a simple implementation of steric interactions is achieved in adding a repulsion torque of magnitude $B = 100v_0/\ell$ and range $b < \ell$ to (4.7).

We do recover the experimental phenomenology which turns out to be qualitatively similar to that of the Lorentz model, Figs. 4.14a and 4.14b. For packing fractions (computed with the hard core radius)

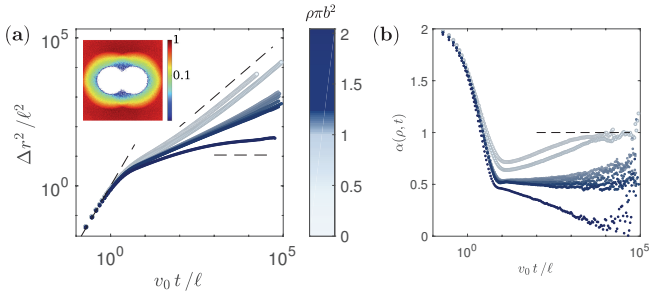

Figure 4.14 | Disentangling the roles of hard-core interactions and finite-range repulsion. (a) Numerical mean squared displacements of the active particles. The color indicates the value of $\rho\pi b^2$ and each curve corresponds to a different value of b at constant $\rho = 2.05/(\pi\ell^2)$ and $B = 5v_0/\ell$. The three dashed lines correspond to power laws with exponents 2, 1 and 0. Inset: Normalized histogram of the roller density (log-scale histogram). (b) Time variations of the instantaneous dynamical exponent corresponding to the MSD plotted in (a). Localization occurs only above the percolation threshold of the hard-core obstacles, viz for $\rho\pi b^2 > \phi_{\mathrm{L}}$.

smaller than the critical fraction at the Lorentz transition, $\rho\pi b^2 < \phi_L$, a ballistic regime is followed by a transient subdiffusive dynamics. However, we see that at long times the dynamics ultimately crosses over toward pure diffusion . Approaching ϕ_L the extent of the transient regime diverges and yields asymptotic subdiffusion with $\alpha = 0.5 \pm 0.02$. Above ϕ_{L} the particles explore finite regions of space and α converges to 0. The gross features of the dynamics are well captured by a Lorentz scenario, as further confirmed by taking into account the finite size of the rollers when computing the critical fraction: $\rho_{\mathrm{c}}\pi(b+a)^2 = \phi_{\mathrm{L}}$. This correction gives $\rho_{\mathrm{c}}\pi b^2 = 0.73$ where we expect $0.5 < \alpha(\rho_{\mathrm{c}}) < 0.66$ from our simulations. Both values are in excellent agreement with our experimental findings, as shown in Figs. 4.9e and 4.10d.

IV Conclusion

We have combined quantitative experiments and extensive simulations to elucidate the dynamics of active particles in random lattices of repelling obstacles. We conclude from this analysis that both repulsion at a distance and excluded volume hinders the exploration of random lattices in the form of transient subdiffusion. We show that active colloids cruising through disordered lattices provide a prototypical realization of a random Lorentz gas undergoing a genuine localization transition at the void percolation threshold.

Acknowledgements

We acknowledge support from ANR grant MiTra, and Institut Universitaire de France (D.B.). Simulations have been performed at the PSMN computation facility at ENS de Lyon. We thank N. Bain and V. Demery for valuable comments on our manuscript. A. M. and V. C. performed the experiments.

D. L. C. performed the numerical simulations. D. B. designed the research. A. M., D. L. C. and D. B. discussed the results and wrote the article. A. M. and D. L. C. have equally contributed to this research.

V Appendix

V.i Experimental and Numerical Methods

Experiments

The rollers are fluorescent Polystyrene colloids of diameter $2a = 4.8\,\mu$m dispersed in a 0.11 mol.L^{-1} AOT-hexadecane solution (Thermo scientific G0500). The suspension is injected in a wide microfluidic chamber made of two parallel glass slides coated by a conducting layer of Indium Tin Oxyde (ITO) (Solems, ITOSOL30, thickness: 80 nm) [13]. The two electrodes are assembled with double-sided scotch tape of homogeneous thickness ($110\,\mu$m). The colloids are confined in a $1\,\text{cm} \times 1\,\text{cm}$ square chambers, by walls made of a positive photoresist resin (Microposit S1818, thickness: 2 μm). Identical cylindrical obstacles of radius $b = 10\,\mu$m made of the same material are included in the chambers. Their position is uniformly distributed with a density ρ. Therefore the obstacles can overlap. This geometry is achieved by means of conventional UV lithography.

The colloids are observed at a 4.8X magnification with a fluorescent Nikon AZ100 microscope. The movies are recorded with a CMOS camera (Basler ACE) at frame rates of 188 fps. The particles are detected to sub-pixel accuracy, and the particle trajectories and velocities are reconstructed using the Crocker and Grier algorithm [29] using an improved version of the Blair and Dusfresne MATLAB code. Measurements are performed in $2.4\,\text{mm} \times 2.4\,\text{mm}$ observation windows.

The Quincke electro-rotation of the colloids is controlled by applying a homogeneous electric field transverse to the two electrodes $\mathbf{E} = E_0\hat{\mathbf{z}}$. The field is applied with a voltage amplifier (TREK 609E-6). All the reported results correspond to an electric field $E_0 = 1.1E_\text{Q}$, where E_Q is the Quincke electro-rotation threshold $E_\text{Q} = 0.9\,\text{V}/\mu\text{m}$.

Simulations

We numerically solve Eqs. (4.6) and (4.7) using a forward Euler integration scheme with an adaptive time step. The time step δt is chosen to be $\delta t = 10^{-3}/B \times \min[1, 1/\sum_j \delta\hat{\mathbf{r}}_\mathbf{j} \cdot \hat{\mathbf{v}}]$ in Eq. 4.7. The summation over the obstacles is performed by first updating the list of the obstacles interacting with each self-propelled particle. ℓ and v_0 set the length and time units. Simulations are performed in 200×200 or 1000×1000 square boxes. The code is parallelised assigning one trajectory to each independent core. Statistics are performed on 320 to 3200 noninteracting particles for a number of independent realizations of disorder ranging from 1 (low densities) to 128 (high densities). Typical simulations are launched on 32 to 128 independent cores for hours to weeks on Intel E5-2670 sandy bridge octacore 2.60 GHz processors.

V.ii Roller-Obstacle Interactions

In this appendix, we first review the self-propulsion of the colloidal rollers. Then, combining experiments and theory, we explain the response of the rollers to external electric and hydrodynamic driving fields. We finally exploit this result to account for the effective repelling interactions with the cylindrical obstacles.

Quincke Motorization

The principle of the Quincke motorization is thoroughly discussed in [13] and [78]. Briefly, when a homogeneous DC electric field is applied to an insulating sphere immersed in a conducting fluid, the conduction charges in the solution polarize the solid surface. For fluids and insulating bodies with standard permittivities, the orientation of the resulting electric dipole points in the direction opposite to the electric field. This situation turns out to be unstable above a critical field amplitude E_{Q}. Above E_{Q} any infinitesimal perturbation of the dipole orientation is exponentially amplified. The finite angle made by the electric dipole $\mathbf{P}$ with the electric field $\mathbf{E}_0$ results in a net electric torque $\frac{\epsilon_1}{\epsilon_0}\mathbf{P}\times\mathbf{E}_0$, where ϵ_1 is the liquid permittivity, Fig. 4.15. Ignoring inertia, mechanical equilibrium is reached when the rotational viscous drag acting on the sphere balances the electric torque. Angular momentum conservation then reads $\eta\mathbf{\Omega}=\frac{\epsilon_1}{\epsilon_0}\mathbf{P}\times\mathbf{E}_0$, where $\mathbf{\Omega}$ is the angular velocity, and η the drag coefficient. Similarly, charge conservation implies the balance between the Ohmic current and the advection of the free charges by the rotation of the sphere. Together these conservation laws set the rotation speed of the sphere to:

$$\Omega=\Omega_0\sqrt{\left(\frac{E_0}{E_Q}\right)^2-1}, \tag{4.8}$$

when $E_0>E_{\mathrm{Q}}$, and to 0 otherwise. Ω_0 is the inverse of the so-called Maxwell relaxation time of the free charges [78]. In our experiments this time scale is typically of the order of 1 ms, which explains the highspeed motion of the colloids. Indeed, when the insulating bead is let to sediment on a solid surface, the above reasoning still applies, and rotation is trivially converted into rolling motion [13]. Applying an electric field also gives rise to electrophoretic forces that act together with gravity to keep the roller in contact with the bottom electrode. As opposed to the colloidal rollers used in [40] which undergo stronger slip on the solid surface, in our experiments, the rolling coefficient is close to unity.

We stress that Quincke rotation stems from a spontaneous symmetry breaking of the surface-charge distribution. Therefore the direction of rotation is *not* prescribed by the external field and can freely rotate around the $\mathbf{E}_0$ axis.

Dynamical response of Colloidal Rollers to Electric and Flow Fields: Experiments and Theory

In our experiment each obstacle locally alters the direction and the magnitude of the electric field due to their permittivity mismatch with the solvent, and possibly to their net electric charge. In addition, these local heterogeneities of the electric field are very likely to induce electroosmotic flows past the electrodes, see e.g. [141, 85]. The specifics of the resulting electric and hydrodynamics perturbations goes far beyond the scope of this article; however given the axisymmetric shape of the posts, we can

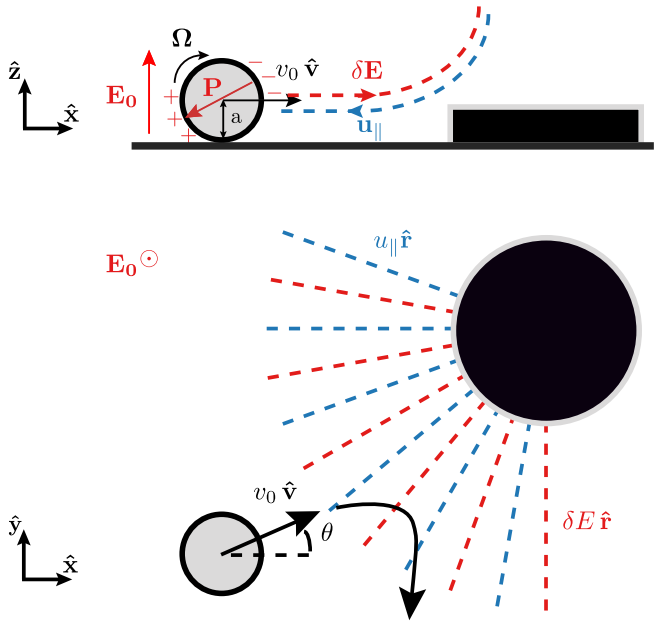

Figure 4.15 | Sketch of a colloidal roller propelling near an obstacle. Top panel: Side view. Bottom panel: Top view. The tilted electric dipole at the surface of the roller stems from the Quincke instability. The resulting electric torque drives the roller at constant speed v_0. The dielectric obstacle induces *radial* perturbations to the electric field (red dashed lines), and to the fluid-velocity field (blue dashed line).

readily infer that both perturbations have a radial symmetry, see Fig. 4.15. The in-plane components of these perturbations can have two consequences on the roller motion: (i) The colloids can be advected by the flow, and, or, pulled by field gradients. This effect is found to be negligible. In our experiments the roller speed is hardly modified as they approach the obstacles, Figs. 4.9a and 4.10a. (ii) The rollers can experience external torques which reorient their electric dipole and velocity, in agreement with the bending of the roller trajectory shown in Fig. 4.9a. Moreover, the out-of- plane component of the electric field increases near the obstacle leading to a broadening of the velocity distribution at high $\rho\pi b^2$, see Fig. 4.10a.

In order to establish a quantitative description of the roller-obstacle repulsion, we combine theory and dedicated experiments. In [13], starting from the Maxwell and Stokes equations we derived the equations of motion of a Quincke roller subject to a flow field $\mathbf{u}_\parallel$ parallel to the solid surface and to an electric field of the form $\mathbf{E} = E_0\hat{\mathbf{z}} + \delta\mathbf{E}$. They take the simple form:

$$\partial_t\mathbf{r} = v_0\hat{\mathbf{v}}, \tag{4.9}$$

$$\partial_t\hat{\mathbf{v}} = (1 - \hat{\mathbf{v}}\hat{\mathbf{v}})\cdot\left(\mu_H\partial_z\mathbf{u}_\parallel - \mu_E\delta\mathbf{E}\right), \tag{4.10}$$

where μ_H and μ_E are two positive mobility coefficients, and where both the local shear $\partial_z\mathbf{u}_\parallel$ and the perturbation $\delta\mathbf{E}$ are evaluated at $z = a$. Given our experimental findings, we ignore the small corrections to the roller speed that could be caused by transverse perturbations of the electric field and by flow advection (i.e. at $z = a$ we assume $|\mathbf{u}| \ll v_0$ and $\delta\mathbf{E}\cdot\mathbf{E}_0 \ll E_0$).

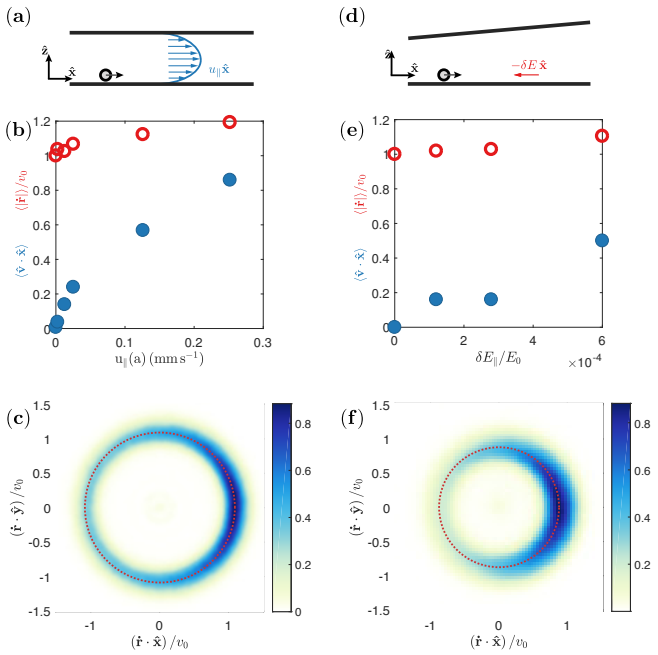

Figure 4.16 | (a) Sketch of a colloidal roller driven by a Poiseuille flow. (b) The speed of the roller is hardly modified by the flow (red open symbols), while the projection of the roller velocity on the flow direction $\hat{\mathbf{x}}$ monotonically increases with the flow (blue filled symbols). (c) PDF of the roller velocity for $u_\parallel = 0.12\,\mathrm{mm/s}$. Note that the distribution remains axisymmetric even at non-zero flow. (d) Sketch of a colloidal roller driven by an electric field. A longitudinal electric field $-\delta E\hat{\mathbf{x}}$ is applied by tilting the top electrode. (e) As in (b), the speed of the roller is hardly modified (red open symbols) while the projection of the roller velocity on the $\hat{\mathbf{x}}$-direction monotonically increases with δE evaluated at $z = a$ (blue filled symbols). (f) PDF of the roller velocity for $u_\parallel = 0.12\,\mathrm{mm/s}$. Note again that the distribution remains axisymmetric even at non-zero δE.

Let us stress that Eqs. (4.9) and (4.10) conform to our experimental findings with two additional experiments. In order to probe the response of colloidal rollers to fluid flows, we apply a Poiseuille flow in an obstacle-free channel, see Fig. 4.16a. We first confirm that the orientational response dominates over advection: the speed of the rollers, measured in a gas of noninteracting particles, hardly increases with the flow (open symbols in Fig. 4.16b). In contrast, as the fluid velocity increases we observe that: (i) the orientational distribution is increasingly asymmetric, Fig. 4.16c, and (ii) the projection of the average velocity on the flow direction increases monotonically, filled symbols in Fig. 4.16b. The same type of experiment is repeated with electrodes having a wedge geometry, see Figs. 4.16d. In this geometry, we add a homogeneous longitudinal perturbation to the electric field. Again, the roller speed is unmodified while the angular response is prominent, see Figs. 4.16e and 4.16f. This set of experiments unambiguously confirm that Eqs. (4.9) and (4.10) correctly describe the roller dynamics in external driving fields.

Effective Interactions with Cylindrical Obstacles

We finally exploit these results to derive the interaction rules with cylindrical obstacles (Eqs. (4.6) and (4.7) in the main text). Let us consider an obstacle located at the origin. At a point $\mathbf{r}$ both $\mathbf{u}_\parallel$ and $\delta\mathbf{E}$ are radial vectors, and therefore Eq. 4.10 can then be recast in the form:

$$\partial_t \hat{\mathbf{v}} = B(r)(1 - \hat{\mathbf{v}}\hat{\mathbf{v}}) \cdot \hat{\mathbf{r}}, \tag{4.11}$$

where $B(r) = \left(\mu_H \partial_z \mathbf{u}_\parallel - \mu_E \delta\mathbf{E}\right) \cdot \hat{\mathbf{r}}$. Projecting this equation on the x-axis readily yields Eq. 4.7. Again the specific expression of $B(r)$ is a complex function of the post shape and of the material properties. $B(r)$ is measured to be positive (repulsion) and to quickly decay with r, with a typical range ℓ set by the obstacle size, Fig. 4.9a. Therefore, for sake of simplicity, we approximate the expression of $B(r)$ by a step function of width ℓ. As a final comment we emphasize that Eqs. (4.6) (4.7), and (4.11) do not depend on the specifics of the roller-obstacle interactions and hold for any short-range repulsion mechanisms primarily acting on the particle orientation.

Article

Distortion and destruction of colloidal flocks in disordered environments

How do flocks, herds and swarms proceed through disordered environments? This question is not only crucial to animal groups in the wild, but also to virtually all applications of collective robotics, and active materials composed of synthetic motile units [64, 131, 4, 105, 102, 35, 118, 100, 117, 13, 91, 16, 73, 88]. In stark contrast, appart from very rare exceptions [25, 97, 96], our physical understanding of flocking has been hitherto limited to homogeneous media [76, 130, 21]. Here we explain how collective motion survives to geometrical disorder. To do so, we combine experiments on motile colloids cruising through random microfabricated obstacles, and analytical theory. We explain how disorder and bending elasticity compete to channel the flow of polar flocks along sparse river networks akin those found beyond plastic depinning in driven condensed matter [98]. Further increasing disorder, we demonstrate that collective motion is suppressed in the form of a first-order phase transition generic to all polar active materials.

We use the experimental system introduced in [13, 12], which consists in colloidal rollers powered by the so-called Quincke electro-rotation mechanism [95], see Methods and Supplementary Methods. The motile colloids experience both hydrodynamic and electrostatic interactions which promote alignement of their translational velocity [13, 12]. When the roller packing fraction, ρ, exceeds 3×10^{-3}, these polar interactions overcome rotational diffusion and macroscopic collective motion emerges [13, 12]. In the homogeneous slab geometry shown in Fig. 4.17a, a seven-millimeter-long flock spontaneously forms and cruises through a dilute ensemble of rollers moving isotropically, see Supplementary Video 1. The flock has a sharp front, a long tail, and endlessly cruises at a constant speed along the x-axis, bouncing back and forth on the confining walls. The flock speed $c_{\rm F}$ is found to be equal to the speed of an isolated roller $v_0 = 1.4 \pm 0.1\,\mathrm{mm\ s^{-1}}$.

Can flocks propagate in disorder media? How does this broken-symmetry phase survive to geometrical disorder? In order to answer these questions, we include randomly distributed circular obstacles of radius $a = 5\,\mu$m in the microfluidic channel. When the obstacle packing fraction $\phi_{\rm o}$ is small, collective

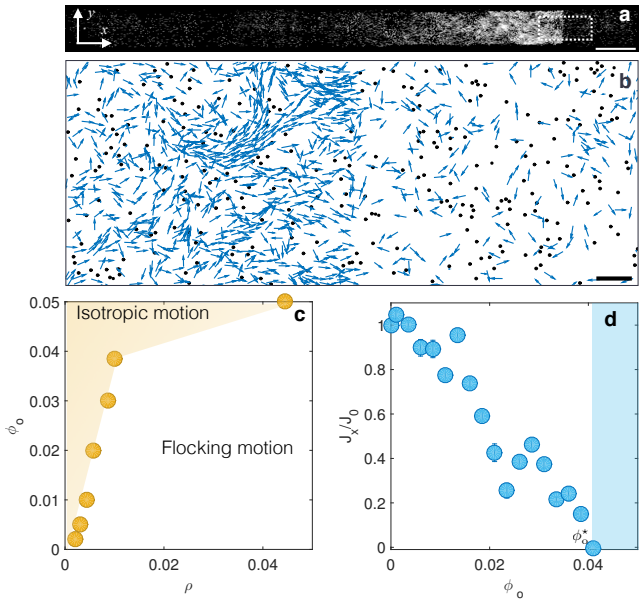

Figure 4.17 | **Emergence and suppression of collective motion. a**, Stitched fluorescent images of a 7 mm-long colloidal flock cruising in a rectangular channel. Total number of colloids: 8,500. Dotted rectangle: region in which the velocity measurements of panel **b** are performed. Scale bar: 1 mm. **b**, Close-up on the head of a colloidal swarm propagating past random obstacles (black dots). The arrows are located at the colloid positions and point along the orientation of their velocity. Obstacle packing fraction: $\phi_o = 2.45 \times 10^{-2}$. Scale bar: $100\,\mu$m. **c**, Flocking phase diagram in the (ρ, ϕ_o) plane. The symbols represent the variations of $\phi_o^\star$ with ρ. Error bars: smaller than the symbols (Defined as the difference between the minimal value of ρ above which flocking was observed and the maximal value below which isotropic motion only was observed). **d**, The x-component of the roller current is normalized by J_0 measured in an obstacle-free channel. J_x/J_0 is plotted as a function of the fraction of obstacles. Orientational order is suppressed in the shaded region. Error bars: 1 sd (17 different flocks).

motion still emerges according to the same nucleation and propagation scenario, see Fig. 4.17b and Supplementary Video 2. However as ϕ_o exceeds a critical value, $\phi_o^\star$, the obstacle collisions suppress any form of global orientational order and macroscopic transport. Correlated motion persists only at short scales, as illustrated in Supplementary Video 3. As expected, dense flocks are more robust to disorder and $\phi_o^\star$ monotonically increases with the roller fraction ρ, Fig. 4.17c.

In all that follows, the sole control parameter of our experiments is the obstacle fraction ϕ_o. The roller fraction is set to a constant value above the flocking threshold in a obstacle-free channel, $\rho = (1.02 \pm 0.06) \times 10^{-2}$. A natural order parameter for the flocking transition is the magnitude J_x of the roller current $\mathbf{J}(\mathbf{r}, t)$ projected on the x-axis, and averaged over time and space. Accordingly J_x monotonically decreases with ϕ_o and vanishes at $\phi_o^\star$, Fig. 4.17d.

Our first goal is to elucidate this loss of orientational order. To do so, we consider the evolution of the flock morphology along the propagation direction upon increasing disorder. This morphology can be equivalently captured by the variations of the local density, current, or polarization fields as demonstrated in a Supplementary Note. For sake of clarity we focus here on the roller current as the main observable. The flock speed c_F is unaltered by disorder and remains very close to the roller velocity for all $\phi_o < \phi_o^\star$, Fig. 4.18a. Therefore the time variations of $J_x(t) \equiv \langle \hat{\mathbf{x}} \cdot \mathbf{J}(x = 0, y, t) \rangle_y$, the longitudinal current averaged over the transverse direction, give an accurate description of the coarse-grained shape of the flocks, see Fig. 4.18b. Three important results are in order: the decrease of the flock length, L_F, echoes that of the global order parameter and vanishes rather smoothly at $\phi_o^\star$, Fig. 4.18c. However, as shown in Fig. 4.18d, the maximal current amplitude, A_F, undergoes a sharp drop and cancels discontinuously at $\phi_o^\star$. Finally, at $\phi_o^\star$, the flocks are intermittent: they repeatedly form and propagate steadily, before spontaneously vanishing and nucleating again. A featureless isotropic state coexists in time with a phase-separated flocking state where macroscopic excitations as large as 1 mm propagate in the channel. Altogether these three observations firmly evidence that disorder suppresses the flocking state in the form of a first-order non-equilibrium transition.

However, the obstacles do not merely reduce the extent of the flocks down to their extinction but also trigger qualitative changes in their inner structure. The snapshots of the roller current $\mathbf{J}(\mathbf{r}, t)$ at four subsequent times in Fig. 4.19a demonstrate that the flocks are strongly heterogeneous spatial patterns, see also Supplementary Video 4. We characterize the local flock morphology by introducing the current field $\boldsymbol{J}_{\text{flock}}(\mathbf{r}) = \langle \mathbf{J}(\mathbf{r}, t) \rangle_{t \in \Delta t_F}$ averaged over the time interval Δt_F taken by the flock to cross the observation window. At low ϕ_o, we observe that colloid-depleted wakes as large as $\sim 50\,\mu$m form downstream each obstacle, see Fig. 4.19b upper panel. However, as ϕ_o increases, the competition between alignment interactions and multiple-obstacle scattering, causes the redistribution of the roller current into a *static* river network, Fig. 4.19b. Virtually no collective motion occurs in the closed regions surrounded by the flowing rivers (black regions in Fig. 4.19b). The extent of the regions where the flow is suppressed can significantly exceed both the typical inter obstacle-distance and the depletion-wake size. Importantly, upon increasing ϕ_o, the river network becomes increasingly sparse and different from the region of space left around the mere superposition of uncorrelated wakes. Comparing the areas of these two very different geometries allows us to quantify the sparsity of the river networks in Fig. 4.19c. In addition, the networks also become increasingly tortuous as demonstrated by the fast increase of the orientational fluctuations of $\boldsymbol{J}_{\text{flock}}$ with ϕ_o in Fig. 4.19d. Above $\phi_o^\star$ orientational order survives

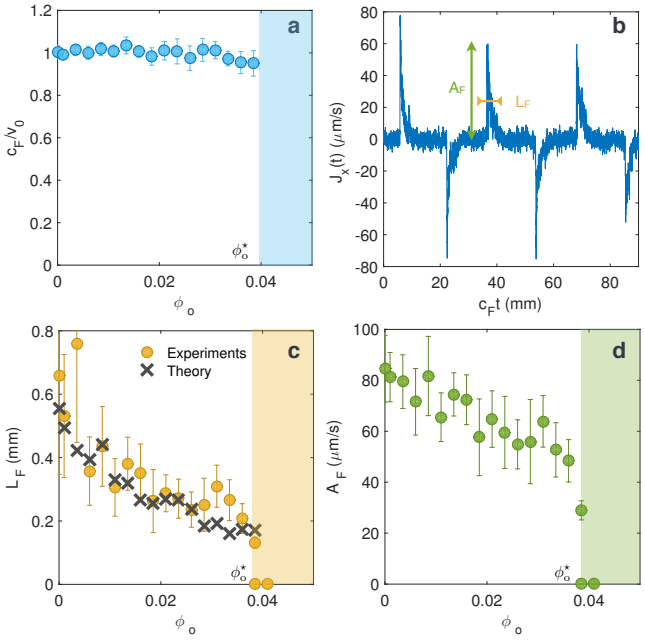

Figure 4.18 | **Flock morphology.** **a**, Flock speed normalized by the roller speed plotted as function of the obstacle fraction. Error bars: 1 sd (17 flocks per data point). **b**, Spatial variations of the longitudinal current. The shape of the steadily propagating flock is readily inferred from the temporal variations of the current averaged in a $25\,\mu\mathrm{m}\times 1\mathrm{mm}$ rectangular region. The flock width L_F is defined as the width of $J(t)$ at 2/3 of the maximal amplitude A_F. **c**, Yellow symbols: Flock length plotted versus the obstacle fraction (averaged over 17 different flocks). Error bars: 1 sd. Black symbols: Analytical prediction of the flock length, see Supplementary Note. Shaded region: isotropic phase. **d**, Maximal amplitude of the longitudinal current plotted versus the obstacle fraction (averaged over 17 different flocks). Shaded region: isotropic phase. Note that at $\phi_\mathrm{o}^\star$ both a flock state and a homogeneous isotropic state coexist. Error bars: 1 sd.

to disorder in finite and short-lived rivers. Any form of macroscopic transport is suppressed as these transient channels are isotropically distributed and do not percolate through the entire system, see Supplementary Video 3 and Supplementary Note. We close this discussion by stressing that these emergent river networks are strikingly similar to that encountered above the plastic depinning threshold when driving an ensemble of elastically-coupled particles through quenched disorder (from vortex lattices in type-II superconductors, to driven colloids and grains) [61, 53, 126, 69, 42, 125, 93, 98, 139].

In order to elucidate the physics underlying the suppression of collective motion and the emergence of channelling networks, we first need a quantitative description of the roller-obstacle interactions. As a roller approaches an obstacle its direction of motion is repelled at a distance yet its speed remains unchanged, Figs. 4.20a and 4.20b. The roller-obstacle and roller-roller repulsions stem from the same physical mechanisms [13]: a dielectric obstacle causes a local radial perturbation of the electric field $\mathbf{E} = E_0\hat{\mathbf{z}}$ used to power the Quincke rotation. As a result, a short-range repulsive *torque* reorients the roller velocity in the direction opposite to the obstacle, see Supplementary Note. This interaction has the same symmetry as that numerically considered in [25, 26]. The scattering plots shown in Fig. 4.20c and Supplementary Note, demonstrate that the repulsive torques are weak and short ranged. A head-on collision merely deflects the initial roller orientation by an angle of 60°. As a consequence, up to $\phi_o = 0.1$, the trajectories in the isotropic phase remain diffusive at long times, and are fully characterized by their rotational diffusivity D, which linearly increases with ϕ_o, Fig. 4.20d.

We can now account for the first-order nature of the flocking transition. The linear increase of D suggests simplifying the interactions between the rollers and the obstacles as uncorrelated binary collisions with random scatterers [26]. Within this Boltzmann approximation, we can generalize the kinetic theory valid at the onset of collective motion, which we introduced in [13]. We show in a Supplementary Note that the roller-obstacle and roller-roller interactions decouple. Increasing the obstacle fraction solely renormalizes the angular noise acting on the rollers, even when they interact in the flock phase. We then readily conclude that the transition to collective motion should belong to the very same universality class as the *first order* flocking transition found in all motile-spin models, starting from the seminal Vicsek model [129, 52, 110]. We quantitatively test the relevance of this scenario, by comparing in Fig. 4.18c, the measured flock length to our theoretical prediction for the shape of such non-linear excitations as detailed in a Supplementary Note. The unambiguous agreement confirms our theoretical explanation: weak quenched disorder triggers a generic Vicsek-like discontinuous transition from collective to isotropic motion.

However this appealing scenario cannot capture the emergence of channeling networks at high obstacle fractions. We now theoretically account for these spatial fluctuations by describing the strongly polarized region close to the flock front in the high ϕ_o regime. Therefore, rather than describing the obstacles as point-wise scatterers, we here consider small spatial fluctuations around a homogeneous obstacle density field. The resulting hydrodynamic equations, derived in a Supplementary Note, are

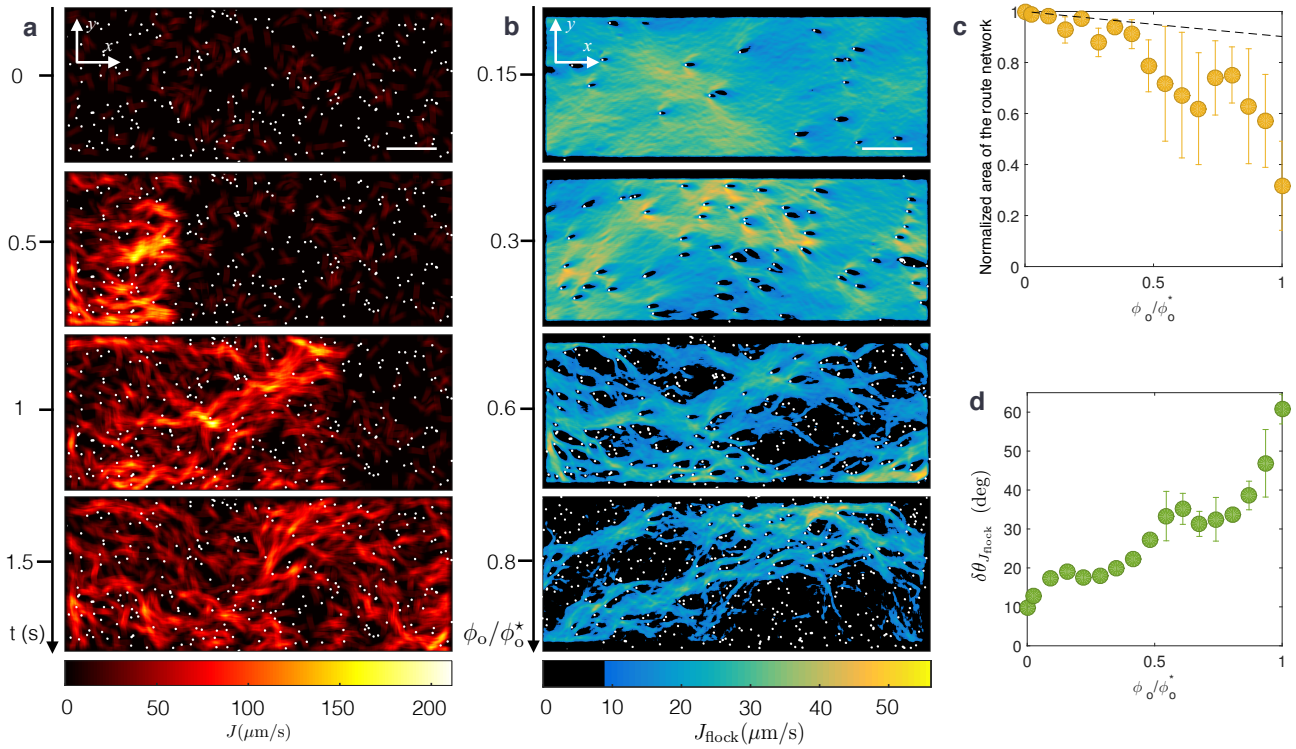

Figure 4.19 | **Flocking through river networks.** **a**, Four subsequent snapshots of the magnitude $|\mathbf{J}(x, y, t)|$ of the current field. Coarse graining over $25\,\mu$m $\times$ $25\,\mu$m bins. Time average over 0.05 s $\phi_o/\phi_o^\star = 0.5$. The rollers flow along preferred channels. Scale bar: $200\,\mu$m. **b**, Magnitude of the flock current J_{flock} plotted for four different obstacle packing fractions. At low ϕ_o colloid-depleted wakes form downstream the obstacles. As ϕ_o increases, a channel network forms and becomes increasingly sparse and tortuous. Coarse graining over $12.5\,\mu$m $\times$ $12.5\,\mu$m bins. Scale bar: $200\,\mu$m. **c**, Circles: Area of the flowing region normalized by the area of the observation window. Error bars: 1 sd (17 flocks per data point). Dashed line: area fraction of the region left around the superposition of spatially uncorrelated wakes. This quantity is computed knowing the fraction of space occupied by a random ensemble of patches having the shape of the wake formed downstream an isolated obstacle: $1 - \exp(-\rho_o a_{wake})$, where ρ_o is the obstacle density and a_{wake} the wake area [63]. **d**, The orientational fluctuations of $\mathbf{J}_{flock}$ sharply increase at the onset of flock destruction. They are defined as $\delta\theta^2_{J_{flock}} = A^{-1}\int\theta^2_{J_{flock}}(\mathbf{r})\,d\mathbf{r}$, where A is the area of the observation region, and $\mathbf{J}_{flock}/J_{flock} \equiv (\cos\theta_{J_{flock}}, \sin\theta_{J_{flock}})$. Error bars: 1 sd (17 flocks per data point).

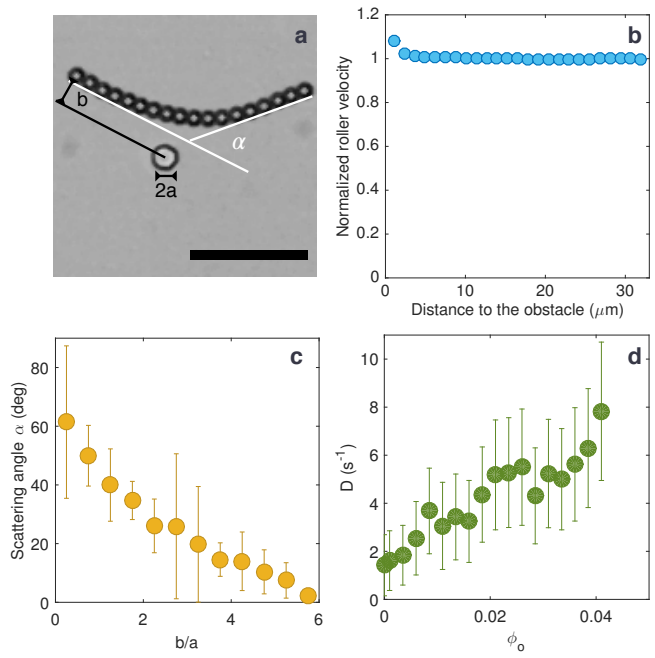

Figure 4.20 | **Roller-obstacle scattering.** **a**, Superimposed picture of a roller colliding an obstacle of radius $a = 5\,\mu$m. b is the impact parameter, α is the scattering angle. Time interval between each picture: 6.7 ms. $E_0/E_Q = 1.8$. Scale bar: 50 μm. **b**, Roller velocity normalized by v_0 as a function of the distance to the obstacle. Same parameters as in **a**. **c**, Scattering angle α plotted versus the normalized impact parameter b/a defined in **a**. $E_0/E_Q = 2$. Error bar: 1 sd. **d**, Rotational diffusivity defined as the decorrelation time of the roller velocity plotted as a function of the obstacle packing fraction, see Methods. $E_0/E_Q = 2$.

analogous to the Navier-Stokes equations for a polar active fluid:

$$\partial_t \rho + \nabla \cdot (\rho \mathbf{\Pi}) = 0, \tag{4.12}$$

$$\partial_t \mathbf{\Pi} + v_0 \mathbf{\Pi} \cdot \nabla \mathbf{\Pi} = \mathbb{P} \cdot [-\beta \nabla \rho + \alpha_2 \Delta (\rho \mathbf{\Pi}) + \gamma \tilde{\Delta} \cdot (\rho \mathbf{\Pi}) + \mathbf{F}_o], \tag{4.13}$$

where we introduce the local polarization $\mathbf{\Pi}(\mathbf{r}, t) \equiv \mathbf{J}(\mathbf{r}, t)/[v_0 \rho(\mathbf{r}, t)]$, and $\mathbb{P} = \mathbb{I} - \mathbf{\Pi}\mathbf{\Pi}$. The convective term on the l.h.s. of Eq. 4.13 stems from self-propulsion, $\beta \nabla \rho$ is a pressure term due to the repulsive interactions between the rollers, and α_2 and γ are the elastic constants of this polar liquid ($\tilde{\Delta}$ is an anisotropic second-order operator). Finally disorder is captured by the quenched force field $\mathbf{F}_o(\mathbf{r}) = -\beta_0 \nabla \phi_o(\mathbf{r})$ which focalizes the rollers in the valleys of an effective potential given by the local obstacle-density field $\phi_o(\mathbf{r})$. The linear response of $\mathbf{\Pi} = \hat{\mathbf{x}} + \delta\theta \hat{\mathbf{y}}$ provides a physical insight into the formation of sparse flowing channels. Within this approximation, the orientational fluctuations are readily computed from Eqs. (4.12) and (4.13):

$$\overline{|\delta\theta_{\mathbf{q}}|^2} = \frac{\beta_o^2 \phi_o}{v_o^2 + q_x^2 (\alpha_2 - \gamma)^2 \rho^2} \left(\frac{q_y}{q_x} \right)^2 \tag{4.14}$$

where $\bar{\cdot}$ stands for average over disorder, and $\mathbf{q}$ is a quasi longitudinal wave vector, see Supplementary Note. Eq. (4.14) establishes that the polarization fluctuations are set by the competition between random stirring, self-propulsion and bending elasticity. Importantly, orientational fluctuations increase at all scales with the number of obstacles. However, the bending stiffness $(\alpha_2 - \gamma)$ suppresses the small wavelength fluctuations required to explore the valleys of $\phi_o(\mathbf{r})$ which become increasingly branched and curved as the number of obstacles increases. This competition therefore selects a small subset of all the possible paths and consistently accounts for the formation of sparse and tortuous river networks upon increasing disorder. This scenario is further confirmed by experiments performed in periodic lattices of obstacles. By construction, these arrangements display minute density fluctuations. Therefore, the random stirring force in Eq. (4.13) is expected to be vanishingly small compared to an equally dense disordered medium. In agreement with our prediction, we find that no river network emerges in periodic lattices, see Supplementary Figure S7 and Supplementary Video 5. This scenario is expected to qualitatively hold beyond linear response. In addition, as it does not depend on the specifics of the colloidal rollers it must be relevant to any flock made of motile bodies obstructed by repelling obstacles, from living-creature groups to swarming robots to soft-active materials.

Methods

We use fluorescent Polystyrene colloids of diameter 4.8 μm dispersed in a 0.15 mol.L^{-1} AOT-hexadecane solution (Thermo scientific G0500). The suspension is injected in a wide microfluidic chamber made of two parallel glass slides coated by a conducting layer of Indium Tin Oxyde (ITO) (Solems, ITOSOL30, thickness: 80 nm) [13]. The two electrodes are assembled with double-sided scotch tape of homogeneous thickness (110 μm). The colloids are confined in a 1 mm $\times$ 15 mm channel, by walls made of a positive photoresist resin (Microposit S1818, thickness: 2 μm). Identical cylindrical obstacles of radius 5 μm made of the same material are included in the main channel. Their position is uniformly distributed with a density ρ_o, and the obstacle fraction is defined as $\phi_o = \pi a^2 \rho_o$ in the main text. Note that some

of the obstacles overlap. This geometry is achieved by means of conventional UV lithography. More details about the design of the microfluidic device are provided in the Supplementary Methods.

The Quincke electro-rotation of the colloids is controlled by applying a homogeneous electric field transverse to the two electrodes $\mathbf{E} = E_0\hat{\mathbf{z}}$. The field is applied with a voltage amplifier (TREK 609E-6). All the reported results correspond to an electric field $E_0 = 2E_Q$, where E_Q is the Quincke electro-rotation threshold $E_Q = 1\,\mathrm{V}/\mu\mathrm{m}$. All the measurements are performed when a steady state is reached for all the observables. The colloids are observed with a 7.2X magnification with a fluorescent Nikon AZ100 microscope. The movies are recorded with a CMOS camera (Basler ACE) at frame rates of 380 fps. The particles are detected to sub-pixel accuracy, and the particle trajectories and velocities are reconstructed using the Crocker and Grier algorithm [29]. Measurements are performed in a $1.22\,\mathrm{mm} \times 0.75\,\mathrm{mm}$ observation window. All measurements have been systematically repeated for 15 to 18 different flocks crossing the same field of view (different initial conditions). In addition we have used four different realization of the disordered arrangements of obstacles. The observation window was set close to the midpoint of the main channel where all the morphological quantities have reached their stationary values. Measurements performed further away from the walls yield identical results.

All the colloids roll at constant speed $v_0 = 1.4 \pm 0.1\,\mathrm{mm\ s^{-1}}$. When isolated, their direction of motion freely diffuses on the unit circle with a diffusivity $D = 1.6 \pm 0.1\,\mathrm{s^{-1}}$. D is defined as the exponential decorrelation rate of the velocity orientation in a isotropic phase, $\langle \hat{\mathbf{v}}_i(0) \cdot \hat{\mathbf{v}}_i(t) \rangle_i \sim \exp(-Dt)$, where $\hat{\mathbf{v}}_i$ is the velocity orientation of the i^{th} roller.

The current field $\mathbf{J}(\mathbf{r}, t)$ is computed by summing the instantaneous roller velocities in $12.5\,\mu\mathrm{m} \times 12.5\,\mu\mathrm{m}$ binning windows. The flock current $\mathbf{J}_{\mathrm{flock}}(\mathbf{r})$ is computed by averaging $\mathbf{J}(\mathbf{r}, t)$ over time. The flowing-path network is defined as the ensemble of points where J_{flock} exceeds $11\,\mu\mathrm{m/s}$. This value has been chosen as the typical average current in the wake left behind an isolated obstacle. None of the results discussed in this letter qualitatively depends on this specific threshold value. The current-free regions referred to in the main text are associated with local current value smaller than this threshold (black areas in Fig. 4.19b).

Supplementary Informations

I Supplementary Methods

We sketch the microfluidic device used to handle the colloidal rollers in Fig. 4.21. The polysterene (PS) colloid solution is flown in a one-centimeter wide channel made of double sided tape. The thickness of the adhesive film (dark grey) sets the gap between the two electrodes: $110\,\mu$m. Both the rectangular chamber and the cylindrical obstacles are made of an insulating resin (blue color). The pattern is achieved using conventional UV lithography. The obstacles are located at random positions with possible overlap as seen in the close-up picture of a colloid-free channel. The thickness of the insulating resin is about $2\,\mu$m. The diameters of the colloids and of the obstacles are respectively $4.8\,\mu$m and $10\,\mu$m. Due to the local perturbation to the orientation and magnitude of the electric field in the vicinity of the insulating walls and obstacles, the colloids are electrostatically repelled from the regions covered by the resin patterns.

II Supplementary Note 1: Flocking-through-disorder experiments

II.i Global flock morphology: current, density and polarization fields

A flock, by definition, corresponds to a region of space where orientational order exists. The amplitude of a flock, and its extent along the propagation direction, can be measured from three different observables: the local current $J_x(\mathbf{r},t)$ introduced in the main text, the local packing fraction of rollers $\rho(\mathbf{r},t)$, and the local polarization field $\Pi(\mathbf{r},t)$ defined as $J_x(\mathbf{r},t) \equiv v_0\rho(\mathbf{r},t)\Pi(\mathbf{r},t)$. Π quantifies the local amount of orientational order regardless of the local area fraction of rollers $\rho(\mathbf{r},t)$. As shown in Fig. 4.22 their time variations averaged over the channel width convey the same information about the flock morphologies. More quantitatively, the flock length, and the maximal amplitude measured from these three observables are plotted versus ϕ_o in Fig. 4.22. The trends are perfectly consistent. The discontinuity of the amplitude drop at $\phi_o^\star$ is even extremely pronounced for the polarization variable.

II.ii Isotropy of the current field above $\phi_o^\star$

Above $\phi_o^\star$, by definition, all the global order parameters quantifying orientational order vanish. However, the rollers do not merely form an uncorrelated gaz phase. As emphasized in the main text, collective motion locally persists along extended yet finite paths. However these paths do not allow any macroscopic transport as they are isotropically oriented and only have a finite life time. The global isotropy of the current in this disordered regime is demonstrated in Fig. 4.23. In Figs. 4.23a and 4.23b, we first recall the typical morphology of the flock-current field below and above $\phi_o^\star$. Above $\phi_o^\star$, $\mathbf{J}_{\rm flock}$ is defined as $\mathbf{J}_{\rm flock}(\mathbf{r}) = \langle \mathbf{J}(\mathbf{r},t)\rangle_{t\in\Delta t_F}$, where the time interval Δt_F is kept equal to that measured at $\phi_o^\star$. In Figs. 4.23c and 4.23d, we plot the flock-current correlation function: $\langle \mathbf{J}_{\rm flock}(\mathbf{r}')\cdot\mathbf{J}_{\rm flock}(\mathbf{r}'+\mathbf{r})\rangle_{\mathbf{r}'}$. Whereas they are clearly anisotropic in the flocking regime, all orientational features are lost in the high-disorder limit.

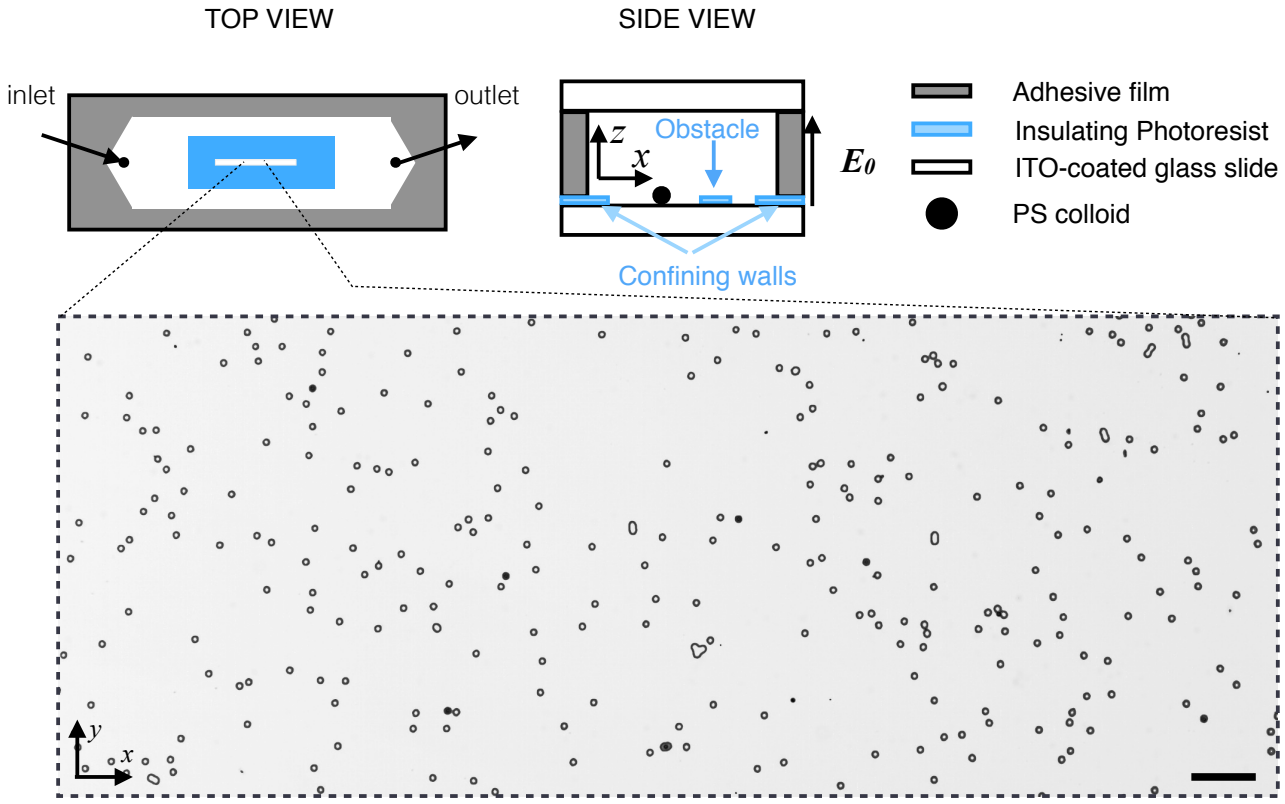

Figure 4.21 | **Sketch of the microfluidic device. Top view.** A one-centimeter wide channel is used to flow the colloidal solution. The rectangular chamber is delimited by an insulating lithographied resin, and includes cylindrical obstacles of radius 5 microns on the bottom ITO-coated glass slide. The picture of a colloid-free device shows a typical distribution of obstacles. Scale bar: 100 μm. **Side view.** The colloids roll on the bottom electrode, the obstacles electrostatically repel the approaching rollers. An adhesive film (double-sided scotch tape) sets the gap between the electrodes.

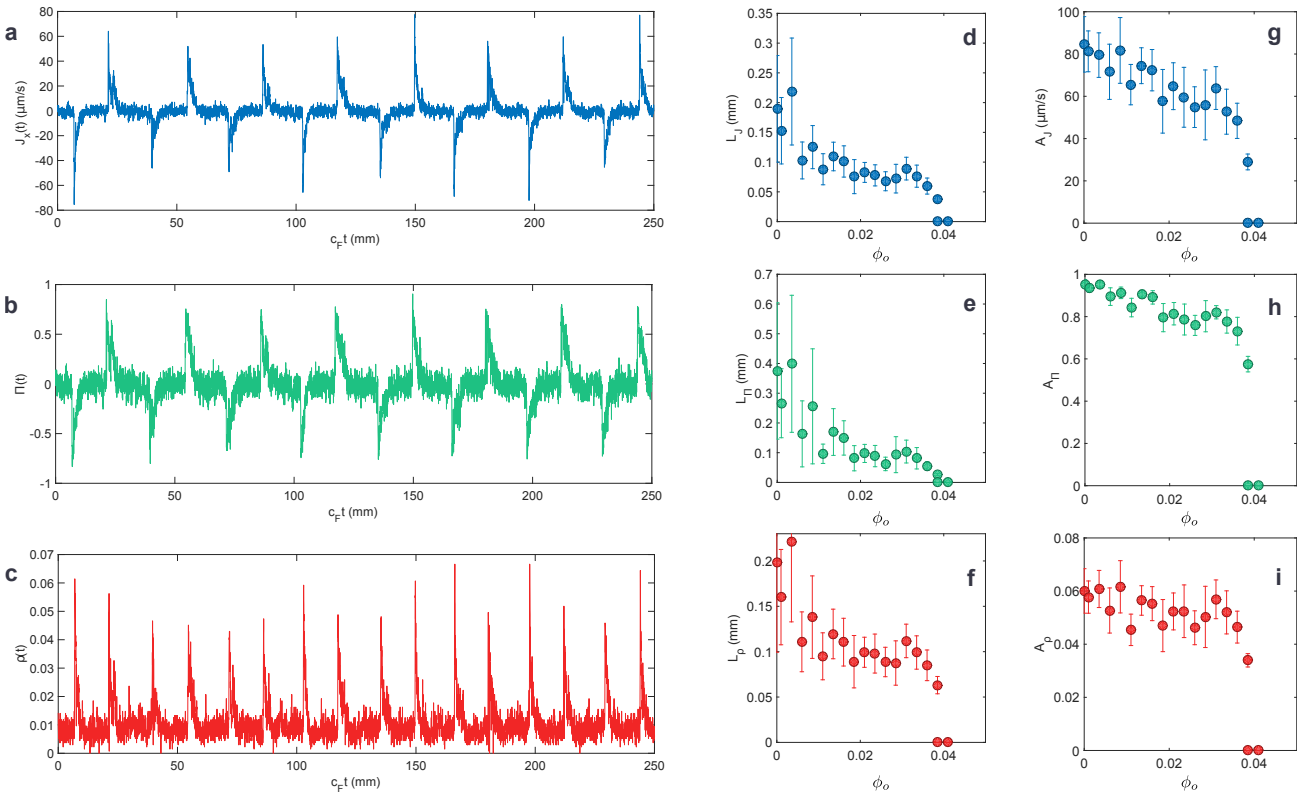

Figure 4.22 | **Three different probes of orientational order: current, polarization and density.** **a**, Time variations of the local current averaged over the microfluidic-channel width. Note that the distance between two subsequent peaks is not a constant as the observation window is not perfectly centered on the microfluidic channel. **b**, Time variations of the local polarization averaged over the microfluidic-channel width. **c**, Time variations of the local roller density averaged over the microfluidic-channel width. **d**, Flock length measured from the current signal as defined in the main text plotted versus the obstacle fraction. **e**, Same plot for the flock length measured from the polarization signal. **f**, Same plot for the flock length measured from the density signal. **g**, Flock-current amplitude plotted versus the obstacle fraction. **h**, Same plot for the flock-polarization amplitude. **h**, Same plot for the flock-density amplitude.

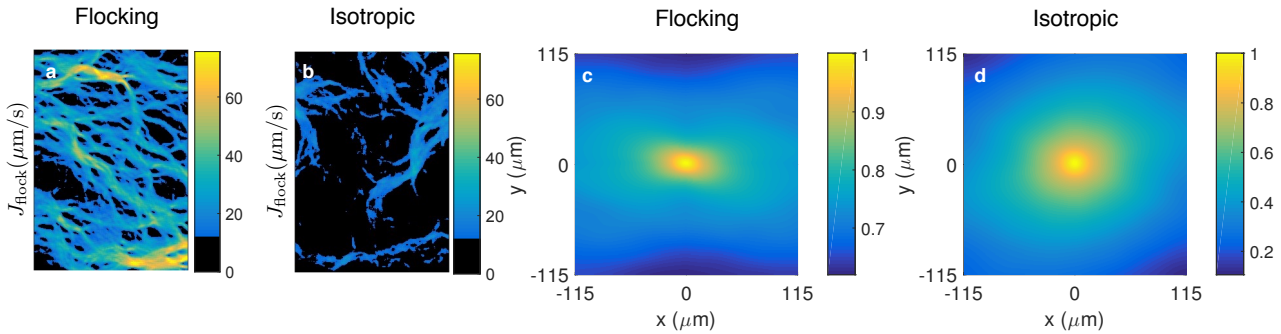

Figure 4.23 | **Current isotropy above $\phi_o^\star$.** **a**, Magnitude of the flock current $J_{\rm flock}$ corresponding to $\phi_o/\phi_o^\star = 0.9$. Spatial coarse graining over $12.5\,\mu$m $\times$ $12.5\,\mu$m bins. **b**, Magnitude of the flock current $J_{\rm flock}$ corresponding to $\phi_o/\phi_o^\star = 1.1$. Spatial coarse graining over $12.5\,\mu$m $\times$ $12.5\,\mu$m bins. The current is averaged over the same time interval as in **a**. **c**, Spatial decay of the normalized flock-current correlations for $\phi_o/\phi_o^\star = 0.9$. The current correlations are anisotropic. **d**, Spatial decay of the normalized flock-current correlations for $\phi_o/\phi_o^\star = 1.1$. The current correlations are isotropic.

II.iii Obstacle-Roller Scattering and Effective Diffusion

Fig. 4.24a shows six scattering diagrams corresponding to six different electric-field amplitudes. The scattering angle is plotted versus the impact parameter b normalized by the obstacle radius a, as defined in Fig. 4a in the main document. The range of the obstacle-roller interaction is defined as the value of the impact parameter where the scattering angle vanishes. This range hardly depends on the field magnitude. However, repeating the same experiments with obstacle of increasing size, we find that the repulsion range is proportional to the obstacle radius, Fig. 4.24b.

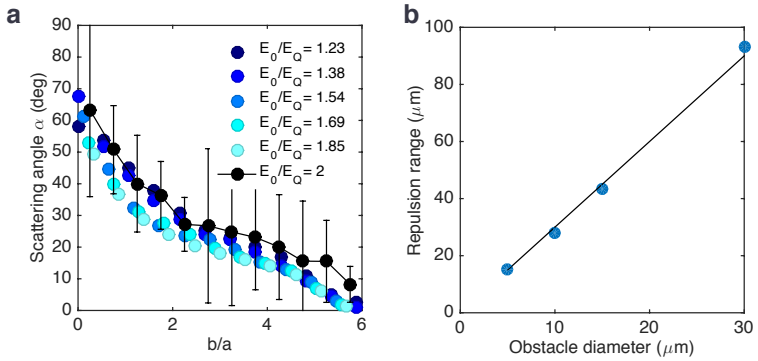

Figure 4.24 | **Single-roller scattering.** **a**, Scattering angle plotted as a function of the normalized impact parameter for six different field amplitudes. Error bars: 1sd, shown only for $E_0/E_Q = 2$ for sake of clarity. **b**, Circles: repulsion range plotted as a function of the obstacle diameter. Solid line: straight line of slope 3.

III Supplementary Note 2: Flocking-through-disorder theory

III.i Equations of motion of interacting colloidal rollers in a homogeneous media

Starting from the Stokes and Maxwell equations, we established in [13] the equations of motion of colloidal particles propelled by the Quincke mechanism. After lengthy algebra, they can be recast into a compact form. The rollers propel at a constant speed, undergo rotational diffusion with a diffusivity D, and interact via effective torques deriving from the angular potential $\mathcal{H}(\mathbf{r};\hat{\mathbf{p}}_i,\hat{\mathbf{p}}_j)$:

$$\partial_t \mathbf{r}_i(t) = v_0 \hat{\mathbf{p}}_i, \tag{4.15}$$

$$\partial_t \theta_i(t) = -\partial_{\theta_i} \sum_{j\neq i} \mathcal{H}(\mathbf{r}_i - \mathbf{r}_j;\hat{\mathbf{p}}_i,\hat{\mathbf{p}}_j) + \sqrt{2D}\xi_i(t), \tag{4.16}$$

where $\mathbf{r}_i(t)$ and $\hat{\mathbf{p}}_i(t) = (\cos\theta_i(t), \sin\theta_i(t))$ are respectively the position and the orientation of the i^{th} roller. The $\xi_i(t)$s are delta-correlated Gaussian white noises of unit variance, and the effective interaction reads:

$$\mathcal{H}(\mathbf{r};\hat{\mathbf{p}}_i,\hat{\mathbf{p}}_j) = A(r)\hat{\mathbf{p}}_i\cdot\hat{\mathbf{p}}_j + B(r)\hat{\mathbf{p}}_i\cdot\mathbf{r} + C(r)\hat{\mathbf{p}}_j\cdot(2\mathbf{rr}-\mathbb{I})\cdot\hat{\mathbf{p}}_i. \tag{4.17}$$

$A(r)$, $B(r)$ and $C(r)$ decay exponentially over a distance H of the order of the microfludic-channel height. They all have the same functional form: $X(\mathbf{r}) = \tau_X^{-1} r^{-n_X}\exp(-r/H)$, with $X = A$, B, C and $n_X > 3$. The characteristic relaxation times τ_X are all of the order $\sim a/v_o$ where a is the colloid radius. Their quantitative expressions and the estimate of their strengths are provided in [13, 12]. We neglect here an additional genuinely long-range interaction associated with a very small coupling constant and which plays no role in the following discussions given the system sizes we consider.

The three terms of the effective potential are *not* specific to colloidal rollers, rather they correspond to the first terms of a systematic multipolar expansion of any effective-interaction potential [18]. The physical meaning of these three terms is clear: $A(r)$ quantifies the strength of the polar interaction promoting the alignment of the roller velocities. This interaction stems from hydrodynamic and electrostatic interactions as well. $B(r)$ corresponds to repulsive interactions. This term is minimized when the direction of the roller i points in the direction opposite to $\mathbf{r}_j - \mathbf{r}_i$. This interaction stems from electrostatics. $C(r)$ combines both hydrodynamic and electrostatic contributions. This third term indicates that the roller i is also prone to align its velocity with a dipolar field centered on the roller j.

III.ii Roller-obstacle interactions

Let us now consider an insulating circular post located at $\mathbf{r} = 0$. This dielectric material deforms the external electric field $\mathbf{E} = E_0\hat{\mathbf{z}}$ used to trigger the Quincke rotation of the colloids. The calculation of the electric-field disturbance induced by a dielectric immersed in a conducting fluid is provided in [13]. Regardless of its specific form, we know that the range of the perturbation is screened over a scale comparable to the distance H between the two electrodes. In addition the obstacle being axisymmetric the perturbation must be radial in the xy-plane, and point toward the center of the dielectric obstacle lithographed on the positive electrode, Fig. 4.25.

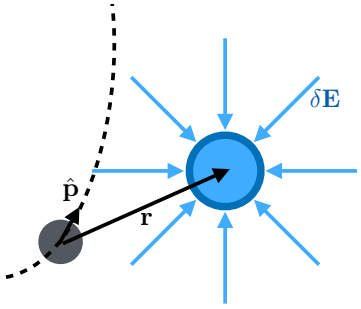

Figure 4.25 | **Single-roller scattering.** Sketch of a roller (small grey disc) interacting with an obstacle (large blue disc). Dotted line: trajectory. $\delta\mathbf{E}$: in-plane component of the electric field perturbation.

An effective torque of the form $\partial_\theta(\hat{\mathbf{p}}\cdot\mathbf{E})$ aligns the roller orientation in the direction opposite to the xy-components of the electric field. Therefore the equations of motion of an isolated roller interacting with a cylindrical obstacle are:

$$\partial_t\mathbf{r}(t) = v_0\hat{\mathbf{p}}, \tag{4.18}$$
$$\partial_t\theta(t) = -\partial_\theta\mathcal{H}_\mathrm{o}(\mathbf{r};\hat{\mathbf{p}}), \tag{4.19}$$

where the effective repulsion potential has the same form as the roller-roller repulsion:

$$\mathcal{H}_\mathrm{o}(\mathbf{r};\hat{\mathbf{p}}) = B_\mathrm{o}(r)\hat{\mathbf{p}}\cdot\mathbf{r}. \tag{4.20}$$

$B_\mathrm{o}(r)$ has the same form as $B(r)$ defined in the previous section: $B_\mathrm{o}(r)\sim\exp(-r/H)/r^4$. The above equations are of course complemented by a hard-core repulsive interaction between the rollers and the insulating post.

III.iii Flocking transition in weak quenched disorder

Kinetic theory

We first outline how to construct the hydrodynamic equations ruling the temporal evolution of the density and current fields in the presence of a dilute ensemble of weak scatterers. We use here a conventional kinetic-theory framework reviewed e.g. in [76]. We first write a conservation equation for the one-point distribution $\psi(\mathbf{r},\theta,t)$, i.e. the probability to find a particle at position $\mathbf{r}$ with an orientation $\hat{\mathbf{p}} = (\cos\theta,\sin\theta)$:

$$\partial_t\psi(\mathbf{r},\theta,t) + v_0\hat{\mathbf{p}}\cdot\nabla\psi(\mathbf{r},\theta,t) - D\partial_\theta^2\psi(\mathbf{r},\theta,t) = -\partial_\theta\mathcal{J}_\mathrm{int}(\mathbf{r},\theta,t) + \mathcal{S}_\mathrm{o}(\mathbf{r},\theta,t) \tag{4.21}$$

For interaction-free particles moving in a homogeneous media, the r.h.s of the above equation vanishes and ψ is merely advected due to self-propulsion, and diffuses in the θ direction due to the angular noise acting on the rollers' direction. The angular current $\mathcal{J}_\mathrm{int}$, and $\mathcal{S}_\mathrm{o}(\mathbf{r},\theta,t)$ account for the roller-roller and the roller-obstacle interactions respectively. Starting from the microscopic equations Eqs. (4.15),(4.16) and (4.17), we derived the functional form of $\mathcal{J}_\mathrm{int}(\mathbf{r},\theta,t)$ in [13]. Briefly, as the range of the effective

potential $\mathcal{H}$ is of the order of 40 colloid radii, in a homogeneous isotropic phase, each colloid interacts on average with ~ 20 neighbors. This large number is even a decade larger when a flock forms, which suggests using a mean field description to establish the functional form of $\mathcal{J}_{\rm int}$. More precisely, assuming that the two points correlation function factorizes: $\psi^{(2)}(\mathbf{r},\hat{\mathbf{p}};\mathbf{r}',\hat{\mathbf{p}}') = \psi(\mathbf{r},\hat{\mathbf{p}})\psi(\mathbf{r}',\hat{\mathbf{p}}')$ and vanishes for $|\mathbf{r}-\mathbf{r}'| < 2a$ (to account for the finite size of the rollers), $\mathcal{J}_{\rm int}$takes the form:

$$\mathcal{J}_{\rm int} = -\psi(\mathbf{r},\theta)\int_{|\mathbf{r}-\mathbf{r}'|>2a} \mathrm{d}\theta'\mathrm{d}\mathbf{r}'\psi(\mathbf{r}',\hat{\mathbf{p}}')\partial_\theta\mathcal{H}(\mathbf{r}-\mathbf{r}';\theta,\theta') \tag{4.22}$$

Two different approximations are used to compute the $\mathcal{S}_{\rm o}$ term in Eq. (4.21). Let us first ignore the specifics of the roller obstacle interactions, and consider a simplified description of the scattering process. Following [26], we focus first on the asymptotic limit of an infinitely dilute ensemble of uncorrelated scatterers, and use a Boltzmann-like approximation. We make the molecular chaos hypothesis and restrain ourselves to binary collisions. Within this framework, at large scales, scattering can be described without loss of generality as a change in the orientation θ by an increment $\pm\epsilon$ upon collision. Provided that the persistence length of a free roller exceeds the typical inter-obstacle distance, which is the case in our experiments, collisions occur at a rate $2v_0\phi_{\rm o}a/(\pi a_o^2)$ which yields in the small-ϵ limit:

$$\mathcal{S}_{\rm o} = (D'\phi_{\rm o})\partial_\theta^2\psi(\mathbf{r},\theta,t), \tag{4.23}$$

where $D' = \frac{1}{2}v_0 a\epsilon^2/(\pi a_o^2)$. The obstacle interactions renormalize the angular diffusivity of the particle which increases in an affine fashion with $\phi_{\rm o}$ in agreement with our experimental findings in the isotropic phases:

$$D(\phi_{\rm o}) = D + D'\phi_{\rm o} \tag{4.24}$$

At large scales, the particle motility converts the collisions with a quenched ensemble of scatterers into a time-dependent angular noise. This scenario is the exact analogous of that observed in a dilute Lorentz gaz where ballistic particles undergo elastic collisions on fixed scatterers.

Given the mean-field description for the roller interactions, and the Boltzmann description of the obstacle scattering, the two types of interactions decouple in Eq. (4.21). Consequently, Eqs. (4.21), (4.22), and (4.23) suggest that the emergence, and suppression, of collective motion in dilute disordered media should belong to the same first-order universality class as the Vicsek transition between a gas and an orientationally ordered state. We recall that the seminal Vicsek model concerns a 2D ensemble of motile spins interacting via ferromagnetic interactions competing with a time-dependent angular noise [129, 52]. Upon decreasing the noise amplitude, the spins undergo a *first order* transition from an isotropic to a polar state, see e.g. [52, 110] and references therein. The first order nature of the transition arises from the nucleation and subsequent steady propagation of nonlinear band-like excitations akin to the colloidal flocks reported in this letter. The global suppression of polar order found in our experiments is therefore strongly expected to be triggered by the increase of rotational diffusion resulting from random scattering processes. We further confirm this hypothesis below, by constructing a hydrodynamic description of the roller flocks cruising through disorder.

Hydrodynamic theory

In order to confirm the relevance of our main hypothesis, namely the Boltzmann approximation to account for interaction with the random scatterers, we first derive the equations of motion of the

hydrodynamic variables $\rho(\mathbf{r},t) \equiv \int \psi(\mathbf{r},\theta)\,\mathrm{d}\theta$ and $\mathbf{J}(\mathbf{r},t) \equiv \int \hat{\mathbf{p}}(\theta)\,\psi(\mathbf{r},\theta)\mathrm{d}\theta$ close to an isotropic state. Within this hydrodynamic framework we are able to make a quantitative prediction regarding the extent of the flocking patterns and to compare them to our experimental findings.

We complement mass conservation:

$$\partial_t \rho(\mathbf{r},t) + \nabla \cdot \mathbf{J}(\mathbf{r},t) = 0, \tag{4.25}$$

by the time evolution of the current field. Multiplying Eq. (4.21) by $\hat{\mathbf{p}}$, averaging over ψ and keeping only the leading order terms in a gradient expansion yields a relation between ρ, $\mathbf{J}$ and the local nematic tensor $\mathbf{Q}$, defined as: $\rho\mathbf{Q} = \langle \hat{\mathbf{p}}\hat{\mathbf{p}} - \frac{1}{2}\mathbb{I}\rangle$, see [13] for more technical details, or [76]:

$$\partial_t \mathbf{J} + v_0^2 \nabla \cdot \left[\rho\left(\mathbf{Q} + \frac{1}{2}\mathbb{I}\right)\right] = -D(\phi_\mathrm{o})\mathbf{J} + \alpha_1 \rho(\mathbb{I} - 2\mathbf{Q})\cdot\mathbf{J} - \beta\frac{v_0}{2}(\mathbb{I} - 2\mathbf{Q})\cdot\rho\nabla\rho \tag{4.26}$$

where α_1 and β are hydrodynamic coefficients defined by the spatial averages of $A(r)$ and $B(r)$, defined in Eq. (4.17). A self-consistent hydrodynamic description of the polar active fluid, requires expressing the local nematic tensor as a function of ρ and $\mathbf{J}$. As we are here interested in describing the onset of collective motion, we use a closure relation valid close to an isotropic state. Following the approach reviewed in [94] we write down a dynamical equation for the $\mathbf{Q}$ field, ignore its temporal variations, discard higher order angular multipoles of the distribution function and consistently restrain ourselves to the lowest order gradient terms. We are then left with a generic form akin to the Toner and Tu equation originally inferred from symmetry considerations [122]:

$$\begin{aligned}\partial_t \mathbf{J} + \frac{3\alpha_1}{8D(\phi_o)}\mathbf{J}\cdot\nabla\mathbf{J} = &\left[\alpha_1\rho - D(\phi_o) - \frac{\alpha_1^2}{2v_0^2 D(\phi_o)}J^2\right]\mathbf{J} - \frac{v_0}{2}\left(v_0 + \beta\rho\right)\nabla\rho \\ &- \frac{5\alpha_1}{8D(\phi_o)}(\nabla\cdot\mathbf{J})\mathbf{J} + \frac{5\alpha_1}{16D(\phi_o)}\nabla(J^2) + \frac{\alpha_1\beta}{2v_0 D(\phi_o)}(\nabla\rho\cdot\mathbf{J})\mathbf{J} + O(\nabla^2)\end{aligned} \tag{4.27}$$

We shall stress that all the hydrodynamic coefficients are computed from the microscopic equation of motion and can be quantitatively measured, or estimated, from our experiments [12]. This equation is the analogous of that derived in [13], replacing the bare rotational diffusivity D, by $D(\phi_\mathrm{o}) = D + D'\phi_\mathrm{o}$.

Flock morphologies

In order to compute the shape of the colloidal flocks we look for localized solutions of Eqs. (4.25) and (4.27) which are homogeneous along the y-direction and steadily propagate along the x-direction with a velocity c: $\mathbf{J}(\mathbf{r},t) = J(x-ct)\hat{\mathbf{x}}$, $\rho(\mathbf{r},t) = \rho(x-ct)$. By doing so, mass conservation, Eq. (4.25), takes the form of a local relation between ρ and $\mathbf{J}$

$$\rho(z) = \rho_\infty + \frac{\mathbf{J}(z)}{c} \tag{4.28}$$

where $z = x - ct$, and ρ_∞ is the fraction of active particles in the isotropic region away from the flock. Similarly, (4.27) reduces to a non-linear ordinary differential equation:

$$\mathcal{D}[J]\ddot{J}(z) + \mathcal{F}[J]\dot{J}(z) + \mathcal{H}[J]J(z) = 0, \tag{4.29}$$

where

$$\mathcal{H}[J] = [\alpha_1\rho_\infty - D(\phi_o)] + \frac{\alpha_1}{c}J - \frac{\alpha_1^2}{2v_0 D(\phi_o)}J^2, \tag{4.30}$$

$$\mathcal{F}[J] = \left[c - \frac{v_0}{2c}\left(v_0 + \beta\rho_\infty\right)\right] - \left[\frac{3\alpha_1}{8D(\phi_o)} + \frac{v_0\beta}{2c^2}\right]J + \frac{\alpha_1\beta}{2v_0 c D(\phi_o)}J^2. \tag{4.31}$$

The second-order term $\mathcal{D}[J]\ddot{J}(z)$ comes from the $\mathcal{O}(\nabla^2)$ terms in Eq. (4.27), it has a lengthy expression which we do not report here as it is useless to compute the flock length.

Eq. (4.29) can be readily written in the form of a dynamical system, and describing the shape of propagating patterns amounts to describe the cycles of this dynamical system, i.e. the periodic solutions of (4.29). We showed in [19, 109] that homoclinic cycles correspond to solitonic band-shape flocks. The typical extent of these localized excitations is estimated by looking at the linear stability of Eq. (4.29) around a homogeneous and isotropic state ($J(z) = 0$). As first pointed out in [5], when propagating solutions exist the resulting linear system has one stable and one unstable eigenvalues corresponding respectively to the width of the flock front, and to the extent of its long tail which is a good approximation of the flock length L_F, see Fig. S2. In the weakly polarized tail the second-order term in Eq. (4.29) remains much smaller than the two others, consistently with the quasi isotropic approximation used to derive Eq. (4.27). Therefore, after straightforward algebra, discarding subdominant corrections in $\mathcal{D}[0]$, we predict the relation:

$$L_\mathrm{F} = \frac{v_0}{\alpha_1}\left[\frac{\frac{c}{v_0} - \frac{v_0}{2c}(1 + \frac{\beta\rho_\infty}{v_0})}{\rho_\mathrm{c}(\phi_\mathrm{o}) - \rho_\infty}\right], \tag{4.32}$$

where $\rho_\mathrm{c}(\phi_\mathrm{o}) = (D + D'\phi_\mathrm{o})/\alpha_1$. The above equation relates the flock length, L_F, the area fraction in the surrounding gaz phase, ρ_∞, the strength of the roller repulsion, β, and of the alignment terms, α_1 at the hydrodynamic level. $\rho_\mathrm{c}(\phi_\mathrm{o})$ compares the strength of the alignment interactions to the angular diffusion which impedes orientational order. It corresponds to the roller fraction above which Eq. (4.27) would predict a mean-field transition toward collective motion (i.e. ignoring all the gradient terms). Eq. (4.32) indicates that the macroscopic band length results from the amplification of the microscopic length scale v_0/α_1 (of the order of the colloid size) by a factor $[\rho_\mathrm{c}(\phi_\mathrm{o}) - \rho_\infty]^{-1}$ which can be arbitrarily large as the roller fraction in the gas approaches ρ_c.

In order to test this prediction, we measure: (i) c which is equal to v_0 in all our experiments, Fig. 2a. (ii) D' from the slope of the linear increase of D with ϕ_o in Fig. 4d, and (iii) the density ρ_∞ in the isotropic phase through which the flocks propagate. In addition, in [12], we measured the value of α_1 from the continuous bifurcation from a gas to a vortex state in circular confinements, and found $\alpha_1 = 3 \times 10^{-3}\,\mathrm{s}^{-1}$. We are hence left with the theoretical prediction with no free fitting parameter. In Fig. 2.c, which we reproduce below, we find an excellent agreement with our experimental measurements.

Given the number of simplifications needed to derive the hydrodynamic model, this agreement confirms the robustness of our results, and our main conclusion: the emergence and suppression of collective motion induced by a dilute ensemble of obstacles is a genuine non-equilibrium first order transition. This transition falls in the same universality class as the flocking transition of the Vicsek type.

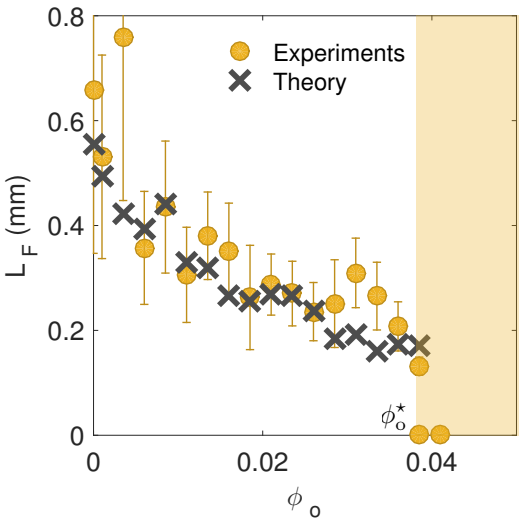

Figure 4.26 | **Variations of the flock length with the obstacle fraction.** Comparison of the measured flock length to the theoretical prediction given by Eq. (4.32).

III.iv Emergence of flowing-channel networks

The theory introduced in the previous section is unable to capture the inner structure of the colloidal flocks. The sole spatial feature of disorder included in this 0^{th} order model is the mean obstacle fraction. However, Eq. (4.27) could be modified to account for the spatial heterogeneities of the obstacle distribution by replacing ϕ_o by its local value $\phi_o(\mathbf{r})$ defined at a scale much larger than the typical inter-obstacle distance. This modified model would endow the rollers with a higher rotational diffusivity, hence a smaller translational diffusivity, in the regions where the obstacle density is large. A direct consequence would be the accumulation of the colloids in the regions where the obstacles are the most concentrated. This prediction is in total contradiction with our experimental observations. In order to go beyond this oversimplified picture, we need to more accurately account for the impact of the spatial heterogeneity of disorder.

Hydrodynamics of a strongly polarized flock of rollers: homogeneous media

A major limitation of the current kinetic theories of polar active matter is that they fail in providing a unified hydrodynamic description valid at all densities and polarizations. As a matter of fact they all rely on closure approximations which are either valid in the weakly polarized or, conversely, in the strongly polarized limit. As we now aim at describing the spatial structure of the flock front which is strongly polarized, Fig. 4.22, we use a closure relation which is different from that used in the previous section to model nearly isotropic states. We neglect the possible local melting of orientational order and solely focus on the orientational fluctuations of the polarization field $\mathbf{\Pi} = \mathbf{J}/(v_0\rho)$ close to the head of the flock. In fact, we make the following ansatz for the one-point function $\psi(\mathbf{r},\theta,t) = \rho(\mathbf{r},t)\delta(\hat{\mathbf{p}} - \mathbf{\Pi}(\mathbf{r},t))$. This ansatz implies that $\mathbf{Q} = \mathbf{\Pi\Pi} - \frac{1}{2}\mathbb{I}$, and the hydrodynamic equation Eq. (4.26) takes a simple form

at leading order in a gradient expansion:

$$\partial_t \mathbf{\Pi} + v_0 \mathbf{\Pi} \cdot \nabla \mathbf{\Pi} = \mathbb{P} \cdot \left[-\beta \nabla \rho + \alpha_2 \nabla^2 (\rho \mathbf{\Pi}) + \gamma \tilde{\Delta} \cdot (\rho \mathbf{\Pi}) \right] \tag{4.33}$$

where the projection operator $\mathbb{P} = \mathbb{I} - \mathbf{\Pi}\mathbf{\Pi}$ constrains the modulus of $\mathbf{\Pi}$ to be a constant, and

$$\tilde{\Delta} = \begin{pmatrix} \partial_{xx} - \partial_{yy} & 2\partial_{xy} \\ 2\partial_{xy} & \partial_{yy} - \partial_{xx} \end{pmatrix}. \tag{4.34}$$

All the terms in Eq. (4.33) have a clear physical meaning. The l.h.s is the convective derivative of the polarization which is advected due to self-propulsion. The first term on the r.h.s is a pressure term. $\beta \nabla \rho$ results from the repulsive interactions between the rollers. Finally, the two positive hydrodynamic coefficients α_2 and γ measure the (anisotropic) stiffness of this broken symmetry fluid. α_2 stems from the alignment interactions, whereas γ derives from the dipolar term in Eq. (4.17). This equation is a simplified version of the hydrodynamic theory provided in [13] where weak local melting was allowed. It is reminiscent of the Toner and Tu theory in the strongly polarized limit yet it includes an additional anisotropic term. We show below that the emergent network of preferred flowing routes is not specific to this anisotropic addition, and is therefore expected to be a robust large-scale feature of any polar liquid flowing through repelling obstacles.

Hydrodynamics of a strongly polarized flock of rollers: heterogeneous media

We now generalize Eq. (4.33) to include the effect of disorder. We here model disorder within another asymptotic approximation. In the same spirit as our roller-roller interaction theory, in the limit of high obstacle density we provide a mean-field description of the $\mathcal{S}_\mathrm{o}$ term in Eq. (4.21) and write it as $\mathcal{S}_\mathrm{o} \equiv -\partial_\theta \mathcal{J}_\mathrm{o}(\mathbf{r}, \theta, t)$, where the angular current $\mathcal{J}_\mathrm{o}$ results from the angular advection of the probability density $\psi(\mathbf{r}, \theta, t)$ by the repulsive torques defined in Eq. (4.19). The net torque felt by a roller at $\mathbf{r}$ and oriented along θ is $\int \phi_o(\mathbf{r}') \partial_\theta \mathcal{H}_\mathrm{o}(\mathbf{r} - \mathbf{r}'; \theta) \mathrm{d}\mathbf{r}'$, where we $\phi_\mathrm{o}(\mathbf{r})$ is the local packing fraction of obstacles. The resulting current is:

$$\mathcal{J}_\mathrm{o} = -\psi(\mathbf{r}, \theta) \int \mathrm{d}\mathbf{r}' \phi_o(\mathbf{r}') \partial_\theta \mathcal{H}_\mathrm{o}(\mathbf{r} - \mathbf{r}'; \theta) \tag{4.35}$$

We then follow the same procedure as in the previous section and establish the hydrodynamic equation of the polarization field. We multiply Eq. (4.21) by $\hat{\mathbf{p}}$, and integrate it over θ using the polar closure ansatz: $\psi(\mathbf{r}, \theta, t) = \rho(\mathbf{r}, t) \delta(\hat{\mathbf{p}} - \mathbf{\Pi}(\mathbf{r}, t))$ and obtain:

$$\partial_t \mathbf{\Pi} + v_0 \mathbf{\Pi} \cdot \nabla \mathbf{\Pi} = \mathbb{P} \cdot \left[-\beta \nabla \rho + \alpha_2 \nabla^2 (\rho \mathbf{\Pi}) + \gamma \tilde{\Delta} \cdot (\rho \mathbf{\Pi}) + \mathbf{F}_\mathrm{o} \right]. \tag{4.36}$$

The only modification to Eq. (4.33) is the additional random-force term $\mathbf{F}_\mathrm{o}$ which accounts for the coupling of the polar fluid to disorder. Remarkably this random-force field derives from a potential: the local obstacle density.

$$\mathbf{F}_\mathrm{o}(\mathbf{r}) = -\beta_\mathrm{o} \nabla \phi_\mathrm{o}, \tag{4.37}$$

where β_o is a positive constant which quantifies the strength or the repelling torque. For a uniform set of spatially uncorrelated obstacles, $\mathbf{F}_\mathrm{o}(\mathbf{r})$ is a quenched random field of zero mean and variance:

$$\overline{\mathbf{F}_\mathrm{o}(\mathbf{r}) \mathbf{F}_\mathrm{o}(\mathbf{r}')} = \beta_\mathrm{o}^2 \phi_\mathrm{o} \nabla \nabla \delta(\mathbf{r} - \mathbf{r}'), \tag{4.38}$$

where $\overline{X}$ denotes the average over disorder of the X observable.

This term has also a very clear physical meaning: $\mathbf{F}_\mathrm{o}$ focalizes the polar liquid in the valleys of the potential defined by ϕ_o. We elucidate below how the pressure arising from the roller repulsion and the effective elasticity stemming from the alignment interactions compete with disorder to set the spatial structure of this polar liquid.

Response to a quenched random field and formation of sparse river networks

The full analytical description of an active fluid randomly stirred by quenched disorder goes far beyond the scope of this article. However a clear physical insight can be gained from a linearized theory. Let us compute the linear response of the density and polarization fields to a static perturbation $\mathbf{F}_\mathrm{o}$. The unperturbed state is assumed to be homogeneously flowing along the $\hat{\mathbf{x}}$ direction. We introduce the angular deviation $\delta\theta(\mathbf{r})$ defined as $\mathbf{\Pi}(\mathbf{r}) = \hat{\mathbf{x}} + \delta\theta(\mathbf{r})\hat{\mathbf{y}} + \mathcal{O}(\delta\theta^2)$, and the density perturbation $\rho(\mathbf{r}) = \bar{\rho} + \delta\rho(\mathbf{r})$. The linearized version of the mass-conservation equation and Eq. (4.33) are:

$$\partial_t\delta\rho + v_0\partial_x\delta\rho + (v_0\bar{\rho})\partial_y\delta\theta = 0, \tag{4.39}$$

$$\partial_t\delta\theta + v_0\partial_x\delta\theta = -\beta\partial_y\delta\rho + (\alpha_2\bar{\rho})\Delta\delta\theta + (\gamma\bar{\rho})(\partial_{yy} - \partial_{xx})\delta\theta + 2\gamma\partial_{xy}\delta\rho + F^\perp, \tag{4.40}$$

where $F^\perp = \mathbf{F}_\mathrm{o}\cdot\hat{\mathbf{y}}$ is the component of the random force field in the direction transverse to the mean spontaneous flow. Let us first briefly sketch the stability of this linear system, without going in the details of the calculation which are unimportant to the network formation. The isotropic elasticity (α_2 term) stabilizes both the splay and the bend deformations of the polarization field. Conversely the anisotropic contribution (γ terms) further stabilizes the splay modes while destabilizing the bend modes. However there always exists a finite range of hydrodynamic coefficients yielding a fully stable dynamics at all wave-lengths provided that $\alpha_2/\gamma < \bar{\rho}$ is sufficiently small. Our estimate from the microscopic parameter values yields $\alpha_2/\gamma \sim 1/10$ [12], which is indeed smaller that the colloid fraction at the flock front. In addition the transverse confinement of the polar flock in a rectangular geometry further suppresses any form of orientational instability. Consistently, we do not observe any sign of spontaneous destruction of polar order, or any density modulation for flock cruising in obstacle-free channels. Therefore, at this stage, we shall focus on the regime where Eqs. (4.39) and (4.40) are linearly stable.

As we are interested in the statistics of the *static* structure of the flock, we ignore the transient and readily solve the linear response in Fourier space introducing the Fourier modes $\delta\theta(\mathbf{r}) = \delta\theta_\mathbf{q}\exp(i\mathbf{q}\cdot\mathbf{r})$, $\delta\rho(\mathbf{r}) = \delta\rho_\mathbf{q}\exp(i\mathbf{q}\cdot\mathbf{r})$, $F^\perp = F^\perp_\mathbf{q}\exp(i\mathbf{q}\cdot\mathbf{r})$. The resulting density and orientational fluctuations are:

$$\overline{|\delta\rho_\mathbf{q}|^2} = \frac{\bar{\rho}^2 q_y^2}{\left(v_0 q_x^2 - \beta\bar{\rho}q_y^2\right)^2 + (\alpha_2-\gamma)^2\left(q_x^3 - q_x q_y^2\right)^2}\overline{|F^\perp_\mathbf{q}|^2} \tag{4.41}$$

and

$$\overline{|\delta\theta_\mathbf{q}|^2} = \frac{q_x^2}{\left(v_0 q_x^2 - \beta\bar{\rho}q_y^2\right)^2 + (\alpha_2-\gamma)^2\left(q_x^3 - q_x q_y^2\right)^2}\overline{|F^\perp_\mathbf{q}|^2} \tag{4.42}$$

These equations indicate that the random force field promotes both density and orientational fluctuations. However these fluctuations are hindered by the effective orientational elasticity, the active-fluid

pressure and self-propulsion. The consequences of these competitions are very clear when looking at the transverse and quasi longitudinal modes.

(i) **Transverse fluctuations:** $\mathbf{q} = q_y\hat{\mathbf{y}}$. Disorder cannot excite any stationary transverse angular mode (pure splay mode), but yields generic density fluctuations. Using Eqs. (4.41), and (4.37) we find:

$$\overline{|\delta\rho_{\mathbf{q}}|^2} = \left(\frac{\beta_o}{\beta}\right)^2 \phi_o \tag{4.43}$$

At all wave-lengths the density fluctuations are set by the competition between the obstacle repulsion which focalizes the rollers in the valley of the potential ϕ_o and the inter-roller repulsion that bounds the maximal local density.

(ii) **Longitudinal fluctuations:** $q_x \gg q_y$. The quasi longitudinal modes corresponds to bend excitations of the polarization field. Again, using Eqs. (4.42), and (4.37) we find:

$$\overline{|\delta\theta_{\mathbf{q}}|^2} = \frac{\beta_o^2\phi_o}{v_o^2 + q_x^2(\alpha_2-\gamma)^2\bar{\rho}^2}\left(\frac{q_y}{q_x}\right)^2 \tag{4.44}$$

In the small-q limit the amplitude of the orientational fluctuations is mostly set by the competition between self-propulsion and obstacle repulsion. This scaling translates a simple phenomenon, for a given obstacle strength the magnitude of the angular perturbation is an increasing function of the time spent in the interaction region. As this time decreases linearly with v_0, angular fluctuations are obviously expected to decay with β_o/v_0. The faster the rollers the less time they feel the obstacle repulsion. The second term in the denominator of Eq. (4.44) has a very different origin, and provides a qualitative explanation for the emergence of sparse river networks. The focalization of the rollers in the valleys of ϕ_o is restrained by the bending elasticity of the polar liquid. The higher α_2, and the smaller γ, the stiffer are the bending modes. In addition, as in all broken symmetry fluid, the mode having the smallest wave-lengths are the stiffest. Therefore even though the random force field drives the rollers along its minima, some of its valleys are much more difficult to flow in as they require a strong bend of the flow lines. The higher the obstacle fraction the more tortuous the valleys of $\phi_o(\mathbf{r})$, thereby limiting the number of paths allowed by the bending stiffness of the active fluid. At the linear-response level the angular fluctuations scale with ϕ_o.

Of course the geometry of a sparse network cannot be quantitatively captured by a mere linear analysis, yet it has allowed us to single out the very mechanisms responsible for their formation.

III.v Disorder-induced melting and emergent river networks: a robust picture

We shall now stress on the robustness of our two main results: (i) the suppression of flocking motion observed in our experiments falls in the same class as the first order Vicsek transition, and (ii) the inner structure of the flocks is that of an increasingly sparse river network. These two results do not rely on any feature specific to colloidal-roller fluids (Quincke propulsion, electrostatic and hydrodynamic interactions, colloidal scale, etc). They apply to *any* polar active material cruising through repelling obstacles.

However, we have focused on situations where the obstacles renormalize the bare diffusivity of isolated rollers. At higher obstacle fraction, or much stronger repulsion, a qualitative change in the

dynamic of motile particles occurs: they do not diffuse at long times, but rather undergo sub-diffusive motion due to long-time trappings as reported in [26]. The generalization of our results to this limit goes far beyond the scope of this paper. In this case, both the very nature of the suppression of orientational order together with the existence of genuine long-range orientational order in 2D remains an open question in this regime [121, 120].

IV Supplementary Note 3: Flocking through periodic lattices

We close this supplementary not by reporting a series of additionnal experiments conducted in ordered lattices of obstacles, see Supplementary Video 5. The obstacles have the same diameter as in the main text ($10\,\mu$m), but form a square lattice with the $(1,1)$ axis parallel to the direction of the main channel, Fig. 4.27a. As in disordered geometries, we find that collective motion is sharply suppressed upon increasing the obstacle fraction ϕ_o, or decreasing the roller density ρ. Irrespective whether the obstacles form a periodic lattice or not, the emergence of collective motion is a first order transition relying on the nucleation and growth of macroscopic band-like excitations. The discontinuity of the transition in both geometries is clearly seen in Fig. 4.27b, which shows how the flock amplitude, ρ_F varies as a function of the mean roller density ρ. Interestingly, we observe that flocks are more robust to random obstacles; colloidal flocks are found at smaller densities of colloids in disordered media. This observation is very consistent with a nucleation picture. In a disordered ensemble of obstacles, a flock can nucleate and grow from a region where the obstacle density is locally small. The flock can then propagate through the river network separating the regions of high obstacle density. For the same value of ϕ_o, no such low-obstacle density region exist in a periodic lattice and no flock is then seen to propagate.

In addition a very strong qualitative difference exist in this ordered geometry. No sparse river network forms. The inner structure and dynamics of the flock remain very homogeneous in the direction transverse to the mean flow, even at the onset of melting, see Fig. 4.27c. The rollers flow through the entire region left around the mere superposition of depleted wakes centered on the obstacle postions. This result is very consistent with the model introduced in the previous section to account for the emergence of river networks in disordered media. When described at scales larger than the lattice spacing, the obstacle-density field is uniform. Therefore the random stirring term in Eq. (4.36) vanishes, hence it cannot result in the bending of the roller flow. Conversely, in random media local fluctuations in the obstacle density drive the roller into increasingly sparse and tortuous valleys as ϕ_o increases yielding a markedly different geometry of the flock current, see Fig. 4.27d.

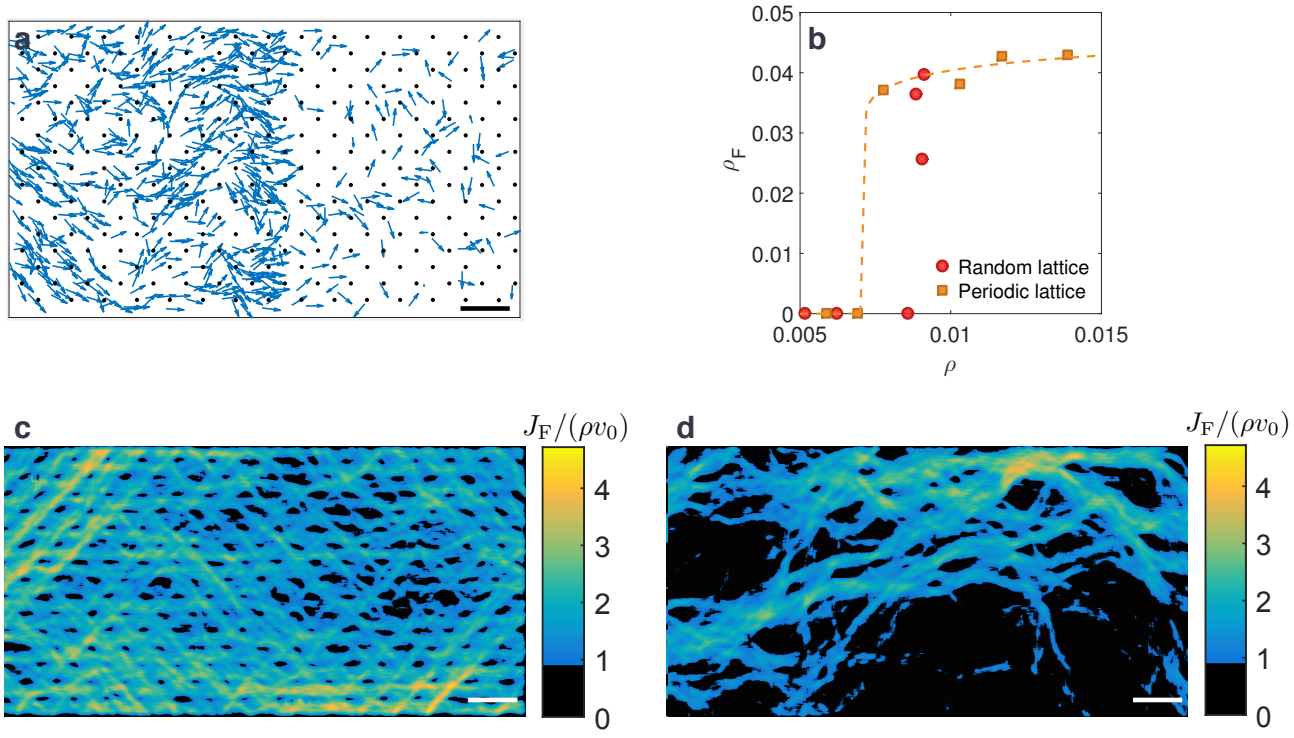

Figure 4.27 | **Flocking through a periodic lattice of obstacles.** **a**, Close-up on the head of a colloidal swarm propagating past a square lattice of obstacles (black dots). The arrows are located at the colloid positions and point along the orientation of their velocities. Obstacle packing fraction: $\phi_o = 3 \times 10^{-2}$. Scale bar: $100\,\mu$m. **b**, Variations of the amplitude of the flock ρ_F as a function of the mean roller fraction. ρ_F is the difference between the maximal density at the flock front and the density away from the flock in the isotropic phase. See Fig. 4.22. **c**, Map of the normalized flock-current $J_F(\mathbf{r})/(\rho v_0)$ at the onset of melting in a periodic lattice ($\phi_o = 3 \times 10^{-2}$, $\rho = 7.76 \times 10^{-3}$). No sparse network forms. The region where the rollers flow corresponds to the area left by the mere superposition of depleted wakes centered on the obstacle postions. **d**, Comparison with the map of the normalized flock-current $J_F(\mathbf{r})/(\rho v_0)$ at the onset of melting in a random lattice ($\phi_o = 3 \times 10^{-2}$, $\rho = 1.0 \times 10^{-2}$). A river network forms. The geometry of the flowing route is very different from **c**.

V Description of the supplementary videos

1. Supplementary video 1: A colloidal flock emerges from a population of $\sim 9,000$ colloids propelling in a 5mm $\times$ 1mm obstacle-free channel. The flock coexists with a gas phase where all the rollers propel themselves along random directions. Colloid diameter: $4.8\,\mu$m. Field amplitude $E_0 = 2\,\mathrm{V}/\mu\mathrm{m}$.

2. Supplementary video 2: A colloidal-roller flock cruises coherently through a random ensemble of circular obstacles placed in a 15mm $\times$ 1mm rectangular chamber. $\phi_o = 2 \times 10^{-2}$. The flock

coexists with an isotropic phase. Colloid diameter: $4.8\,\mu$m. Obstacle diameter: $10\,\mu$m. Field amplitude $E_0 = 2\,\mathrm{V}/\mu\mathrm{m}$.

3. Supplementary video 3: Colloidal rollers propelling themselves through a random ensemble of circular obstacles placed in a 15mm × 1mm rectangular chamber. $\phi_o = 5 \times 10^{-2}$. No large-scale collective motion can emerge. Colloid diameter: $4.8\,\mu$m. Obstacle diameter: $10\,\mu$m. Field amplitude $E_0 = 2\,\mathrm{V}/\mu\mathrm{m}$.

4. Supplementary video 4: Evolution of the local roller current $|\mathbf{J}(x, y, t)|$ as a flock crosses the field of view. The rollers are focalized along a self-organized network of sparse flowing routes. Dark red color: no current, light red color: maximal current value. $\phi_o = 2 \times 10^{-2}$. Obstacle diameter: $10\,\mu$m. Field amplitude $E_0 = 2\,\mathrm{V}/\mu\mathrm{m}$. The current is defined as in Fig. 3a.

5. Supplementary video 5: A colloidal-roller flock cruises coherently through a square lattice of circular obstacles placed in a 15mm×1mm rectangular chamber. Obstacle fraction: $\phi_o = 3\times10^{-2}$. Roller fraction: $\rho = 1.0 \times 10^{-2}$. Colloid diameter: $4.8\,\mu$m. Obstacle diameter: $10\,\mu$m. Field amplitude $E_0 = 2\,\mathrm{V}/\mu\mathrm{m}$.

Sounds and hydrodynamics of polar active fluids

Spontaneously flowing liquids have been successfully engineered from a variety of biological and synthetic self-propelled units [102, 100, 133, 34, 87, 41, 35, 13, 24, 65, 88]. Together with their orientational order, wave propagation in such active fluids have remained a subject of intense theoretical studies [122, 123, 127, 106, 104, 112]. However, the experimental observation of this phenomenon has remained elusive. Here, we establish and exploit the propagation of sound waves in colloidal active materials with broken rotational symmetry. We demonstrate that two mixed modes coupling density and velocity fluctuations propagate along all directions in colloidal-roller fluids. We then show how the six materials constants defining the linear hydrodynamics of these active liquids can be measured from their spontaneous fluctuation spectrum, while being out of reach of conventional rheological methods. This active-sound spectroscopy is not specific to synthetic active materials and could provide a quantitative hydrodynamic description of herds, flocks and swarms from inspection of their large-scale fluctuations [21, 50, 15, 20].

We exploit the so-called Quincke mechanism to motorize inert colloidal particles and turn them into self-propelled rollers [95, 78, 68, 13]. When rolling on a solid surface they interact via velocity-alignment interactions triggering a flocking transition as their area fraction exceeds $\rho_0 = 0.02$ [13]. As illustrated in Fig. 3.7a and Supplementary Video 1, millions of rollers interacting in a microfluidic channel self-organize to move coherently along the same direction, all propelling with the same average velocity $\langle \boldsymbol{\nu}_i \rangle = \nu_0 \hat{\mathbf{x}}$, Figs. 28a and 28b. However, the flock does not move as a rigid body. Instead, it forms a homogeneous active liquid with strong orientational and little positional order, Figs. 28b, 28c. Let us note $\nu_i^{\parallel}$ and $\nu_i^{\perp}$ the longitudinal and transverse components of the velocity fluctuations: $\boldsymbol{\nu}_i = (\nu_0 + \nu_i^{\parallel})\hat{\mathbf{x}} + \nu_i^{\perp}\hat{\mathbf{y}}$. The correlations of the longitudinal component, $\mathcal{C}_{\parallel}(\mathbf{r})$, and of the liquid structure, are both short ranged and decay over few particle radii, Figs. 28c, 28d. In stark contrast, the correlations of the transverse velocity modes, $\mathcal{C}_{\perp}(\mathbf{r})$, are anisotropic and decay algebraically, Figs. 28e and 28f. This algebraic decay demonstrates that the transverse velocity fluctuations are soft modes associated with the spontaneous symmetry breaking of the roller orientations [124, 76]. In addition, self-propulsion couples these soft orientational modes to density fluctuations, thereby causing the giant number fluctuations illustrated in Fig. 28g. Such anomalous fluctuations are common to all orientationally ordered active fluids, see e.g. [124, 76, 87] and references therein. The density-fluctuation measurements, and the discrepancy with [13] are thoroughly

discussed in Supplementary Note 1.

Altogether these results establish that colloidal rollers self-assemble into a prototypical polar active fluid. Their ability to support underdamped sound modes, regardless whether the dynamics of their microscopic units is overdamped, is one of the most remarkable, yet unconfirmed, theoretical prediction for active fluids with broken rotational symmetry [122, 127, 124, 76]. We provide below an experimental demonstration of this counterintuitive prediction, and establish a generic method to measure the material constants of active fluids from their sound spectrum.

Let us consider the spatial Fourier components, $\rho_{\mathbf{q}}(t)$ and $v_{\mathbf{q}}(t)$, of the density and transverse velocity fields, where $\mathbf{q} = q(\cos\theta, \sin\theta)$ is a wave vector making an angle θ with the mean flow direction, see Methods. We show in Figs. 29a and 29b that the time correlations of $\rho_{\mathbf{q}}$ and $v_{\mathbf{q}}$ oscillate over several periods before being damped, thereby demonstrating that both density and velocity waves propagate in the active liquid, see also Supplementary Videos 2 and 3. We emphasize, that we here consider the propagation of *linear* waves as opposed to the density fronts, or bands, seen at the onset of collective motion [76, 102, 31, 13]. In Fig. 29c the power spectra $|\rho_{q,\omega}|^2$ and $|v_{q,\omega}|^2$ evaluated at $\theta = \pi/4$ both display two peaks located at identical oscillation frequencies $\omega_{\pm}$. They define the frequencies of two mixed modes involving both density and velocity fluctuations intimately coupled by the mass-conservation relation: $\partial_t\rho(\mathbf{r},t)+\nabla\cdot[\rho(\mathbf{r},t)\mathbf{v}(\mathbf{r},t)] = 0$. Repeating the same analysis for all wave lengths, we readily infer the dispersion relations $\omega = \omega_{\pm}(q)$ of the two sound modes as illustrated in Fig. 29d. They both propagate in a dispersive fashion. Two speeds of sound can however be unambiguously defined at long wave lengths where: $\omega = c_{\pm}q$. Remarkably, both modes propagate in all directions and their dispersion relation strongly depends on θ, Figs. 29d, 29e and 29f. In particular, we find that the speed of sound $c_{\pm}(\theta)$ varies non-monotonically as shown in the polar plot of Fig. 29g. Measuring the angular variations of the speed-of-sound in active liquids with different area fractions, ρ_0, we find that the shape of the $c_{\pm}(\theta)$ curves is preserved, Figs. 29g, 29h, 29i and does not depend on the channel geometry, see Supplementary Note 2. Sound propagates faster in denser liquids.

We now exploit these wave spectra to infer the hydrodynamics of the active-roller liquids from their spontaneous fluctuations. The Navier-Stokes equations describing the flows of isotropic Newtonian liquids merely involve two material constants: density and viscosity. In contrast, in the absence of momentum conservation, and given their intrinsic anisotropy, the hydrodynamics of polar active liquids involve at least fourteen material constants, see e. g. [124, 66] and Supplementary Note 3. We here focus on the linear dynamics of the density and velocity fields around a homogeneous and steady flow along the $\hat{\mathbf{x}}$ direction. We note $\rho(\mathbf{r},t)$ the fluctuations of the density field around ρ_0, and $\boldsymbol{v}(\mathbf{r},t) = [u_0 + u(\mathbf{r},t)]\,\hat{\mathbf{x}} + v(\mathbf{r},t)\hat{y}$ the local velocity field. As detailed in Supplementary Note 3, they evolve according to:

$$\partial_t\rho + \rho_0\partial_y v + u_0\partial_x\rho = D'\partial_x^2\rho, \tag{45}$$

$$\partial_t v + \lambda_1 u_0\partial_x v = -\sigma\partial_y\rho + D_\perp\partial_y^2 v + D_\parallel\partial_x^2 v + u_0 D_\rho\partial_{xy}^2\rho, \tag{46}$$

$$u = -\frac{D'}{\rho_0}\partial_x\rho. \tag{47}$$

Eq. (45) corresponds to mass conservation, and Eq. (46) describes the slow dynamics of the soft transverse-velocity mode. Eq. (47) indicates that $u(\mathbf{r},t)$ is a fast mode. Longitudinal fluctuations quickly relax at all scales and are slaved to $\partial_x\rho(\mathbf{r},t)$, see Supplementary Note 3 and [122, 76, 81]. The linear hydrodynamics of the active fluid is therefore fully prescribed by the emergent flow speed $u_0(\rho_0)$, Fig. 30a, and six material constants all having a clear physical meaning. D' is a diffusion constant readily measured from the linear relation between longitudinal velocity fluctuations and density gradients defined by Eq. (47) and confirmed by Fig 30b. λ_1 measures how fast velocity waves are convected by the mean flow and would be equal to one if momentum were conserved [123]. σ is the active-liquid compressibility. $D_\perp$ and $D_\parallel$ can either be thought as viscosities, or orientational elastic constants. Finally D_ρ stems for the couplings between orientational and positional degrees of freedom between the active units. Looking for plane-wave solutions of Eqs. (45) and (46), we readily infer the dispersion relations of mixed density and velocity waves. In the long-wave-length limit, they take the compact form predicted in [123]: $\omega = \left[c_{\pm}(\theta)q + \mathcal{O}(q^2)\right] + i\Delta\omega_{\pm}(\theta)$, where $c_{\pm}$ is the speed of sound and the imaginary part $\Delta\omega_{\pm}(\theta) = \mathcal{O}(q^2)$ corresponds to the widths of the power spectra exemplified in Fig. 29c. The angular

variations of the speed of sound are given by:

$$2c_{\pm}(\theta) = (1+\lambda_1)\, u_0 \cos\theta \pm \sqrt{(\lambda_1-1)^2\, u_0^2 \cos^2\theta + 4\sigma\rho_0 \sin^2\theta}. \quad (48)$$

This prediction is in excellent agreement with the speed of sound measurements showed in Figs. 29g, 29h, and 29i for three different densities. As the mean-flow speed $u_0(\rho_0)$ is measured independently, fitting our data requires only two unknown functional parameters $\sigma(\rho_0)$ and $\lambda_1(\rho_0)$. The variations of $c_{\pm}(\theta)$ therefore provide a direct measurement of the active-fluid compressibility and advection coefficients, Figs. 30c and 30d. The consistency of this method is further established by repeating the same measurements in two different channel geometries, and comparing the density dependence of the hydrodynamic coefficients with the kinetic-theory predictions of [13, 12, 84], see Supplementary Note 3. Figure 30c shows a good agreement for the variations of $\sigma(\rho_0)$ over a range of densities. As in standard liquids, the compressibility increases with ρ_0. In the case of λ_1 the agreement is also satisfactory but not as accurate, see Fig.30d. Nonetheless theory predicts the correct order of magnitude, and more importantly the absence of variations of λ_1 with ρ_0. We now measure the elastic constants of the active fluid from the damping of the sound waves. Their damping time is set by the inverse of the spectral widths $\Delta\omega_{\pm} = q^2\Delta_{\pm}(\theta)$, where the expression of the angular functions $\Delta_{\pm}(\theta)$ is given in Supplementary Note 3. Fig. 30e agrees with the q^2 scaling behavior, and we show in Fig. 30f that the angular variations of $\Delta_{\pm}(\theta)$ are correctly fitted by the linear hydrodynamic theory. Given the shape of the power spectra, Fig. 29f, measuring $\Delta_{\pm}$ at small θ is out of reach of our experiments at high packing fractions. We therefore focus on two high angle values. For $\theta = \pi/2$ and $\theta = \pi/4$, the spectral widths take the simple forms: $\Delta\omega_{\pm}(\pi/2) = q^2 D_{\perp}/2$ and $\Delta\omega_{\pm}(\pi/4) = q^2\left[\frac{1}{4}(D_{\perp}+D_{\parallel}+D') \pm (\rho_0 D_{\rho} u_0)/\sqrt{4\sigma\rho_0}\right]$, as detailed in Supplementary Note 3. A quadratic fit of $\Delta\omega_{\pm}(\pi/2)$ therefore provides a direct measure of $D_{\perp}$, Fig. 30e. Similarly, a quadratic fit of $[\Delta\omega_{+}(\pi/4) + \Delta\omega_{-}(\pi/4)] = \frac{1}{2}(D_{\perp}+D_{\parallel}+D')q^2$ gives the value of $(D_{\perp}+D_{\parallel})$ as $D' = 4\times10^{-6}\,\mathrm{mm}^2/\mathrm{s}$ is four orders of magnitude smaller than $D_{\perp} \sim D_{\parallel} \sim 10^{-2}\,\mathrm{mm}^2/\mathrm{s}$, see Fig 30b. The measured values of the elastic constants $D_{\perp}$ and $D_{\parallel}$ are shown in Figs. 30g and 30h for different packing fractions. Their order of magnitude, Fig. 30e, and more importantly their linear increase with ρ_0, Figs. 30g and 30h, are consistent with kinetic theory which also predicts that D' should be vanishingly small. In principle, D_{ρ} could be measured for any polar active liquid from the value of $\Delta\omega_{+}(\theta) - \Delta\omega_{-}(\theta) \sim D_{\rho}q^2$. In the specific case of the colloidal rollers, kinetic theory predicts that D_{ρ} should be independent of ρ. The precision of our measurements is however not sufficient for an accurate estimate of the variations of $\Delta\omega_{\pm}$ with the roller fraction. For all fractions below $\rho_0 = 0.24$ we find $D_{\rho} = 1 \pm 0.5\,10^{-2}\,\mathrm{mm}^2/s$. Analysing the spontaneous fluctuations of the polar active fluids, we have measured all its six materials constants, thereby providing a full description of its linear hydrodynamics.

Before closing this letter, two comments are in order. Firstly, the q^2 damping of the sound modes implies a $\Delta N^2 \sim N^2$ scaling for the number fluctuations [76]. While giant number fluctuations are consistently found in all our experiments, linear theory overestimates their amplitude, see Fig. 28g. This last observation might suggest that the largest scales accessible in our experiments are smaller but not too far from the onset of hydrodynamic breakdown predicted in [122, 123]. Secondly, we here focus on homogeneous active materials. A natural extension to this work concerns sound propagation in more complex active media such as microfluidic lattices [112], or curved surfaces [104] where topologically-protected chiral sound modes are theoretically predicted.

In conclusion, two decades after the seminal predictions of Toner and Tu, we have experimentally demonstrated that the interplay between motility and soft orientational modes results in sound-wave propagation in colloidal active liquids. We have exploited this counter-intuitive phenomenon to lay out a generic spectroscopic method, which could give access to the material constants of all active materials undergoing spontaneous flows. Active-sound spectroscopy applies beyond synthetic active materials [22, 140], and could be used to quantitatively describe large-scale flocks, schools, and swarms as continuous media [21, 50, 15, 20].

Acknowledgements. We acknowledge support from ANR program MiTra and Institut Universitaire de France. We thank O. Dauchot, A. Souslov and especially H. Chaté, B. Mahault, S. Ramaswamy, Y. Tu and J. Toner for invaluable comments and discussions.

Author Contributions. D. B. conceived the project. D. G. and D. B. designed the experiments. D. G. and A. M. performed the experiments. D. G. and D. B.

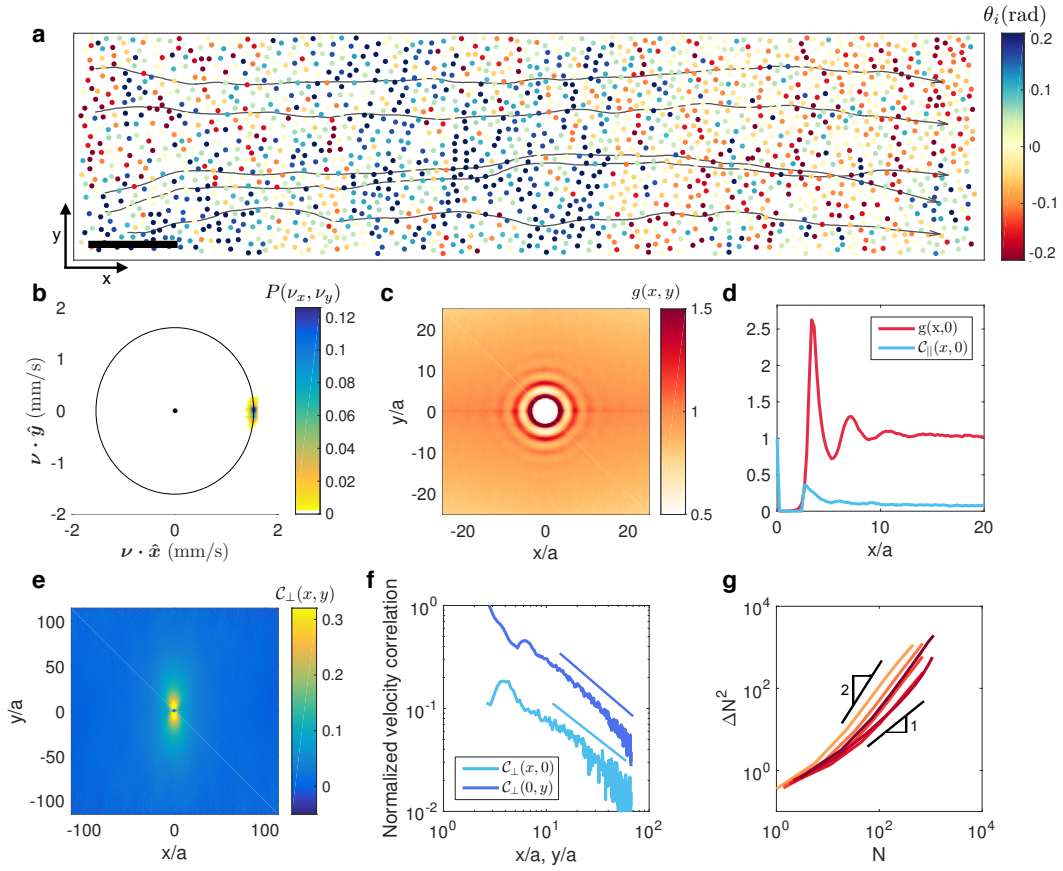

Figure 28 | **Colloidal rollers self-assemble into a spontaneously-flowing liquid.** **a**, Close up on a microfluidic channel including $\sim 3 \times 10^6$ colloidal rollers forming a homogeneous polar liquid. The color of the particles indicates the value of the angle, θ_i, between their instantaneous velocity and the direction of the mean flow. Five trajectories illustrate the typical motion of the rollers. $\rho_0 = 0.11$. Scale bar: $100\,\mu$m. **b**, Probability density function of the roller velocities, $\nu_i(t)$, (ensemble and time integration). All the rollers propel along the same average direction. $\rho_0 = 0.24$ as in all following panels. **c**, The color indicates the value of the density pair correlation function $g(x, y)$ evaluated at positions (x, y). Structural correlations are short ranged and display only weak anisotropy. **d**, Cuts along the flow direction of the pair distribution functions, $g(x, 0)$ [54], and of the longitudinal velocity correlations $\mathcal{C}_{\parallel}(x, 0)$, where $\mathcal{C}_{\parallel}(\mathbf{r}) \equiv \langle \nu_i^{\parallel}(t)\nu_j^{\parallel}(t)\rangle_{(\mathbf{r}_i-\mathbf{r}_j)=\mathbf{r},t} / \langle (\nu_i^{\parallel})^2(t)\rangle_{i,t}$. Both structural, and longitudinal- velocity correlations decay over few particle radii. **e**, Correlations of the transverse velocity fluctuations (ensemble and time average): $\mathcal{C}_{\perp}(\mathbf{r}) \equiv \langle \nu_i^{\perp}(t)\nu_j^{\perp}(t)\rangle_{(\mathbf{r}_i-\mathbf{r}_j)=\mathbf{r},t} / \langle (\nu_i^{\perp})^2(t)\rangle_{i,t}$. The transverse fluctuations are long ranged and strongly anisotropic. **f**, The correlations of the transverse velocity fluctuations, $\mathcal{C}_{\perp}(\mathbf{r})$, decay algebraically in both directions. The solid lines correspond to best algebraic fits: $\mathcal{C}_{\perp}(x, 0) \sim x^{-0.84}$, and $\mathcal{C}_{\perp}(0, y) \sim y^{-0.76}$. **g**, Giant number fluctuations. Variance, $\Delta N^2(\ell)$, of the number of particles measured in square regions of size ℓ. $\Delta N^2(\ell)$ is plotted as a function of the average number of particle $N(\ell)$ for five different polar active liquids of average area fractions $\rho_0 = 0.12, 0.18, 0.18, 0.24, 0.30, 0.39$ labeled by colors of increasing darkness. Solid lines: scaling $\Delta N^2(\ell) \sim N(\ell)$ corresponding to normal density fluctuations as in equilibrium fluids, and $\Delta N^2(\ell) \sim N^2(\ell)$ scaling law predicted from linear hydrodynamic theory, see e.g. [76]. Details about number fluctuation measurements and power-law fit values are provided in Supplementary Note 1.

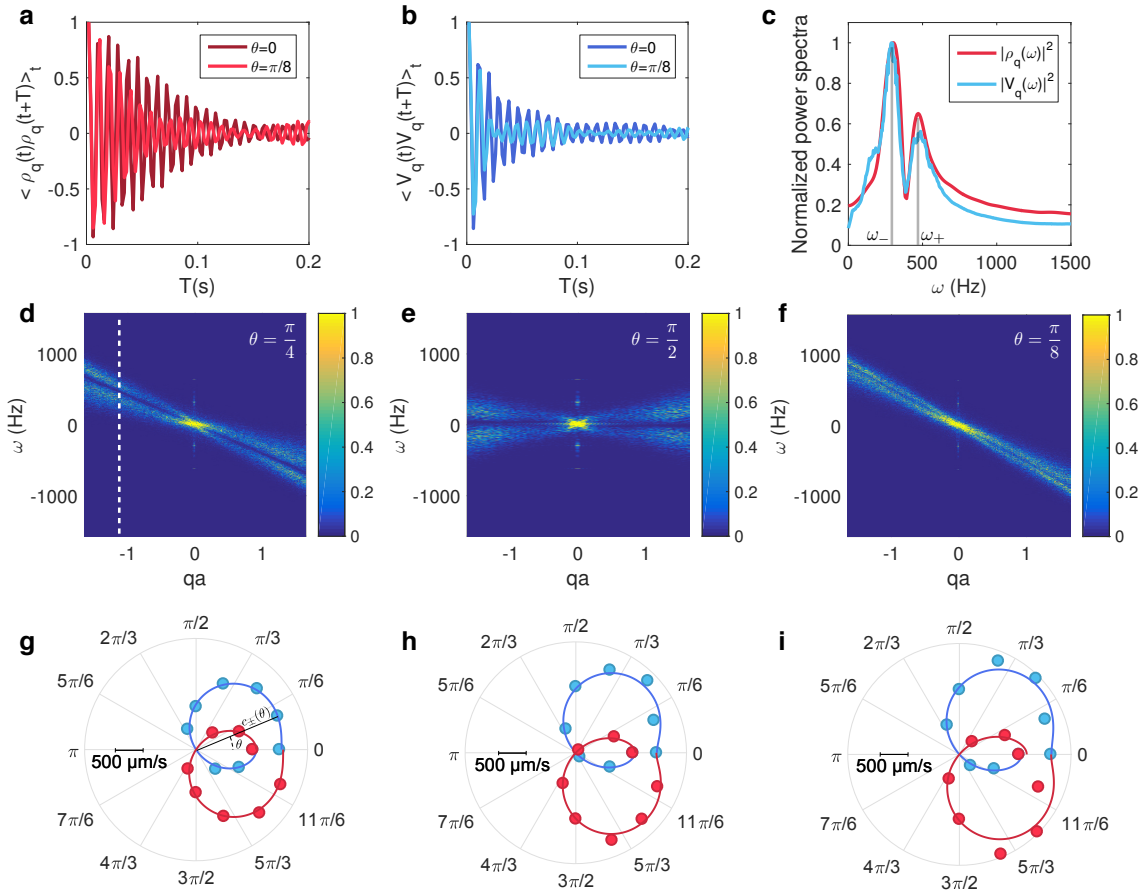

Figure 29 | **Sound modes in polar active fluids. a**, Two-time autocorrelations of the density fluctuations of wave vector **q**, with $q = 0.52\,\mu m^{-1}$, for two different directions of propagations, $\theta = 0$ and $\theta = \pi/8$. $\rho_0 = 0.11$. **b**, Two-time autocorrelations of the transverse velocity fluctuations for the same wave vectors as in **a**. $\rho_0 = 0.11$. **c**, Density (red) and velocity (blue) power spectra for $q = 0.39$ and $\theta = \pi/4$. The two spectra have two peaks located at the same frequency $\omega_\pm$ and have identical width $\Delta\omega_\pm$. Both spectra reflect the propagation of the same mixed modes combining velocity and density excitations. $\rho_0 = 0.11$. **d**, **e** and **f**, Full power spectra of the transverse velocity fluctuations $\langle|v_{q,\omega}|^2\rangle/\langle|v_{q=0,\omega=0}|^2\rangle$. They clearly show the dispersion relations of the mixed sound modes along three different directions $\theta = \pi/4$, $\theta = \pi/2$ and $\theta = \pi/8$. The dashed line in panel **d** corresponds to the cut showed in **c**. Sound modes propagate in a non dispersive fashion only at small qs. $\rho_0 = 0.11$. **g**, **h** and **i**, Polar plots of the speed of sound, $c_\pm(\theta) = \lim_{q\to 0}[\omega \pm (\theta)/q]$ measured from the slope at $q = 0$ of the dispersion relations. Experimental data: Red dots (resp. blue dots) correspond to $c_+(\theta)$ (resp. $c_-(\theta)$). Solid lines: theoretical fits from Eq. (48). The roller area fractions are $\rho_0 = 0.11$ in **g**, $\rho_0 = 0.18$ in **h**, and $\rho_0 = 0.24$ in **i**.

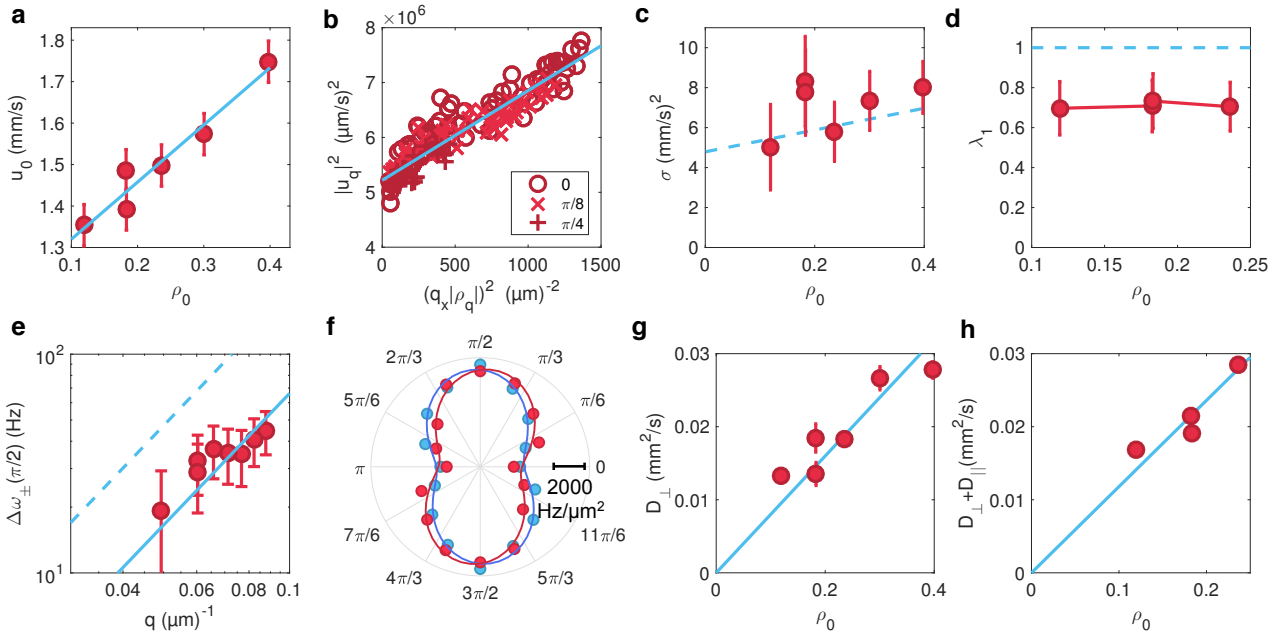

Figure 30 | **Active-fluid spectroscopy.** Red dots: experimental data. Blue line: best linear fit. Dashed line theoretical prediction with no free fitting parameter deduced from kinetic theory, see Supplementary Note 3. The hydrodynamic description of the active fluid is inferred from: **a**, Variations of the mean-flow speed with the mean area fraction. Error bar: 100 μm/s, 1std. Denser fluids flow faster. **b**, Parametric plot of the longitudinal velocity fluctuations $|u_q|^2$ varrying linearly with $(q_x|\rho_q|^2)$ for three propagation angles. The slope gives a measure of $D' = 4\times10^{-6}\,\mathrm{mm}^2/\mathrm{s}$. The offset at $q_x = 0$ comes from the noise acting on the u mode, see Supplementary Note 3. **c**,**d**, The compressibility coefficient, σ and advection coefficient, λ_1, are plotted versus the mean area fraction ρ_0. Both quantities are measured from the best fit of the speed of sound (Figs. 29g, 29h, 29). The error bars defined applying the uncertainty-propagation formula on $\sigma = c_\pm(\pi/2)^2/\rho_0$ and $\lambda_1 = c_+(0)/c_-(0)$. The uncertainties on c and ρ_0 are respectively 100 μm/s and 0.02. **e**, Spectral width $\Delta\omega_\pm(\pi/2)$ of the modes propagating at $\theta = \pi/2$ plotted versus q (log-log plot). $\Delta\omega_\pm(\pi/2)$ grows quadratically with q. Error bars: 10 Hz estimated comparing several Lorentzian fits. Solid line: best quadratic fit. The bare prediction from the simplified kinetic theory overestimates $\Delta\omega_\pm(\pi/2)$ by a factor of 3. The possible origins of this overestimate are discussed in Supplementary Note 3. **f**, Polar plot of the spectral width normalized by q^2 and averaged over all wave vectors $\Delta_\pm = \langle\Delta\omega_\pm(\theta)/q^2\rangle_q$. Red (resp. Blue) dots: experimental data corresponding to Δ_+ (resp. Δ_-). Solid lines: best fits using the relation $\Delta_\pm = \frac{1}{4}[-(D'+D_\perp+D_\parallel)-(D'+D_\parallel-D_\perp)\cos(2\theta)\pm D_\rho u_0\sqrt{\rho_0/\sigma}\sin(2\theta)]$, see Supplementary Note 3. **g**, Variations of the elastic constant $D_\perp$ with ρ_0. $D_\perp$ is measured from the quadratic fit shown in **e**, see main text. Error bars defined as the 0.95 confidence interval of the quadratic fit in **e**. The elastic constant increases linearly with the particle density. **h**, Variations of the average elastic constant $D_\parallel + D_\perp$ with ρ_0. $D_\perp + D_\perp$ measured from the quadratic fit of $\Delta\omega_+(\pi/4) + \Delta\omega_-(\pi/4)$, see main text. Error bars defined as in **g**.

analyzed and discussed the results. D. G. and D. B. wrote the paper.

Author Information. Correspondence and requests for materials should be addressed to D. B. (email: denis.bartolo@ens-lyon.fr).

Methods

We use Polystyrene colloids of diameter $2a = 4.8\,\mu$m dispersed in a 0.15 mol.L^{-1} AOT-hexadecane solution (Thermo scientific G0500). The suspension is injected in a wide microfluidic channel made of two parallel glass slides coated by a conducting layer of Indium Tin Oxyde (ITO) (Solems, ITOSOL30, thickness: 80 nm) [13]. The two electrodes are assembled with double-sided scotch tape of homogeneous thickness ($H = 110\,\mu$m). More details about the design of the microfluidic device are provided in the Supplementary Figure 5.

The colloids are confined in a 2 mm $\times$ 30 mm race track. The walls are made of a positive photoresist resin (Microposit S1818, thickness: 2 μm). This geometry is achieved by means of conventional UV lithography. After injection the colloids are let to sediment onto the positive electrode. Once a monolayer forms, Quincke electro-rotation is achieved by applying a homogeneous electric field transverse to the two electrodes $\mathbf{E} = E_0\hat{\mathbf{z}}$. The field is applied with a voltage amplifier (TREK 609E-6). All reported results correspond to an electric field $E_0 = 2E_{\rm Q}$, where $E_{\rm Q}$ is the Quincke electro-rotation threshold $E_{\rm Q} = 1\,{\rm V}/\mu$m. The colloids are electrostatically repelled from the regions covered by the resin film thereby confining the active liquid in the racetrack. Upon applying E_0 the rollers propel instantly and quickly self-organize into a spontaneously flowing colloidal liquid. All measurements are performed after the initial density heterogeneities have relaxed and a steady state is reached for all the observables. The waiting time is typically of the order of 10 minutes.

The colloids are observed with a 9.6x magnification with a fluorescent Nikon AZ100 microscope. The movies are recorded with a 4 Mpix CMOS camera (Basler ACE) at frame rates of 500 fps. The particles are detected with a one pixel accuracy, and the particle trajectories and velocities are reconstructed using the Crocker and Grier algorithm [29]. Measurements are performed in a 1146 μm $\times$ 286 μm observation window. The individual particle velocities are averaged over 4 subsequent frames.

The spatial Fourier transform of the density and transverse velocity fields are respectively defined as:

$$\rho_q(t) = \sum_i e^{iq[x_i(t)\cos\theta + y_i(t)\sin\theta]}, \tag{49}$$

$$\mathbf{v}_q(t) = \sum_i \boldsymbol{\nu}_i(t) e^{iq[x_i(t)\cos\theta + y_i(t)\sin\theta]}, \tag{50}$$

where $x_i(t)$ and $y_i(t)$ are the instantaneous particle coordinates. The sum is performed over all detected particles. Time Fourier transforms are then performed using the MATLAB implementation of the FFT algorithm. The positions of the maxima, $\omega_\pm$, and the width $\Delta\omega_\pm$ of the velocity power spectra are determined by fitting the $|v_q(\omega)|^2$ curve by the sum of two Lorentzian functions.

Code avaibility

Matlab scripts used in this work are avaible from the corresponding author upon reasonnable request.

Data avaibility

The data that support the findings of this study are avaible upon request from the corresponding author.

Supplementary videos legends

Supplementary video 1. An active polar liquid composed of $\sim 3\times10^6$ colloidal rollers flows in a microfluidic racetrack. We show the trajectories of five particles, and the instantaneous orientation of their velocity (black arrows). They fluctuate around the average direction of the emergent flow. The polar liquid does not move like a rigid body, the particles rearrange. The area fraction of the colloids is $\rho_0 = 0.11$. Colloid diameter: 4,8 μm. Field amplitude: $E_0 = 2\,{\rm V}/\mu$m. Movie recorded at 500 fps, played at 30 fps.

Supplementary video 2. An active polar liquid composed of $\sim 3 \times 10^6$ colloids flows in a microfluidic racetrack. The color indicates the magnitude of the velocity-component transverse to the mean flow. Blue particles are moving up, red particles are moving down. Transverse velocity fluctuations propagate through the polar liquid. The area fraction of the colloids is ρ_0=0,11. Colloid diameter: 4,8 μm. Field amplitude: E_0=2 V/μm. Movie recorded at 500 fps, played at 20 fps.

Supplementary video 3. Density field of a polar liquid flowing in a microfluidic racetrack. The density field is defined in the Voronoi cells centred on the particles. The color of the cells indicates the inverse of the cell area, and therefore corresponds to the local colloid density. The density fluctuations propagate in different directions when the polar liquid flows. The area fraction of the colloids is ρ_0=0,11. Colloid diameter: 4,8 μm. Field amplitude: E_0=2 V/μm. Movie recorded at 500 fps, played at 20 fps.

Supplementary Note 1 : Giant density fluctuations

1 Colloidal roller liquids display giant density fluctuations

Giant number fluctuations are one of the most remarkable features of active liquids with uniaxial orientational order [76, 124]. This phenomenon has been consistently reported for a variety of experimental systems ranging from shaken grains, to bacteria suspensions and motility assays, see [87] for a comprehensive list and a critical assessment of the available measurements and simulations. Even though there is no doubt about the existence of giant number fluctuations in ordered liquids assembled from motile particles, their measurement is extremely delicate as subject to a number of possible artefacts. The determination of the exact scaling law relating the fluctuations, $\Delta N^2(\ell)$, of the number of particles in a box of size ℓ to the average number $N(\ell)$ goes beyond the scope of this letter. We however unambiguously establish that the number fluctuations in polar active liquids assembled from colloidal rollers are giant. Performing measurements on six different polar liquids of average packing fractions comprised between $\rho = 0.12$ and $\rho = 0.39$, we find $\Delta N^2 \sim N^\alpha$ with $1.46 < \alpha < 2.04$, as detailed below.

Number fluctuations are all measured in steady state, and in the most homogeneous region of our device. The homogeneity of the polar liquid was checked by measuring the time average density field in the entire observation window as illustrated in Fig. 31a. Number fluctuations are computed only in regions of space where the static spatial heterogeneities are less than 10%. The statistics is accumulated over 5,000 frames. The number of particules is counted in square boxes of increasing length. The results of the number statistics are shown separately for each experiment in Figs. 31b to 31g. A power law fit of the data is performed for values of N larger than 10. The values of the α exponent are systematically found to be larger than 1 establishing the existence of giant number fluctuations in all roller fluids. Importantly, we stress that this anomalous scaling does not originate from the static heterogeneities of the density field. The static fluctuations of ΔN^2 are found to be between one and two orders of magnitude smaller than the dynamical fluctuations.

The unambiguous existence of giant number fluctuations calls for a critical discussion of the conflicting measurement reported in [13].

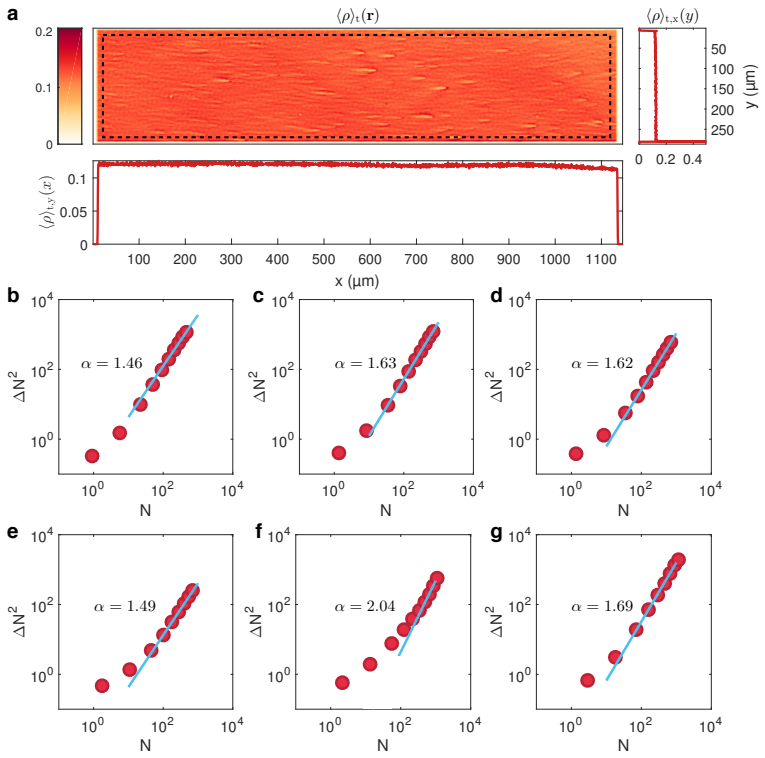

Figure 31 | **Giant number fluctuations.** **a**, Time averaged density field of a polar liquid with an average area fraction of $\rho_0 = 0.12$. The color on the heat map indicates the local value of the time averaged area fraction. Dashed line: region where the number fluctuations are computed.The corresponding x and y averaged density profiles are plotted respectively below and on the right hand side of the density plot. **b**-g, Number fluctuations ΔN^2 plotted versus the average number of particles N for average area fractions of $\rho_0 = 0.119$, $\rho_0 = 0.182$, $\rho_0 = 0.183$, $\rho_0 = 0.236$, $\rho_0 = 0.300$ and , $\rho_0 = 0.397$. Solid line bets power law fit and value of the fitted power law.

2 Critical discussion of the results published in [13]

In [13] using the same experimental system (aside from minor technical differences: slightly different AOT salt concentration, different gap between the electrodes and use of another insulating layer to confine the colloids), polar liquids assembled from colloidal rollers were reported to display normal density fluctuations. This conclusion was erroneous and certainly due to a poorer statistics. The results reported in Fig. 4c from [13] are reproduced in Fig. 32a below. The quality of the data does not make it possible to distinguish between any value of α comprised between 1 (dashed line) and 1.2 (Solid line and best power-law fit).

We have also analysed two additional experiments published in [13], including the polar-liquid movie presented in Supplementary Video 4 from [13] and corresponding to $\rho_0 = 0.18$. The number fluctuations computed over the entire ensemble of available frames using the same algorithm as in the present study are plotted in Figs. 31b and 31c. Again the number fluctuations significantly deviates from a normal behavior. The values of the α exponents are consistent with that found in the present study. From this complementary analysis, we rectify the conclusion drawn in [13] and conclude that colloidal roller fluids display the giant number fluctuations

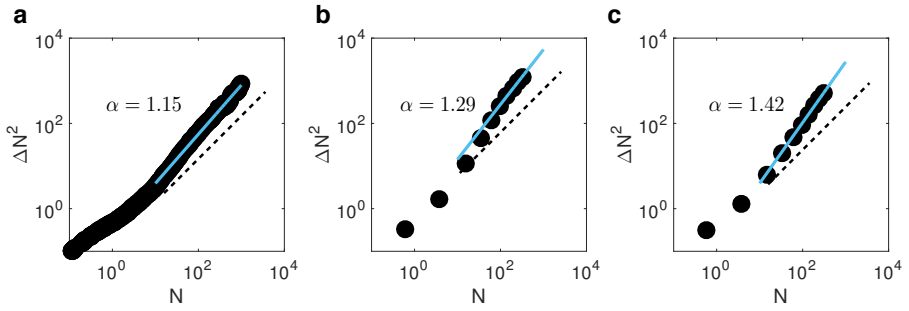

Figure 32 | **Giant number fluctuations, comparison with the results from [13].** **a**, Number fluctuations ΔN^2 plotted versus the average number of particles N. Average area fractions of $\rho_0 = 0.095$. These data correspond to that of Fig. 4c in [13]. Dashed line: normal fluctuations $\Delta N^2 \sim N$. Solid line: best power law fit giving $\Delta N^2 \sim N^\alpha$ with $\alpha = 1.15$. **b** and **c** Number fluctuations ΔN^2 plotted versus the average number of particles N measured from two different movies including Supplementary Video 4 from [13] (average area fractions of $\rho_0 = 0.18$). The number fluctuations are found to be giant with exponents $\alpha = 1.29$ and $\alpha = 1.42$.

typical to all uniaxial active liquids.

We conclude this critical discussion, by addressing the theoretical explanation put forward in [13] to justify the apparent lack of anomalous number fluctuations. The microscopic theory of roller interactions includes long range hydrodynamic interactions that were predicted to damp splay and density fluctuations at long wave lengths. Our speed of sound measurements indicate that these long-range interactions do not have any impact on the roller dynamics at the scale of our experiments. As a matter of fact, this damping term would result in a dispersion relation scaling as $\omega \sim$ const as $q \to 0$. This prediction is not supported by our experimental measurements, Fig. 2 in the main text. The reason for this discrepancy is very likely to be due to the very small magnitude of the long-range hydrodynamic interactions having a strength set by the ratio $a/H = 2 \times 10^{-2}$ between the colloid radius a and the distance between the two electrodes H. Probing the potential impact of these hydrodynamic interactions would require performing experiments at much larger scales out of reach of our current setup.

Supplementary Note 2 : Independence of the material parameters on the channel geometry

In order to ascertain that the material parameters measured by active-sound spectroscopy correspond to bulk properties. We conducted a series of two experiments in microfluidc channels of width 1 mm and 2 mm. Figs. 33a and 33a indicates that the velocity fluctuation spectra are not altered by confinement. Accordingly, the angular variations of the speed of sound measured in the two channels are indistinguishables within our experimental accuracy. Fitting the speed of sound with the Toner Tu prediction gives $\lambda_1 = 0.75 \pm 0.1$ and $\sigma = 1.1 \pm 0.1$ (mm/s)^2. All measurements reported in the main text correspond to experiments performed in 2 mm-wide channels and therefore correspond to bulk properties.

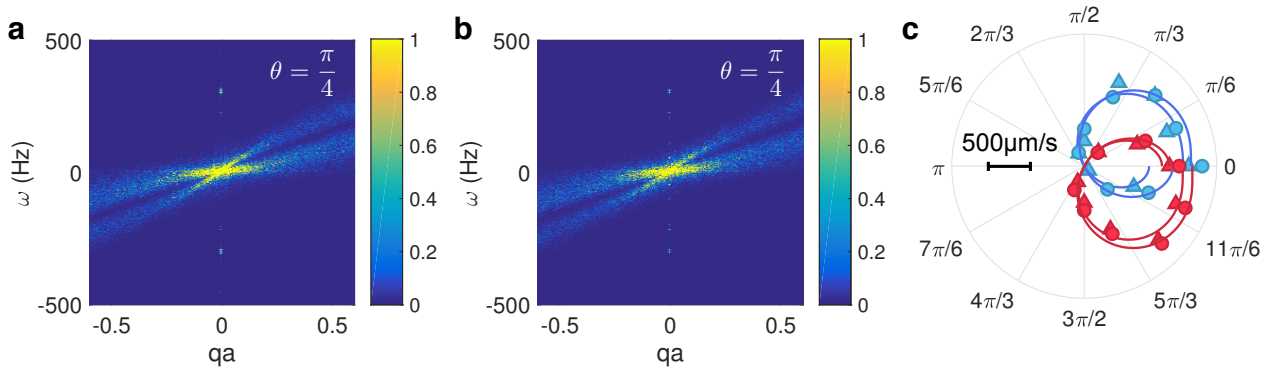

Figure 33 | **Impact of confinement on sound propagation** **a**, Power spectrum of the transverse velocity fluctuations $\langle|v_{q,\omega}|^2\rangle/\langle|v_{q=0,\omega=0}|^2\rangle$, in a channel of width 1 mm. $\theta = \pi/4$ and $\rho_0 = 0.06$. **b**, Power spectrum of the transverse velocity fluctuations $\langle|v_{q,\omega}|^2\rangle/\langle|v_{q=0,\omega=0}|^2\rangle$, in a channel of width 2 mm. $\theta = \pi/4$ and $\rho_0 = 0.07$. **c**, Polar plots of the speed of sound, $c_\pm(\theta) = \lim_{q\to 0}[\omega \pm (\theta)/q]$ measured from the slope at $q = 0$ of the dispersion relations. Experimental data: dots (1 mm wide channel), triangles (2 mm wide channel). Solid lines: theoretical fits. Same experimental conditions as in **a** and **b**.

Supplementary Note 3: Hydrodynamic theory of polar active liquids

1 Toner and Tu hydrodynamics

We recall below the hydrodynamic description of polar flocks, also termed polar active liquids, as first introduced by Toner and Tu in [122] and reviewed in [124, 76]. These active materials are associated with two hydrodynamic fields: the liquid density $\rho(\mathbf{r},t)$, and the local velocity field $\mathbf{v}(\mathbf{r},t)$. $\rho(\mathbf{r},t)$ is a slow variable because particle number is conserved, while $\mathbf{v}(\mathbf{r},t)$ is a slow variable only in the polar-liquid phase where rotational symmetry is spontaneously broken. As a matter of fact, we are dealing here with an instance of dry active matter where momentum is not conserved [76]. In the case of active colloids propelling on a substrate, the solid surface acts as a momentum sink. Toner and Tu constructed a set of phenomenological equations of motion using only symmetry and conservation principles. Since then, these equations have been confirmed by kinetic theories constructed both from minimalistic and realistic microscopic models [5, 43, 13]. For a 2D active liquid, in their most general form, Toner and Tu equations read:

$$\partial_t \rho + \nabla\cdot(\mathbf{v}\rho) = D\Delta\rho, \tag{51}$$

and,

$$\begin{aligned}\partial_t \mathbf{v} + \lambda_1(\mathbf{v}\cdot\nabla)\mathbf{v} + \lambda_2(\nabla\cdot\mathbf{v})\mathbf{v} + \lambda_3\nabla(|\mathbf{v}|^2) = {} & a_2\mathbf{v} - a_4|\mathbf{v}|^2\mathbf{v} - \sigma_1\nabla\rho - \sigma_2\left(\mathbf{v}\cdot\nabla\rho\right)\mathbf{v} \\ & + D_B\nabla\left(\nabla\cdot\mathbf{v}\right) + D_T\nabla^2\mathbf{v} + D_2\left(\mathbf{v}\cdot\nabla\right)^2\mathbf{v} \\ & + D_{\rho 1}\Delta\rho\mathbf{v} + D_{\rho 2}\left[\left(\mathbf{v}\cdot\nabla\right)^2\rho\right]\mathbf{v} + D_{\rho 3}\nabla\left(\mathbf{v}\cdot\nabla\rho\right).\end{aligned} \tag{52}$$

Eqs. (51) and (52) include 14 unknown materials constants which a priori all depend on ρ. Before recalling the physical meaning of these lengthy equations, we note that the last three terms were neglected in [122]. We

keep them here as they are allowed by symmetry and are of the same order in a gradient expansion. The λ_is are all convective coefficients. $\lambda_2 = \lambda_3 = 0$ and $\lambda_1 = 1$ is a normal, passive fluid. The a_2 and a_4 terms are the usual Ginsburg Landau term allowing for spontaneous symmetry breaking. Their ratio sets the magnitude of the mean flow speed in the ordered phase. The $D_{\rm B}$, $D_{\rm T}$ and D_2 terms in Eq. (52) are the anisotropic elastic (Frank) constants of this broken symmetry fluid. The D_ρs couple density and elastic deformations. D is the translation diffusion of the active particles which we neglect below.

2 Linear fluctuations

We are interested in describing the linear fluctuations of the density and velocity fields in a homogeneous polar liquid of average density $\rho = \rho_0 + \delta\rho$ and velocity $\mathbf{v}(\mathbf{r},t) = [u_0 + u(\mathbf{r},t)]\,\hat{\mathbf{x}} + v(\mathbf{r},t)\hat{\mathbf{y}}$. Once linearized around this steady state, the three equations of motion take the form:

$$\partial_t\rho + \rho_0\left(\partial_x u + \partial_y v\right) + u_0\partial_x\rho = 0, \tag{53}$$

$$\begin{aligned}\partial_t u + \lambda_1 u_0\partial_x u + \lambda_2 u_0\left(\partial_x u + \partial_y v\right) + 2\lambda_3 u_0\partial_x u = &-2a_4u_0^2u - \sigma\partial_x\rho \\ &+ (D_T + D_B + D_2u_0^2)\partial_{xx}u + D_B\partial_{xy}v + D_{\rm T}\partial_{yy}u \\ &+ u_0(D_{\rho1} + D_{\rho3} + u_0^2D_{\rho2})\partial_{xx}\rho + D_{\rho1}u_0\partial_{yy}v,\end{aligned} \tag{54}$$

$$\begin{aligned}\partial_t v + \lambda_1 u_0\partial_x v + 2\lambda_3 u_0\partial_y u = &-\sigma\partial_y\rho + D_{\rho3}u_0\partial_{xy}\rho \\ &+ (D_T + D_B)\partial_{yy}v + D_B\partial_{xy}u + (D_2u_0^2 + D_{\rm T})\partial_{xx}v,\end{aligned} \tag{55}$$

We have also ignored the anisotropy of the liquid compressibility by setting $\sigma_2 = 0$ and noted $\sigma_1 = \sigma$ as it will play no role in all that follows. Eq. (54) indicates that longitudinal velocity fluctuations relax in a finite time of the order $1/(2a_4u_0^2)$. In the hydrodynamic limit the variations of u are therefore slaved to ρ and v. Focusing on time scales larger than $1/(2a_4u_0^2)$, and length scales larger than $\lambda_1/(2a_4u_0)$, Eq. (54) readily simplifies into:

$$u = -\frac{\sigma}{2a_4u_0^2}\partial_x\rho + \mathcal{O}(\nabla^2). \tag{56}$$

This relation is verified in our experiments, see Fig. 3b in the main text. Plugging Eq. (56) into Eqs. (53) and (55), the linear dynamics of the only two slow modes take the much simpler form:

$$\partial_t\rho + \rho_0\left(\partial_y v\right) + u_0\partial_x\rho = D'\partial_x^2\rho \tag{57}$$

$$\partial_t v + \lambda_1 u_0\partial_x v = -\sigma\partial_y\rho + D_\perp\partial_y^2 v + D_\parallel\partial_x^2 v + u_0D_\rho\partial_{xy}^2\rho \tag{58}$$

where,

$$D_\perp = D_T + D_B \tag{59}$$

$$D_\parallel = D_2u_0^2 + D_{\rm T} \tag{60}$$

$$D_\rho = D_{\rho_3} - \frac{\lambda_3\sigma}{a_4u_0^2} \tag{61}$$

$$D' = \frac{\sigma\rho_0}{2a_4u_0^2} \tag{62}$$

While D' is measured from the linear relation between density and longitudinal-velocity fluctuations, Fig. 3b, a more careful analysis of the fluctuation spectra is required to measure the values of the five other material constant characterizing the linear hydrodynamics of the polar fluid: λ_1, σ, $D_\perp$, $D_\parallel$, and D_ρ.

3 Dispersion relations of the slow modes

Let us look for for plane-wave solutions of the two linear equations defined by Eqs. (57) and (58). Writing the wave amplitudes $\rho(\mathbf{q},\omega)$ and $v(\mathbf{q},\omega)$, where ω is the frequency and $\mathbf{q} = q(\cos\theta, \sin\theta)$ is the wave vector, we find that they obey the matrix equation:

$$i\omega \begin{bmatrix} \rho(\mathbf{q},\omega) \\ v(\mathbf{q},\omega) \end{bmatrix} = \mathbf{M} \cdot \begin{bmatrix} \rho(\mathbf{q},\omega) \\ v(\mathbf{q},\omega) \end{bmatrix}. \tag{63}$$

The response matrix $\mathbf{M}$ is defined as $\mathbf{M} = iq\mathbf{C} - q^2\mathbf{D}$, where

$$\mathbf{C} = \begin{pmatrix} u_0 \cos(\theta) & \rho_0 \sin(\theta) \\ \sigma \sin(\theta) & \lambda_1 u_0 \cos(\theta) \end{pmatrix}, \tag{64}$$

and

$$\mathbf{D} = \begin{pmatrix} D' \cos^2\theta & 0 \\ \frac{1}{2} u_0 D_\rho \sin(2\theta) & D_\parallel \cos^2(\theta) + D_\perp \sin^2(\theta) \end{pmatrix}. \tag{65}$$

The eigenvectors of the linear system defined by Eq. (63) are mixed modes coupling density and transverse velocity fluctuations. Their dispersion relations are defined by the eigenvalues $\omega_\pm(q,\theta)$ of $\mathbf{M}(\mathbf{q})$ which take a simple form in the limit of small wavevectors:

$$\omega_\pm(q,\theta) = \left[c_\pm(\theta) q + \mathcal{O}(q^3)\right] + i\Delta\omega_\pm(q,\theta). \tag{66}$$

The associated eigenmodes correspond to non-dispersive plane waves propagating with a phase velocity $c_\pm$ and attenuated over a time $2\pi/(\Delta\omega_\pm)$.

4 Speed of sound

Unlike sound waves in isotropic passive liquids, $c_\pm$ depends on the direction of propagation θ. As predicted first by Toner and Tu [122], we find:

$$2c_\pm(\theta) = (1+\lambda_1)\, u_0 \cos\theta \pm \sqrt{(\lambda_1 - 1)^2 u_0^2 \cos^2\theta + 4\sigma\rho_0 \sin^2\theta}. \tag{67}$$

The non-monotonic angular variations of the speed of sound are in excellent agreement with our experimental findings, see Figure 2 g,h,i in the main text. Analysing the angular variations of the speed of sound, we infer both the convective coefficient λ_1 and the compressibility σ, see Fig. 3c. As thoroughly explained below, measuring the orientational elasticity of the polar liquid requires inspecting the damping dynamics, or equivalently the spectral width of the density and velocity fluctuations.

5 Sound-wave damping and measurement of the orientational-elasticity constants

Let us consider the linear response of the polar liquid to a random white noise $\boldsymbol{\xi} = (\xi_\rho(\mathbf{r},t), \xi_v(\mathbf{r},t))$. ξ_ρ is conserved while ξ_v is a non conserved random force field acting respectively on ρ and v. In Fourier space the stochastic equations of motion are:

$$i\omega \begin{bmatrix} \rho(\mathbf{q},\omega) \\ v(\mathbf{q},\omega) \end{bmatrix} = \mathbf{M} \cdot \begin{bmatrix} \rho(\mathbf{q},\omega) \\ v(\mathbf{q},\omega) \end{bmatrix} + \boldsymbol{\xi}(\mathbf{q},\omega). \tag{68}$$

The power spectra of both ρ and v are easily computed from Eq. (68) and take the same functional form:

$$|v(\mathbf{q},\omega)|^2 = \frac{\alpha_+}{(\omega - c_+ q)^2 + \Delta\omega_+^2} + \frac{\alpha_-}{(\omega - c_- q)^2 + \Delta\omega_-^2} \tag{69}$$

where the noise variance sets the values of the amplitude factors $\alpha_\pm$ which are irrelevant to all that follows. The velocity spectrum is the sum of two Lorentzian functions peaked along the dispersion relations $\omega = c_\pm(\theta)q$. This low-q theory accurately predicts the non-dispersive part of the dispersion relation, but obviously fails in describing wave dispersion at short wave lengths, Figs. 2d,e,f. The spectral width $\Delta\omega_\pm$ is computed from Eq. (63):

$$\Delta\omega_\pm(q,\theta) = \frac{q^2}{4}\left[-(D' + D_\perp + D_\parallel) - (D' + D_\parallel - D_\perp)\cos(2\theta) \pm D_\rho u_0\sqrt{\frac{\rho_0}{\sigma}}\sin(2\theta)\right] + \mathcal{O}(q^3) \tag{70}$$

This expression is rather complex, yet it is clear that the spectral width of the sound modes is set by the elastic constants of the broken symmetry fluid. Their values and their variations with the average fluid density are easily computed when inspecting the two cases corresponding to $\theta = \pi/2$ and $\theta = \pi/4$.

Transverse waves: $\theta = \pi/2$

The case of sound waves propagating along the transverse direction $\theta = \pi/2$ is straightforward. The two dispersion relations are symmetric, see Fig. 2e, the two speeds of sound are opposite, $c_\pm(\pi/2) = \pm\sqrt{\sigma\rho_0}$, and their spectral width grows quadratically with q^2 as expected:

$$\Delta\omega_\pm(\pi/2) = \frac{1}{2}D_\perp q^2. \tag{71}$$

High-q distortions are more effectively suppressed by the alignment interactions between the active particles, or equivalently by orientational elasticity. Fitting the variations of $\Delta\omega_\pm(\pi/2)$ by a quadratic function provides a direct measurement of $D_\perp$. Repeating the same procedure for all densities we find that $D_\perp$ increases linearly with ρ_0. The denser the polar liquid, the stiffer.

Oblique waves: $\theta = \pi/4$

Repeating the same analysis at $\theta = \pi/4$, we find that the two sound modes propagate at $c_\pm(\pi/4) = \frac{\left(u_0 \pm \sqrt{\sigma\rho_0}\right)}{\sqrt{2}}$. The spectral width of the two modes grows again as q^2, and are related to the elastic constants by

$$\Delta\omega_+\left(\frac{\pi}{4}\right) + \Delta\omega_-\left(\frac{\pi}{4}\right) = \left(D_\perp + D_\parallel + D'\right)q^2, \tag{72}$$

and

$$\Delta\omega_+\left(\frac{\pi}{4}\right) - \Delta\omega_-\left(\frac{\pi}{4}\right) = \frac{\rho_0 D_\rho u_0}{\sqrt{\sigma\rho_0}}q^2. \tag{73}$$

Fitting $\Delta\omega_+\left(\frac{\pi}{4}\right) + \Delta\omega_-\left(\frac{\pi}{4}\right)$ by a quadratic function of the wave vector provides a direct measurement of the average elastic constant $\left(D_\perp + D_\parallel + D'\right)$, see Eq. (72). As shown in the main text, we find a value 4 orders of magitude larger than that of D' which can therefore be neglected. As $D_\perp$ is known from the previous analysis at $\theta = \pi/2$, $D_\parallel$ is readily deduced from the quadratic fit of $\Delta\omega_+\left(\frac{\pi}{4}\right) + \Delta\omega_-\left(\frac{\pi}{4}\right)$.

The last material constant to be determined is D_ρ. In principle, it could be measured by fitting $\Delta\omega_+\left(\frac{\pi}{4}\right) - \Delta\omega_-\left(\frac{\pi}{4}\right)$ by a quadratic function of q, as both u_0 and σ were already measured independently (from velocity and sound speed measurements, see Fig. 34 and Eq. (67)). In the specific case of our colloidal-roller experiments, the precision of our measurements of $\Delta\omega_\pm$ prevents us from determining $D_\parallel$. Nonetheless, this last material constant can be estimated exploiting our quantitative understanding of the colloidal-roller interactions as explained.

6 Colloidal-roller hydrodynamics

Microscopic dynamics

We briefly recall the kinetic-theory framework used to derive of the Toner and Tu equations for the polar-liquid phase of colloidal rollers. In [13], starting from the Maxwell and Stokes equations, and after lengthy algebra, we showed that the rollers propel at constant speed, ν_0, and interact via their orientational degree of freedom only. Noting $\mathbf{r}_i$ the position of their center of mass, and θ_i the orientation of their velocity $\boldsymbol{\nu}_i(t) = \nu_0(\cos\theta_i, \sin\theta_i)$, their translational and angular dynamics can be recast into the compact form:

$$\partial_t \mathbf{r}_i(t) = \nu_0 \hat{\boldsymbol{\nu}}_i, \tag{74}$$

and

$$\partial_t \theta_i(t) = -\partial_{\theta_i} \sum_{j\neq i} \mathcal{H}(\mathbf{r}_i - \mathbf{r}_j; \theta_i, \theta_j) + \sqrt{2D_{\mathrm{R}}}\xi_i(t) \tag{75}$$

where the ξ_i are uncorrelated Gaussian white noises of unit variance, and where the effective interaction potential $\mathcal{H}$ is given by

$$\mathcal{H}(\mathbf{r}_i - \mathbf{r}_j; \theta_i, \theta_j) = A(r)\hat{\boldsymbol{\nu}}_i \cdot \hat{\boldsymbol{\nu}}_j + B(r)\hat{\boldsymbol{\nu}}_i \cdot \mathbf{r} + C(r)\hat{\boldsymbol{\nu}}_j \cdot (2\hat{\mathbf{r}}\hat{\mathbf{r}} - \mathbb{I}) \cdot \hat{\boldsymbol{\nu}}_i. \tag{76}$$

This functional form turns out to be very generic [18] and corresponds to the first three terms of a systematic multipolar expansion of the angular interactions. In the specific case of interacting rollers the three kernels $A(r)$, $B(r)$ and $C(r)$ can be approximated within a far field approximation for the hydrodynamic and electrostatic interactions:

$$A(r) = A_1 \left(\frac{a}{r}\right)^3 \Theta(r) + A_2 \left(\frac{a}{r}\right)^5 \Theta(r), \tag{77}$$

$$B(r) = B_1 \left(\frac{a}{r}\right)^4 \Theta(r), \tag{78}$$

$$C(r) = C_1 \left(\frac{a}{r}\right)^3 \Theta(r) + C_2 \left(\frac{a}{r}\right)^5 \Theta(r) + C_3 \left(\frac{a}{r}\right)^2. \tag{79}$$

The A term in Eq. (76) is akin to a ferromagnetic coupling, and stems both from hydrodynamic (A_1) and electrostatic interactions (A_2). The B term is a repelling torque that originates from the electrostatic interactions between the electrostatic dipoles formed by the surface charges of the rollers. Finally, the C term promotes alignment of the roller i along a dipolar field centered on roller j. This term has three different origins. The C_1 and C_2 terms have the same microscopic origin as A_1 and A_2, while C_3 stems from the finite size of the rollers and vertical confinement which altogether result in genuinely long-range interactions. All other interactions are indeed screened over a distance set by the channel height H. For the sake of simplicity, we approximate the screening function $\Theta(r)$ by a step function $\Theta(r) = 1$ if $r \leq H/\pi$ and $\Theta(r) = 0$ otherwise.

All the scalar coefficients in Eqs. (77), (78) and (79) have units of inverse time scales, and are all of the order of the so-called Maxwell relaxation rate $\tau^{-1} \sim 3\,\mathrm{kHz}$ [78, 13]. Rotational diffusion was measured from the exponential decay of the correlations of the roller orientation in the gas phase [13, 12, 84]. Within our experimental conditions, we find [84]:

$$A_1 = A_2 = B_1 = C_1 \sim \tau^{-1} \tag{80}$$

$$C_2 \sim 1.7\tau^{-1} \tag{81}$$

$$C_3 \sim (4.5 \times 10^{-2})\tau^{-1} \tag{82}$$

$$D_{\mathrm{R}} \sim 3\,\mathrm{s}^{-1} \tag{83}$$

As C_3 is a thousand times smaller that all the other interaction strengths, we henceforth neglect this contribution to Eq. (79). This simplification is further supported by the very good agreement between our measurements

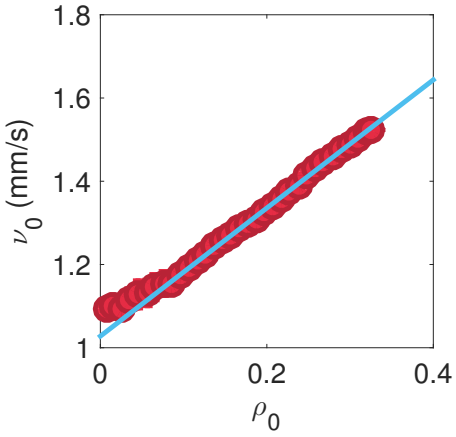

Figure 34 | **Roller speed.** Red dots: Variations of the roller speed with the roller area fraction ρ_0. Blue line: best linear fit.

and our hydrodynamic theory described in the main text. The last two parameters needed to fully specify the dynamics of the rollers are the screening distance $H = 110\,\mu$m, and the roller speed ν_0. Our simplified model predicts a constant roller speed at all densities. To go beyond this approximation we measured the variations of ν_0 with the average density ρ_0 and use this relation as a phenomenological law Fig. 34.

Kinetic theory of the polar-liquid phase

We now outline the construction of the hydrodynamic equations for the density and velocity fields in the polar-liquid phase. We use here a conventional kinetic-theory framework reviewed e.g. in [76]. We first write a conservation equation for the one-point distribution function $\psi(\mathbf{r},\theta,t)$, viz the probability to find a particle at position $\mathbf{r}$ with an orientation θ:

$$\partial_t\psi(\mathbf{r},\theta,t) + \nu_0\hat{\boldsymbol{\nu}}\cdot\nabla\psi(\mathbf{r},\theta,t) - D_{\mathrm{R}}\partial_\theta^2\psi(\mathbf{r},\theta,t) = \partial_\theta\mathcal{I}_{\mathrm{int}}(\mathbf{r},\theta,t) \tag{84}$$

For interaction-free particles moving in a homogeneous media, the r.h.s of the above equation would vanish. ψ would be merely advected due to self-propulsion, and would diffuse in the θ direction due to angular noise. The angular current $\mathcal{J}_{\mathrm{int}}$ accounts for the roller-roller interactions. Starting from the microscopic equations of motion, Eqs. (74) and (75), we derived the functional form of $\mathcal{J}_{\mathrm{int}}(\mathbf{r},\theta,t)$ in [13]. In brief, as the range of the effective potential $\mathcal{H}$ is of the order of 40 colloid radii, even at the lowest colloid fraction, each particle interacts on average with $\sim$ 200 neighbors. This large number suggests using a mean-field description to establish the functional form of $\mathcal{J}_{\mathrm{int}}$. We therefore assume that the two-point function factorizes as: $\psi^{(2)}(\mathbf{r},\theta;\mathbf{r}',\theta') = \psi(\mathbf{r},\theta)\psi(\mathbf{r}',\theta')$ and vanishes for $|\mathbf{r}-\mathbf{r}'| < 2a$, in order to account for the finite size of the rollers. $\mathcal{J}_{\mathrm{int}}$ then takes the form:

$$\mathcal{J}_{\mathrm{int}} = -\psi(\mathbf{r},\theta)\int_{|\mathbf{r}-\mathbf{r}'|>2a}\mathrm{d}\theta'\mathrm{d}\mathbf{r}'\psi(\mathbf{r}',\theta')\partial_\theta\mathcal{H}(\mathbf{r}-\mathbf{r}';\theta,\theta') \tag{85}$$

Integrating the above equation over θ, we recover the mass conservation relation:

$$\partial_t\rho(\mathbf{r},t) + \nabla\cdot\mathbf{J}(\mathbf{r},t) = 0, \tag{86}$$

where the roller current $\mathbf{J}(\mathbf{r},t)$ and velocity fields are defined as $\mathbf{J} \equiv \nu_0\int\mathrm{d}\theta\,\hat{\boldsymbol{\nu}}\psi(\mathbf{r},\theta,t)$, and $\mathbf{J} \equiv \rho\mathbf{v}$. The dynamical evolution of $\mathbf{J}(\mathbf{r},t)$ is obtained by multiplying Eq. 84 by $\hat{\mathbf{v}}$ and integrating it over the angular variable.

At leading order in a systematic gradient expansion it takes the form:

$$\partial_t \mathbf{J} + v_0^2 \nabla \cdot \left[\rho \left(\mathbf{Q} + \frac{1}{2}\mathbb{I} \right) \right] = - D_{\mathrm{R}} \mathbf{J} + \alpha_1 \rho (\mathbb{I} - 2\mathbf{Q}) \cdot \mathbf{J} - \beta \frac{v_0}{2} (\mathbb{I} - 2\mathbf{Q}) \cdot \rho \nabla \rho + \alpha_2 \rho (\mathbb{I} - 2\mathbf{Q}) \cdot \Delta \mathbf{J} + \gamma_2 \rho (\mathbb{I} - 2\mathbf{Q}) \cdot \tilde{\Delta} \mathbf{J}, \tag{87}$$

where

$$\tilde{\Delta} = \begin{pmatrix} \partial_{xx} - \partial_{yy} & 2\partial_{xy} \\ 2\partial_{xy} & \partial_{yy} - \partial_{xx} \end{pmatrix}, \tag{88}$$

and where $\alpha_1 = 0.5\,\tau^{-1}$ and the elastic constant $\alpha_2 = \frac{Ha}{7}\,\tau^{-1}$ stem for the velocity-alignment interactions at the microscopic level (A terms in Eq. (75)). $\beta = \frac{a}{2}\,\tau^{-1}$ originates from the repulsive interactions (B terms in Eq. (75)). finally the anisotropic elasticity constant γ_2 results from the C terms in Eq. (75) which couple the roller orientations and relative positions.

At this stage, we do not have a closed set of hydrodynamic equations but only a relation between ρ, $\mathbf{J}$ and the local nematic tensor $\mathbf{Q}$, defined as: $\rho\mathbf{Q} = \langle \hat{\boldsymbol{\nu}}\hat{\boldsymbol{\nu}} - \frac{1}{2}\mathbb{I} \rangle$. An additional closure relation is required to establish the hydrodynamic theory of this active material.

Hydrodynamic theory

Deep in the polar-liquid phase we assume Gaussian fluctuations of the velocity field. This ansatz imposes the relation

$$\mathbb{Q} = \frac{1}{\nu_0^6} v^4 \left(\mathbf{v}\mathbf{v} - \frac{\nu_0^2}{2}\mathbb{I} \right). \tag{89}$$

Using this relation in Eq. (87) we find the hydrodynamic equation of the polar liquid formed by interacting colloidal rollers. Once linearized around a homogeneous flow field $\mathbf{v} = (u_0 + u)\hat{\mathbf{x}} + v\hat{\mathbf{y}}$ it takes the very same form as the linearized Toner and Tu equations:

$$\partial_t \rho + \rho_0 \partial_y v + u_0 \partial_x \rho = D' \partial_x^2 \rho \tag{90}$$

$$\partial_t v + \lambda_1 u_0 \partial_x v = -\sigma \partial_y \rho + D_\perp \partial_y^2 v + D_\parallel \partial_x^2 v + u_0 D_\rho \partial_{xy}^2 \rho \tag{91}$$

where all the hydrodynamic coefficients are now defined from the microscopic interaction parameters:

$$\lambda_1 = \frac{u_0^2}{\nu_0^2} \tag{92}$$

$$\sigma = \frac{a^2}{2\tau} u_0(\rho_0) \tag{93}$$

$$D_\perp = \frac{5Ha\rho_0}{14\tau} \tag{94}$$

$$D_\parallel = \frac{3Ha\rho_0}{14\tau} \tag{95}$$

$$D_\rho = \frac{D_\perp - D_\parallel}{\rho_0} \tag{96}$$

$$D' = 0 \tag{97}$$

Eqs. (90) to (97) fully prescribe the linear hydrodynamic equations of colloidal-roller liquids. Several comments are in order. All material constants depend on the liquid density. However deep in the polar phase the

polar liquid flows at a speed indistinguishable from the individual roller speed ν_0 and $\lambda_1 \sim$ constant. D' is vanishingly small in agreement with our experimental measurements. D' is indeed measured to be 4 orders of magnitude smaller than all the other elastic constants, see Fig. 3. $D_\perp$, $D_\parallel$ and D_ρ are related by Eq. (96). The value of $D_\parallel$, which we cannot measure directly, can thus be inferred from $D_\perp$ and D_ρ

These predictions are confronted to our spectroscopy method in Figure 3 in the main document and validate the relevance of active-sound spectroscopy to infer the material constants of broken-symmetry active materials from their fluctuation spectra.

Critical discussion of the kinetic theory

We highlight in this section the numerous assumptions required to derive the hydrodynamic equations for the colloidal-roller liquid starting from the microscopic description of the Quincke phenomenon, at the single-colloid level [13]. Despite these numerous approximations the convective coefficient (λ_1), and the compressibility (σ) of the active fluid are correctly predicted. The elastic constants are however overestimated. Kinetic theory only provides the correct orders of magnitude and more importantly their variations with ρ_0. A better theory should address the following issues:

1. *Quincke rotation near a conducting wall.* Our description of the Quincke mechanism is classically performed in the limit of vanishingly small Debye length. This approximation might be too severe when, as in our experiments, the colloids lie on a charged surface.

2. *Orientational interactions.* When describing the interactions between Quincke rollers, we neglect the interaction forces, and focus on the interactions torques. Simply put we assume the roller velocity ν_0 to be a constant, and the roller velocity to be slaved to their orientation. This approximation is theoretically justified by the fact that the Quincke mechanism results from a spontaneous symmetry breaking. Therefore, the single-colloid orientation is slaved to a soft-mode. In practice, we do observe fluctuations of ν_0 of the order of 10 %. An improved theory should take into account the interaction forces as well.

3. *Far-field interactions.* The disturbances to the electric and hydrodynamic fields induced by the rollers were computed in the far-field limit. The resulting interactions are therefore an approximate of the actual interactions which also include near-field contributions.

4. *Interaction range.* Both the hydrodynamic and electric field induced by the roller motion are exponentially screened over a distance of the order of the channel height H. In our theory we approximate this screening by a step function.

5. *Mean-field approximation in the kinetic theory.* Another severe approximation is the mean-field assumption used to factorize the two-point function as $\psi^{(2)}(\mathbf{r},\theta,t;\mathbf{r}',\theta',t) = \psi(\mathbf{r},\theta,t)\psi(\mathbf{r}',\theta',t)$. This approximation is especially questionable deep in the ordered phase where we do observe local structural correlations.

6. *Gaussian approximation.* In order to close the hierarchy of equations for all the angular moments of ψ, we had to resort to a Gaussian approximation for the angular fluctuations of the roller orientation.

These approximations are numerous, and some are uncontrolled. The fair agreement with our measurements points toward a remarkable robustness of this simplified model. Going beyond these approximations is a significant challenge for active matte theorists.

Experimental setup

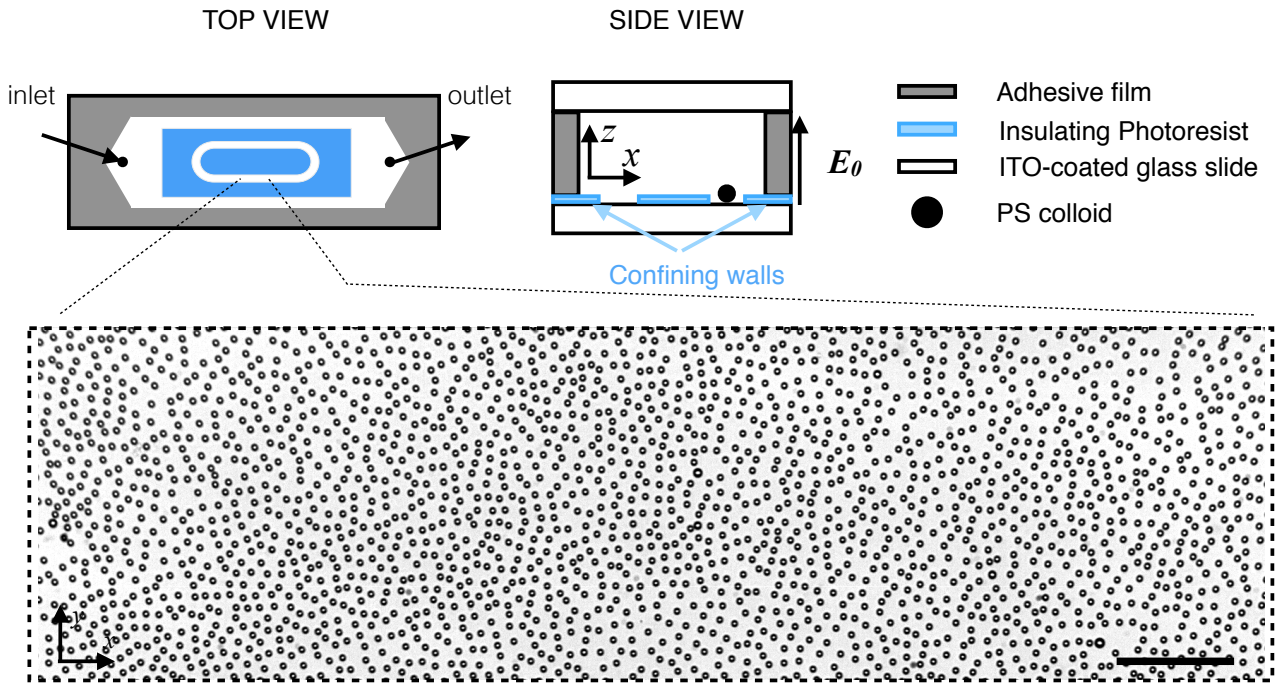

Figure 35 | **Sketch of the microfluidic device. Top view.** A one-centimeter wide channel is used to flow the PS colloids. A pattern in the shape of a racetrack confines the rollers. The picture shows a snapshot of a polar liquid flowing along the racetrack. Scale bar: 100 μm. The observation window shows only a small part of the colloidal liquid. **Side view.** The colloids roll on the bottom electrode, the obstacles electrostatically repel the rollers. An adhesive film (double-sided scotch tape) sets the gap between the electrodes.

References

[1] Michele Ballerini, Nicola Cabibbo, Raphael Candelier, Andrea Cavagna, Evaristo Cisbani, Irene Giardina, Vivien Lecomte, Alberto Orlandi, Giorgio Parisi, Andrea Procaccini, et al. Interaction ruling animal collective behavior depends on topological rather than metric distance: Evidence from a field study. *Proceedings of the national academy of sciences*, 105(4):1232–1237, 2008 (cit. on p. 8).

[2] Teresa Bauer, Felix Höfling, Tobias Munk, Erwin Frey, and Thomas Franosch. The localization transition of the two-dimensional lorentz model. *The European Physical Journal Special Topics*, 189(1):103–118, 2010 (cit. on pp. 76, 79, 81).

[3] Clemens Bechinger, Roberto Di Leonardo, Hartmut Löwen, Charles Reichhardt, Giorgio Volpe, and Giovanni Volpe. Active particles in complex and crowded environments. *Reviews of Modern Physics*, 88(4):045006, 2016 (cit. on pp. 75, 79).

[4] Spring Berman, Radhika Nagpal, and Adám Halász. Optimization of stochastic strategies for spatially inhomogeneous robot swarms: A case study in commercial pollination. In *Intelligent Robots and Systems (IROS), 2011 IEEE/RSJ International Conference on*, pages 3923–3930. IEEE, 2011 (cit. on p. 91).

[5] Eric Bertin, Michel Droz, and Guillaume Grégoire. Hydrodynamic equations for self-propelled particles: microscopic derivation and stability analysis. *Journal of Physics A: Mathematical and Theoretical*, 42(44):445001, 2009 (cit. on pp. 17, 108, 127).

[6] Silvio Bianchi, Filippo Saglimbeni, and Roberto Di Leonardo. Holographic imaging reveals the mechanism of wall entrapment in swimming bacteria. *Physical Review X*, 7(1):011010, 2017 (cit. on p. 75).

[7] Daniel Blair and Eric Dufresne. The matlab particle tracking code repository. retrieved from http://physics.georgetown.edu/matlab/ (cit. on pp. 41, 62).

[8] Daniel L Blair, T Neicu, and Arshad Kudrolli. Vortices in vibrated granular rods. *Physical Review E*, 67(3):031303, 2003 (cit. on p. 8).

[9] Jean-Philippe Bouchaud and Antoine Georges. Anomalous diffusion in disordered media: statistical mechanisms, models and physical applications. *Physics reports*, 195(4-5):127–293, 1990 (cit. on pp. 75, 83).

[10] Guillaume Briand, Michael Schindler, and Olivier Dauchot. Spontaneously flowing crystal of self-propelled particles. *Physical review letters*, 120(20):208001, 2018 (cit. on p. 10).

[11] Antoine Bricard. *Dynamiques collectives de colloïdes auto-propulsés*. PhD thesis, Université Paris Diderot (Paris 7), 2014 (cit. on p. 27).

[12] Antoine Bricard, Jean-Baptiste Caussin, Debasish Das, Charles Savoie, Vijayakumar Chikkadi, Kyohei Shitara, Oleksandr Chepizhko, Fernando Peruani, David Saintillan, and Denis Bartolo. Emergent vortices in populations of colloidal rollers. *Nature communications*, 6:7470, 2015 (cit. on pp. 24, 39, 52, 76, 91, 104, 107, 108, 111, 119, 131).

[13] Antoine Bricard, Jean-Baptiste Caussin, Nicolas Desreumaux, Olivier Dauchot, and Denis Bartolo. Emergence of macroscopic directed motion in populations of motile colloids. *Nature*, 503(7474):95, 2013 (cit. on pp. 8, 11, 18, 24, 27, 32, 34, 35, 36, 37, 38, 39, 51, 52, 54, 59, 62, 64, 76, 85, 86, 87, 91, 95, 98, 104, 105, 107, 110, 117, 118, 119, 123, 124, 125, 126, 127, 131, 132, 134).

[14] Aidan T Brown, Ioana D Vladescu, Angela Dawson, Teun Vissers, Jana Schwarz-Linek, Juho S Lintuvuori, and Wilson CK Poon. Swimming in a crystal. *Soft Matter*, 12(1):131–140, 2016 (cit. on p. 75).

[15] J Buhl, Gregory A Sword, and Stephen J Simpson. Using field data to test locust migratory band collective movement models. *Interface Focus*, 2(6):757–763, 2012 (cit. on pp. 117, 119).

[16] Ivo Buttinoni, Julian Bialké, Felix Kümmel, Hartmut Löwen, Clemens Bechinger, and Thomas Speck. Dynamical clustering and phase separation in suspensions of self-propelled colloidal particles. *Physical review letters*, 110(23):238301, 2013 (cit. on p. 91).

[17] Jean-Baptiste Caussin. *Collective dynamics of self-propelled particles : waves , vortex , swarm , braiding*. PhD thesis, ENS de Lyon, 2015 (cit. on pp. 17, 27, 32).

[18] Jean-Baptiste Caussin and Denis Bartolo. Tailoring the interactions between self-propelled bodies. *The European Physical Journal E*, 37(6):55, 2014 (cit. on pp. 104, 131).

[19] Jean-Baptiste Caussin, Alexandre Solon, Anton Peshkov, Hugues Chaté, Thierry Dauxois, Julien Tailleur, Vincenzo Vitelli, and Denis Bartolo. Emergent spatial structures in flocking models: A dynamical system insight. *Physical Review Letters*, 112(14):1–5, 2014 (cit. on pp. 16, 71, 108).

[20] Andrea Cavagna, Daniele Conti, Chiara Creato, Lorenzo Del Castello, Irene Giardina, Tomas S Grigera, Stefania Melillo, Leonardo Parisi, and Massimiliano Viale. Dynamic scaling in natural swarms. *Nature Physics*, 13(9):914, 2017 (cit. on pp. 117, 119).

[21] Andrea Cavagna and Irene Giardina. Bird flocks as condensed matter. *Annu. Rev. Condens. Matter Phys.*, 5(1):183–207, 2014 (cit. on pp. 91, 117, 119).

[22] Andrea Cavagna, Irene Giardina, Tomas S Grigera, Asja Jelic, Dov Levine, Sriram Ramaswamy, and Massimiliano Viale. Silent flocks: constraints on signal propagation across biological groups. *Physical review letters*, 114(21):218101, 2015 (cit. on p. 119).

[23] Hugues Chaté, Francesco Ginelli, Guillaume Grégoire, and Franck Raynaud. Collective motion of self-propelled particles interacting without cohesion. *Physical Review E*, 77(4):046113, 2008 (cit. on p. 14).

[24] Qian Chen, Sung Chul Bae, and Steve Granick. Directed self-assembly of a colloidal kagome lattice. *Nature*, 469(7330):381, 2011 (cit. on p. 117).

[25] Oleksandr Chepizhko, Eduardo G Altmann, and Fernando Peruani. Optimal noise maximizes collective motion in heterogeneous media. *Physical review letters*, 110(23):238101, 2013 (cit. on pp. 22, 23, 91, 95).

[26] Oleksandr Chepizhko and Fernando Peruani. Diffusion, subdiffusion, and trapping of active particles in heterogeneous media. *Physical review letters*, 111(16):160604, 2013 (cit. on pp. 67, 68, 75, 76, 79, 95, 106, 113).

[27] Iain D Couzin, Jens Krause, Richard James, Graeme D Ruxton, and Nigel R Franks. Collective memory and spatial sorting in animal groups. *Journal of theoretical biology*, 218(1):1–11, 2002 (cit. on p. 76).

[28] Adama Creppy, Olivier Praud, Xavier Druart, Philippa L Kohnke, and Franck Plouraboué. Turbulence of swarming sperm. *Physical Review E*, 92(3):032722, 2015 (cit. on p. 51).

[29] John C Crocker and David G Grier. Methods of digital video microscopy for colloidal studies. *Journal of colloid and interface science*, 179(1):298–310, 1996 (cit. on pp. 40, 62, 85, 99, 123).

[30] András Czirók, H Eugene Stanley, and Tamás Vicsek. Spontaneously ordered motion of self-propelled particles. *Journal of Physics A: Mathematical and General*, 30(5):1375, 1997 (cit. on pp. 15, 20, 21, 51).

[31] Linda J Daniels and DJ Durian. Propagating waves in a monolayer of gas-fluidized rods. *Physical Review E*, 83(6):061304, 2011 (cit. on p. 118).

[32] Rakesh Das, Manoranjan Kumar, and Shradha Mishra. Polar flock in the presence of random quenched rotators. *arXiv preprint arXiv:1802.08861*, 2018 (cit. on pp. 22, 23).

[33] Pierre-Gilles de Gennes. La percolation: un concept unificateur (percolation a unifying concept). *La Recherche*, 1976 (cit. on p. 65).

[34] Stephen J DeCamp, Gabriel S Redner, Aparna Baskaran, Michael F Hagan, and Zvonimir Dogic. Orientational order of motile defects in active nematics. *Nature materials*, 14(11):1110, 2015 (cit. on p. 117).

[35] Julien Deseigne, Olivier Dauchot, and Hugues Chaté. Collective motion of vibrated polar disks. *Physical review letters*, 105(9):098001, 2010 (cit. on pp. 8, 10, 18, 19, 27, 91, 117).

[36] Julien Deseigne, Sébastien Léonard, Olivier Dauchot, and Hugues Chate. Vibrated polar disks: spontaneous motion, binary collisions, and collective dynamics. *Soft Matter*, 8(20):5629–5639, 2012 (cit. on pp. 10, 19).

[37] Nicolas Desreumaux. *Emulsions microfluidiques et rouleurs colloïdaux : effets collectifs en matière molle forcée hors-équilibre*. PhD thesis, Université Pierre et Marie Curie, 2015 (cit. on p. 27).

[38] Nicolas Desreumaux, Jean Baptiste Caussin, Raphael Jeanneret, Eric Lauga, and Denis Bartolo. Hydrodynamic fluctuations in confined particle-laden fluids. *Physical Review Letters*, 111(11):1–5, 2013 (cit. on p. 34).

[39] Knut Drescher, Jörn Dunkel, Luis H Cisneros, Sujoy Ganguly, and Raymond E Goldstein. Fluid dynamics and noise in bacterial cell–cell and cell–surface scattering. *Proceedings of the National Academy of Sciences*, 108(27):10940–10945, 2011 (cit. on p. 75).

[40] Michelle Driscoll, Blaise Delmotte, Mena Youssef, Stefano Sacanna, Aleksandar Donev, and Paul Chaikin. Unstable fronts and motile structures formed by microrollers. *Nature Physics*, 13(4):375, 2017 (cit. on p. 86).

[41] Perry W Ellis, Daniel JG Pearce, Ya-Wen Chang, Guillermo Goldsztein, Luca Giomi, and Alberto Fernandez-Nieves. Curvature-induced defect unbinding and dynamics in active nematic toroids. *Nature Physics*, 14(1):85, 2018 (cit. on p. 117).

[42] Michael Chance Faleski, M Cristina Marchetti, and AA Middleton. Vortex dynamics and defects in simulated flux flow. *Physical Review B*, 54(17):12427, 1996 (cit. on p. 95).

[43] FDC Farrell, MC Marchetti, D Marenduzzo, and J Tailleur. Pattern formation in self-propelled particles with density-dependent motility. *Physical review letters*, 108(24):248101, 2012 (cit. on p. 127).

[44] Etienne Fodor and M Cristina Marchetti. The statistical physics of active matter: From self-catalytic colloids to living cells. *Physica A: Statistical Mechanics and its Applications*, 08 2017 (cit. on p. 43).

[45] Aden Forrow, Francis G Woodhouse, and Jörn Dunkel. Mode selection in compressible active flow networks. *Physical review letters*, 119(2):028102, 2017 (cit. on pp. 50, 60, 62).

[46] Thomas Franosch, Markus Spanner, Teresa Bauer, Gerd E Schröder-Turk, and Felix Höfling. Space-resolved dynamics of a tracer in a disordered solid. *Journal of Non-Crystalline Solids*, 357(2):472–478, 2011 (cit. on p. 76).

[47] Sumit Gangwal, Olivier J Cayre, Martin Z Bazant, and Orlin D Velev. Induced-charge electrophoresis of metallodielectric particles. *Physical review letters*, 100(5):058302, 2008 (cit. on p. 8).

[48] Delphine Geyer, Alexandre Morin, and Denis Bartolo. Sounds and hydrodynamics of polar active fluids. *Nature Materials*, 2018 (cit. on pp. 18, 19, 34, 36, 37).

[49] Francesco Ginelli. The Physics of the Vicsek model. *European Physical Journal: Special Topics*, 225(11-12):2099–2117, 2016 (cit. on p. 37).

[50] Francesco Ginelli, Fernando Peruani, Marie-Helène Pillot, Hugues Chaté, Guy Theraulaz, and Richard Bon. Intermittent collective dynamics emerge from conflicting imperatives in sheep herds. *Proceedings of the National Academy of Sciences*, 112(41):12729–12734, 2015 (cit. on pp. 117, 119).

[51] F Ginot, I Theurkauff, F Detcheverry, C Ybert, and C Cottin-Bizonne. Aggregation-fragmentation and individual dynamics of active clusters. *Nature communications*, 9(1):696, 2018 (cit. on p. 8).

[52] Guillaume Grégoire and Hugues Chaté. Onset of collective and cohesive motion. *Physical review letters*, 92(2):025702, 2004 (cit. on pp. 95, 106).

[53] Niels Grønbech-Jensen, AR Bishop, and Daniel Domínguez. Metastable filamentary vortex flow in thin film superconductors. *Physical review letters*, 76(16):2985, 1996 (cit. on p. 95).

[54] Jean-Pierre Hansen and Ian R McDonald. *Theory of Simple Liquids*. Academic Press, Oxford, fourth edition, 1990 (cit. on p. 120).

[55] Shlomo Havlin and Daniel Ben-Avraham. Diffusion in disordered media. *Advances in physics*, 51(1):187–292, 2002 (cit. on p. 75).

[56] Felix Höfling and Thomas Franosch. Crossover in the slow decay of dynamic correlations in the lorentz model. *Physical review letters*, 98(14):140601, 2007 (cit. on p. 79).

[57] Felix Höfling and Thomas Franosch. Anomalous transport in the crowded world of biological cells. *Reports on Progress in Physics*, 76(4):046602, 2013 (cit. on p. 75).

[58] Felix Höfling, Thomas Franosch, and Erwin Frey. Localization transition of the three-dimensional lorentz model and continuum percolation. *Physical review letters*, 96(16):165901, 2006 (cit. on pp. 76, 79, 81).

[59] Jonathan R Howse, Richard AL Jones, Anthony J Ryan, Tim Gough, Reza Vafabakhsh, and Ramin Golestanian. Self-motile colloidal particles: from directed propulsion to random walk. *Physical review letters*, 99(4):048102, 2007 (cit. on p. 8).

[60] Michael B Isichenko. Percolation, statistical topography, and transport in random media. *Reviews of modern physics*, 64(4):961, 1992 (cit. on p. 75).

[61] HJ Jensen, A Brass, and AJ Berlinsky. Lattice deformations and plastic flow through bottlenecks in a two-dimensional model for flux pinning in type-ii superconductors. *Physical review letters*, 60(16):1676, 1988 (cit. on p. 95).

[62] Yuliang Jin and Patrick Charbonneau. Dimensional study of the dynamical arrest in a random lorentz gas. *Physical Review E*, 91(4):042313, 2015 (cit. on p. 76).

[63] Albrecht M Kellerer. On the number of clumps resulting from the overlap of randomly placed figures in a plane. *Journal of applied probability*, 20(1):126–135, 1983 (cit. on p. 96).

[64] Serge Kernbach. *Handbook of collective robotics: fundamentals and challenges*. CRC Press, 2013 (cit. on p. 91).

[65] Nitin Kumar, Harsh Soni, Sriram Ramaswamy, and AK Sood. Flocking at a distance in active granular matter. *Nature communications*, 5:4688, 2014 (cit. on pp. 10, 117).

[66] Nikos Kyriakopoulos, Francesco Ginelli, and John Toner. Leading birds by their beaks: the response of flocks to external perturbations. *New Journal of Physics*, 18(7):073039, 2016 (cit. on pp. 15, 21, 43, 51, 63, 64, 118).

[67] Eric Lauga and Thomas R Powers. The hydrodynamics of swimming microorganisms. *Reports on Progress in Physics*, 72(9):096601, 2009 (cit. on p. 75).

[68] Oleg D Lavrentovich. Active colloids in liquid crystals. *Current Opinion in Colloid & Interface Science*, 21:97–109, 2016 (cit. on p. 117).

[69] Pierre Le Doussal and Thierry Giamarchi. Moving glass theory of driven lattices with disorder. *Physical Review B*, 57(18):11356, 1998 (cit. on p. 95).

[70] Guangxun Liao, Ivan I Smalyukh, JR Kelly, Oleg D Lavrentovich, and Antal Jakli. Electrorotation of colloidal particles in liquid crystals. *Physical Review E*, 72(3):031704, 2005 (cit. on p. 76).

[71] Hendrik Antoon Lorentz. The motion of electrons in metallic bodies i. *Koninklijke Nederlandse Akademie van Wetenschappen Proceedings Series B Physical Sciences*, 7:438–453, 1904 (cit. on pp. 67, 68, 75, 81).

[72] Peter J Lu, Peter A Sims, Hidekazu Oki, James B Macarthur, and David A Weitz. Target-locking acquisition with real-time confocal (tarc) microscopy. *Optics express*, 15(14):8702–8712, 2007 (cit. on pp. 40, 62).

[73] Enkeleida Lushi, Hugo Wioland, and Raymond E Goldstein. Fluid flows created by swimming bacteria drive self-organization in confined suspensions. *Proceedings of the National Academy of Sciences*, 111(27):9733–9738, 2014 (cit. on p. 91).

[74] Jonathan Machta and Steven M Moore. Diffusion and long-time tails in the overlapping lorentz gas. *Physical Review A*, 32(5):3164, 1985 (cit. on p. 79).

[75] M Cristina Marchetti, Yaouen Fily, Silke Henkes, Adam Patch, and David Yllanes. Minimal model of active colloids highlights the role of mechanical interactions in controlling the emergent behavior of active matter. *Current Opinion in Colloid & Interface Science*, 21:34–43, 2016 (cit. on p. 79).

[76] M Cristina Marchetti, Jean-François Joanny, Sriram Ramaswamy, Tanniemola B Liverpool, Jacques Prost, Madan Rao, and R Aditi Simha. Hydrodynamics of soft active matter. *Reviews of Modern Physics*, 85(3):1143, 2013 (cit. on pp. 51, 91, 105, 107, 117, 118, 119, 120, 124, 127, 132).

[77] K Martens, L Angelani, R Di Leonardo, and L Bocquet. Probability distributions for the run-and-tumble bacterial dynamics: An analogy to the lorentz model. *The European Physical Journal E*, 35(9):84, 2012 (cit. on p. 79).

[78] JR Melcher and GI Taylor. Electrohydrodynamics: a review of the role of interfacial shear stresses. *Annual review of fluid mechanics*, 1(1):111–146, 1969 (cit. on pp. 27, 62, 76, 86, 117, 131).

[79] N David Mermin and Herbert Wagner. Absence of ferromagnetism or antiferromagnetism in one-or two-dimensional isotropic heisenberg models. *Physical Review Letters*, 17(22):1133, 1966 (cit. on p. 15).

[80] Ralf Metzler and Joseph Klafter. The random walk's guide to anomalous diffusion: a fractional dynamics approach. *Physics reports*, 339(1):1–77, 2000 (cit. on p. 75).

[81] Shradha Mishra, Aparna Baskaran, and M Cristina Marchetti. Fluctuations and pattern formation in self-propelled particles. *Physical Review E*, 81(6):061916, 2010 (cit. on p. 118).

[82] Alexandre Morin and Denis Bartolo. Flowing active liquids in a pipe: Hysteretic response of polar flocks to external fields. *Physical Review X*, 2018 (cit. on p. 34).

[83] Alexandre Morin, David Lopes Cardozo, Vijayakumar Chikkadi, and Denis Bartolo. Diffusion, subdiffusion, and localization of active colloids in random post lattices. *Physical Review E*, 96(4):042611, 2017 (cit. on pp. 52, 69).

[84] Alexandre Morin, Nicolas Desreumaux, Jean-Baptiste Caussin, and Denis Bartolo. Distortion and destruction of colloidal flocks in disordered environments. *Nature Physics*, 13(1):63, 2017 (cit. on pp. 34, 52, 62, 72, 74, 76, 78, 119, 131).

[85] F Nadal, Françoise Argoul, P Kestener, B Pouligny, C Ybert, and A Ajdari. Electrically induced flows in the vicinity of a dielectric stripe on a conducting plane. *The European Physical Journal E*, 9(4):387–399, 2002 (cit. on pp. 66, 86).

[86] Vladimir I Nekorkin. *Introduction to nonlinear oscillations*. John Wiley & Sons, 2015 (cit. on p. 60).

[87] Daiki Nishiguchi, Ken H Nagai, Hugues Chaté, and Masaki Sano. Long-range nematic order and anomalous fluctuations in suspensions of swimming filamentous bacteria. *Physical Review E*, 95(2):020601, 2017 (cit. on pp. 18, 117, 124).

[88] Daiki Nishiguchi and Masaki Sano. Mesoscopic turbulence and local order in janus particles self-propelling under an ac electric field. *Physical Review E*, 92(5):052309, 2015 (cit. on pp. 8, 51, 91, 117).

[89] Jérémie Palacci, Cécile Cottin-Bizonne, Christophe Ybert, and Lydéric Bocquet. Sedimentation and effective temperature of active colloidal suspensions. *Physical Review Letters*, 105(8):088304, 2010 (cit. on p. 8).

[90] Jérémie Palacci, Stefano Sacanna, Anaïs Abramian, Jérémie Barral, Kasey Hanson, Alexander Y Grosberg, David J Pine, and Paul M Chaikin. Artificial rheotaxis. *Science advances*, 1(4):e1400214, 2015 (cit. on p. 52).

[91] Jeremie Palacci, Stefano Sacanna, Asher Preska Steinberg, David J Pine, and Paul M Chaikin. Living crystals of light-activated colloidal surfers. *Science*, page 1230020, 2013 (cit. on p. 91).

[92] Andrea Perna and Guy Theraulaz. When social behaviour is moulded in clay: on growth and form of social insect nests. *Journal of Experimental Biology*, 220(1):83–91, 2017 (cit. on p. 75).

[93] Alexandros Pertsinidis and Xinsheng Sean Ling. Statics and dynamics of 2d colloidal crystals in a random pinning potential. *Physical review letters*, 100(2):028303, 2008 (cit. on p. 95).

[94] Anton Peshkov, Eric Bertin, Francesco Ginelli, and Hugues Chaté. Boltzmann-ginzburg-landau approach for continuous descriptions of generic vicsek-like models. *The European Physical Journal Special Topics*, 223(7):1315–1344, 2014 (cit. on p. 107).

[95] G Quincke. Ueber rotationen im constanten electrischen felde. *Annalen der Physik*, 295(11):417–486, 1896 (cit. on pp. 27, 28, 62, 76, 91, 117).

[96] David A Quint and Ajay Gopinathan. Topologically induced swarming phase transition on a 2d percolated lattice. *Physical biology*, 12(4):046008, 2015 (cit. on pp. 22, 91).

[97] C Reichhardt and CJ Olson Reichhardt. Active matter transport and jamming on disordered landscapes. *Physical Review E*, 90(1):012701, 2014 (cit. on p. 91).

[98] Charles Reichhardt and CJ Olson Reichhardt. Depinning and nonequilibrium dynamic phases of particle assemblies driven over random and ordered substrates: a review. *Reports on Progress in Physics*, 80(2):026501, 2016 (cit. on pp. 91, 95).

[99] Craig W Reynolds. Flocks, herds and schools: A distributed behavioral model, 1987 (cit. on p. 76).

[100] Tim Sanchez, Daniel TN Chen, Stephen J DeCamp, Michael Heymann, and Zvonimir Dogic. Spontaneous motion in hierarchically assembled active matter. *Nature*, 491(7424):431, 2012 (cit. on pp. 8, 27, 51, 91, 117).

[101] Volker Schaller and Andreas R Bausch. Topological defects and density fluctuations in collectively moving systems. *Proceedings of the National Academy of Sciences*, 110(12):4488–4493, 2013 (cit. on pp. 9, 19).

[102] Volker Schaller, Christoph Weber, Christine Semmrich, Erwin Frey, and Andreas R Bausch. Polar patterns of driven filaments. *Nature*, 467(7311):73, 2010 (cit. on pp. 8, 9, 18, 27, 51, 91, 117, 118).

[103] Simon K Schnyder, Markus Spanner, Felix Höfling, Thomas Franosch, and Jürgen Horbach. Rounding of the localization transition in model porous media. *Soft Matter*, 11(4):701–711, 2015 (cit. on p. 81).

[104] Suraj Shankar, Mark J Bowick, and M Cristina Marchetti. Topological sound and flocking on curved surfaces. *Physical Review X*, 7(3):031039, 2017 (cit. on pp. 117, 119).

[105] Adi Shklarsh, Gil Ariel, Elad Schneidman, and Eshel Ben-Jacob. Smart swarms of bacteria-inspired agents with performance adaptable interactions. *PLoS computational biology*, 7(9):e1002177, 2011 (cit. on p. 91).

[106] R Aditi Simha and Sriram Ramaswamy. Hydrodynamic fluctuations and instabilities in ordered suspensions of self-propelled particles. *Physical review letters*, 89(5):058101, 2002 (cit. on p. 117).

[107] Orsolya Sipos, K Nagy, R Di Leonardo, and P Galajda. Hydrodynamic trapping of swimming bacteria by convex walls. *Physical review letters*, 114(25):258104, 2015 (cit. on p. 75).

[108] Thomas OE Skinner, Simon K Schnyder, Dirk GAL Aarts, Jürgen Horbach, and Roel PA Dullens. Localization dynamics of fluids in random confinement. *Physical review letters*, 111(12):128301, 2013 (cit. on pp. 76, 81).

[109] Alexandre P Solon, Jean-Baptiste Caussin, Denis Bartolo, Hugues Chaté, and Julien Tailleur. Pattern formation in flocking models: A hydrodynamic description. *Physical Review E*, 92(6):062111, 2015 (cit. on pp. 16, 108).

[110] Alexandre P Solon, Hugues Chaté, and Julien Tailleur. From phase to microphase separation in flocking models: The essential role of nonequilibrium fluctuations. *Physical review letters*, 114(6):068101, 2015 (cit. on pp. 95, 106).

[111] Alexandre. P. Solon and Julien Tailleur. Revisiting the Flocking Transition Using Active Spins. *Physical Review Letters*, 111(7):078101, 2013 (cit. on p. 36).

[112] Anton Souslov, Benjamin C van Zuiden, Denis Bartolo, and Vincenzo Vitelli. Topological sound in active-liquid metamaterials. *Nature Physics*, 13(11):1091, 2017 (cit. on pp. 117, 119).

[113] Dietrich Stauffer and Ammon Aharony. *Introduction to percolation theory*. CRC press, 1994 (cit. on pp. 76, 81).

[114] Ryo Suzuki and Andreas R Bausch. The emergence and transient behaviour of collective motion in active filament systems. *Nature communications*, 8(1):41, 2017 (cit. on p. 9).

[115] Ryo Suzuki, Christoph A Weber, Erwin Frey, and Andreas R Bausch. Polar pattern formation in driven filament systems requires non-binary particle collisions. *Nature physics*, 11(10):nphys3423, 2015 (cit. on p. 9).

[116] Daisuke Takagi, Jérémie Palacci, Adam B Braunschweig, Michael J Shelley, and Jun Zhang. Hydrodynamic capture of microswimmers into sphere-bound orbits. *Soft Matter*, 10(11):1784–1789, 2014 (cit. on p. 75).

[117] I Theurkauff, C Cottin-Bizonne, J Palacci, C Ybert, and L Bocquet. Dynamic clustering in active colloidal suspensions with chemical signaling. *Physical review letters*, 108(26):268303, 2012 (cit. on pp. 27, 91).

[118] Shashi Thutupalli, Ralf Seemann, and Stephan Herminghaus. Swarming behavior of simple model squirmers. *New Journal of Physics*, 13(7):073021, 2011 (cit. on pp. 8, 27, 91).

[119] John Toner. Reanalysis of the hydrodynamic theory of fluid, polar-ordered flocks. *Physical Review E*, 86(3):031918, 2012 (cit. on p. 17).

[120] John Toner, Nicholas Guttenberg, and Yuhai Tu. Hydrodynamic theory of flocking in the presence of quenched disorder. *arXiv preprint arXiv:1805.10326*, 2018 (cit. on pp. 23, 113).

[121] John Toner, Nicholas Guttenberg, and Yuhai Tu. Swarming in the dirt: Ordered flocks with quenched disorder. *arXiv preprint arXiv:1805.10324*, 2018 (cit. on pp. 23, 113).

[122] John Toner and Yuhai Tu. Long-range order in a two-dimensional dynamical xy model: how birds fly together. *Physical review letters*, 75(23):4326, 1995 (cit. on pp. 15, 17, 36, 41, 107, 117, 118, 119, 127, 129).

[123] John Toner and Yuhai Tu. Flocks, herds, and schools: A quantitative theory of flocking. *Physical review E*, 58(4):4828, 1998 (cit. on pp. 17, 117, 118, 119).

[124] John Toner, Yuhai Tu, and Sriram Ramaswamy. Hydrodynamics and phases of flocks. *Annals of Physics*, 318(1):170–244, 2005 (cit. on pp. 36, 51, 57, 117, 118, 124, 127).

[125] MA Topinka, BJ LeRoy, RM Westervelt, SEJ Shaw, R Fleischmann, EJ Heller, KD Maranowski, and AC Gossard. Coherent branched flow in a two-dimensional electron gas. *Nature*, 410(6825):183, 2001 (cit. on p. 95).

[126] AM Troyanovski, J Aarts, and PH Kes. Collective and plastic vortex motion in superconductors at high flux densities. *Nature*, 399(6737):665, 1999 (cit. on p. 95).

[127] Yuhai Tu, John Toner, and Markus Ulm. Sound waves and the absence of galilean invariance in flocks. *Physical review letters*, 80(21):4819, 1998 (cit. on pp. 17, 117, 118).

[128] Balth. van der Pol Jun. D.Sc. Lxxxviii. on "relaxation-oscillations". *The London, Edinburgh, and Dublin Philosophical Magazine and Journal of Science*, 2(11):978–992, 1926 (cit. on p. 49).

[129] Tamás Vicsek, András Czirók, Eshel Ben-Jacob, Inon Cohen, and Ofer Shochet. Novel type of phase transition in a system of self-driven particles. *Physical review letters*, 75(6):1226, 1995 (cit. on pp. 12, 43, 95, 106).

[130] Tamás Vicsek and Anna Zafeiris. Collective motion. *Physics Reports*, 517(3-4):71–140, 2012 (cit. on pp. 51, 91).

[131] Justin Werfel, Kirstin Petersen, and Radhika Nagpal. Designing collective behavior in a termite-inspired robot construction team. *Science*, 343(6172):754–758, 2014 (cit. on p. 91).

[132] Hugo Wioland, Enkeleida Lushi, and Raymond E Goldstein. Directed collective motion of bacteria under channel confinement. *New Journal of Physics*, 18(7):075002, 2016 (cit. on p. 51).

[133] Hugo Wioland, Francis G Woodhouse, Jörn Dunkel, John O Kessler, and Raymond E Goldstein. Confinement stabilizes a bacterial suspension into a spiral vortex. *Physical review letters*, 110(26):268102, 2013 (cit. on pp. 51, 117).

[134] Francis G Woodhouse and Jörn Dunkel. Active matter logic for autonomous microfluidics. *Nature communications*, 8:15169, 2017 (cit. on pp. 50, 60, 62).

[135] Francis G Woodhouse, Aden Forrow, Joanna B Fawcett, and Jörn Dunkel. Stochastic cycle selection in active flow networks. *Proceedings of the National Academy of Sciences*, 113(29):8200–8205, 2016 (cit. on pp. 50, 60, 62).

[136] Kun-Ta Wu, Jean Bernard Hishamunda, Daniel TN Chen, Stephen J DeCamp, Ya-Wen Chang, Alberto Fernández-Nieves, Seth Fraden, and Zvonimir Dogic. Transition from turbulent to coherent flows in confined three-dimensional active fluids. *Science*, 355(6331):eaal1979, 2017 (cit. on p. 51).

[137] Daizou Yamada, Tsuyoshi Hondou, and Masaki Sano. Coherent dynamics of an asymmetric particle in a vertically vibrating bed. *Physical Review E*, 67(4):040301, 2003 (cit. on p. 8).

[138] Jing Yan, Ming Han, Jie Zhang, Cong Xu, Erik Luijten, and Steve Granick. Reconfiguring active particles by electrostatic imbalance. *Nature materials*, 15(10):1095, 2016 (cit. on pp. 11, 12, 51).

[139] Le Yan, Antoine Barizien, and Matthieu Wyart. Model for the erosion onset of a granular bed sheared by a viscous fluid. *Physical Review E*, 93(1):012903, 2016 (cit. on p. 95).

[140] Xingbo Yang and M Cristina Marchetti. Hydrodynamics of turning flocks. *Physical review letters*, 115(25):258101, 2015 (cit. on p. 119).

[141] Syun-Ru Yeh, Michael Seul, and Boris I Shraiman. Assembly of ordered colloidal aggregrates by electric-field-induced fluid flow. *Nature*, 386(6620):57, 1997 (cit. on pp. 66, 86).

[142] David Yllanes, M Leoni, and MC Marchetti. How many dissenters does it take to disorder a flock? *New Journal of Physics*, 19(10):103026, 2017 (cit. on p. 22).

[143] Maria Zeitz, Katrin Wolff, and Holger Stark. Active brownian particles moving in a random lorentz gas. *The European Physical Journal E*, 40(2):23, 2017 (cit. on pp. 75, 79).

[144] He-Peng Zhang, Avraham Be'er, E-L Florin, and Harry L Swinney. Collective motion and density fluctuations in bacterial colonies. *Proceedings of the National Academy of Sciences*, 107(31):13626–13630, 2010 (cit. on p. 7).

[145] Jie Zhang, Erik Luijten, Bartosz A Grzybowski, and Steve Granick. Active colloids with collective mobility status and research opportunities. *Chemical Society Reviews*, 46(18):5551–5569, 2017 (cit. on p. 51).

[146] Andreas Zöttl and Holger Stark. Emergent behavior in active colloids. *Journal of Physics: Condensed Matter*, 28(25):253001, 2016 (cit. on p. 75).

Summary Directed collected motion within herds, swarms and flocks, is a phenomenon that takes place at all scales in living systems. Physicists have rationalized the emergence of such collective behavior. They have described these systems as active materials. These materials are assembled from self-propelled units that spontaneously move in the same direction. By experimentally studying synthetic flocks, this work uncovers some properties of polar active materials in situations that disfavor their self-organization: their dynamics in disordered environments and their response to external perturbations.

Colloidal rollers with alignment interactions are confined within microfluidic devices. At high density, they spontaneously form a flock which is characterized by the emergence of orientational long-ranged order. These colloidal flocks are prototypical realizations of polar active matter.

We have studied the response of a polar active liquid assembled from colloidal rollers. We have shown that they display a hysteretic response to longitudinal perturbations. We have theoretically accounted for this non-linear behavior. We have used this behavior to realize autonomous microfluidic oscillators.

We have also studied the dynamics of colloidal flocks that propagate through heterogeneous environments. Randomly positioned obstacles focalize flocks along favored channels that form a sparse and tortuous network. Increasing disorder leads to the destruction of flocks. We have demonstrated that the suppression of collective motion is a discontinuous transition generic to all polar active materials.

Résumé Le déplacement cohérent dirigé au sein de troupeaux, d'essaims, de nuées, prend place à toutes les échelles du vivant. En cherchant à rationaliser l'émergence de tels mouvements collectifs, les physiciens ont décrit ces assemblées comme des matériaux actifs. Ces matériaux sont formés de constituants auto-propulsés qui se déplacent spontanément dans une direction commune. Cette thèse expérimentale s'appuie sur la réalisation de troupeaux synthétiques pour explorer les propriétés de la matière active polaire dans des situations défavorables à son auto-organisation : leur dynamique en milieux désordonnés et leur réponse à des perturbations externes.

Des rouleurs colloïdaux aux interactions d'alignement sont confinés au sein de dispositifs microfluidiques. Au-delà d'une densité seuil, ils forment un troupeau caractérisé par l'émergence d'un ordre en orientation de longue portée. Ces troupeaux colloïdaux font office de prototypes de la matière active polaire.

Nous avons étudié la réponse d'un liquide actif polaire assemblé à partir de rouleurs colloïdaux. Nous avons montré que face à une perturbation longitudinale leur réponse est hystérétique. Nous avons expliqué théoriquement ce comportement non-linéaire et l'avons exploité pour réaliser des oscillateurs microfluidiques autonomes.

Nous avons également étudié la dynamique de troupeaux colloïdaux qui se propagent dans des environnements hétérogènes. La présence d'obstacles distribués aléatoirement focalise les troupeaux le long de chemins privilégiés qui forment un réseau épars et tortueux. Augmenter le désordre conduit à la destruction du troupeau. Nous avons démontré que la suppression du mouvement collectif consiste en une transition discontinue, générique à tous les matériaux actifs polaires.